Role of Regulated Necrotic Cell Death in Acute Injury: Ferroptosis, Necroptosis, Parthanatos

by

Andrew Michael Lamade

Bachelor of Arts, College of Wooster, 2013

Submitted to the Graduate Faculty of the

School of Medicine in partial fulfillment

of the requirements for the degree of

Doctor of Philosophy

University of Pittsburgh

2020

UNIVERSITY OF PITTSBURGH

SCHOOL OF MEDICINE

This dissertation was presented

by

Andrew Michael Lamade

It was defended on

August 17, 2020

and approved by

Valerian E. Kagan, Professor, Department of Environmental and Occupational Health

Robert S.B. Clark, Professor, Department of Critical Care Medicine & Pediatrics

Bennett Van Houten, Professor, Department of Pharmacology and Chemical Biology

Adam C. Straub, Associate Professor, Department of Pharmacology and Chemical Biology

Dissertation Director: Hülya Bayır, Professor, Departments of Critical Care Medicine & Pharmacology and Chemical Biology

Role of Regulated Necrotic Cell Death in Acute Injury:
Ferroptosis, Necroptosis, Parthanatos

Andrew Michael Lamade, PhD

University of Pittsburgh, 2020

Regulated necrotic cell death (RND) is a core feature of acute disease. Cells recognized as a liability to the organism are eliminated deliberately through genetically predetermined and tightly regulated mechanisms. Each death mode is initiated and propagated by distinct molecular mechanisms but, to varying degrees, are all interconnected. RND is a subset classification for all non-apoptotic death mechanisms, which are morphologically necrotic and immunogenic. The pro-inflammatory nature of RNDs hints to their physiologic antimicrobial and anti-neoplastic roles. However, acute pathology yields excessive RND that exacerbates and prolongs tissue dysfunction. The cycle of RND, inflammation, and secondary RND persists days to weeks after the inciting injury and is a clinically relevant therapeutic target. Ferroptosis, necroptosis, and parthanatos are three established RND mechanisms that cooperate across a range of diseases *in vivo*. Understanding the precise mechanisms and (co)regulation schemas for these pathways will enable more rational drug design and application.

In the first part of this work, we interrogate the role of mitochondrial Poly(ADP-ribose) polymerase (mtPARP1) in parthanotic ischemia-reperfusion and oxidative neuronal injury. Oxidative insult activates mtPARP1, which consumes nicotinamide adenine dinucleotide (NAD^+) and poly-ADP-ribosylates mitochondrial proteins. The action of mtPARP1 exacerbates mitochondrial pathology. In contrast, nuclear PARP1 preserves genomic DNA integrity. We developed a novel neuroprotective mitochondria-targeted PARP inhibitor, XJB-veliparib, which

localizes specifically to the inner mitochondrial membrane and matrix. XJB-veliparib preserves mitochondrial morphology and NAD^+ without hindering nuclear DNA repair. XJB-veliparib provides an opportunity to integrate mtPARP1 pathology and enables the development of clinically effective anti-parthanotic therapies.

In the second part of this work, we provide the first mechanistic reasoning for the interaction between ferroptosis and necroptosis. We demonstrate through computational, genetic, biochemical, and redox lipidomics approaches that phosphatidylethanolamine binding protein 1 (PEBP1) coregulates the ferroptosis and necroptosis death programs *in vitro* and *in vivo*. PEBP1 allosterically regulates RIP3 kinase activity to inhibit necroptosis. Genetic or pharmacologic conditions that dissociate PEBP1 from RIP3 and other binding partners promote ferroptosis. Interaction of PEBP1 with 15-lipoxygnease (15LOX) enables ferroptotic arachidonoyl-phosphatidylethanolamine (AA-PE) peroxidation. Our work indicates that anti-RND therapies must simultaneously target the ferroptosis and necroptosis pathways to maximize clinical benefit.

Table of Contents

List of Tables

List of Figures

Preface

Thank you to my graduate mentor and advisor Dr. Hülya Bayır for her patience and dedication to my personal and professional development.
She has instilled lessons that I endeavor to carry forward down the path of a physician scientist

Additionally, I wish to convey my gratitude to:
My advisors, Dr. Valerian Kagan and Dr. Robert Clark,
for their time, week-to-week guidance, and support.
My committee members, Dr. Adam Straub and Dr. Bennet Van Houten,
for their vital recommendations.

Most importantly, I wish to convey my endless love and gratitude to my parents
for their constant support and guidance.

The work done in this thesis would not have been possible without the diligent efforts of all co-authors and especially Tamil S. Anthonymuthu, Zhentai Huang, Claudette M. St Croix, Michael W. Epperly, Lina Du, Haider Dar, Oleksandr Kapralov, Indira Shrivastava, and Mark Ross.

This doctoral thesis work was supported by NIH grants:
F30HL142130, U19AI068021, R01NS084604, R01NS061817, R01NS076511

1.0 General Introduction and Review of Literature

1.1 Regulated Cell Death

Cell death is a necessary end that balances and preserves life. Cells recognized as dysfunctional and a liability to the organism are eliminated deliberately. Regulated cell death (RCD) involves tightly regulated, genetically predetermined mechanisms that bring about the irreversible cessation of all cellular homeostatic functions. RCD can lead to pathologic consequences if deficient or excessive (Thompson, 1995). A delicate balance must be maintained between rescuing the salvageable and clearing the way for restoration after injury. Recent discoveries have expanded our understanding of the complex and interconnected nature of RCD, as well as their diverse roles in health and disease.

The genetic underpinnings of RCD emerged in the mid-1960s with the observation that during development cells relied on the expression of endogenous genes to die (Lockshin & Williams, 1964). Early descriptions of cell death reaching back to the 19th century were recontextualized in the 1970s when the first ultra-structural hallmarks of various RCD mechanisms were reported (Vogt, 1842). The first attempts to classify cell death focused on morphology (Schweichel & Merker, 1973) and dichotomized death as either genetically programmed or accidental/circumstantial. Given several names over the decades, apoptosis was the first recognized genetically programmed cell death mechanism. Apoptotic cells exhibit cytoplasmic and nucleus (pyknosis) contraction, chromatin condensation (karyorrhexis), nuclear fragmentation, and retention of membrane integrity (J. Kerr, 1971; J. F. Kerr, Wyllie, & Currie, 1972). Later studies found that the remnants of apoptotic cells (apoptotic bodies) are efficiently

phagocytosed by monocyte lineage cells in an immunologically silent manner (Flora & Gregory, 1994).

In contrast, necrosis is characterized by early bioenergetic failure, cellular swelling, loss of plasma membrane integrity, and spillage of pro-inflammatory cytosolic constituents into the extracellular space. Morphologically necrotic death was considered the result of overwhelming trauma and not controlled. The insufficiency of this morphologic definition became increasingly evident over the following decades. Tumor necrosis factor-alpha (TNFα) was shown to alternatively induced apoptotic or a genetically-determined necrotic death (Laster, Wood, & Gooding, 1988). Since 2005, the Nomenclature Committee on Cell Death (NCCD) had generated consensus for the definition and interpretation of cell death mechanisms (Kroemer et al., 2005). Twelve distinct RCD mechanisms now recognized (Galluzzi et al., 2018). Each RCD mode is initiated and propagated by distinct molecular mechanisms but, to varying degrees, are all interconnected. RCD mechanisms manifest along a spectrum of morphological features ranging from fully necrotic to entirely apoptotic. Likewise, the immunomodulatory profile of RCD ranges from apoptosis' anti-inflammatory and tolerogenic profile to necrosis' pro-inflammatory and immunogenic characteristics.

Regulated necrotic cell death (RND) is a broad classification for all non-apoptotic RCD programs that demonstrate a necroptotic morphology and are immunogenic. Whenever a cell undergoes RND, its intracellular content is released as damage-associated molecular patterns (DAMPs) (Sarhan, Land, Tonnus, Hugo, & Linkermann, 2018). DAMPs function as paracrine signals that mediate immune recruitment and provoke secondary RND. The cycle of RND, inflammation, and secondary RND – collectively termed necroinflammation – persists days to weeks after the inciting injury and is a clinically relevant therapeutic target. Ferroptosis,

necroptosis, and parthanatos are three established RND mechanisms that (co)operate in acute oxidative injury induced by ischemia-reperfusion, trauma, and ionizing radiation injury. Understanding the precise mechanisms and (co)regulation schemas for these pathways enable more rational drug design and application. The following sections review the core mechanisms of these selected necrotic death pathways and consider their role in acute disease.

1.2 Ferroptosis

Ferroptosis is among the most recently characterized RCD pathways. Precise mechanistic descriptions of ferroptosis began emerging just over a decade ago (Seiler et al., 2008), and its official conceptualization as a distinct RND pathway followed shortly after (S. J. Dixon et al., 2012). It does not possess any readily identifiable morphologic features to differentiate it from other RND pathways. Similarly, there is no simple biomarker that defines ferroptosis execution, meaning ferroptosis is functionally defined. It is a glutathione peroxidase 4 (GPX4)-inhibitable, iron-dependent, and lipid peroxidation-driven process that leads to cell death (**Figure 1**), which is preventable by specific anti-ferroptotic lipophilic antioxidants (e.g., ferrostatins [Fer-1] and liproxstatins [Lip-1]), iron chelators, depletion of phospholipids containing oxidable polyunsaturated acyl chains, or lipoxygenase inhibitors (Angeli et al., 2014; V. E. Kagan et al., 2017; Wan Seok Yang et al., 2016; Wan Seok Yang et al., 2014). A growing body of evidence indicates ferroptotic lipid peroxidation is enzymatically regulated by 15-lipoxygenase (15LOX) and phosphatidylethanolamine binding protein 1 (PEBP1) complexes – as opposed to random, non-enzymatic free radical reactions (Wenzel et al., 2017). Ferroptosis is implicated in a diverse array of acute and chronic pathologic process, but many questions remain in terms of mechanisms

of its execution and regulation. Uncovering ferroptosis' precise regulatory mechanisms and relations to other RCDs will aid in the development of anti-RND treatment approaches. The ferroptosis program encompasses three major and intertwined metabolic pathways, **1**) glutathione, **2**) iron, and **3**) lipid peroxidation.

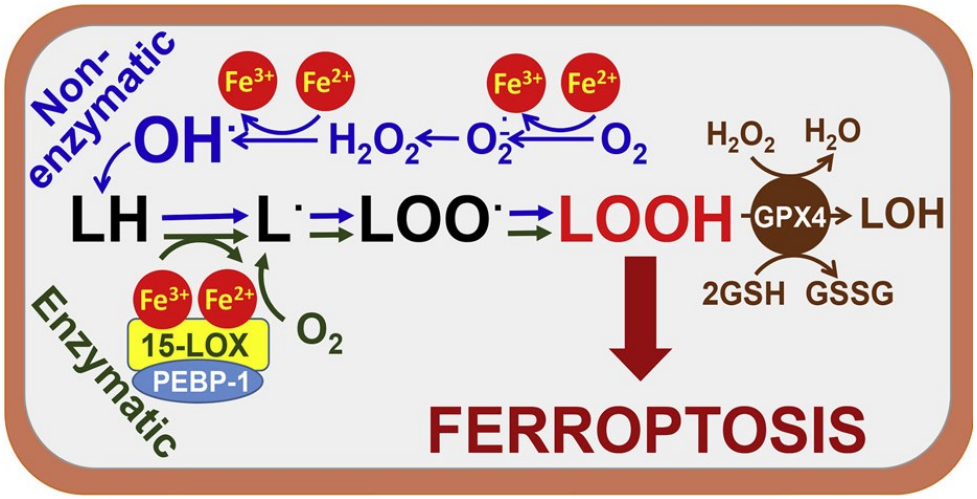

Figure 1. Ferroptosis Mechanism Overview

Ferroptosis is a regulated necrotic death mechanism governed by three major metabolic pathways, 1) glutathione (GSH), 2) labile iron (Fe3+), and 3) lipid peroxidation. Polyunsaturated free and esterified fatty acids (LH) are oxidized either enzymatically by non-heme iron-containing 15-lipoxygenase (15LOX) and phosphatidylethanolamine binding protein 1 (PEBP1) complexes or non-enzymatically by Fe3+-mediated free radical reactions. GSH depletion or glutathione peroxidase 4 (GPX4) inhibition results in the accumulation of peroxidated lipids (LOOH) and ferroptosis execution.

1.2.1 Glutathione and GPX4

Ferroptosis execution follows the accumulation of lethal lipid peroxides (L-OOH) and their downstream electrophilic breakdown products. Accordingly, ferroptosis sensitivity is influenced primarily by the activity of the endogenous systems responsible for preventing lipid peroxidation

– namely pathways surrounding the synthesis and activity of glutathione (γ-glutamylcysteinylglycine, GSH) or GPX4 (**Figure 2**).

GSH is required for many vital functions: **1**) modulating protein s-glutathionylation (Dalle-Donne, Rossi, Colombo, Giustarini, & Milzani, 2009); **2**) supplying cysteine for protein synthesis (A. Meister & Anderson, 1983); **3**) DNA synthesis (Suthanthiran, Anderson, Sharma, & Meister, 1990); **4**) immune response (Furukawa, Meydani, & Blumberg, 1987); **5**) metal ion (iron) storage and homeostasis (Jozefczak, Remans, Vangronsveld, & Cuypers, 2012); **6**) maintaining protein redox states (e.g., glutaredoxins); and **7**) providing an antioxidant defense (Lu, 2009). GSH is synthesized *de novo* in cytosol (Griffith & Meister, 1985) and is abundant (1-10 mM). First, cystine is imported in exchange for glutamate (Glu) export at a 1:1 ratio by the System Xc^- (SLC7A11) antiporter (**Figure 2**). Cystine is rapidly converted into cysteine (Cys) by thioredoxins (TRX) or by GSH. The rapid cystine to Cys conversion ensures cytosolic cystine levels remain low, favoring continued cystine import. However, the cytosolic-to-extracellular Glu gradient is more variable. Decreased cytosolic or increased extracellular Glu both inhibit System Xc^- activity. Increased mitochondrial glutaminolytic activity reduces cytosolic [Glu], while pathology-associated excitotoxic injury increases extracellular [Glu]. Both mechanisms lead to relative System Xc^- inhibition. Following import, Cys is combined with glutamate by glutamate-cysteine ligase (GLS) to yield γ-glutamylcysteine (γ-GluCys). The final addition of glycine to γ-GluCys by glutathione synthetase (GS) yields GSH. Intact GSH is also transported bi-directionally across the plasma membrane by several transporter families (Bachhawat, Thakur, Kaur, & Zulkifli, 2013).

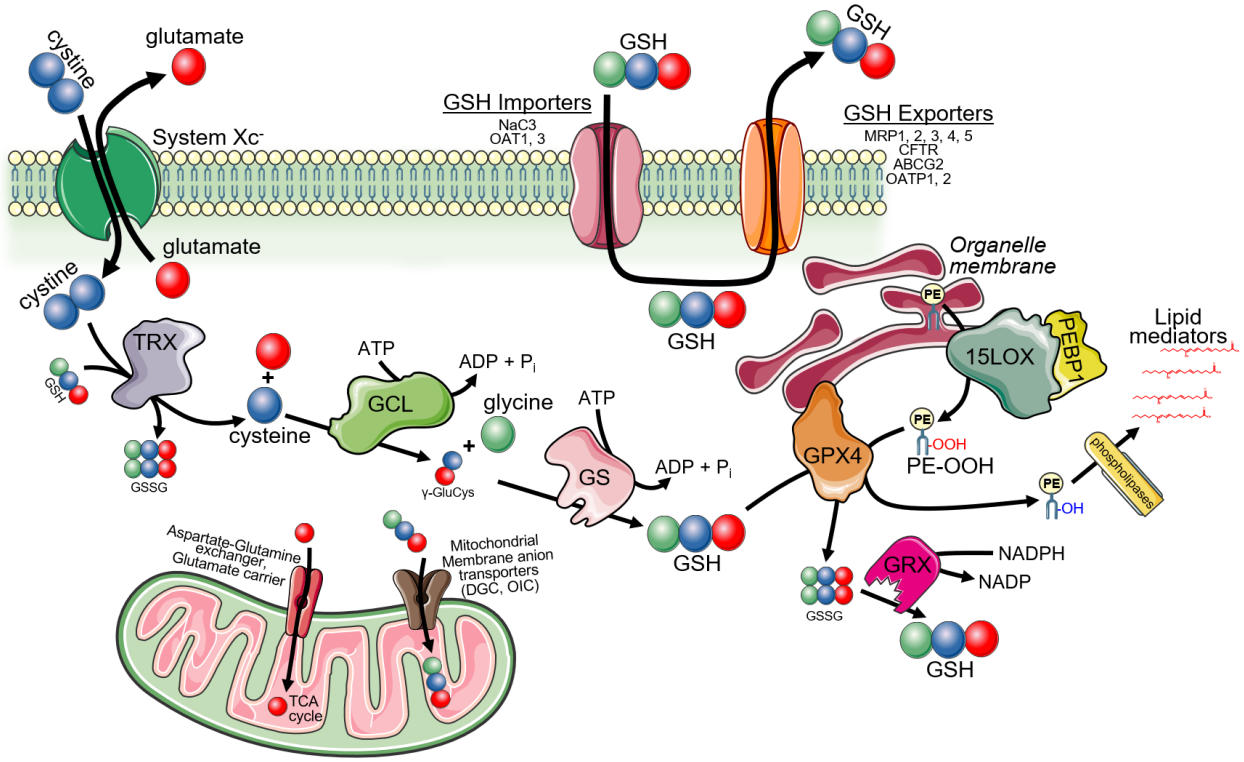

Figure 2. Metabolism of GSH.

Cystine is imported into the cells at the expense of glutamate by System X_c^- (SLC7A11). Increased cytosolic-to-extracellular Glu ratio promotes cystine import. Cystine is converted to cysteine by TRX or by GSH. Cysteine is then converted to γ-glutamylcysteine (γ-GluCys) by glutamate-cysteine ligase (GCL); GSH is formed by addition of a glycine group to γ-GluCys by glutathione synthetase (GS). Cytosolic Glu levels are strongly influenced by mitochondria metabolism. Mitochondria import Glu via aspartate glutamate exchanger and glutamate carrier. Glu is catabolized by glutaminolysis (conversion to α-ketoglutarate). The selenoprotein GPX4 uses 2 GSH to reduce membrane-associated lipid hydroperoxides (e.g., phosphatidylethanolamine hydroperoxide [PE-OOH]) into non-lethal lipid hydroxides. Oxidized GSSG is converted back to 2 GSH by glutathione reductase (GRX), which derives its reducing equivalents from NADPH.

Glutathione peroxidase (GPX) family is responsible for a plurality of enzymatic GSH oxidation reactions. GPX family members are among the most active constituents of cells' enzymatic antioxidant defense, second only to the superoxide dismutase (SOD)/catalase system. GPXs utilize GSH to reduce H_2O_2 or organic peroxides to H_2O or organic hydroxides, respectively. Eight members of the GPX family have been identified in humans (Brigelius-Flohé & Maiorino, 2013). GPX1-4 and 6 are selenoproteins, using selenocysteine (Sec) rather than Cys in their

catalytic redox cycle. Sec is essential for these GPXs due to its lower pK_a and reduction potential than Cys; mutants containing a Sec → Cys substitution are up to 100-fold less active vs. their wild-type counterparts. The primary substrate of GPX1, 3, 7, and 8 is H_2O_2. GPX1, 3 reduce H_2O_2 but also have expanded activity towards small molecule, soluble organic peroxides (e.g., peroxidated free fatty acids).

GPX4 is unique; it is the only GPX capable of reducing membrane-bound L-OOH (e.g., peroxidated phospholipids, cholesterols, and cholesterol esters) (Brigelius-Flohé & Maiorino, 2013). GPX4 localizes to most cellular compartments. It is particularly enriched in mitochondria (m-GPX4) owing to the organelle's high preponderance of reactive oxygen species (ROS) and oxidizable polyunsaturated lipids (i.e., tetralinolyl cardiolipin, CL). GPX4's large hydrophobic surface enables it to interface with lipid membranes (Ursini & Bindoli, 1987). The cationic region near GPX4's active site coordinates the anionic lipid headgroup to orient the peroxidated acyl chain towards GPX4's selenocysteine redox center (Cozza et al., 2017). Mechanistically, GPX4 and other selenocysteine GPXs utilize a two-stage ping-pong mechanism. The first step reduces the target lipid peroxide (L-OOH → L-OH) while oxidizing selenocysteine (GPX4-Se^- [selenol] → GPX4-SeO^- [selenenic acid]). An additional oxidation step may be possible at this point (GPX4-SeO^- [selenenic acid] → GPX4-$SeOO^-$ [seleninic acid]), reducing an additional L-OOH (Borchert et al., 2018). In step two, GSH is oxidized to regenerate reduced selenocysteine (GPX4-SeO^- + 2GSH→ GPX4-Se^- + GS-SG) and active enzyme (Brigelius-Flohé & Maiorino, 2013). Glutathione reductase then converts oxidized GSH (GS-SG dimers) back into free GSH using reducing potential derived from NADPH. Alternatively, GSH-mediated reduction can proceed non-enzymatically. In this case, GSH reacts directly with hydroxyl radical, nitric oxide, or superoxide radical (Dringen, 2000) producing the strongly oxidizing thiyl radical ($GS^\bullet$). The

reactive thiyl radical is a liability for cells. Therefore, this non-enzymatic mechanism is likely not the primary pathway of GSH-mediated protection, but thiyl radical abundance, measured by electron paramagnetic resonance spectrometry (EPR), can reflect the cellular redox state (Sagristá, GarcÍa, De Madariaga, & Mora, 2002; Sturgeon et al., 1998).

Ferroptosis is induced *in vitro* by small molecule inhibitors of the GSH and GPX4 systems. Erastin inhibits the system Xc^- cystine/glutamate antiporter, blocking *de novo* GSH production (S. J. Dixon et al., 2012). (1*S*,3*R*)-RSL3 ("RLS3") directly inhibits the GSH-consuming phospholipid peroxidase GPX4. Similarly, knockdown or knockout of GPX4 is enough to induce ferroptosis. Pharmacologic or genetic suppression of the GSH/GPX4 system similarly leads to an overwhelming accumulation of lipid peroxidation products and death *in vivo*. Homozygous knockout of *Gpx4* (*Gpx4*$^{-/-}$) is embryonically lethal by midgestation in mice (E7.5) (Imai et al., 2003; Yant et al., 2003). Neuron-specific *Gpx4*$^{-/-}$ mice were similarly nonviable (Seiler et al., 2008). Even beyond the embryonic and neonatal stages of rapid development, GPX4 is necessary for the survival of adult animals. Tamoxifen-induced whole-body GPX4 ablation (*Gpx4*$^{f/f}$*;CreER*^{T2}) caused a precipitous decrease in body weight, mitochondrial dysfunction, neurodegeneration, acute renal failure, and was universally lethal by the third week of induction (Angeli et al., 2014; Yoo et al., 2012). The lethality of GPX4 inhibition in cells and tissue can be countered by specific anti-ferroptotic agents (e.g., lipophilic antioxidants, iron chelators, genetic/pharmacologic lipoxygenase inhibition).

1.2.2 Iron in Ferroptosis: Enzymatic vs. Non-Enzymatic Lipid Peroxidation

Ferroptosis is iron-dependent (S. J. Dixon et al., 2012). Disturbances in iron homeostasis through inhibition of nuclear receptor coactivator 4 (NCOA4)-dependent ferritinophagy or iron-

responsive element-binding protein 2 (IREB2) alters iron uptake, metabolism, and expression of storage-related genes, which influence ferroptosis sensitivity (Scott J. Dixon et al., 2012; M. Gao et al., 2016; X. Sun et al., 2015). Limiting iron import and availability (iron chelators) reliably protects against ferroptosis (Cozzi et al., 2019; Yao et al., 2019). Conversely, activation of the RAS-RAF-MEK pathway can promote iron uptake through the transferrin (TFR) receptor that is linked to enhanced ferroptosis sensitivity (W. S. Yang & Stockwell, 2008). Debate endures concerning the mechanism of iron-dependent ferroptotic lipid peroxidation – whether it is regulated by iron-containing enzymes or if it is the result of random, free radical Fenton reactions. Growing evidence points towards the controlled, enzymatic mechanism, but review of iron chaperoning and mechanisms of iron-dependent lipid oxidation helps highlight the merits and potential deficiencies for each possibility. Iron (Fe) in cells can be categorized into three main pools: **1**) stored iron (ferritin), **2**) cofactors (heme, iron-sulfur clusters, non-heme mono-/diiron centers) and **3**) labile iron (mostly ferrous Fe^{2+}). Cofactor iron is the dominant (>90% total iron) and steady-state form. In comparison, the amount of iron stored with ferritin can vary widely over time (Chakrabarti et al., 2015). Labile iron is everything else that is not coordinated as a cofactor or with ferritin.

Based on cytosolic reduction potential, almost all of this low molecular weight labile iron is ferrous (Fe^2, Fe(II)) (Williams, 1982), with the level of free, chelatable iron in cells typically ranging from 0.5 to 5 μM (Y. Ma, de Groot, Liu, Hider, & Petrat, 2006; Petrat, de Groot, Sustmann, & Rauen, 2002). While free ferric (Fe^{3+}) iron can interact with a variety of small molecules (e.g., citrate, ATP/AMP, inositol phosphates), labile ferrous iron preferential interacts with free thiols – Cys and GSH. In most cell types, GSH is on the order of a 1000-fold more abundant than free Cys (Alton Meister, 1988). An estimated 95% of labile Fe^{2+} forms 1:1 complexes with GSH (Hider &

Kong, 2013; Patel et al., 2019). Since labile iron is only a small fraction of total cellular iron, only a minor proportion (~0.1 mol % in neurons) of all GSH participates in Fe^{2+} coordination (Xiaojian Sun et al., 2006). Labile iron is strictly chaperoned as it transits between cellular compartments to minimize reactivity. The Poly(rC)-binding protein (PCBP) family serves a leading role in cellular Fe^{2+} chaperoning and distribution to sites of storage and utilization (Philpott & Jadhav, 2019).

PCBPs are multifunctional proteins that are capable of binding nucleic acids, proteins, and iron. PCBP1 and PCBP2 are iron chaperones and, despite their high structural conservation, are independently required for normal development (Philpott & Jadhav, 2019). PCBPs coordinates Fe^{2+}, preferably GSH-Fe^{2+} complexes (Patel et al., 2019), to/from storage sites (ferritin) (Leidgens et al., 2013), transport proteins (divalent metal ion transporter, ferroportin 1) (Yanatori, Richardson, Imada, & Kishi, 2016), and various iron-containing enzymes (prolylhydroxylase, deoxyhypusine hydroxylase, heme oxygenase-1, BolA family member-2) (Frey et al., 2014). PCBPs have only a minor role in iron-sulfur cluster or heme synthesis. PCBP1 is recognized for its role in the delivery of Fe^{2+} to enzymatic mono- and dinuclear iron centers, which is necessary for the recipient protein's catalytic function. Non-heme iron-containing enzymes are necessary for ferroptosis – from interconversion of PUFAs by fatty acid desaturases (Lee, Lee, Kang, & Park, 2016) to the enzymatic peroxidation of PL-PUFAs by lipoxygenases (Boyington, Gaffney, & Amzel, 1993; Reimann, Huth, Thiele, & Thiele, 2002). PCBP2 is more associated with the chaperoning of iron at membranes (e.g., transporters, heme iron released from endoplasmic reticulum) (Yanatori, Richardson, Toyokuni, & Kishi, 2017). PCBP1-deficiency in the liver results little to no increase in oxidized PLs. Of the few PL-OOH species that were increased with PCBP1 inhibition, including 4 of the 53 identified oxidized phosphatidylcholine species, none were previously linked to ferroptosis execution (V. E. Kagan et al., 2017; Stoyanovsky et al., 2019). It

is important to recognize that the direct effect of PCBP1-deficiency on labile iron levels was not measured in these experiments, nor was pro-ferroptotic stimuli applied. Therefore, further investigation is warranted to decipher the role of PCBPs in ferroptosis.

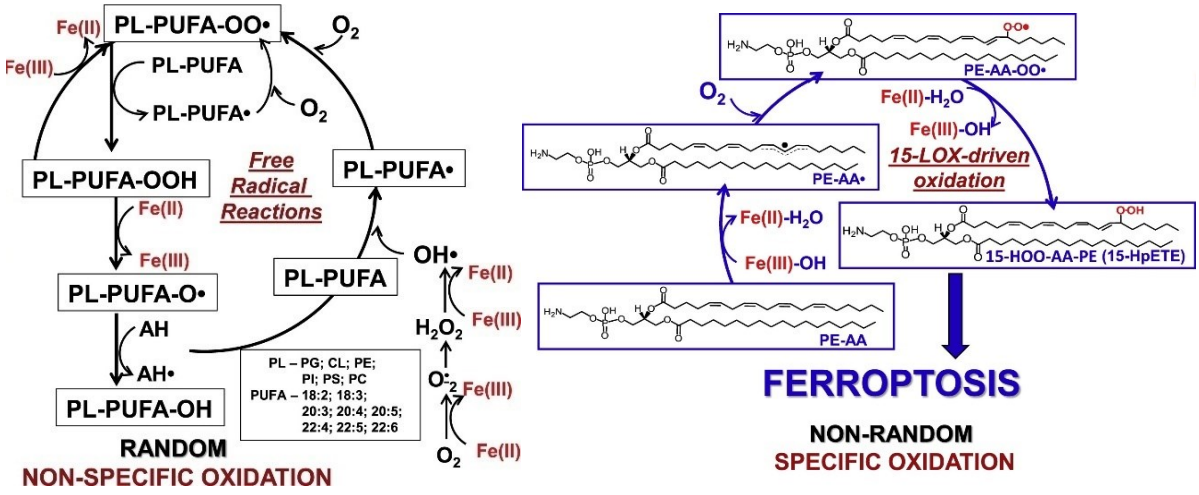

Figure 3. Reaction Mechanism of Random Non-enzymatic vs. Enzymatic Peroxidation of Membranous PUFA-containing Phospholipids.

Both non-enzymatic (non-selective, *left*) and enzymatic (selective, *right*) lipid oxidation starts with abstraction of a bis-allylic hydrogen, rearrangement of the radical resonance structure, and addition of two oxygens (molecular oxygen) to form a peroxyl radical and final product, a hydroperoxyl lipid. The random, non-specific mechanism is mediated by labile, free iron where the initial oxidizing radical arises from endogenous H_2O_2 that is converted into a hydroxyl radical via a Fenton reaction. The initial radical can then interact any of the bis-allylic hydrogen contained in the PUFA-containing phospholipid (PL-PUFA). The reaction rate increDases as the number of readily abstractable bis-allylic hydrogens increases (most cells contain PUFAs with 2, 3, 4, 5, 6 double bonds per acyl chain). However, the position of oxidation addition is random. In comparison, oxidation of PL-PUFA by lipoxygenases (e.g., 15-LOX, 15LOX) is substrate selective, site-specific, and stereo-selective. 15LOX complexes with phosphatidylethanolamine binding protein 1 (PEBP1), yielding the functional unit of regulated ferroptotic lipid oxidation. The 15LOX/PEBP1 complex preferentially oxidizes arachidonic acid (AA, 20:4)- and adrenic/docosatetraenoic acid (AdA, 22:4)-containing phosphatidylethanolamine (PE) yielding specific 15-HOO-AA-PE species. Unlike the random free radical mechanism, the addition of molecular oxygen to AA-PE by 15LOX/PEBP1 is position selective.

Iron catalyzes both non-enzymatic and enzymatic lipid peroxidation (**Figure 3**). Non-enzymatic, labile Fe^{2+}-catalyzed lipid oxidation begins with the conversion of endogenous H_2O_2 to the highly reactive hydroxyl radical (HO·) or various high energy oxo-ferryl species via the

Fenton reaction (Merkofer, Kissner, Hider, Brunk, & Koppenol, 2006; Yamamoto, Koga, & Nagaoka, 2012). While the rate constant of free iron with H_2O_2 is typically low ($< 10^2$ $M^{-1}s^{-1}$), Fe-ligation may significantly accelerate the reaction (up to 10^4 $M^{-1}s^{-1}$). These radicals react rapidly with nearby macromolecules in a near diffusion limited rate. In the context of lipid peroxidation, HO· abstracts the bis-allylic hydrogen in polyunsaturated acyl chains (PUFA)-containing lipids, and in the presence O_2, a peroxyl radical intermediate (LO_2·) forms. With the continued aid of labile iron, the lipid radical oxidizes nearby PUFA-containing lipids in a chain reaction. The rate of non-enzymatic oxidation is correlated to the level of PUFA unsaturation (rate increases from 2 → 6 double bonds), but this mechanism lacks any positional or stereo-specificity. Therefore, if ferroptotic lipid oxidation was governed primarily through a random free radical mechanism, all classes of soluble PUFAs and PL-PUFAs would be equal opportunity oxidation targets. L-OOH speciation would depend solely on the abundance of a given PUFA or PL-PUFA, their relative level of unsaturation, and their proximity to free Fe^{2+}/H_2O_2 (HO· reactions are diffusion-limited). Since phosphatidylcholine is the most abundant membrane lipid, PC-OOH should represent the majority of L-OOH generated during ferroptosis. Instead, the ferroptosis program favors the accumulation of peroxidated AA-PE and AdA-PE (**Figure 4**), specifically 15-hydroxyeicosatetraenoic 15-HpETE-PE (V. E. Kagan et al., 2017; Wenzel et al., 2017). Consequently, this deviation in selectivity of the peroxidation from this principle of raw oxidizability governed by the number of bis-allylic sites can be viewed a strong argument against the participation of free radical chemical reaction in the overall peroxidation process.

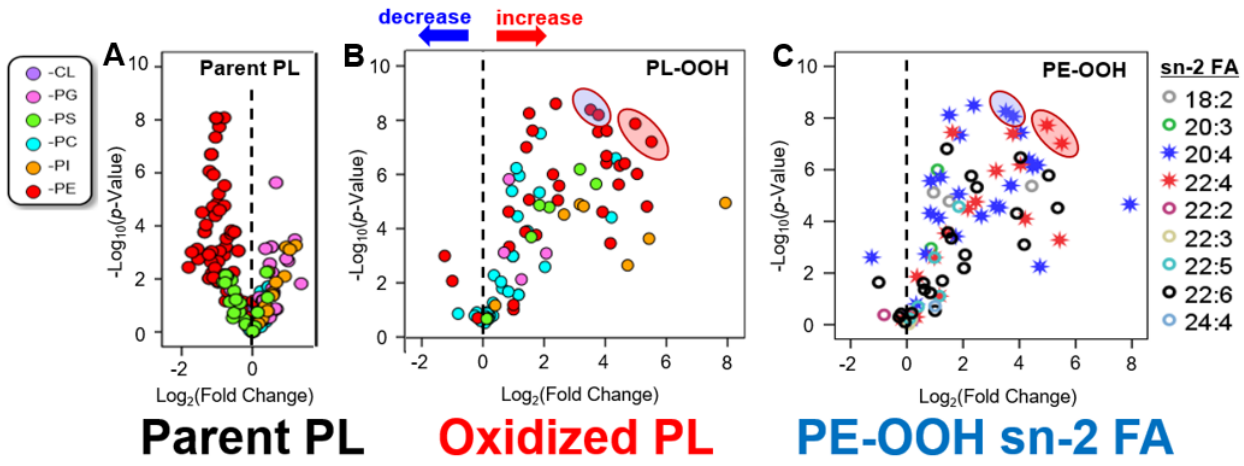

Figure 4. Ferroptosis Preferentially Induces Oxidation of Arachidonic (20:4) and Adrenic acid (22:4)-containing Phosphatidylethanolamine Species

(**A**) Volcano plot RSL3-induced changes in levels of non-oxidized parent phospholipids (PL) and (**B**) levels of oxygenated phospholipids in ferroptotic (cell death ≥15%, number of replicate data points = 18) versus live cells (cell death ≤15%, number of replicate data points = 26). (**C**) Volcano plot of RSL3-induced changes in oxygenated phospholipids after recategorization based on fatty acyls (FA) in *sn*-2 positions (CL = cardiolipin, PG = phosphatidylglycerol, PS = phosphatidylserine, PC = phosphatidylcholine, PI = phosphatidylinositol, PE = phosphatidylethanolamine)

The enzymatic ferroptosis mechanism can be divided into two arms **1**) production of oxidizable PL-PUFA and **2**) regulation of iron-dependent PL-PUFA peroxidation. First, cells must have access to AA and AdA. The majority of AA/AdA is obtained through diet or converted from ω-6 PUFAs (e.g., linoleic acid) by the action iron-containing Δ6 and Δ5 fatty acid desaturases and elongases (Lee et al., 2016). Esterification of PUFA into PL requires the formation of intermediate PUFA-CoA. Acyl-CoA synthetase long-chain 4 (ACSL4) generates of AA-CoA and other long-chain polyunsaturated-CoAs (Küch et al., 2014). Genetic or pharmacologic (triacin C, thiazolidinediones) ACSL4 inhibition protects against ferroptosis, including in *Gpx4*$^{-/-}$ cells (S. Doll et al., 2017; V. E. Kagan et al., 2017). Inhibition of the GSH/GPX4 system or complex injury (e.g., acute brain injury, ischemia-reperfusion injury, asthma) promotes the formation of 15LOX-PEBP1 complexes – the "redox phospholipoxysome" (Wenzel et al., 2017). Typically, 15LOX

preferentially oxidizes solubilized free AA, but its union with PEBP1 induces a substrate specificity switch to AA/AdA-containing PE. Formation of the 15LOX-PEBP1 complex is associated with 15-HpETE-PE accumulation. Disruption of the 15LOX-PEBP1 complex by expression of the $PEBP1^{P112E}$ mutant prevents ferroptosis and reduces 15-HpETE-PE levels. Overexpression or knockdown of 15LOX and PEBP1 enhances or inhibits ferroptosis, respectively (V. E. Kagan et al., 2017; Wenzel et al., 2017). This evidence indicates ferroptotic lipid oxidation is mediated enzymatically by lipoxygenases, regulated by PEBP1, and executed through the formation of specific PE-OOH signals.

Several questions surrounding the 15LOX/PEBP1 mechanism needs to be resolved. Raw 15-LOX inhibition potency is not a good predictor of the anti-ferroptotic effect (Shah, Shchepinov, & Pratt, 2018). Zileuton, a specific 5-LOX inhibitor, protects against glutamate toxicity (system Xc^- inhibition)-induced ferroptosis in HT22 cells (Y. Liu et al., 2015), and 15-LOX (± 12-LOX) inhibition by PD146176 or baicalin inhibits ferroptosis in a variety of *in vitro* and *in vivo* models (Kenny et al., 2019; Y. Xie et al., 2016). LOX inhibitor potency is measured by the capacity to block unesterified PUFA peroxidation, which is not relevant for ferroptosis. Instead, effective anti-ferroptotic LOX inhibitors should specifically inhibit the 15LOX-PEBP1 or other ferroptosis-implicated enzymatic complexes. Second, earlier work indicated ferroptosis-defining lipophilic antioxidants (Lip-1, Fer-1) function as radical trapping antioxidants and block propagation of the non-enzymatic free radical chain reaction (Zilka et al., 2017). While the physiologic relevance of liposomal model systems is datable, Zilka *et al.* found Fer-1 did not alter levels of 5-, 12-, and 15-PUFA-OOH in ferroptosis (Zilka et al., 2017). Since unesterified HpETE is has not been found to be a useful biomarker of ferroptosis *in vivo*, Fer-1's effect on HpETE levels is immaterial. Fer-1 treatment reduces levels of 15LOX-PEBP1 synthesized 15-HpETE-PE *in vitro* (data unpublished).

Further, Lip-1 treatment reduces 15-HpETE-PE levels but increases levels of the chemically reduced counterpart, 15-HETE-PE (see results section). Rather than only blocking propagation of the free radical chain reaction, Lip-1 may have a role as a GPX4 mimetic.

1.2.3 Role of Mitochondria in Ferroptosis

Ferroptosis is a pro-oxidative and iron-dependent RND that entails formation of perilous L-OOH. Mitochondria are significant sources of ROS, participate in iron homeostasis, and contain many oxidizable lipids – including phosphatidylethanolamine (PE) species, which are produced from phosphatidylserine (PS) by inner mitochondrial membrane (IMM)-localized PS decarboxylase, Psd1p. The ETC is a major site of superoxide anion radical ($O_2^{\cdot-}$) and hydrogen peroxide (H_2O_2) production. ETC dysregulation following acute injury enhances ROS levels, which fuel non-enzymatic lipid peroxidation (discussed in the following sections) (Jastroch, Divakaruni, Mookerjee, Treberg, & Brand, 2010; Loschen, Azzi, Richter, & Flohé, 1974). Dehydrogenases also generate significant amounts of ROS in mitochondria. Chief among them is the TCA cycle's α-ketoglutarate dehydrogenase (α-KGDH) and pyruvate dehydrogenase complex (PDHC), whose E3 subunits generates $O_2^{\cdot-}$/ H_2O_2 at a rate dependent on the NADH/NAD^+ ratio (Adam-Vizi & Tretter, 2013; Mailloux, Young, O'Brien, & Gill, 2018; O'Brien, Chalker, Slade, Gardiner, & Mailloux, 2017). Additionally, mitochondrial α-glycerophosphate dehydrogenase (α-GPDH, GPD2) is an IMM protein that, together with cytosolic α-GPDH (GPD1), shuttle NADH-derived reducing equivalents across the IMM. As mitochondrial Ca^{2+} levels increase, particularly following ischemic, traumatic, or excitotoxic injury, GPD2-associated ROS production increases, and its NADH shuttling function is inhibited. Regardless of origin, nascent mitochondrial $O_2^{\cdot-}$ is rapidly dismutated to H_2O_2 by colocalized mitochondrial manganese superoxide dismutase

(MnSOD, SOD2). H_2O_2 is then eliminated in mitochondria by the GPX system or diffuses out into cytosol to be eliminated by catalase. Alternatively, select metalloenzymes, particularly heme-peroxidases, use H_2O_2 as a source of oxidizing equivalents to feed a variety of reactions yielding oxidized products, including oxidized lipids with signaling functions (Valerian E Kagan et al., 2005; Kanner, German, & Kinsella, 1987).

Mitochondria have two independent defense systems against ferroptosis, ferroptosis suppressor protein 1 (FSP1; apoptosis-inducing factor mitochondria-associated 2, AIF2) and GPX4 (Sebastian Doll et al., 2019). FSP1 is an NADH:ubiquinone oxidoreductase that chemically reduces coenzyme Q_{10} (CoQ_{10}, ubiquinone) and, in unison with GPX4 and α-tocopherol (α-TOH, Vitamin E), suppresses accumulation of ferroptotic L-OOH (Elguindy & Nakamaru-Ogiso, 2015; Frei, Kim, & Ames, 1990). NADH, and by extension TCA cycle flux, is necessary for FSP1 function. Decreased mitochondrial NADH (e.g., due to parthanotic mtPARP1 activity) inhibits FSP1 and sensitizes cells to ferroptosis. The GPX system directly eliminates intramitochondrial H_2O_2, and GPX4 reduces L-OOH. A significant proportion (10-15%) of cellular GSH is partitioned to mitochondria (Griffith & Meister, 1985). GSH is passively transported across the outer mitochondrial membrane (OMM) and is actively transported across the IMM by dicarboxylate carrier (DIC, SLC25A10) or the 2-oxoglutarate carrier (OGC, SLC25A11) (Lash, 2006; Meijer, Brouwer, Reijngoud, Hoek, & Tager, 1972). Beyond consuming GSH in GPX-mediated reactions, mitochondrial metabolism indirectly modulates GSH synthesis. Glutaminolytic glutamate dehydrogenase (GDH) and alanine/aspartate transaminases (TAs) convert glycine (Gln) and Glu into α-ketoglutarate (α-KG) (Watford, 2000). Increased mitochondrial glutaminolysis activity reduces the cytosolic-to-extracellular Glu ratio, which inhibits system Xc^- Cystine/Glu antiporter activity, cystine import, and *de novo* GSH production (Lu, 2009). Glutaminolysis' downstream

effects on α-KG levels and tricarboxylic acid (TCA) cycle flux may be as important in ferroptosis sensitization as its indirect effects on cytosolic Glu levels and system Xc^-. Blocking any part of the glutaminolysis pathway – glutamine (Gln) import, glutaminase 2 (GLS2, glutamine → Glu conversion), or transaminases (Glu → α-KG) – inhibits ferroptosis *in vivo* and in select *in vitro* models (Minghui Gao, Monian, Quadri, Ramasamy, & Jiang, 2015).

Mitochondrial glutaminolysis activity is required for Cys deprivation-induced (CDI) ferroptosis, but mitochondria are dispensable for GPX4 inhibition-induced ferroptosis (Minghui Gao et al., 2019). The role of mitochondria in ferroptosis is model-dependent and likely differs *in vitro* vs. *in vivo*. Mitochondrial copy number reduction, Δψm depletion, ETC inhibition confer resistance to CDI ferroptosis (Minghui Gao et al., 2019). Conversely, α-KG, succinate, fumarate, or malate supplementation sensitizes cells to CDI ferroptosis, suggesting that anaplerosis mediates glutaminolysis' pro-ferroptosis effect. Providing TCA intermediates increases TCA flux, $NADH/NAD^+$ ratio, and ETC oxygen consumption, which each promote ROS formation that may fuel non-enzymatic ferroptotic lipid peroxidation – particularly in the setting of relative GPX4 inhibition (Cys deficiency). However, this proposed anaplerosis mechanism lacks specificity. Mitochondrial ROS contributes to many death modes. For example, mitochondrial ROS activates the pro-apoptosis cytochrome *c*/CL peroxidase complex (Valerian E. Kagan et al., 2009), receptor interacting kinase 1 (RIP1) oxidation promotes necroptosis (Y. Zhang et al., 2017), and mitochondrial ROS activates mt-PARP1 and parthanatos (Brunyanszki, Szczesny, Virag, & Szabo, 2016a). An alternate explanation for glutaminolysis' pro-ferroptotic effect focuses on boosting citrate levels, which is an important source of acetyl-CoA used in oxidizable fatty acid metabolism (Minghui Gao et al., 2015; Luo et al., 2018). The interaction between mitochondria and ferroptosis is complex and current studies provide conflicting, model-dependent explanations. Further study

of mitochondria's role in ferroptosis across a broad range of conditions, cell/tissue types, and disease states, is needed.

1.2.4 Ferroptosis Execution

The greatest unexplored mystery of ferroptosis is how it is executed. In other words, what is the most proximate cause of cellular demise after cells irreversibly commit to ferroptosis? Other RND mechanisms executed by the assembly of lethal membrane pores (necroptosis, pyroptosis) or direct fragmentation DNA (parthanatos), but there is no discernible ferroptosis executor. The answer may be simple. L-OOH are broken down non-enzymatically in iron- or copper-mediated reactions into a wide variety of small mono- or multifunctional reactive electrophiles (Ayala, Muñoz, & Argüelles, 2014; Schopfer, Cipollina, & Freeman, 2011); the most studied of these are 4-hydroxynonenal (4-HNE) and malondialdehyde (MDA). These electrophiles have a short half-life, on the order of minutes. They are either enzymatically eliminated (via glutathione-*S*-transferases, aldehyde dehydrogenase, aldo-keto reductases) or react with nucleophilic functional groups on DNA or peptides/proteins via Michael addition to form various activity-modifying or toxic adducts (Spickett, 2013). However, the fact that virtually any L-OOH may breakdown into 4-HNE raises the question of why cells bother with specific PE-OOH production by the 15LOX-PEBP1 complex. The specific identity of the L-OOH accumulated does not matter in some ferroptosis models. Shah *et al*. reported that Fer-1 inhibitable death follows accumulation of ~20 μM of total free 5-/12-/15-HpETE (Shah et al., 2018). Since accumulation of unesterified HpETE is not typically associated with ferroptosis, the relevance of this finding is questionable. Regulation of the 15LOX-PEBP1 complex formation provides cells with a mechanism to turn on ferroptosis, although the mechanisms governing this union is currently unknown. PE-OOH's membrane

disorganizing geometry and specific breakdown products may serve as specific ferroptosis execution signals. Proteolipidomic studies are ongoing in search of specific ferroptosis executioners.

1.2.5 Defining the Physiologic Roles of Ferroptosis

The physiologic and evolutionary role of ferroptosis is unclear. It may be a method to eliminate cells with irreparably dis-coordinated redox regulation systems. Rather than allowing such dysfunctional cells to persist – spreading lethal and immunoactive oxidized lipid metabolites – ferroptosis helps eliminate these liabilities from the community. Emerging evidence points towards ferroptosis' adaptive role in the elimination of malignant cells or cells infected with intracellular pathogens. Compared to other RCDs that rely on the energy-intensive activity of kinases, proteases, or transcription/translation, ferroptosis activation lies on a narrower and more universal biochemical pathway involving cysteine availability. Cys is imported, subsequently converted into GSH, which in turn fuels the GPX4-mediated inhibition of pro-ferroptotic lipid peroxidation. While the balance of known and unknown negative regulators of ferroptosis varies between different cells and tissues, one might surmise that a unified cell death system that responds to a single metabolic input (i.e., Cys/GSH) can be useful in various circumstances (Dixon, 2017). Even transient disruptions or increased local competition for Cys may promote ferroptosis.

Chronically increased oxidative stress is observed in malignant cells, particularly in solid tumors (Nogueira & Hay, 2013). Increased ROS is not only a result of increased proliferation and metabolic activity but also from reduced levels or dysregulation of various antioxidant systems. While compensatory mechanisms often develop, cancer cells remain sensitized to chemotherapeutic regimens that induce a high level of reactive oxygen species (Trachootham,

Alexandre, & Huang, 2009). Likewise, malignancy-associated disruption of the Cys/GSH/GPX4 systems and concatenate pro-oxidative state can promote ferroptotic tumor suppression (Combs & DeNicola, 2019). This ferroptosis-centered anti-neoplastic mechanism may become important as malignant cells evade more conventional control systems. For example, both wild-type p53 (TP53) and mutant $p53^{3KR}$ – an acetylation-defective mutant that is unable to induce cell cycle arrest, senescence, or apoptosis – inhibit Cys import by downregulating the system Xc^- antiporter and sensitizes cells to ferroptosis (L. Jiang et al., 2015). Additionally, several infectious states (e.g., human immunodeficiency virus, Kaposi's-associated sarcoma herpesvirus, *Mycobacterium tuberculosis*) are associated with enhanced oxidative stress and inhibition of GSH synthesis, theoretically promoting ferroptosis of infected cells (Amaral et al., 2016; Choi et al., 2000; Reshi, Su, & Hong, 2014). Compared to immunologically silent apoptosis, ferroptosis and other RND mechanisms promote a robust immune response (Sarhan et al., 2018). Supporting this immune-focused role, inducible nitric oxide synthase (iNOS) expression by M1 polarized macrophages and microglia protects against ferroptosis. This anti-ferroptotic mechanism may help preserve immune function when Cys is scarce (e.g., tumor microenvironment) or system Xc^- is inhibited (e.g., ischemia/trauma-induced glutamate release). Additionally, iNOS may help monocytes survive as they phagocytize ferroptotic debris containing parlous L-OOH (Kapralov et al., 2020).

1.3 Necroptosis

Necroptosis is an evolutionarily conserved and enzymatically regulated inflammatory RCD death pathway. The first clear description of necroptosis was published three decades ago when tumor necrosis factor-alpha (TNFα) was found to induce apoptosis or a necrosis-like death

(Laster et al., 1988). Since then, study of necroptosis has paved the way for the recognition of other RND pathways. Necroptosis is triggered by an array of death, pattern recognition, adhesion, and dependence receptors (Vanden Berghe, Kaiser, Bertrand, & Vandenabeele, 2015). It depends on the sequential activation of the serine/threonine receptor interacting kinase 3 (RIP3) and mixed linage kinase domain like pseudokinase (MLKL) (He et al., 2009). In the absence of caspase-8 activity, death receptors activate RIP1 and trigger the formation of the RIP1-RIP3-MLKL "necrosome" amyloid. MLKL executes necroptosis by binding to and disrupting the plasma membrane (Holler et al., 2000; H. Wang et al., 2014). Each member of the necroptosis program has roles in inflammation and other RND pathways (e.g., pyroptosis). While the full scope of necroptosis' adaptive utility is not understood, it likely serves a role in antiviral immunity (Nailwal & Chan, 2019). Like other RND mechanisms, the study of necroptosis rose to prominence as its influence in numerous acute and chronic diseases became clear.

Necroptosis is pro-inflammatory and immunogenic, both in terms of its initiation and outcome. It is canonically initiated by the TNF receptor superfamily. The superfamily consists of 29 receptors divided into three groups: TNFα receptor-associated factor (TRAF) interacting receptors, death receptors (DR), and decoy receptors – the latter binds ligand but does not transduce the signal (Dempsey, Doyle, He, & Cheng, 2003; Locksley, Killeen, & Lenardo, 2001). Among these, the TNF receptor 1 (TNFR1), FasR (CD95), and death receptor 4/5 (DR4, DR5) and their ligands TNFα, Fas ligand (CD95L), TNF-related apoptosis-inducing ligand (TRAIL, CD253), respectively, have received the most attention (Vanden Berghe et al., 2015). These receptors each contain a homotypic death domain (DD) that facilitates interaction with other DD-containing proteins, like receptor interacting kinase 1 (RIP1) that can activate RIP3 by phosphorylation (pRIP3) (Cho et al., 2009). Alternatively, toll-like receptors 3 and 4 (TLR) and

Z-DNA binding protein 1 (ZBP1, DAI) can bypass RIP1 and directly activate RIP3 (Kaiser et al., 2013; Lin et al., 2016). The following sections will review the mechanism and the regulation of **1**) TNFR1 signaling, **2**) RIP3- and MLKL-dependent necroptosis, and **3**) the role of mitochondria in necroptosis.

1.3.1 TNF receptor 1 Signaling in Regulated Cell Death

TNFR1 is the prototypical type 1 transmembrane death receptor (Wajant & Scheurich, 2011). Binding of a TNFα trimer induces trimerization of TNFR1 and assembly of the membrane-associated pro-survival complex I or pro-death cytosolic complex II (Chan, 2007; Micheau & Tschopp, 2003). Upon TNFα binding to TNFR1, the TNFR1 trimers undergo a confirmation shift that causes the rapid formation of the high molecular weight complex I consisting of RIP1, Tumor necrosis factor receptor type 1-associated DEATH domain protein (TRADD), Fas-associated protein with death domain (FADD), TNF receptor-associated factor 2, 3, 5 (TRAF2/TRAF3/TRAF5), and the E3 ubiquitin ligases cellular inhibitor of apoptosis 1, 2 (cIAP1/cIAP2), linear ubiquitin chain assembly complex (LUBAC). TRADD or Fas-associated protein with death domain (FADD) is recruited to TNFR1 or FasR, respectively, through their DD. Although RIP1 also contains a DD, TRADD is reported to regulate the RIP1-TNFR1 interaction (L. Wang, Chang, Feng, Yu, & Chen, 2020; Zheng et al., 2006). TRADD additionally recruits TRAF proteins, which in turn, recruit and stabilize E3 ligases (Csomos, Brady, & Duckett, 2009). cIAP1/cIAP2 and LUBAC catalyze the Lys63- and Met1-linked polyubiquitination of complex I and RIP1 (Ub-Lys377) (Tonnus et al., 2019; Witt & Vucic, 2017). Deubiquitination untethers complex I from the plasma membrane and encourages the formation of the lethal complex II. NF-κB essential modulator (NEMO, IKKγ) binds to Lys63 polyubiquitin chains of RIP1 and recruits

the IkB kinase (IKK) complex (IKKα and IKKβ), TGF-β-activated kinase 1 (TAK1), and TAK1-associated binding protein (TAB) (Ea, Deng, Xia, Pineda, & Chen, 2006; H. Li, Kobayashi, Blonska, You, & Lin, 2006). IKKα/β phosphorylate RIP1 at Ser25, further inhibiting complex II assembly (Dondelinger et al., 2015). Together, IKKs and TAK complex activate NK-κB's pro-survival, proliferation, and pro-inflammatory functions (**Figure 5**).

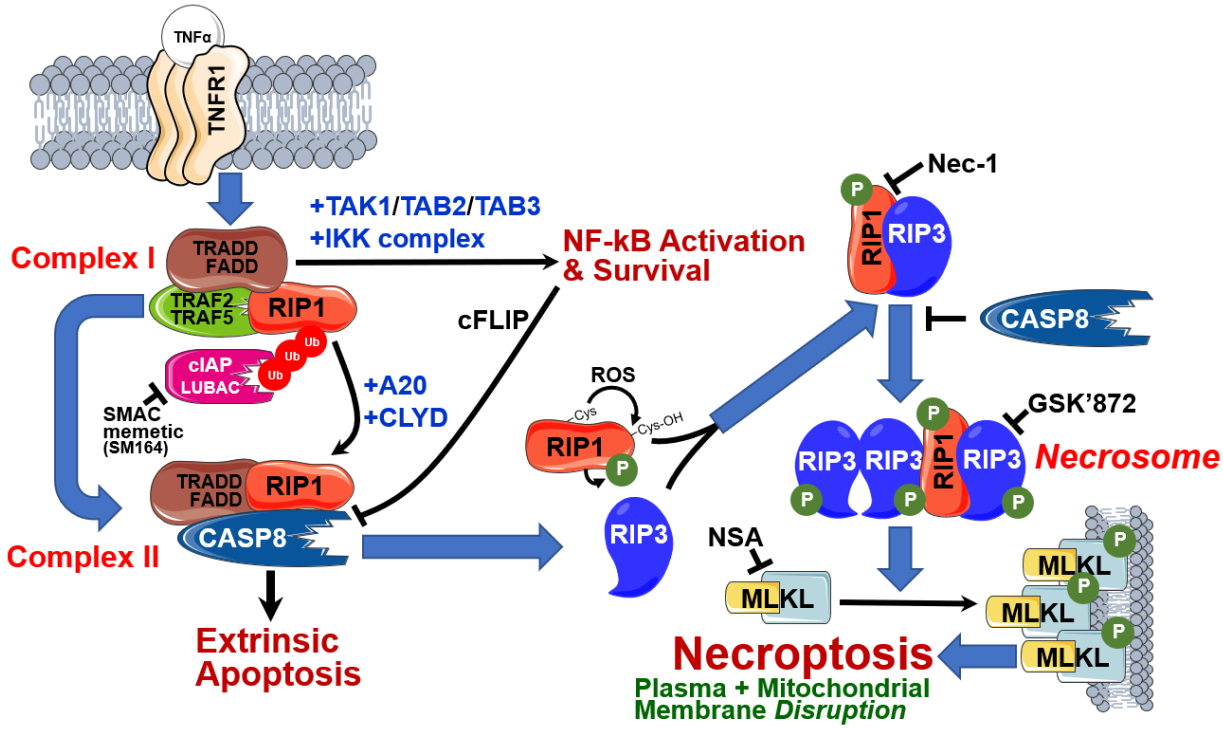

Figure 5. Necroptosis Mechanism Overview

TNF superfamily mediates both extrinsic apoptosis and necroptosis. TNFα induces TNFR1 trimerization and death domain-dependent assembly of the membrane-associated Complex I, primarily consisting of Receptor interacting kinase 1 (RIP1), Tumor necrosis factor receptor type 1-associated DEATH domain protein (TRADD), TNF receptor-associated factor 2, 3, 5 (TRAF2/TRAF3/TRAF5), and the E3 ubiquitin ligases cellular inhibitor of apoptosis 1, 2 (cIAP1/cIAP2), linear ubiquitin chain assembly complex (LUBAC). cIAP/LUBAC-dependent ubiquitination of RIP1 stabilizes Complex I and activates the NF-κB pathway that suppresses apoptotic caspase-8 (CASP8) activity by upregulating $cFLIP_{L/S}$. Activation of A20 and CLYD deubiquitinates RIP1 causing the dissolution of Complex I and formation of the pro-death cytosolic Complex II. If caspase-8 (CASP8) is present and $cFLIP_L$ levels are low, FADD facilitates pro-CASP8 oligomerization and maturation to pro-apoptotic p18/p10 CASP8 leading to extrinsic apoptosis. Alternatively, if CASP8 is inhibited, RIP3 is recruited through RIP1 kinase activity and RHIM domain-dependent formation of the insoluble necrosome amyloid-like complex. Subsequent RIP3-RIP3 homodimerization activates RIP3's kinase domain and prompts MLKL phosphorylation. Oligomeric MLKL translocates to the plasma membrane and interacts with phosphatidylinositol and phosphatidylinositol phosphates, executing necroptosis by membrane rupture and release on intercellular contents into the extracellular space.

Formation of the pro-death complex II requires that RIP1 is dephosphorylated (Ser25) and deubiquitinated by CYLD Lys63 deubiquitinase (CYLD) and A20 (**Figure 5**) (de Almagro et al., 2017). Complex II has two forms (IIa and IIb). Complex IIa consists of Fas-associated protein with

death domain (FADD), TRADD, RIP1, and CASP8 (Vanden Berghe et al., 2015). FADD facilitates pro-CASP8 oligomerization and maturation to pro-apoptotic p18/p10 CASP8 resulting in activation of downstream caspases and cleavage of BH3 Bcl2-interacting proteins that leads to release of cytochrome *c* from mitochondria (Karch et al., 2015). CASP8 activation in complex IIa is RIP1 kinase activity-independent but is facilitated by transient TAK1 catalyzed RIP1 phosphorylation (Ser321) (Geng et al., 2017). Inhibition or knockout of cIAPs and TAK1/IKK complex permit formation of complex IIb, which is composed of FADD, RIP1, and CASP8 – but not TRADD (Guo et al., 2016). RIP1 kinase activity is required for complex IIb-mediated apoptosis (Feoktistova et al., 2011). With both complex IIa and IIb, if levels of **1**) RIP3 and MLKL are sufficient and **2**) CASP8 is inhibited/absent, necroptosis is induced by sequential RIP1 kinase-mediated RIP3 recruitment and necrosome formation.

In summary, the TNFR1 complex I membrane-associated activates NF-κB and promotes survival. Cytosolic complex II leads to CASP8-mediated apoptosis in either RIP1 kinase activity-independent (complex IIa) or -dependent (complex IIb) fashion. If complex II forms but CASP8 is inhibited/absent, then RIP3/MLKL-dependent necroptosis ensues. The next section reviews the mechanisms and regulation of RIP3 and MLKL necroptosis.

1.3.2 Core Mechanism of Necroptosis: RIP3 & MLKL

Only RIP3 and MLKL are necessary for necroptosis. In the context of complex IIa/IIb signaling, RIP1 undergoes DD- and Lys599-dependent homodimerization (Meng et al., 2018). RIP1 autophosphorylation and kinase activity-dependent RIP1 (re)ubiquitination (Ub-Lys115) by the Lys63 pellino E3 ubiquitin protein ligase (PELI1) enables RIP3 recruitment (Huibing Wang et al., 2017). Genetic or pharmacologic RIP1 kinase inhibition blocks TNFR1-/DR-induced

necroptosis but not apoptosis (Polykratis et al., 2014). Active RIP1 heterodimerizes with RIP3 through their mutual RIP homotypic interaction motif (RHIM) domains (IQIG and VQVG, respectively). The heteromeric RIP1-RIP3 complex further polymerizes into filamentous double β-amyloid structures consisting of parallel β strands, the "necrosome" (J. Li et al., 2012). Necrosome formation is negatively regulated by E3 ligase carboxyl terminus of Hsp70-interacting protein (CHIP, STUB1), which polyubiquitinates (Lys63- and Lys48-linked) active RIP3 (Ub-Lys5) and together with Tripartite motif-containing protein 11 (TRIM11), targets the necrosome for lysosomal degradation (Seo et al., 2016; Y. Xie et al., 2020). If RIP3 is not ubiquitinated, the RIP1-RIP3 interaction facilitates R69-mediated RIP3-RIP3 homodimerization and autophosphorylation (T231/S232). In some circumstances, the initial RIP3 activation by RIP1 is substituted by other RHIM-containing proteins, such as the TLR3/TLR4 adaptor TRIF and the DNA sensor DAI/ZBP (Kaiser et al., 2013; Lin et al., 2016).

RIP3 homodimerization is crucial for necroptosis (**Figure 5**) (Wu et al., 2014). The crystal structure of mouse RIP3 homodimers shows the kinase domains arranged side-by-side in a similar fashion to b-RAF and c-RAF (RAF1) (Raju et al., 2018; T. Xie, Peng, Yan, et al., 2013). This structural resemblance implies the RIP3 activation mechanism is equivalent to that of RAF. The dimer interface of RAF is principally composed of a loop between the αC helix and the β4 strand (Thevakumaran et al., 2015). R509 on b-RAF is positioned at the apex of the αC-β4 loop and embraces R509 on the opposing RAF protomer in a "handshake pose." RIP3's dimer interface assumes a similar configuration where the (murine) R69 residue in the αC-β4 loop interfaces with R69 on the partner RIP3. Binding is reinforced by the interaction of R96 and H156 with E71 and E154 on the opposing RIP3 protomer, respectively (Raju et al., 2018). RIP3 dimerization mutants (R69H) retain their kinase activity *in vitro*, but cells expressing $RIP3^{R69H}$ are resistant to

TNFα/zVAD-fmk-induced T231/S232 phosphorylation (human: S227) and necroptosis. Dimerization allows for one of the kinases to allosterically activate the catalytic domain of the second kinase (Hu et al., 2015). The V471F mutation in b-RAF1 hydrophobic C-spine inhibits kinase activity but preserves its allosteric activator function (Yuan et al., 2018). Similarly, $RIP3^{V36F}$ lacks kinase activity, but cells expressing the forced $RIP3^{V36F}$-$RIP3^{WT}$ fusion dimer die necroptotically. $RIP3^{V36F}$ death is rescued by combined R69H mutation; the $RIP3^{V36F/R69H}$-$RIP3^{WT}$ fusion is not lethal (Raju et al., 2018). Other RIP3 kinase-inactive mutants ($RIP3^{D161N}$) and small molecule inhibitors (GSK'872) preserve RIP3's allosteric activator function but signal upstream triggering RIP1-dependent apoptosis or, if wildtype RIP3 is coexpressed, necroptosis (Mandal et al., 2014; Raju et al., 2018). These reports highlight that RIP3 homodimerization is critical for necroptotic function. Similar endogenous mechanisms that modulate RAF dimerization may also regulate RIP3-RIP3 interactions.

RIP3-RIP3 dimers phosphorylate MLKL (human: T357/S358; murine: S345) (Rodriguez et al., 2016). MLKL is composed of a C-terminal pseudokinase domain and an N-terminal four-helical bundle domain (4HBD). MLKL pseudokinase domain phosphorylation promotes oligomerization. In murine MLKL, Q343 hydrogen bonds with L219 and S345. Disruption of this coordinated state by phospho-S345 destabilizes the monomeric structure and induces oligomerization. The MLKL oligomer (trimers/tetramers/amyloids) interaction is reinforced by C86 (human) disulfide bonds. Necrosulfonamide (NSA) inhibits necroptosis by covalently modifying C86 (S. Liu et al., 2017). Activated MLKL migrates to the plasma membrane where its 4HBD binds PI and phosphatidylinositol phosphates (PIPs) and directly disrupts membrane integrity (Dondelinger et al., 2014). Depletion of PI(5)P and PI(4,5)P2 protects against MLKL-mediated necroptosis while genetic disruption (murine: K219M, Q343A, or S345D) of the

aforementioned H-bond structure initiates RIP3-independent necroptosis (H. Wang et al., 2014). Together, RIP3 and MLKL mediate necroptosis.

1.4 Parthanatos

Parthanatos is a caspase-independent RND mechanism mediated by poly(ADP-ribose) polymerase 1 (PARP1) hyperactivation. Parthanatos is a portmanteau term (par-thanatos) derived from 'PAR' for the poly(ADP-ribose) polymer (PAR) synthesized by PARP1, and 'Thanatos,' the Greek mythologic personification of death. Once activated, PARP1 consumes nicotinamide adenine dinucleotide (NAD^+) to generate PAR polymers. PARP1 overactivation depletes NAD^+ while PAR accumulation culminates in **1**) bioenergetic and redox catastrophe; **2**) mitochondrial depolarization ($\downarrow\Delta\psi m$), electron transport chain (ETC) inhibition, decreased mitochondrial DNA (mtDNA) integrity, and mitochondrial outer membrane permeabilization (MOMP); and **3**) mitochondria-to-nuclear translocation of apoptosis-inducing factor (AIF, AIFM1) that triggers macrophage migration inhibitory factor (MIF)-mediated large-scale (~50 kb) DNA fragmentation (Y. Wang et al., 2016; Yingfei Wang et al., 2011; Yu et al., 2002). Parthanatos is inhibited directly by PARP1 inhibition or indirectly by **1**) promoting PAR catabolism via ADP-ribosylhydrolase like 2 (ARH3, ADPRHL2) and poly(ADP-ribose) glycohydrolase (PARG) activity, **2**) sequestering PAR with selective binding proteins such as Iduna (poly(ADP-ribose)-binding protein ring finger protein 146, RNF146), or **3**) inhibiting MIF-mediated DNA degradation (Andrabi et al., 2011; Meyer-Ficca, Meyer, Coyle, Jacobson, & Jacobson, 2004; Meyer, Meyer-Ficca, Whatcott, Jacobson, & Jacobson, 2007; Y. Wang et al., 2016). Parthanotic death is an clinically relevant mediator of acute pathologies, such as ischemia-reperfusion injury, ionizing irradiation injury,

traumatic brain injury, and septic shock, among others (Fatokun, Dawson, & Dawson, 2014; Oliver et al., 1999; Whalen et al., 1999).

The poly(ADP-ribose) polymerase family of transferases is composed of 18 members. PARP1 through PARP5 catalyze the post-translational (auto)modification of negatively charged, branching PAR polymers to target proteins. Other members of the PARP family are only capable of mono-ADP-ribosylation or are inactive due to their inability to bind NAD^+ (Vyas, Chesarone-Cataldo, Todorova, Huang, & Chang, 2013). PARP1 is the most abundant and active family member. The 116 kDa protein contains three domains, **1**) an N-terminal domain with two DNA-binding zinc finger motifs responsible for DNA binding and protein-protein interactions, along with a nuclear localization sequence, **2**) a central automodification domain, and **3**) a C-terminal catalytic domain containing the NAD^+ binding site and PAR synthesizing domain (Kameshita, Matsuda, Taniguchi, & Shizuta, 1984). The primary structure of PARP1 is highly conserved across eukaryotes. PARP1's catalytic domain contains the so-called PARP signature sequence, which is a 50 amino acid block showing complete homology in vertebrates (Virág & Szabó, 2002). PARP1 is involved in the regulation of DNA integrity, gene expression, cell proliferation, cell differentiation, mitochondrial function, and parthanotic cell death (Fatokun et al., 2014; Gagné et al., 2012).

1.4.1 PARP1 Activation and Role in Nuclear DNA Repair

PARP1 best known for its role as a nuclear DNA (nDNA) damage sensor and repair factor. PARP1 activity is not required for normal cellular homeostasis (de Murcia et al., 1997; Ray Chaudhuri & Nussenzweig, 2017; Schultz, Lopez, Saleh-Gohari, & Helleday, 2003). *Parp1*$^{-/-}$ animals and cells are viable due to compensatory upregulation of PARP1-independent nDNA

repair mechanisms (Simbulan-Rosenthal et al., 1999). PARP1 activity is crucial following acute oxidative, genotoxic injury – particularly if alternate PARP1-independent repair pathways are unavailable. PARP1 activity must be balanced after injury – activity must be sufficient to facilitate efficient nDNA repair but minimized to avoid parthanatos.

PARP1's two zinc finger domains (ZnF1 and ZnF2) recognize a variety of damaged DNA structures, most notably single- (SSB) and double-strand breaks (DSB) but also several non-B-form structures and bulky lesions that disrupt normal base-stacking in at least one strand (Bryant et al., 2009; Lonskaya et al., 2005; Vodenicharov, Ghodgaonkar, Halappanavar, Shah, & Shah, 2005). The mechanism of PARP1-mediated DNA damage sensing and activation is controversial and varies between model systems. Both PARP1 zinc finger domains are needed to maximize recruitment and retention of PARP1 at DNA lesions (Ali et al., 2012; M.-F. Langelier, J. L. Planck, S. Roy, & J. M. Pascal, 2011). PARP1's ZnF1 has a role in scanning undamaged nDNA while ZnF2 engages upon encountering an nDNA lesion (M. F. Langelier, J. L. Planck, S. Roy, & J. M. Pascal, 2011). Formation of the PARP1 break-recognition complex leads to auto-poly-ADP-ribosylation (PARylation) on PARP1's automodification domain (Ali et al., 2012; Kouyama et al., 2019; L. Liu et al., 2017; Pion et al., 2005). Activated PARP1 catalyzes the creation and covalent N-, O-, or S-glycosidic linkage of ADP-ribose to various nucleophilic amino acid side chains in histones and non-histone proteins (e.g., glutamate, aspartate, serine, arginine, cysteine, lysine, asparagine) (Dantzer et al., 2006). Repeating units of ADP-ribose are attached through 2′,1″-O-glycosidic ribose–ribose bonds, extending approximately 200 units in length and branching very 20-50 units (Hassa & Hottiger, 2008). Proteins necessary for DNA damage repair are recruited to the site of damage by either covalent PARylation or non-covalent PAR interaction. Target proteins that interact non-covalently with free or PARP1/chromatin-localized PAR do so via specific PAR-

binding modules, including the PAR binding consensus motif (PBMs), PAR-binding zinc finger motifs (PBZs), microdomain folds, and WEE domain (Teloni & Altmeyer, 2016). PARylation and PAR binding regulate the target protein's localization, DNA-protein interaction (e.g., chromatin remodeling), protein-protein interaction, and enzymatic activity (Krietsch et al., 2013; Ray Chaudhuri & Nussenzweig, 2017).

Single base modifications are the most common type of DNA damage and are usually repaired by excision repair mechanisms – base excision repair (BER), single-stranded break repair (SSBR), and nucleotide excision repair (NER). BER is the dominant repair mechanism for oxidized, alkylated, or deaminated base lesions (Pachkowski et al., 2009). BER and SSBR share multiple overlapping factors. DNA glycosylases recognize and excise modified bases (Friedman & Stivers, 2010). AP endonucleases process the resultant apurinic/apyrimidinic site, yielding a SSB. Recent data indicates PARP1, X-ray repair cross-complementing proteins (XRCC1), and polymerases β, δ, or ϵ are required for SSB repair following purine BER, but PARP1 is dispensable for pyrimidine BER (Reynolds, Cooper, Lomax, & O'Neill, 2015). PARP1 activity is critical for *de novo* SSBR (i.e., SSB induced by ROS or ionizing radiation rather than as a BER intermediate) by promoting XRCC1 recruitment (Fisher, Hochegger, Takeda, & Caldecott, 2007; Hanzlikova, Gittens, Krejcikova, Zeng, & Caldecott, 2017). XRCC1 inactivation increases the number of unprocessed SSB, causing PARP1 hyperactivation and parthanatos (Hoch et al., 2017). Conversely, PARP1 inhibition or trapping at the lesion site hinders SSBR and may culminate in evolution of the SSB to a DSB. PARP1 also aids global genome nucleotide excision repair (GG-NER), the dominant type of NER, by acting in parallel with DNA damage-binding protein 1,2 (DDB1, DDB2) to recruit xeroderma pigmentosum group C-complementing protein (XPC) to

bulky DNA lesions (e.g., UV dimers) and catalytic activation of (King, Cooper, Liu, & Hudson, 2012; Maltseva, Rechkunova, Sukhanova, & Lavrik, 2015; Pines et al., 2012).

DSB are less common but are more dangerous than SSB (Mehta & Haber, 2014). Two dominant mechanisms of DSB repair are error-free homologous recombination (HR) and (relatively) error-prone non-homologous end joining (NHEJ). Formation of the PARP1 break-recognition complex at DSBs hastens the recruitment of kinase ataxia telangiectasia mutated (ATM), meiotic recombination 11 (MRE11) recruitment, and Breast cancer type 1, 2 susceptibility protein (BRCA1, BRCA2) (Haince et al., 2007; Haince et al., 2008; M. Li & Yu, 2013). Critically, PARP1-deficiency only delays HR rather than eliminating it. Cells lacking PARP1 activity display a hyper-recombinogenic phenotype with an increased number of sister chromatid exchanges and RAD51 foci (Oikawa, Tohda, Kanai, Miwa, & Sugimura, 1980). When HR is not possible or preferred, PARP1 participates in NHEJ. NHEJ is active throughout the cycle but is the preferred the DSB repair mechanism in G1 and post-mitotic cells (G0). PARP1 activity may promote classic NHEJ (c-NHEJ) through chromatin remodeling, direct activation of DNA-dependent protein kinase catalytic subunit (DNA-PKcs), and modulation of KU70/80 DSB binding (Luijsterburg et al., 2016; Ruscetti et al., 1998). PARP1 appears to have a more significant role in KU-independent alternative NHEJ (a-NHEJ, microhomology-mediated end joining) by facilitating MRE11 and DNA polymerase θ (Pol θ) recruitment to the DSB (Cheng et al., 2011; M. Wang et al., 2006).

PARP1 activity is critical for nDNA integrity, especially in the setting of acute oxidative and genotoxic injury, but PARP1 hyperactivation is lethal. PARP1 activity is required for purine BER, SSBR, NER, and a-NHEJ. But, PARP1 only has a minor role in HR and c-NHEJ while it has no discernible contribution to pyrimidine BER. PARP1's conflict between promoting repair and parthanotic death may be especially relevant in G0 post-mitotic cells (e.g., neurons,

cardiomyocytes). Non-dividing cells typically have diminished HR activity capacity and are therefore more reliant on PARP1-mediated nDNA repair (Welty et al., 2018). Untargeted PARP1 inhibition in post-mitotic cells inadvertently causes senescence, apoptosis, and autophagic cell death despite inhibiting parthanatos (Alotaibi et al., 2016; Filipovic, Meng, & Reeves, 1999). Untargeted PARP1 inhibitors (PARPi) have failed to clinically translate for the treatment of acute injury in part due to this limitation. Current application of PARPi as a mono- or adjunct therapy are restricted to disease states where nDNA damage is expressly desired (e.g., PARPi monotherapy in BRCA1/2 mutant ovarian and breast cancer) (Nowsheen & Yang, 2012). Fortunately, mitochondria have a central role in PARP1 pathophysiology. Controversy exists as to whether the characteristic mitochondrial dysfunction of PAR-induced death results from intrinsic mitochondrial PARP1 activity or extrinsic signaling events (i.e., nuclear PARP1 to mitochondrial crosstalk). Specific mitochondrial PARP1 inhibition provides the opportunity to minimize PAR-mediated pathology while preserving nDNA repair activity.

1.4.2 Roles of Mitochondrial PARP1

PARP1 is expressed in mitochondria and contributes to mitochondrial pathology following acute oxidative injury. Multiple independent reports demonstrate the presence of mitochondria-localized PARP1 (mt-PARP1) and ADP-ribosyl protein hydrolase-3 (ARH3) (A. Masmoudi, Islam, & Mandel, 1988b; Ahmed Masmoudi & Mandel, 1987; Mosgoeller, Steiner, Hozák, Penner, & Wesierska-Gadek, 1996). PARP1 lacks a canonical mitochondrial localization sequence and instead relies on the mitochondrial inner membrane organizing system (MINOS) protein, mitofilin (Mic60), for import – although the precise mechanism is unclear (Rossi et al., 2009; J. Xie, Marusich, Souda, Whitelegge, & Capaldi, 2007). Mt-PARP1 PARylates a range of mitochondrial

proteins under pro-oxidative conditions. Importantly, extranuclear/mitochondrial PAR accumulates and mitochondrial pathology is observed before detectable nuclear PARP1 activation suggesting that mitochondrial PARylation is not due to nuclear-to-mitochondrial PAR transfer (A. Brunyanszki, G. Olah, C. Coletta, B. Szczesny, & C. Szabo, 2014; Gagné et al., 2008; Gagné et al., 2012; Lai et al., 2008; Bartosz Szczesny, Attila Brunyanszki, Gabor Olah, Sankar Mitra, & Csaba Szabo, 2014). The specific effects of mitochondrial protein PARylation are mostly unknown (**Figure 6**). The mechanism of mt-PARP1 activation is also unclear but may involve detection of mtDNA lesions analogous to nuclear PARP1, as discussed in the previous section. Mt-PARP1 is shown to interact with mtDNA (Rossi et al., 2009). During the hyperacute stage of oxidative injury, protein kinase A (PKA)-mediated phosphorylation of mt-PARP1 Ser465 (automodification domain) and Ser782/785 (catalytic domain) enhances mitochondrial PAR levels and mitochondrial dysfunction (Attila Brunyanszki, Gabor Olah, Ciro Coletta, Bartosz Szczesny, & Csaba Szabo, 2014). β-adrenergic receptor/cAMP/PKA axis adrenoceptor agonists enhance mt-PARP1 activity while inhibition is protective (A. Brunyanszki et al., 2014; Brunyanszki et al., 2016a; Gagné et al., 2012). The c-Jun N-terminal kinase (JNK1), RIP1, and TRAF2 have also implicated in parthanotic mitochondrial dysfunction, but their effect on mt-PARP1 are unknown (Xu, Huang, Liu, & Han, 2006).

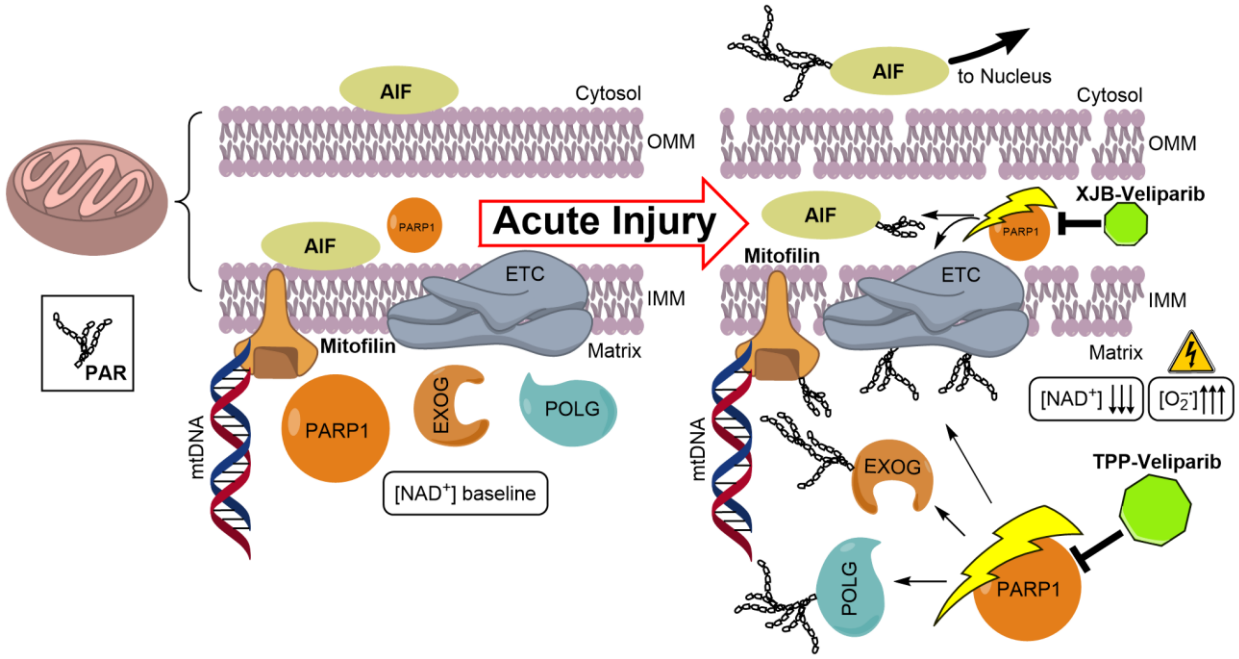

Figure 6. Proposed Effects of Mitochondrial PARP Overactivation

Under physiological conditions, mt-PARP1 is associated with mitofilin (a key component of the mitochondrial contact site and cristae organizing system, MICOS) and has low basal catalytic activity. During ischemia-reperfusion (or trauma, ionizing radiation injury), PARP1 activity increases (potentially mediated by protein kinase A, PKA), differentially PARylating many mitochondrial proteins. Critically, these modifications have been observed hours before significant nuclear PARP activation. The addition of bulky, negatively charged PAR to key mtDNA repair enzymes, POLG and EXOG, is hypothesized to inhibit their catalytic activity or delay the assembly of mtDNA repair complexes. In addition to mt-PARP1-mediated mitochondrial NAD^+ depletion, ETC complex 1, 3, 4 PARylation is associated with a reduced rate of electron transport and increased ROS production. Finally, AIF, primarily located at the IMM of the IMS (30% associated with OMM), binds PAR and translocates to the nucleus where it facilitates the execution of parthanatos. Specific mt-PARP1 inhibition through mt-veliparib can reduce deleterious mitochondrial PARylation events and preserve mitochondrial NAD^+ stores without perturbing beneficial nuclear PARP1-mediated nDNA repair. PAR = poly(ADP-ribose), IMS = intermembrane space, OMM = outer mitochondrial membrane, IMM = inner mitochondrial membrane, ETC = electron transport chain, ROS = reactive oxygen species (e.g., superoxide)

Mt-PARP1 mediated mitochondrial NAD^+ consumption and PARylation of AIF, ETC complexes, and mtDNA repair enzymes contribute to mitochondrial dysfunction and bioenergetic failure after acute oxidative injury (**Figure 6**) (Brunyanszki et al., 2016a). Mitochondrial NAD^+ cannot be directly replenished by import of cytosolic NAD^+. Illustrating this functional

compartmentalization, mitochondrial NAD^+ levels are preserved for ≥24 hours after cytoplasmic NAD^+ depletion (Stein & Imai, 2012). While recent reports suggest the existence of a previously unrecognized mammalian NAD (or NADH) transporter, mitochondria NAD^+ is largely synthesized from nicotinamide mononucleotide (NMN) by nicotinamide mononucleotide adenylyltransferase (NMNATs) in an ATP-dependent mechanism (Fatokun et al., 2014; Stein & Imai, 2012). Therefore, as limited mitochondrial NAD^+ stores are consumed, ATP production and NAD^+/NADH-dependent reactions are inhibited, culminating in irreversible $\Delta\psi m$ dissipation (Davila et al., 2018; Stein & Imai, 2012). PAR-AIF interaction induces AIF's release into cytosol/nucleus and subsequent MIF-mediated chromatin condensation and large-scale nDNA fragmentation (Galluzzi et al., 2018). PARylation of ETC complexes 1, 3, 4 reduces oxygen consumption (Lai et al., 2008; H. Z. Zhou et al., 2006). Partial ETC uncoupling and increased $O_2^{\cdot-}$ production can potentiate mt-PARP1 activation by increasing the number of oxidized bases, abasic sites, and SSB within mtDNA. Contrasting with PARP1's beneficial effect on nDNA repair, mt-PARP1 activity and PARylation of the mtDNA repair factors, endo/exonuclease G (EXOG) and polymerase-γ (POLγ), impairs recruitment of mtDNA repair factors (AP endonuclease, Ligase 3), prevents formation of the mtDNA BER complex, and reduces mtDNA integrity (Bartosz Szczesny et al., 2014; Wen, Yin, & Garg, 2018). The effect of Polymerase-θ PARylation, another mitochondrial polymerase tasked with maintaining mtDNA integrity under pro-oxidative conditions, is unknown (Wisnovsky, Sack, Pagliarini, Laposa, & Kelley, 2018). The "double hit" of injury-induced oxidative mtDNA damage and reduced repair capacity potentiates mitochondrial injury (Van Houten, Hunter, & Meyer, 2016). Therefore, specific mt-PARP1 inhibition can prevent mitochondrial NAD^+ depletion, promote ETC function, and increase mtDNA integrity without perturbing necessary nDNA repair following acute injury (Corcoran, Clarkson, Stuchbery,

& Hovens, 2016). Targeted mt-PARP1 inhibition may be particularly beneficial for post-mitotic and oxidative phosphorylation-dependent cell types (i.e., neurons and cardiomyocytes). Clinically effect anti-parthanotic pharmacologic strategies must target the detrimental actions of mt-PARP1 but spare the beneficial effects of nuclear PARP1.

Nuclear PARP1 and mt-PARP1 are ostensibly identical, which represents a challenge for the development of a specific mt-PARP1 inhibitor. Veliparib (1,2-[(S)-2-methylpyrrolidin-2-yl]-1H-benzimidazole-4-carboxamide, also, ABT-888) is a potent PARP1 inhibitor that currently in clinical trials for use as a radio- and chemotherapy adjunct therapy in several forms of reproductive, breast, lung, and brain cancers ("Clinical Trials Using Veliparib," 2020; "Veliparib (ABT-888), an Oral PARP Inhibitor, and VX-970, an ATR Inhibitor, in Combination With Cisplatin in People With Refractory Solid Tumors," 2020). Veliparib can potently inhibit PARP1 with a K_i of 5.2 nM (Cherrie K. Donawho et al., 2007). It is widely distributed (including across the blood-brain barrier, BBB) and renally excreted unchanged with minor contribution by hepatic CYP2D6 (X. Li, Delzer, Voorman, de Morais, & Lao, 2011). It was found not to inhibit or induce activities of major human P450s or phase II enzymes reducing the risk of drug-drug interactions. Additionally, compared to other clinically tested PARP1 inhibitors, veliparib has minimal PARP trapping activity (Murai et al., 2012). Embedded ribonucleotides and resultant repair intermediates are the most common form of PARP trapping lesion, and ribonucleotides are more persistent in mtDNA than nDNA (Wanrooij & Chabes, 2019; Zimmermann et al., 2018). Therefore, the chosen mt-PARP1 inhibitor possess minimal PARP trapping activity in order to maximize the benefit on mtDNA integrity. The first strategy of mitochondrial targeting of veliparib is accomplished by taking advantage of the shared ancestry between bacteria and mitochondria. The Leu-d-Phe-Pro-Val-Orn segment of the antimicrobial gramicidin S (XJB) has a high affinity for the inner

mitochondrial membrane (IMM) lipid, CL, and enriches in the intermembrane space (IMS) (J. Jiang et al., 2007; Valerian E Kagan et al., 2009). Our biochemical studies show that XJB conjugated veliparib (XJB-veliparib) and unmodified veliparib are equally potent at inhibiting recombinant PARP1 activity (**Figure 10**). Triphenylphosphonium (TPP)-veliparib serves as an alternative mt-PARP1 targeting strategy. TPP relies on an intact $\Delta\psi m$ to accomplish matrix localization (Lamade et al., 2019; M. P. Murphy, 2008). Acute oxidative injury can significantly alter neuronal $\Delta\psi m$, reducing TPP-derivative drug targeting efficiency. In contrast, XJB-veliparib may be more resistant to alterations in $\Delta\psi m$, but this has yet to be experimentally verified. Since TPP- and XJB-veliparib are thought to localize to the matrix and IMS, respectively, their efficacies may differ based on relative colocalization with mt-PARP1 and pathology-relevent PARylation targets (**Figure 6**). For example, if mt-PARP1 is primarily activated by mtDNA lesions, and its inhibitory effect on mtDNA repair is the dominant pathogenic mechanism, then matrix-targeted TPP-veliparib may be the superior therapeutic. If inhibition of IMS/IMM-localized AIF PARylation is paramount, then IMS/IMM-targeted XJB-veliparib may be more adept at inhibiting AIF release than TPP-veliparib. These innovative and proven approaches to mitochondrial delivery of therapeutics offer an exciting new avenue for drug development and treatment of mitochondrial dysfunction.

1.5 Copyright

Several figures included in the General Introduction are modified from:

Bayır, H., Anthonymuthu, T.S., Tyurina, Y.Y., Patel, S.J., Amoscato, A.A., Lamade, A.M., Yang, Q., Vladimirov, G.K., Philpott, C.C., and Kagan, V.E. (2020). Achieving Life through Death: Redox Biology of Lipid Peroxidation in Ferroptosis. Cell Chem Biol *27*, 387-408.

Kagan, V.E., Mao, G., Qu, F., Angeli, J.P., Doll, S., Croix, C.S., Dar, H.H., Liu, B., Tyurin, V.A., Ritov, V.B., et al. (2017). Oxidized arachidonic and adrenic PEs navigate cells to ferroptosis. Nature chemical biology 13, 81-90.

2.0 Summary and Rationale

Regulated necrotic cell death (RND) is a core feature of acute injury. Contrasting with apoptosis, RND mechanism are delayed hours to days following the inciting injury and are intrinsically pro-inflammatory and immunogenic. Cells' susceptibility to necroptosis, ferroptosis, and parthanatos influenced by the local environment and inflammatory state. Conversely, all RND pathways are pro-inflammatory – or necroinflammatory. They each cause plasma membrane rupture and release of pro-inflammatory DAMPs. This cycle of death and inflammation may persist days and weeks after the inciting injury and presents as a clinically relevant window of opportunity for intervention. Due to cell type and environmental heterogeneity, RND pathways rarely operate independently of one another. The RND mechanism executed depends on the expression of core machinery/substrates, cell type, and various pathology-dependent factors. The work attempts to expand our knowledge on the core mechanism and coregulation of three RND pathways – ferroptosis, necroptosis, and parthanatos. This knowledge enables the rational design of clinically effective pharmacologic strategies for treatment of acute oxidative injury, such as ischemia-reperfusion injury, trauma, ionizing irradiation injury, sepsis.

The specific aims of the unified project are:

1) To investigate mitochondria poly(ADP)ribose polymerase 1 (mt-PARP1) as a potential target for acute neuronal injury. We tested the mitochondrial localization, neuroprotective efficacy, and mechanism of the specific mt-PARP1 inhibitor, XJB-veliparib, in neuronal excitotoxic and ischemic injury *in vitro*.

2) To define the mechanism of ferroptosis and necroptosis coregulation in both *in vitro* and *in vivo* ionizing irradiation injury.

3.0 Results

3.1 Synthesis and Evaluation of a Mitochondria-Targeting Poly(ADP-ribose) Polymerase-1 Inhibitor

Published in:

American Chemical Society (ACS) Chemical Biology

September 5th, 2018

Andrew M. Lamade[1,†], Tanja Krainz[2,†], Lina Du[1], Taber S. Maskrey[2], Michael Calderon[3], Simon C. Watkins[3], Michael W. Epperly[4], Joel S. Greenberger[4], Hülya Bayır[1,5,6], Peter Wipf[2], Robert S. B. Clark[1,6]

[1]Department of Chemistry, University of Pittsburgh, Pittsburgh, Pennsylvania 15260, USA

[2]Department of Critical Care Medicine, Safar Center for Resuscitation Research, University of Pittsburgh School of Medicine, Pittsburgh

[3]Department of Cell Biology, Center for Biologic Imaging, University of Pittsburgh

[4]Department of Radiation Oncology, University of Pittsburgh Cancer Institute

[5]Department of Environmental and Occupational Health, Center for Free Radical and Antioxidant Health, University of Pittsburgh

[6]Children's Neuroscience Institute, Department of Paediatrics, Children's Hospital of Pittsburgh of UPMC, University of Pittsburgh School of Medicine

3.1.1 Acknowledgements

This work was supported by grants from the NIH U19 AI068021 (HB, ME, JG, PW), R01 NS084604 (HB, RC, PW), and F30 HL142130 (AML).

We thank D. Franicola for technical assistance with the comet assay. HT22 cells were a generous gift from D. Schubert (The Salk Institute, La Jolla, CA).

United States Patent Application No. 62/407,639 and International Patent Application PCT/US2017/056503 have been filed for Mitochondrially Targeted PARP Inhibitors.

3.1.2 Copyright

3.1.3 Note

Correspondence: Hülya Bayır, M.D., bayihx@ccm.upmc.edu

Robert S. B. Clark, M.D., clarkrs@ccm.upmc.edu

Peter Wipf, Ph.D., pwipf@pitt.edu

3.1.4 Summary

The poly(ADP-ribose) polymerase (PARP) family of enzymes plays a crucial role in cellular and molecular processes including DNA damage detection and repair, and transcription; indeed, PARP inhibitors are under clinical evaluation as chemotherapeutic adjuncts given their capacity to impede genomic DNA repair in tumor cells. Conversely, overactivation of PARP can lead to NAD^+ depletion, mitochondrial energy failure, and cell death. Since PARP activation facilitates genomic but impedes mitochondrial DNA repair, non-selective PARP inhibitors are likely to have opposing effects in these cellular compartments. Herein, we describe the synthesis and evaluation of the mitochondria-targeting PARP inhibitor, XJB-veliparib. Attachment of the hemigramicidin S pentapeptide isostere for mitochondrial targeting using a flexible linker at the primary amide site of veliparib did not disrupt PARP affinity or inhibition. XJB-veliparib was effective at low nanomolar concentrations (10-100 nM) and more potent than veliparib in protection from oxygen glucose deprivation (OGD) in primary cortical neurons. Both XJB-veliparib and veliparib (10 nM) preserved mitochondrial NAD^+ after OGD; however, only XJB-veliparib prevented release of NAD^+ into cytosol. XJB-veliparib (10 nM) appeared to inhibit poly(ADP-ribose) polymer formation in mitochondria and preserve mitochondrial cytoarchitecture after OGD in primary cortical neurons. After 10 nM exposure, XJB-veliparib was detected by LC-MS in mitochondria- but not nuclear-enriched fractions in neurons and was observed in mitoplasts stripped of the outer mitochondrial membrane obtained from HT22 cells. XJB-veliparib was also effective at preventing glutamate-induced HT22 cell death at micromolar concentrations. Importantly, in HT22 cells exposed to H_2O_2 to produce DNA damage, XJB-veliparib (10 μM) had no effect on nuclear DNA repair, in contrast to veliparib (10 μM) where DNA repair was retarded. XJB-veliparib and analogous mitochondria-targeting PARP inhibitors warrant further evaluation

in vitro and *in vivo*, particularly in conditions where PARP overactivation leads to mitochondrial energy failure and maintenance of genomic DNA integrity is desirable, e.g., ischemia, oxidative stress, and radiation exposure.

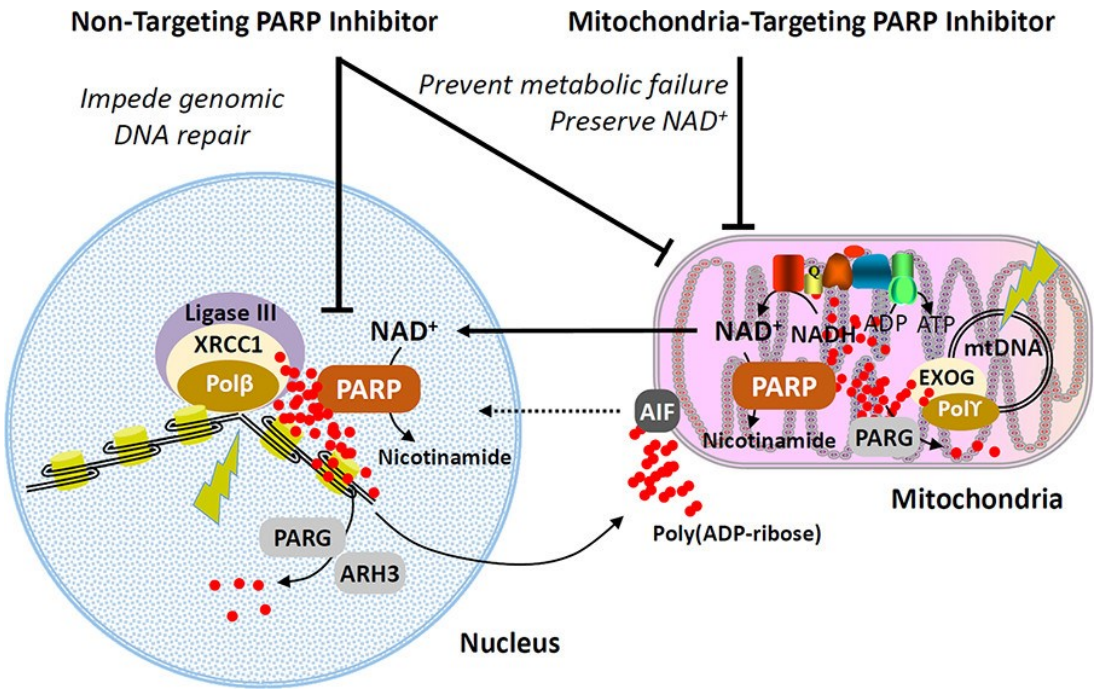

Figure 7. Graphical Abstract. Proposed mechanisms of action for mitochondria-targeting PARP inhibitors.

Abbreviations: AIF, apoptosis-inducing factor; ARH3, ADP-ribosylhydrolase 3; EXOG, exo/endonuclease G; mtDNA, mitochondrial DNA; PARG, poly(ADP-ribose) glycohydrolase; PARP, poly(ADP-ribose) polymerase; Polβ, DNA polymerase β; Polγ, DNA polymerase γ; XRRC1, X-ray repair cross-complementing protein 1.

Keywords: Hypoxia-ischemia; mtPARP1; PARP1; Veliparib; XJB-veliparib; Parthanatos

3.1.5 Introduction

Poly(ADP-ribosyl)ation (PARylation) plays a crucial role in cellular and molecular processes including DNA damage detection and repair, transcription, and the maintenance of genomic integrity.(Curtin & Szabo, 2013) The currently identified 17 members of the poly(ADP-ribose) polymerase (PARP) family induce the cleavage of NAD^+ into nicotinamide and ADP-ribose moieties and mediate their polymerization on target proteins, with links to cellular redox homeostasis, inflammatory, and metabolic networks.(Bai, 2015; Jubin et al., 2016) PARP1 binds to nuclear DNA single-strand break (SSBs) sites and recruits repair proteins to the DNA, subsequently dissociating itself from the SSB. The most potent small-molecule inhibitors, rather than just off-setting PARP1's enzymatic activity, trap it at the site of DNA damage and stabilize PARP–DNA complexes, ultimately causing DNA double-strand breaks that require more complex repair mechanisms.(Shen, Aoyagi-Scharber, & Wang, 2015)

DNA damage induced by irradiation or oxidative stress leads to overactivation of PARP1 and induces depletion of cellular NAD^+ and ATP levels, leading to cell dysfunction and necrotic cell death. The primary location of NAD^+ is in mitochondria, where it is utilized for oxidative phosphorylation. Furthermore, mitochondrial DNA (mtDNA) is constantly being exposed to damaging species such as reactive oxygen and nitrogen species and is efficiently repaired through at least a subset of the mechanisms involved in nuclear DNA repair, including regulation by PARP1.(Brunyanszki, Szczesny, Virag, & Szabo, 2016b) However, opposing roles for PARP1 have been observed in genomic versus mtDNA repair with PARP1 facilitating DNA repair in the nucleus and impeding DNA repair in mitochondria.(B. Szczesny, A. Brunyanszki, G. Olah, S. Mitra, & C. Szabo, 2014) Overactivation of PARP1 and NAD^+ depletion has been linked to the pathogenesis of central nervous system (CNS) disorders, including ischemia, traumatic brain

injury (TBI), neuroinflammation, and neurodegenerative diseases such as Alzheimer's and Parkinson's diseases, which have a pronounced mitochondrial component.(Curtin & Szabo, 2013; Martire, Mosca, & d'Erme, 2015) Preserving NAD^+ levels may reverse mitochondrial dysfunction and prevent energy failure.(Guarente, 2014) If suitable PARP inhibitors could be targeted exclusively to the mitochondria, they might reduce NAD^+ depletion-associated energy failure while allowing repair of damaged DNA in the nucleus and facilitating mtDNA repair (B. Szczesny et al., 2014).

We have previously reported evidence for the localization of PARP in mitochondria and mitochondria-specific PARylation by immunocytochemistry, electron microscopy, and by western blot analysis of purified mitochondrial fractions.(Du et al., 2003; Lai et al., 2008) Furthermore, we demonstrated that the inhibition of mtPARP preserved mitochondrial transmembrane potential and reduced neuronal cell death triggered by oxidative stress or excitotoxicity.(Du et al., 2003) However, to the best of our knowledge, the hypothesis that mitochondria-targeted PARP-inhibitors would be therapeutically effective in neurodegeneration and other CNS and non-CNS conditions associated with energy failure, and a desire to maintain genomic integrity, has not yet been addressed.

While there are broader therapeutic implications for synthetic PARP modulators, research and development of poly(ADP-ribose) polymerase-1 (PARP1) inhibitors in cancer research has intensified since the regulatory approval of olaparib and rucaparib for patients with *BRCA1/2* mutant ovarian cancer, and niraparib for recurrent gynecologic cancers (Figure 1).(Brown, Kaye, & Yap, 2016; Sisay & Edessa, 2017; Y. Q. Wang et al., 2016) Veliparib (**1**, 2-[(*S*)-2-methylpyrrolidin-2-yl]-1*H*-benzimidazole-4-carboxamide, ABT-888) is a promising PARP1 inhibitor that has entered clinical phase I/II/III trials for several forms of cancer, including breast

cancer and solid tumor neoplasm, either as a single agent or as a combination with chemotherapeutics. A phase III trial is currently ongoing to assess the efficacy, safety and tolerability of veliparib in patients with previously untreated ovarian cancer.(Wagner, 2015) The (*S*)- and (*R*)-enantiomers of veliparib have been shown to have identical biological activity,(Penning et al., 2009) and relative to other FDA approved PARP1 inhibitors veliparib seems to be the least potent in terms of trapping PARP at the site of DNA damage.(Pommier, O'Connor, & de Bono, 2016)

The XJB pentapeptide isostere is a mitochondrial targeting unit (Frantz & Wipf, 2010; Hoye, Davoren, Wipf, Fink, & Kagan, 2008; Wipf et al., 2005; Yamada & Harashima, 2008) derived from the cyclopeptide antibiotic gramicidin S (GS). The XJB moiety has been used successfully to deliver various payloads to mitochondria, including nitroxides,(Wipf et al., 2005) a nitric oxide synthase (NOS) antagonist (AMT),(Kanai et al., 2007) and a derivative of the natural anticancer product β-lapachone.(J. Ma et al., 2015) In line with these previous studies, we used XJB to deliver the payload veliparib to mitochondria. Here we show that XJB-veliparib is enriched in mitochondria, and that the compound potently inhibits PARP-mediated cell death in multiple models of cytotoxicity. XJB-veliparib is particularly effective in preventing cell death from hypoxia-ischemia in neurons, warranting further evaluation and development of this class of mitochondria-targeting PARP inhibitors for neurological diseases.

3.1.6 Methods

3.1.6.1 Synthesis of XJB-veliparib

For the synthesis of mitochondrially targeted veliparib, XJB-Veliparib, *N*-Cbz-L-proline methyl ester (**7**) was treated with NaHMDS and MeI, followed by saponification, to give the acid

9 in 98% yield over 2 steps (**Figure 8**). One-pot EDCl coupling to methyl 2,3-diaminobenzoate (**10**) and acid-catalyzed cyclization provided the benzimidazole **11** in good overall yield. Hydrolysis of the methyl ester followed by acylation with the *N*-Boc-1,3-diaminopropane spacer group afforded **12**. Removal of the Cbz-group via hydrogenation followed by Boc-deprotection provided **13**, which was coupled to the mitochondrial targeting sequence **14** (Skoda, Davis, & Wipf, 2012) to afford the desired XJB-Veliparib conjugate **15**.

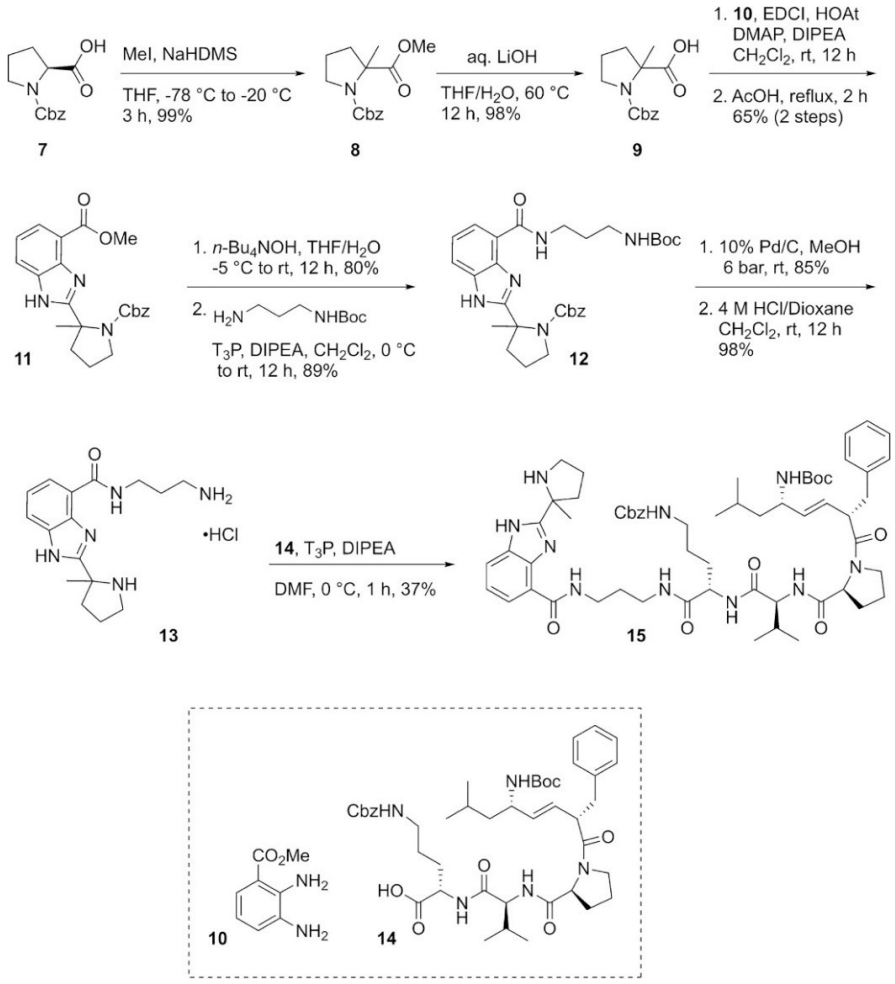

Figure 8. Synthesis of XJB–Veliparib.

General Experimental Conditions. All moisture- and air-sensitive reactions were performed in oven dried glassware under a positive pressure of argon. All reagents and solvents were used as received unless otherwise specified. THF and Et_2O were distilled over sodium/benzophenone ketyl; CH_2Cl_2 was distilled over CaH_2, MeCN and DMF were dried over molecular sieves. Reactions were monitored by TLC analysis (pre-coated silica gel 60 F_{254} plates, 250 μm layer thickness) and visualization was accomplished with a 254/280 nm UV light and/or by staining with $KMnO_4$ solution (1.5 g $KMnO_4$ and 1.5 g K_2CO_3 in 100 mL of a 0.1% NaOH solution), a ninhydrin solution (2 g ninhydrin in 100 mL EtOH), a PMA solution (5 g phosphomolybdic acid in 100 mL EtOH), or a *p*-anisaldehyde solution (2.5 mL *p*-anisaldehyde, 2 mL AcOH and 3.5 mL conc. H_2SO_4 in 100 mL EtOH). Flash chromatography was performed on silica gel (40-63 μm). Melting points were determined on a Mel-Temp II capillary melting point apparatus fitted with a Fluke 51 II digital thermometer. Infrared spectra were recorded on an ATR spectrometer. NMR spectra were recorded on 300, 400, 500 or 700 MHz instruments. Chemical shifts were reported in parts per million (ppm) and referenced to residual solvent. ^{1}H NMR spectra are tabulated as follows: chemical shift, multiplicity (br = broad, s = singlet, d = doublet, t = triplet, q = quartet, m = multiplet), coupling constant(s), number of protons. ^{13}C NMR spectra were obtained using a proton-decoupled pulse sequence and are tabulated by observed peak. LC-MS analyses were performed on a Shimadzu UFLC instrument equipped with an Applied Biosystem MDS SCIEX API 2000 mass spectrometer (ESI), under the following conditions: column: Varian Polaris C18-A (100 x 4.6 mm, 5μm) equilibrated at 40 °C; buffer A: 0.1% aqueous AcOH, buffer B: 0.1% AcOH in MeCN; 30 min gradient: 5% buffer B in buffer A for 1 min, then 5 to 95% buffer B in buffer A over 13 min, then 95% buffer B in buffer A for 4 min, then 95-5% buffer B in buffer A over 7 min, then 5% buffer B in buffer A for 5 min; flow rate: 0.2 mL/min; detection: TIC and/or

UV λ = 254/280 nm. Intracellular distribution and HRMS data were obtained on a Thermo Scientific Exactive Orbitrap LC-MS (ESI positive ion mode) coupled to a Thermo Scientific Accela HPLC system using a 3.5 μM Water XTerra C18 column (2.1 x 50 mm; 10 min gradient elution with MeCN/H_2O/ MeOH containing 0.1% formic acid at a flow rate of 500 μL/min from 3:92:5 at 0-0.5 min to 93:2:5 at 4.0 min, back to 3:92:5 from 6.0 to 7.5 min).

1-Benzyl 2-methyl 2-methylpyrrolidine-1,2-dicarboxylate (8). To a -78 °C solution of *N*-Cbz-*L*-proline **7** (0.43 mL, 1.9 mmol) and iodomethane (0.24 mL, 3.8 mmol) in THF (3.5 mL) was added dropwise NaHMDS (1 M in THF, 3.8 mL, 3.8 mmol). The resulting mixture was warmed to -20 °C, stirred for 3 h, quenched with H_2O, acidified with 2N HCl and extracted with EtOAc (3 x). The combined organic layers were washed with brine (1x), dried over $MgSO_4$, filtered and concentrated to dryness. The residue was purified by chromatography on SiO_2 (30% EtOAc/hexanes) to give **8** as a pale yellow oil (0.52 g, 99%). Spectral data of the mixture of rotamers are in accordance with literature values (Bai et al., 2011). ^{1}H NMR (300 MHz, $CDCl_3$) δ 1.54 (s, 1.5 H), 1.61 (s, 1.5 H), 1.86-1.99 (m, 3 H), 2.13-2.24 (m, 1 H), 3.46 (s, 1.5 H), 3.56-3.69 (m, 2 H), 3.71 (s, 1.5 H), 4.99-5.23 (m, 2 H), 7.24-7.40 (m, 5 H).

1-((Benzyloxy)carbonyl)-2-methylpyrrolidine-2-carboxylic acid **(9).** Methyl ester **8** (1.53 g, 5.52 mmol) was dissolved in THF (10.5 mL) and H_2O (5.4 mL) and treated with a solution of LiOH (265 mg, 11.0 mmol) in H_2O (5.4 mL). MeOH (1.5 mL) was then added and the resulting homogenous solution heated to 60 °C overnight. The organic solvents were removed and the aqueous layer acidified to pH 2 using 2 N HCl and extracted with EtOAc (3x). The combined organic layers were washed with water (1x), dried ($MgSO_4$) filtered and concentrated to dryness to give **9** as a colorless solid (1.42 g, 98%). Spectral data of the mixture of rotamers are in accordance with literature values (Bai et al., 2011). ^{1}H NMR (500 MHz, DMSO-d_6) δ 1.44 (s, 1.5

H), 1.45 (s, 1.5 H), 1.80-1.96 (m, 3 H), 2.02-2.19 (m, 1 H), 3.43-3.53 (m, 2 H), 4.94-5.11 (m, 2 H), 7.24-7.41 (m, 5 H), 12.51 (br s, 1 H).

Methyl 2-(1-((benzyloxy)carbonyl)-2-methylpyrrolidin-2-yl)-1*H*-benzo[*d*]imidazole-4-carboxylate (**11**). To a solution of **9** (200 mg, 0.760 mmol) and methyl diaminobenzoate **10** (189 mg, 1.14 mmol) in CH_2Cl_2 (15 mL) was added DIPEA (0.13 mL, 0.76 mmol) followed by addition of EDCI (218 mg, 1.14 mmol), HOAt (155 mg, 1.14 mmol) and DMAP (9.3 mg, 0.076 mmol), and the resulting solution was stirred at room temperature overnight. The reaction mixture was quenched with sat. aqueous NH_4Cl solution and extracted with CH_2Cl_2 (2x). The combined organic layers were washed with brine (1x), dried ($MgSO_4$), filtered and concentrated to give the product as a brown oil. The crude residue was redissolved in AcOH (5 mL) and heated at reflux for 2 h. The solvent was evaporated, the crude residue poured onto sat. aqueous $NaHCO_3$ and extracted with EtOAc (3x). The combined organic layers were washed with brine (1x), dried ($MgSO_4$) and concentrated. The crude residue was purified via chromatography on SiO_2 (30-90% EtOAc/hexanes) to give **11** as a pale yellow oil (198 mg, 65% over 2 steps): HRMS (ESI^+) *m/z* calcd for $C_{22}H_{24}N_3O_4$ [M+H] 394.1761, found 394.1758.

2-(1-((Benzyloxy)carbonyl)-2-methylpyrrolidin-2-yl)-1*H*-benzo[*d*]imidazole-4-carboxylic acid. Methyl ester **11** (280 mg, 0.712 mmol) was dissolved in THF/H_2O (14:1, 21 mL) and cooled to -5 °C. A 40% *n*-Bu_4NOH (aqueous) solution (4.6 mL, 7.1 mmol) was added slowly and the reaction mixture was stirred for 30 min at -5 °C and at room temperature over night. The solution was acidified with aqueous AcOH and extracted with EtOAc (3x). The combined organic layers were washed with brine, dried ($MgSO_4$), filtered and concentrated under reduced pressure. The crude residue was purified by chromatography on SiO_2 (0-10% MeOH/CH_2Cl_2) to give 2-(1-((benzyloxy)carbonyl)-2-methylpyrrolidin-2-yl)-1*H*-benzo[*d*]imidazole-4-carboxylic acid as a

pale-yellow foam (215 mg, 80%): ^{1}H NMR (400 MHz, DMSO-d_6) δ 7.86 (br s, 1 H), 7.78 (d, J = 7.5 Hz, 1 H), 7.41 – 7.36 (m, 4 H), 7.33 – 7.30 (m, 1 H), 7.30 – 7.25 (m, 1H), 7.06 (t, J = 7.4 Hz, 0.5 H), 6.91 (t, J = 7.0 Hz, 1H), 6.70 (br s, 1 H), 5.15 – 5.09 (m, 0.5 H), 5.07 – 5.04 (m, 1H), 3.87 – 3.54 (m, 3 H), 2.76 (br s, 1 H), 1.92 (s, 3 H), 1.87 (br s, 2 H), 1.86 (br s, 1 H); ^{13}C-NMR (700 MHz, DMSO-d_6) δ 167.5, 160.5, 159.8, 154.4, 154.1, 137.4, 136.8, 128.9, 128.2, 127.9, 127.7, 127.1, 124.4, 124.3, 121.7, 66.3, 66.2, 62.9, 55.4, 48.8, 48.3, 42.7, 40.5, 24.4, 24.2, 22.9, 22.4; IR (ATR, neat) 1682.8, 1407.6, 1351.5, 1255.8, 746.4 cm^{-1}; Mp 102.3 – 104.6 °C; HRMS (ESI^{+}) *m/z* calcd for $C_{21}H_{22}N_3O_4$ [M+H] 380.1605, found 380.1610.

Benzyl 2-(4-((3-((*tert*-butoxycarbonyl)amino)propyl)carbamoyl)-1*H*-benzo[*d*]imidazol-2-yl)-2-methylpyrrolidine-1-carboxylate **(12). To a solution of** *N*-Boc-1,3-propanediamine (0.28 mL, 1.6 mmol) and 2-(1-((benzyloxy)carbonyl)-2-methylpyrrolidin-2-yl)-1*H*-benzo[*d*]imidazole-4-carboxylic acid (342 mg, 1.05 mmol) in CH_2Cl_2 (12 mL) at 0 °C was added DIPEA (0.46 mL, 2.6 mmol), followed by the dropwise addition of T_3P (50 wt% in EtOAc, 0.92 mL, 1.6 mmol). The resulting mixture was stirred at room temperature overnight, washed with 5% aqueous Na_2CO_3 and brine, dried ($MgSO_4$), filtered and concentrated. The crude residue was purified via chromatography on SiO_2 (100% CH_2Cl_2 to 10% MeOH/CH_2Cl_2) to give **12** as a pale-yellow foam (503 mg, 89%): ^{1}H NMR (600 MHz, DMSO-d_6) δ 12.76 (br s, 0.5 H), 12.69 (br s, 0.5 H), 9.93 (br s, 1H), 7.86 – 7.80 (m, 1 H), 7.64 (d, J = 7.7 Hz, 0.5 H), 7.60 (d, J = 7.7 Hz, 0.5 H), 7.39 – 7.34 (m, 2 H), 7.33 – 7.27 (m, 2 H), 6.94 – 6.81 (m, 2 H), 6.73 – 6.65 (m, 1 H), 5.09 – 4.97 (m, 1 H), 4.94 – 4.79 (m, 1 H), 3.86 – 3.77 (m, 1 H), 3.70 – 3.60 (m, 1 H), 3.47 – 3.37 (m, 2 H), 3.11 – 3.00 (m, 2 H), 2.28 – 2.10 (m, 2 H), 2.02 – 1.94 (m, 2 H), 1.91 (br s, 1.5 H), 1.89 (br s, 1.5 H), 1.73 – 1.65 (m, 3 H), 1.38 (s, 9 H); ^{13}C-NMR (600 MHz, DMSO-d_6) δ 165.1, 160.4, 160.2, 156.1, 154.1, 153.7, 140.7, 140.6, 137.5, 136.7, 135.3, 135.2, 128.8, 128.2, 127.8, 127.7, 127.0, 122.5, 122.4,

122.3, 122.2, 122.1, 115.2, 115.1, 77.9, 66.2, 62.6, 62.2, 55.4, 49.0, 48.2, 43.4, 42.1, 38.2, 36.9, 30.3, 30.3, 28.7, 24.4, 23.3, 23.0, 22.5 (mixture of rotamers); Mp 112.7 – 116.2 °C; HRMS (ESI^+) *m/z* calcd for $C_{29}H_{38}N_5O_5$ [M+H] 536.2867, found 536.2867.

tert-Butyl (3-(2-(2-methylpyrrolidin-2-yl)-1*H*-benzo[*d*]imidazole-4-carboxamido)propyl) carbamate. A mixture of **12** (500 mg, 0.933 mmol) and 10% Pd/C (99 mg, 0.093 mmol) in MeOH (5 mL) in a high-pressure hydrogenator was purged with argon and flushed with hydrogen (3x). The pressure was set to 6 bar and the mixture was stirred at this pressure at room temperature overnight. The solution was filtered through a plug of Celite® and washed with CH_2Cl_2. The filtrate was concentrated and the crude residue was purified via chromatography on SiO_2 (100% CH_2Cl_2 to 10% MeOH/CH_2Cl_2) to give *tert*-butyl (3-(2-(2-methylpyrrolidin-2-yl)-1*H*-benzo[*d*]imidazole-4-carboxamido)propyl)carbamate as a white foam (375 mg, 85%): ^{1}H NMR (600 MHz, DMSO-d_6) δ 12.50 (br s, 2 H), 9.94 (br s, 1 H), 7.78 (d, J = 7.5 Hz, 1 H), 7.62 (d, J = 7.5 Hz, 1 H), 7.25 (t, J = 7.7 Hz, 1 H), 6.92 – 6.87 (m, 1 H), 3.45 – 3.38 (m, 2 H), 3.12 – 3.04 (m, 3H), 2.93 – 2.86 (m, 1 H), 2.45 – 2.38 (m, 1 H), 1.89 – 1.80 (m, 2 H), 1.72 – 1.64 (m, 3 H), 1.59 (br s, 3 H), 1.38 (s, 9 H); ^{13}C-NMR (600 MHz, DMSO-d_6) δ 165.3, 156.2, 122.1, 121.8, 79.7, 79.4, 79.2, 77.9, 62.6, 60.2, 55.4, 49.1, 46.4, 38.1, 36.8, 30.4, 28.7, 27.6, 25.7, 21.3, 14.6; IR (ATR, neat) 3269, 2973, 1694, 1645, 1612, 1523, 1406, 1365, 1245, 1166, 1046, 988, 758 cm^{-1}; Mp 79.8 – 83.2 °C; HRMS (ESI^+) *m/z* calcd for $C_{21}H_{32}N_5O_3$ [M+H] 402.2500, found 402.2499.

N-(3-Aminopropyl)-2-(2-methylpyrrolidin-2-yl)-1*H*-benzo[*d*]imidazole-4-carboxamide hydrochloride (**13**)**.** To a solution of *tert*-butyl (3-(2-(2-methylpyrrolidin-2-yl)-1*H*-benzo[*d*]imidazole-4-carboxamido)propyl)carbamate (32.8 mg, 0.0817 mmol) in CH_2Cl_2 (1 mL) was added 4 M HCl in dioxane (0.2 mL, 0.8 mmol). The resulting mixture was stirred at room temperature for 2 h. The product was filtered off, washed with hexanes, and the resulting white

solid (27.1 mg, 98%) was used in the next step without further purification: HRMS (ESI^+) *m/z* calcd for $C_{16}H_{24}N_5O$ [M+H] 302.1975, found 302.1974.

tert-Butyl ((4*S*,7*S*,*E*)-7-benzyl-2-methyl-8-((2*S*)-2-(((2*S*)-3-methyl-1-(((8*S*)-15-(2-(2-methylpyrrolidin-2-yl)-1*H*-benzo[*d*]imidazol-4-yl)-3,9,15-trioxo-1-phenyl-2-oxa-4,10,14-triazapentadecan-8-yl)amino)-1-oxobutan-2-yl)carbamoyl)pyrrolidin-1-yl)-8-oxooct-5-en-4-yl)carbamate **("XJB-Veliparib", 15).** To a solution of XJB-acid **14** (36.9 mg, 0.0458 mmol) and **13** (23.2 mg, 0.0687 mmol) in DMF (0.92 mL, 0.05M) at 0 °C was added DIPEA (40 µL, 0.23 mmol), followed by the dropwise addition of T_3P (50% in DMF, 35 µL, 0.060 mmol). The reaction mixture was stirred at 0 °C for 1 h, quenched with aqueous NH_4Cl, and extracted with CH_2Cl_2 (3x). The combined organic layers were washed with 5% aqueous LiCl solution (1x), dried ($MgSO_4$), filtered and concentrated to give the crude product as a pale yellow oil that was purified by chromatography on SiO_2 (100% CH_2Cl_2 to 15% MeOH/CH_2Cl_2) to afford **15** as a colorless solid (18.5 mg, 37%): ^{1}H NMR (400 MHz, DMSO-d_6, 100 °C) δ 9.32 (br s, 1 H), 7.88 (d, *J* = 7.44 Hz, 1 H), 7.72 (d, *J* = 7.96 Hz, 1 H), 7.69 – 7.59 (m, 1 H), 7.47 – 7.38 (m, 1 H), 7.37 – 7.31 (m, 5 H), 7.30 – 7.26 (m, 1 H), 7.25 – 7.12 (m, 5 H), 6.79 (br s, 1 H), 6.12 (d, *J* = 7.72 Hz, 1 H), 5.52 – 5.42 (m, 2 H), 5.02 (s, 2 H), 4.44 – 4.37 (m, 1 H), 4.30 – 4.23 (m, 1 H), 4.18 – 4.09 (m, 1 H), 3.93 – 3.84 (m, 1 H), 3.53 – 3.35 (m, 6 H), 3.29 – 3.21 (m, 3 H), 3.10 – 3.03 (m, 4 H), 2.72 – 2.00 (m, 3 H), 1.98 – 1.88 (m, 2 H), 1.84 (br s, 3 H), 1.80 – 1.71 (m, 5 H), 1.66 – 1.57 (m, 1 H), 1.55 – 1.43 (m, 3 H), 1.38 (s, 9 H), 1.30 – 1.25 (m, 4 H), 0.90 – 0.78 (m, 12 H); ^{13}C NMR (700 MHz, DMSO-d_6) δ 172.7, 172.5, 172.2, 171.9, 171.8, 171.7, 171.4, 171.3, 171.2, 164.8, 156.6, 155.3, 155.2, 139.7, 139.5, 137.7, 135.0, 134.6, 129.6, 128.8, 128.4, 128.3, 128.2, 127.8, 126.4, 126.2, 122.8, 78.0, 77.8, 65.6, 64.9, 64.6, 59.7, 59.6, 59.3, 58.2, 53.1, 53.0, 50.7, 50.5, 49.3, 48.8, 47.2, 47.1, 45.5, 38.9, 38.2, 36.5, 36.4, 35.2, 32.4, 30.9, 30.7, 30.2, 29.8, 28.7, 26.5, 25.0, 24.7, 24.4, 24.3,

23.8, 23.0, 22.8; Mp 147.2 – 152.6 °C; IR (ATR, CH_2Cl_2) 3291.7, 2955.8, 1647.1, 1528.8, 1439.1, 1365.7, 1248.0, 1167.2, 1028.3, 758.2, 698.1 cm^{-1}; HRMS (ESI) *m/z* calcd for $C_{60}H_{85}N_{10}O_9$ 1089.6496, found 1089.6495.

3.1.6.2 Recombinant PARP1 Activity

The capacity to inhibit PARP1 was determined using a commercial assay (Trevigen, Gaithersburg, MD) as per manufacturer's direction. Various concentrations of XJB-veliparib or veliparib were added to histone-coated wells containing active PARP1 enzyme and NAD^+ in surplus.

3.1.6.3 Cell Culture

Primary cortical neuron-enriched cultures were prepared from 16-17 day old Sprague-Dawley rat embryos as described.(Du et al., 2003) Dissociated cell suspensions were filtered through a 70 μm nylon cell strainer and seeded in 96-well plates (5×10^4 cells/well) or on poly-D-lysine coated glass coverslips, and maintained in Neurobasal medium with B27 supplements (Life Technologies, Carlsbad, CA). Experiments were performed 12 days *in vitro* (DIV).

HT22 cells were cultured at 37°C in Dulbecco's modified Eagle's medium (DMEM) (Invitrogen Inc., Carlsbad, CA) supplemented with 10% fetal bovine serum (FBS) (Thermo Fisher Scientific, San Jose, CA) and 1% penicillin-streptomycin (ATCC, Manassas, VA) in an atmosphere containing 5% CO_2. Cells were cultured for 24 to 48 h before use.

3.1.6.4 Separation of Subcellular Proteins

Separation of cytosol-, nuclear-, and mitochondria-enriched protein fractions was performed using differential centrifugations as previously described.(X. Zhang et al., 2002)

Samples were homogenized in lysis buffer then centrifuged at 1025 *g* for 15 min at 4°C to separate nuclei. Pellets containing nuclei were resuspended in buffer and centrifuged at 16,000 *g* at 4°C for 20 min with these supernatants containing nuclear-enriched fractions. Supernatants after separation of nuclei containing mitochondria and cytosolic proteins were then centrifuged at 20,000 *g* for 50 min at 4°C to separate cytosol-enriched protein fractions. The pellets were lysed, sonicated until frothy, and re-suspended in lysis buffer then centrifuged at 16,000 *g* for 25 min at 4°C. These mitochondria-enriched pellets were then washed in 5 μM CaCl and centrifuged at 1,600 *g* for 10 min. Western blots were performed using antibodies against cytochrome c oxidase (BD Biosciences, San Jose, CA) and histone H3 (Abcam, Cambridge, MA) to verify purity of subcellular fractions.

3.1.6.5 Isolation of Mitoplasts

Mitochondria from HT22 cells (25 x 10^6 cells/mL) were isolated using differential centrifugation following a standardized protocol using a commercial isolation kit (#89874; ThermoFisher Scientific, San Jose, CA). A low spin speed (3,000 *g*) was used to collect only heavy mitochondria for OMM removal. Mitochondria were resuspended in 325 μL mitochondrial isolation reagent C, then 100 μL of suspension was centrifuged at 3,000 *g*. The pellet was then digested with 0.15 – 1.5 mg/mL freshly dissolved digitonin in 125 μL volume. The samples were agitated at 750 rpm for 15 min at 4ºC, then digestion was stopped by adding an equal volume of reagent C. Suspensions were then centrifuged at 10,000 *g* for 10 min at 4ºC with the pellet containing mitoplasts (IMM and matrix) and the supernatant containing OMM and protein from the intermembrane space. The purity of the mitoplast containing fractions was verified by the absence of TOM40 and presence of MnSOD on western blot.

3.1.6.6 Quantification of XJB-veliparib

The mitochondrial fraction (50 µL) or nuclear fraction (50 µL), treated with XJB-veliparib was added to a 5:1 ratio of CH_2Cl_2:MeOH (950 µL) and vortexed (30 sec). Water (150 µL) was added and the solution was vortexed (15 sec) and set aside to equilibrate at room temperature (30 min). The resulting suspension was placed in an Eppendorf Centrifuge 5702 (4400 rpm, 20 °C) for 12 min. The organic layer was extracted and filtered through a 0.45 µm filter for analysis.

XJB-veliparib was quantified on a Thermo Scientific Exactive Orbitrap LC-MS (ESI positive ion mode) coupled to a Thermo Scientific Accela HPLC system using a 3.5 µM Water XTerra C18 column (2.1 x 50 mm; 20 min gradient elution with MeCN/H_2O containing 0.1% formic acid at a flow rate of 500 µL/min from 5:95 at 0-1.0 min to 95:5 at 12.0 min, back to 5:95 from 16.0 to 16.1 min). Calibration curves for XJB-veliparib were run in duplicate from 102 nM to 5.7 nM. Samples (10 µL) were injected in triplicate and Thermo Xcalibur software was used to determine the concentration of XJB-veliparib in mitochondrial and nuclear fractions (n = 3). The concentration was reported as pM concentration of XJB-veliparib per 10 µg of protein with corresponding standard deviation values.

3.1.6.7 Oxygen-glucose Deprivation

To model ischemia-reperfusion *in vitro*, culture medium was replaced with a pre-equilibrated low glucose (0.5 mM) medium. Neurons were transferred into a sealed hypoxic chamber (Coy Laboratory Products Inc., Grass Lake, MI) set to an atmosphere of 95% N_2 with 5% CO_2 at 37°C for 2 h. After OGD neurons were removed from the chamber and returned to the incubator.

3.1.6.8 Excitotoxicity

To model excitotoxicity in primary cortical neurons, cells were exposed to 10 μM L-glutamate with 10 μM glycine. Neuronal cells from HT22 cell line were exposed to 5 mM L-glutamate.

3.1.6.9 Assessment of Cell Death

Cell death was quantified by measuring lactate dehydrogenase (LDH) released into supernatant using a colorometric assay (Du et al., 2003). LDH values were normalized to 100% cell death caused by 0.5% Triton X-100 exposure. Data are reported as the percentage of dead cells relative to total cells and presented as mean ± standard deviation (SD).

3.1.6.10 Measurement of NAD+

NAD^+ levels were quantified in subcellular fractions by the enzymatic cycling method using alcohol dehydrogenase as described (Du et al., 2003). A standard curve was generated using known concentrations of NAD^+ and levels were calculated.

3.1.6.11 Stimulated emission depletion (STED) microscopy

Neurons grown on poly-D-lysine coated glass coverslips were fixed in 2% paraformaldehyde and permeabilized with TritonX-100. Coverslips were then incubated in a 1:200 dilution of mouse monoclonal antibody against PAR (SA216, ENzo Life Sciences, Inc., Farmingdale, NY) and an antibody against TOMM20 (Abcam, Cambridge, MA) followed by incubation in the appropriate secondary antibodies. STED imaging was performed using a Leica TCS SP8 super resolution STED microscope with a pulsed white light laser and AOBS detection system was used (Leica Microsystems, Wetzlar, Germany). Images were collected using the 775

nm STED laser line with 30% 3D STED using the Leica STED WHITE oil objective lens (HC PL APO 100x/1.40 OIL) with a 200 Hz scan speed and 2× line averaging. Pixel size was set to 45 nm/pixel, step size was set to 160 µm, and pinhole was set at 132.8 µm (0.875 AU). TOMM20 was visualized using Alexa Fluor 555, exciting at 553 nm and detecting between 558-599 nm and temporally gate between 0.83-4.33 nm. PAR was visualized with Alexa Fluor 594, exciting at 598 nm and detecting between 603-666 nm and temporally gated between 0.3-6.0 nsec. DRAQ5 (ThermoFisher Scientific, Waltham, MA) used to label cell nuclei was excited at 662 and detected between 667 to 780 nm and temporally gated between 0.3-6.0 nsec. Channels were collected between stacks, sequentially.

3.1.6.12 COMET Tail Assay

HT22 cells were incubated for 60 min at 37°C in growth media (DMEM) with vehicle (DMSO, 0.1%), 10 µM XJB-veliparib, or 10 µM veliparib. Cells were then washed with PBS and exposed to 200 µM H_2O_2 in the presence of vehicle, XJB-veliparib, or veliparib for 30 min on ice. Cells were rewashed to remove H_2O_2, and warmed media (37 °C, 5% CO_2) containing vehicle, XJB-veliparib, or veliparib was replaced for specified times (37 °C, 5% CO_2) before collection via rubber policeman. Cells were washed in 4°C PBS, counted, resuspended in DMEM (10% DMSO, 40% FBS), and frozen (-80°C) for batch analysis. The comet tail intensity assay was performed as previously described (Berhane et al., 2014).

3.1.7 Results and Discussion

3.1.7.1 Mitochondria-targeting Veliparib

The chemical synthesis of the mitochondria-targeting XJB-veliparib hybrid molecule is shown in **Figure 8** and fully described in the Methods. Since (*S*)- and (*R*)-enantiomers of veliparib have shown identical biological activity (Penning et al., 2009), we utilized racemic veliparib for the preparation of the XJB-linked hybrid molecule. Furthermore, we hypothesized that the attachment of a flexible linker at the primary amide would be unlikely to disrupt veliparib's high PARP affinity since, while energetically not as favored, the amide could adopt a *cis*-configuration and engage Gly429 in PARP with two hydrogen bonds, or, in the *trans*-amide configuration, a hydrophopic alkyl linker chain could reinforce the single remaining amide carbonyl hydrogen bond to Gly429 (Karlberg, Hammarstrom, Schutz, Svensson, & Schuler, 2010). We selected the XJB pentapeptide isostere as the mitochondrial targeting sequence (**Figure 9**) (Frantz & Wipf, 2010; Hoye et al., 2008; Wipf et al., 2005; Yamada & Harashima, 2008). The alkene peptide isostere segment in XJB is a surrogate of the leucyl-D-phenylalanine dipeptide in the bacterial membrane-associating antibiotic gramicidin S (GS), and its side chain-protected ornithylvalylproline tripeptide subunit is taken directly from GS. The D-Phe-Pro sequence is based on the reverse turn inducing sequence of GS and folds into a type II′ β-turn structure that buries several polar amide groups inside the molecule and thus may facilitate membrane transport (R, Jeffrey, Siahaan, Gangwar, & Pauletti, 1997; Wipf, Xiao, & Stephenson, 2009; Xiao, Weisblum, & Wipf, 2005, 2006). This moiety has previously been used in combination with a nitroxide payload to generate XJB-5-131, a reactive oxygen species (ROS) scavenger that validated the targeting design and was found to be ca. 600-fold enriched in mitochondria over the cytosol (Wipf et al., 2005). XJB-5-131 has shown *in vivo* efficacy in rodent models of Huntington's disease (HD)

(A. Polyzos et al., 2016; A. A. Polyzos et al., 2018; Xun et al., 2012), TBI (Ji et al., 2012), ischemia-reperfusion injury (Escobales et al., 2014; Ji et al., 2015), and hemorrhagic shock (Macias et al., 2007). In the radiation protector XJB-AMT, a nitric oxide synthase (NOS) antagonist (AMT) was conjugated to the targeting sequence, with the goal to counteract the activation of mitochondrial NOS by ionizing radiation, which can lead to inhibition of the respiratory chain, a burst of superoxide and peroxynitrite, and cellular damage (Kanai et al., 2007). XJB-Lapachone introduced a derivative of the natural anticancer compound β-lapachone into mitochondria and triggered extensive cellular vacuolization and autophagy, as well as stimulating ROS generation in mitochondria (J. Ma et al., 2015).

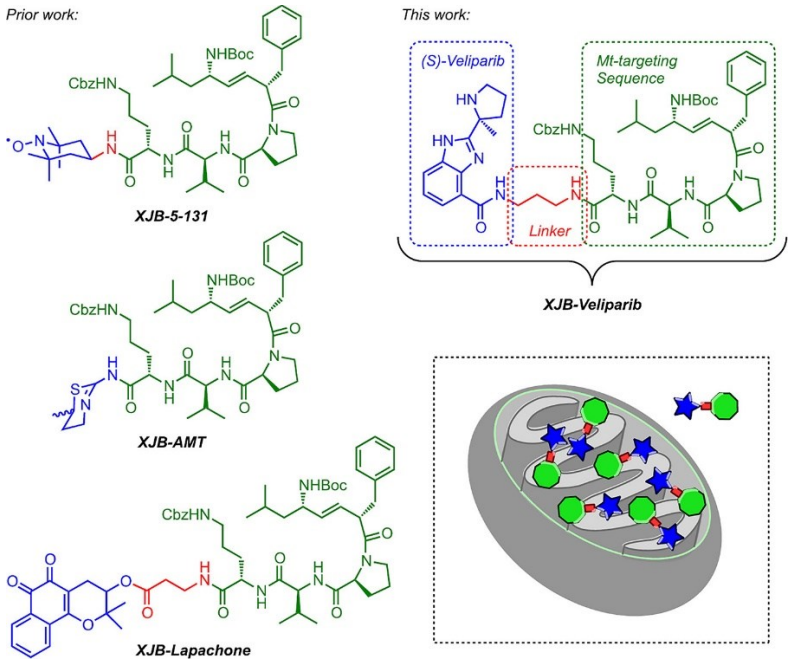

Figure 9. Structures of mitochondrially targeted 4-amino-TEMPO (XJB-5-131), lapachone (XJB-lapachone), and veliparib (XJB-veliparib).

The therapeutically active payload is in shown blue; the linker region is in red, and the XJB mitochondrial targeting moiety is in green.

3.1.7.2 XJB-veliparib and Veliparib PARP1 Enzyme Inhibition in vitro

To determine whether the linkage to the mitochondria-targeting moiety on **15** affected PARP1 inhibition, we tested the capacity of veliparib and XJB-veliparib to inhibit active PARP1 enzyme (10 U) *ex vivo*. PARP1 inhibition was similar between untargeted veliparib and the XJB-veliparib conjugate **15** (**Figure 10**; experiments performed in triplicate), and is consistent with the reported K_i of veliparib of 5.2 nmol/L (C. K. Donawho et al., 2007).

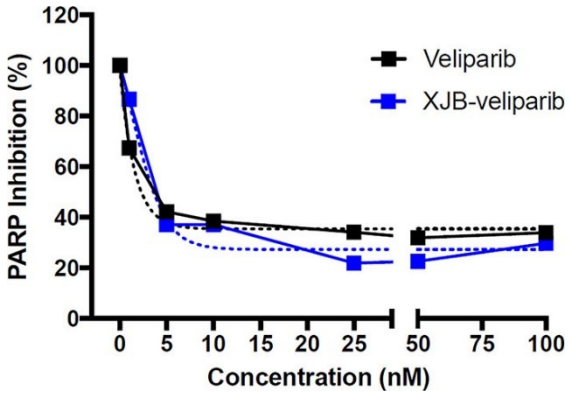

Figure 10. Capacity of XJB-veliparib to inhibit PARP1 enzyme.

Varying concentrations of XJB-veliparib or veliparib (0–100 nM) were applied to active PARP1 enzyme (10 U) *ex vivo* (performed in triplicate). Data generated in collaboration with Lina Du.

3.1.7.3 XJB-veliparib and Veliparib Cytotoxicity in Primary Cortical Neurons

To investigate the biological properties and potential cytotoxicity of XJB-veliparib, we exposed rat primary cortical neurons to varying concentrations of XJB-veliparib and veliparib. Cytotoxicity was assessed by lactate dehydrogenase (LDH) release from dying neurons at 24 h. Both XJB-veliparib and veliparib showed a concentration-dependent cytotoxicity profile; however, XJB-veliparib was significantly less toxic compared with unconjugated veliparib (**Figure 11**; n = 6/group; mean ± standard deviation [SD]; $*P < 0.05$). Neurotoxicity defined as >10% cell death was seen with veliparib at 1 μM concentration, vs. a 10 μM concentration required

for XJB-veliparib. Significant cytotoxicity has previously been reported when leukemia cells are exposed to micromolar concentrations of veliparib (Horton et al., 2009). Cytotoxicity produced by PARP inhibitors in clinical use, including veliparib, have been associated with inability to efficiently repair DNA damage and genomic instability (Ito, Murphy, Doubrovina, Jasin, & Moynahan, 2016). However, recent evidence further points to trapping of PARP1 enzyme itself in double-strand DNA (dsDNA) breaks by PARP1 inhibitors (Pommier et al., 2016). Trapped PARP-dsDNA complexes retain catalytic activity and enhance genotoxicity and lethality of chemotherapeutic agents. Relevant here, veliparib concentrations of > 100 μM are tumoricidal in most cancer cell lines (Murai et al., 2012). Importantly, mitochondria-targeting PARP inhibitors would avoid formation of trapped PARP-dsDNA complexes, and accordingly may have lower toxicity and a therapeutic advantage where prevention of cell death is desired.

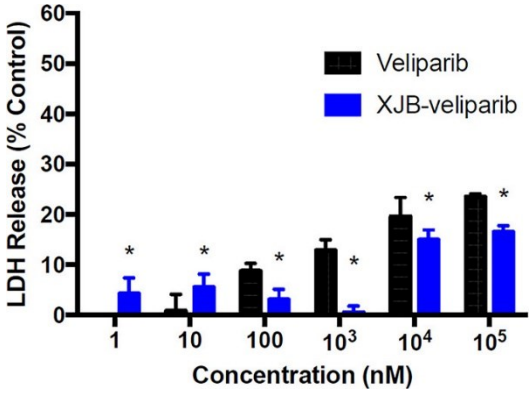

Figure 11. XJB-veliparib Cytotoxicity.

Rat primary cortical neurons (DIV 10) were exposed to varying concentrations of XJB-veliparib or veliparib (0–100 μM) for 24 h. Cytotoxicity was determined by LDH release measured at 24 h (n = 6/group; mean ± SD). Data generated in collaboration with Lina Du.

3.1.7.4 Effect of XJB-veliparib and Veliparib after Oxygen-glucose Deprivation in Primary Cortical Neurons

To determine whether mitochondria-targeting XJB-veliparib can promote neuronal survival in ischemia-like conditions *in vitro*, we subjected primary cortical neurons at 12 DIV to oxygen-glucose deprivation (OGD) (Ji et al., 2015). Cultured neurons were exposed to a hypoxic and glucose-depleted environment for 2 h, followed by normal culture conditions for 24 h to mimic ischemia/reperfusion injury. As shown in **Figure 12A**, treatment with XJB-veliparib significantly attenuated OGD-induced cell death at low nanomolar concentrations. Specifically, 10 nM XJB-veliparib reduced cell death by 65% (LDH release 12.1 ± 3.1% vs. 34.2 ± 4.0%, 10 nM XJB-veliparib vs. vehicle; n = 30/group; mean ± SD; $*P < 0.05$). Treatment with concentrations >100 nM of either veliparib or XJB-veliparib conjugate provided no additional protection. Both XJB-veliparib and non-targeting veliparib appear more protective against OGD compared with other published PARP1 inhibitors, where protection is observed in micromolar ranges (Chiarugi et al., 2003; Moroni et al., 2001). *In vivo*, PARP1 inhibition is highly effective at reducing neuronal death caused by ischemia-reperfusion injury (Eliasson et al., 1997).

To determine whether XJB-veliparib and veliparib related neuroprotection was associated with preservation of intracellular NAD^+, NAD^+ concentrations in mitochondria- and cytosol-enriched fractions were measured 24 h after OGD in primary cortical neurons. Ten nM XJB-veliparib or non-targeting veliparib preserved mitochondrial NAD^+ stores after OGD (**Figure 12B**; n = 6/group; mean ± SD; $*P < 0.05$ vs. vehicle). However, XJB-veliparib, but not veliparib, also prevented efflux of NAD^+ from the mitochondria to the cytosol after OGD ($**P < 0.05$ vs. vehicle and veliparib). These results are consistent with preservation of mitochondrial NAD^+ as one of the mechanisms behind PARP-mediated neuroprotection after OGD.

To evaluate the impact of XJB-veliparib on mitochondrial structure after OGD, we used stimulation emission depletion (STED) microscopy and immunohistochemistry. Primary rat cortical neurons were treated with 10 nM XJB-veliparib or vehicle and then exposed to OGD for 2 h. Vehicle treated neurons showed increased PARP activation at 1 h, assessed by immunofluorescence staining with anti-PAR antibody, and swollen, circular mitochondria (labelled with translocase of outer mitochondrial membrane (OMM) 20 [TOMM20]), consistent with fission vs. coiling and compaction compared with control (no ischemia) neurons (**Figure 12C**; performed in triplicate). In contrast, PAR immunoreactivity was reduced in neurons treated with XJB-veliparib (vs. vehicle) and mitochondrial architecture appeared partially preserved. The relative increase in PAR immunoreactivity observed in mitochondria vs. nuclei in neurons after OGD may be explainable by more effective PAR metabolism by poly(ADP-ribose) glycohydrolase in cell nuclei vs. ADP-ribosylhydrolase 3 in mitochondria (Narne, Pandey, Simhadri, & Phanithi, 2017).

To verify mitochondrial enrichment at a therapeutic dose, rat primary cortical neurons were exposed to 10 nM XJB-veliparib for 24 h. Mitochondria- and nuclear-enriched subcellular fractions were obtained as described and verified by western blot using antibodies against the cytochrome oxidase subunit Vα (COX Vα) and histone H3, respectively (**Figure 12D**) (Du et al., 2003). Liquid chromatography-mass spectrometry (LC-MS) analysis of XJB-veliparib showed a concentration of 40.5 ± 15.8 pmol/10 μg protein in mitochondria-enriched fractions (**Figure 12D**; mean ± SD; n = 3 independent experiments). XJB-veliparib was undetectable in nuclear-enriched fractions.

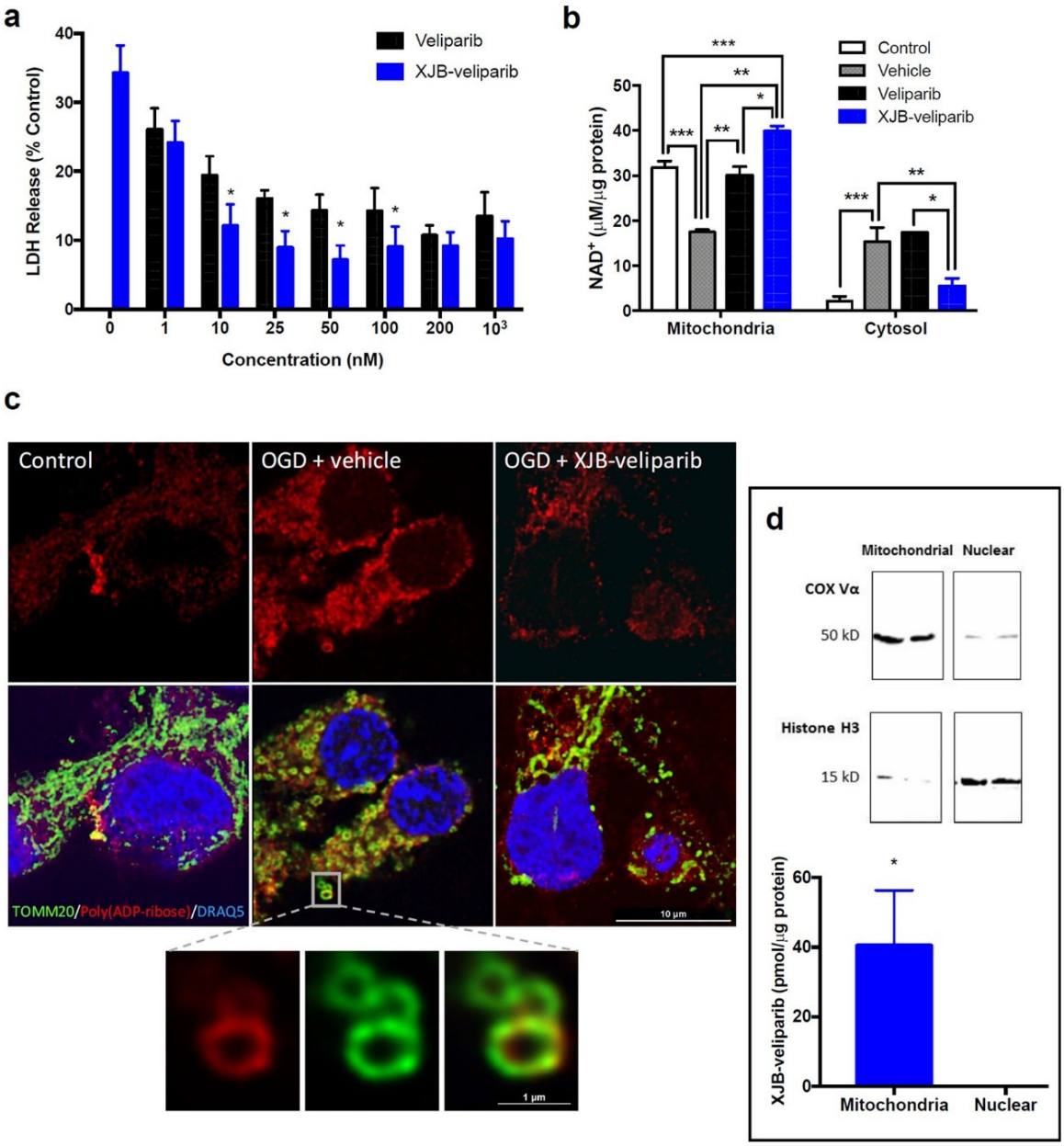

Figure 12. Ischemia-reperfusion injury (2 h of OGD) in rat primary cortical neurons treated with XJB-veliparib or veliparib.

(**a**) Cell death was determined by LDH release at 24 h. Drug concentrations of 1 nM to 1 μM were protective against OGD, and XJB-veliparib was more potent than veliparib at concentrations of 10–100 nM (*P < 0.05 vs veliparib; n = 12–30/group; mean ± SD). (**b**) Mitochondrial and cytosolic NAD^+ concentration in primary cortical neurons 24 h after OGD. XJB-veliparib or veliparib (each 10 nM) administered before OGD preserved mitochondrial NAD^+ concentration (*P < 0.05 vs veliparib; **P < 0.05 vs vehicle; ***P < 0.05 vs control; n = 6/group; mean ± SD). (**c**) STED images showing mitochondrial morphology and PAR polymers 24 h after OGD. Mitochondria were labeled with anti-TOMM20 antibody (green); PAR polymers were labeled with anti-PAR antibody (red), and nuclei were labeled with DRAQ5 (blue). XJB-veliparib (10 nM) was administered before OGD and immunohistochemistry was

performed 24 h after OGD. PAR colocalization in mitochondria after OGD is shown in higher magnification. (**d**) Mitochondrial enrichment of XJB-veliparib. Rat primary cortical neurons (DIV 10) were exposed to 10 nM XJB-veliparib for 24 h. Cells were then harvested, and mitochondrial and nuclear-enriched subfractions were obtained. XJB-veliparib was detected in mitochondria but not nuclear-enriched fractions (3 independent experiments). Western blot showing mitochondrial and nuclear enrichment using antibodies against COX Vα and histone H3, respectively. Data generated in collaboration with Lina Du and Michael Calderon.

3.1.7.5 Detection of XJB-veliparib in Mitoplasts

To verify that XJB-veliparib detected in mitochondria-enriched fractions shown in Figure 5d was not simply associated with the OMM, we isolated mitoplasts stripped of the OMM obtained from HT22 cells exposed to 10 nM XJB-veliparib for 45 min. Mitochondria were isolated using differential centrifugation following a standardized protocol (ThermoFisher #89874). The OMM was stripped from the inner mitochondrial membrane (IMM)/matrix using digitonin (0.15 – 1.5 mg/mL). The purity of the mitoplast containing fractions was verified by the absence of translocase of the outer mitochondrial membrane 40 (TOM40) and presence of manganese superoxide dismutase (MnSOD) observed on western blot. LC-MS analysis of XJB-veliparib showed a concentration of 62.6 ± 16.3 pM (6.94 ± 1.43 pmol/10 μg protein) in mitoplast fractions (**Figure 13**; mean ± SD; n = 8 samples from 3 independent experiments). For comparison, the concentration of XJB-veliparib in whole mitochondria was 85.1 ± 5.3 pM (7.7 ± 0.48 μg protein) in HT22 cells after a 45 min exposure to 10 nM XJB-veliparib (n = 3).

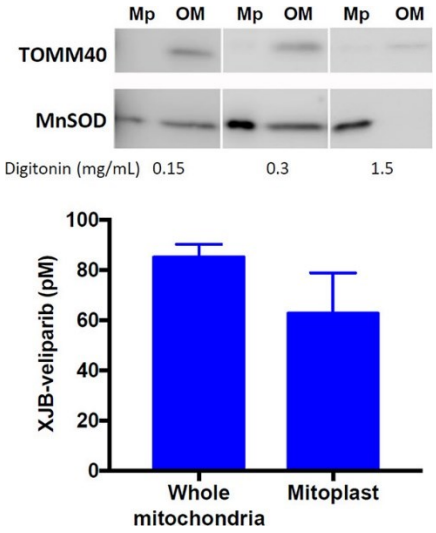

Figure 13. XJB-veliparib concentrates in mitoplasts obtained from HT22 cells exposed to 10 nM XJB-veliparib for 45 min.

The OMM was digested from IMM and matrix containing mitoplasts using digitonin (0.15–1.5 mg mL^{-1}). The purity of the mitoplast containing fractions was verified by the absence of TOM40 and presence of MnSOD observed on Western blot (mean ± SD; n = 8 samples from 3 independent experiments). For comparison, the concentration of XJB-veliparib in whole mitochondria from HT22 cells exposed to 10 nM XJB-veliparib for 45 min is shown (n = 3). Mp, mitoplast; OM, outer mitochondrial membrane.

3.1.7.6 Effect of XJB-veliparib and Veliparib after Excitotoxic Injury in Primary Cortical Neurons and Hippocampal Neuronal Cells

Previous studies have shown an important role for nuclear PARP1 activation in inhibiting excitotoxic neuronal death *in vitro* (J. Zhang, Dawson, Dawson, & Snyder, 1994). In addition, PARP1 inhibition *in vivo* is effective at reducing N-methyl-D-aspartate (NMDA) but not non-NMDA excitotoxicity (Mandir et al., 2000). To determine whether XJB-Veliparib was also effective in attenuating excitotoxic cell death *in vitro,* primary cortical neurons were exposed to 10 μM L-glutamate and 10 μM glycine with varying concentrations of XJB-Veliparib or naked veliparib for 24 h as previously described (Du et al., 2003). PARP inhibition reduced cell death after glutamate/glycine exposure in a concentration-dependent manner (**Figure 14A**; n = 6/group;

mean ± SD; *$P < 0.05$ vs. vehicle). Differing from *in vitro* ischemia/reperfusion, veliparib was more potent than XJB-veliparib in reducing LDH release. The underlying basis for the differential effectiveness of targeting versus non-targeting PARP inhibitors in models of OGD versus excitotoxicity is beyond the scope of the present study. However, one possible explanation is that since glutamate stimulates DNA repair via activation of transcription factors including cyclic AMP response element binding protein and upregulation of apurinic endonuclease 1 (J. L. Yang, Sykora, Wilson, Mattson, & Bohr, 2011), any impact of non-targeting PARP inhibitors on nuclear DNA repair and formation of trapped PARP-dsDNA complexes may be mitigated.

In addition to rat primary cortical neuron cultures, we also determined the effect of veliparib and XJB-veliparib in a stable mouse hippocampal neuronal cell line HT22, in which ferroptotic cell death is induced by high concentrations of glutamate (Y. Liu et al., 2015). HT22 cells grown to confluence were exposed to 5 mM glutamate and various concentrations of veliparib or XJB-veliparib with LDH release measured at 24 h. Both veliparib and XJB-veliparib similarly inhibit glutamate-induced ferroptosis in HT22 cells, with XJB-veliparib slightly more effective than veliparib at higher (10 μM) concentrations (**Figure 14B**; n = 5/group; mean ± SD; *$P < 0.05$ vs. vehicle).

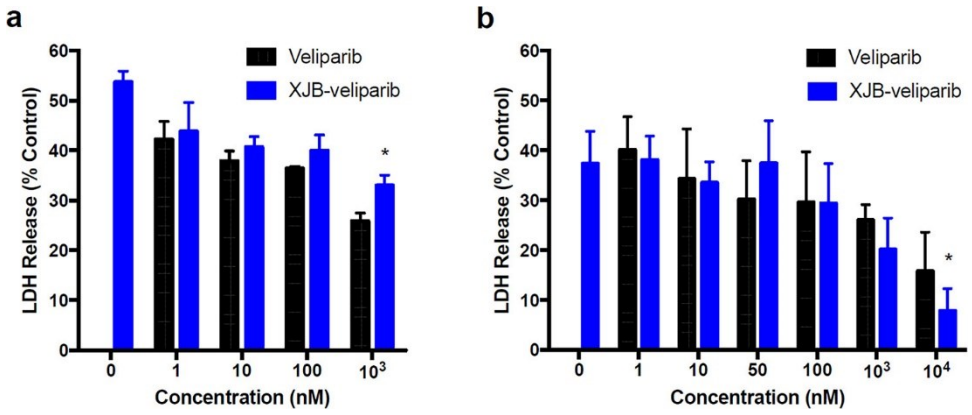

Figure 14. Excitotoxicity in rat primary cortical neurons or HT22 cells treated with XJB-veliparib or veliparib.

(**a**) Glutamate–glycine excitotoxicity in primary cortical neurons. Neurons were exposed to 10 μM l-glutamate and 10 μM glycine, with 1–100 μM of XJB-veliparib or veliparib for 24 h (**P* < 0.05 vs veliparib, *n* = 6/group; mean ± SD). (**b**) Glutamate excitotoxicity in an immortalized hippocampal neuronal HT22 cell line. XJB-veliparib and veliparib were both effective at inhibiting excitotoxic cell death, with XJB-veliparib slightly more effective at higher doses (**P* < 0.05 vs nontargeting veliparib; *n* = 5/group; mean ± SD). Data generated in collaboration with Lina Du.

3.1.7.7 Effect of XJB-veliparib on DNA Repair in Hippocampal Neuronal Cells Exposed to H2O2

To determine whether XJB-veliparib and/or veliparib impacted DNA repair, we evaluated DNA damage serially in HT22 cells exposed to 200 μM H_2O_2 using the comet tail intensity assay as previously described (Berhane et al., 2014). Exposure to H_2O_2 produced DNA damage with evidence of DNA repair over 30 min (**Figure 15**). Veliparib, but not XJB-veliparib (both 10 μM), impeded DNA repair (Fig. 8; **P* < 0.05 vs. veliparib; ***P* < 0.05 vs. vehicle; n = 52-60 cells/group; mean ± SEM). These data suggest that mitochondria-targeting PARP inhibitors at a dose that protects HT22 cells from glutamate toxicity (Fig. 7b) do not impact repair of damaged DNA.

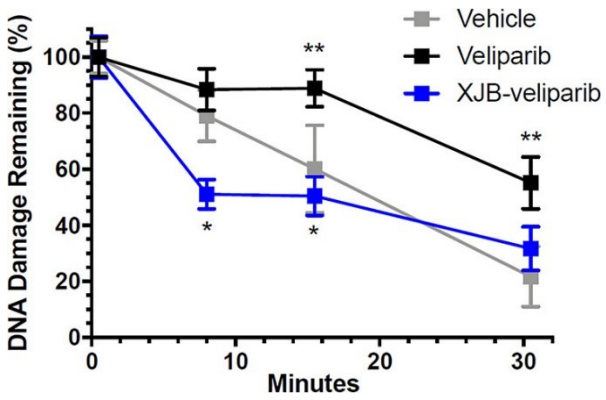

Figure 15. DNA damage and repair in HT22 cells exposed to H_2O_2 treated with XJB-veliparib (10 µM) or veliparib (10 µM).

HT22 cells were exposed to 200 µM H_2O_2 for 30 min. Tail moments were determined for each condition using the comet tail intensity assay and expressed as percent DNA damage remaining. Exposure to H_2O_2 produced DNA damage with evidence of DNA repair over 30 min. Veliparib, but not XJB-veliparib, impeded DNA repair (*$P < 0.05$ vs veliparib; **$P < 0.05$ vs vehicle; n = 52–60 cells/group; mean ± SEM).

3.1.7.8 Role for Mitochondrial-targeting PARP Inhibitors

An undisputed role for mitochondrial PARP, and in particular mitochondrial PARP1, in health and disease is controversial (Hong, Dawson, & Dawson, 2004); however, at least a partial role for mitochondrial PARP in mtDNA repair and cellular metabolism is becoming more apparent (Brunyanszki et al., 2016b). Several early studies have shown the presence of ADP-ribosylation in mitochondria from testes (Burzio, Saez, & Cornejo, 1981), liver (Kun, Zimber, Chang, Puschendorf, & Grunicke, 1975; Richter, Winterhalter, Baumhuter, Lotscher, & Moser, 1983), and brain (A. Masmoudi, Islam, & Mandel, 1988a). More recently, inhibition of mitochondrial PARP1 using genetic approaches was shown to *increase* the efficiency of mtDNA base excision repair via interaction with exo/endonuclease G and DNA polymerase γ;(B. Szczesny et al., 2014) as opposed to inhibition of *nuclear* PARP1 which decreases the efficiency of genomic DNA repair (Audebert, Salles, & Calsou, 2004). Here we show that mitochondria-targeting XJB-veliparib has no effect

on nuclear DNA repair after H_2O_2 exposure in neuronal cells, in contrast to non-targeting veliparib (**Figure 15**).

PARP1 inhibition has been shown to increase mitochondrial metabolism via silent mating type information regulation 2 homolog 1 (SIRT1) (Bai et al., 2011) and directly preserve mitochondrial function and prevent cell death via maintenance of NAD^+ stores (Ying, Alano, Garnier, & Swanson, 2005). Here, we show that mitochondria-targeting XJB-veliparib is very effective at preserving mitochondrial NAD^+ levels and preventing efflux of NAD^+ into cytosol in neurons after OGD (**Figure 12B**). We have previously reported PARylation of the electron transport chain proteins F_1F_0 ATPase, cytochrome c oxidase, and cytochrome c reductase, and preservation of respiration in isolated brain mitochondria under conditions of nitrosative stress with PARP inhibition or addition of poly(ADP-ribose) glycohydrolase (Lai et al., 2008). In addition, we have shown that mitochondrial PARP inhibition using *PARP1* gene deletion or relatively selective PARP1 inhibitors protects primary cortical neurons and fibroblasts from oxidative stress and excitotoxicity (Du et al., 2003).

Powerful neuroprotection using non-mitochondria targeting PARP inhibitors or *PARP* gene deletion has been demonstrated in pre-clinical models of stroke (Eliasson et al., 1997), TBI (Satchell et al., 2003), and neurodegenerative disease (Fan, Dawson, & Dawson, 2017; Narne et al., 2017; Whalen et al., 1999). In these and other CNS diseases, an important role for mitochondrial energy failure is implicated. XJB-veliparib (and similar compounds) that concentrate in mitochondria would be expected to directly inhibit mitochondrial PARP, reduce NAD^+ depletion, prevent energy failure, and reduce cell death while having minimal impact on genomic DNA repair and integrity (**Figure 7**). Furthermore, XJB-veliparib (and similar compounds) may also enhance mtDNA repair when used to treat these diseases (B. Szczesny et

al., 2014). Mitochondria-targeting PARP inhibitors may also reduce PARylation of apoptosis-inducing factor (AIF), potentially mitigating AIF release from mitochondria, translocation of AIF into nuclei, and parthanatos-related cell death (Y. Wang et al., 2011).

3.1.8 Conclusions

Mitochondria-targeting PARP inhibitors may have unique and important advantages over PARP inhibitors that are non-selective to cellular compartments, including directly preserving mitochondrial function and viability and preventing mitochondrial energy failure. Moreover, mitochondria-targeting PARP inhibitors could have clinical efficacy in diseases where the pathophysiology includes mitochondrial dysfunction and/or energy failure, but efficient nuclear DNA repair is desired – such as ischemia-reperfusion injury, radiation toxicity, and other diseases involving oxidative stress. As PARP inhibitors are being reconsidered for many clinical indications (Berger et al., 2017), further development and *in vitro* and *in vivo* evaluation of mitochondria-targeting PARP inhibitors appears warranted.

3.2 Deadly Duality of PEBP1: Shutting off Necroptosis, Turning on Ferroptosis

Published in: *In submission*

Andrew M. Lamade[1,2,3], Haider Dar[3], Heather L. Mentrup[7], Indira Shrivastava[2,3,4], Michael W. Epperly[5], Claudette M. St Croix[6], Tamil S. Anthonymuthu[1,2,3], Limin Wu[9], Qin Yang[1,2,3], Aleksandr A. Kapralov[3], Zhentai Huang[2,3], Gaowei Mao[3], Andrew A. Amoscato[3], Zachary E. Hier[2,3], Margarita A. Artyukova[3], Galina Shurin[3], Joel C. Rosenbaum[8], Peter J. Gough[10], John Bertin[11], Andrew P. VanDemark[8], Simon C. Watkins[6], Kevin P. Mollen[7], Ivet Bahar[4], Joel S. Greenberger[5], Michael J. Whalen[9,13], Valerian E. Kagan[3,12,13], Hülya Bayır[1,2,3,13]

[1]Safar Center for Resuscitation Research, University of Pittsburgh, Pittsburgh, PA

[2]Department of Critical Care Medicine, University of Pittsburgh Medical Center, Pittsburgh, PA

[3]Center for Free Radical and Antioxidant Health, Department of Environmental and Occupational Health, University of Pittsburgh School of Public Health, Pittsburgh, PA

[4]Department of Computational and Systems Biology, University of Pittsburgh, Pittsburgh, PA

[5]Department of Radiation Oncology, University of Pittsburgh Medical Center, Pittsburgh, PA

[6]Department of Cell Biology, University of Pittsburgh School of Medicine, Pittsburgh, PA

[7]Division of Pediatric General and Thoracic Surgery, UPMC Children's Hospital of Pittsburgh, Pittsburgh, PA

[8]Department of Biological Sciences, University of Pittsburgh, Pittsburgh, PA, USA

[9]Neuroscience Center and Department of Pediatrics, Massachusetts General Hospital and Harvard Medical School, Charlestown, MA

[10]Inzen Therapeutics, Boston, MA

[11]Pattern Recognition Receptor Discovery Performance Unit, Immuno-inflammation Therapeutic Area, GlaxoSmithKline, Collegeville, PA

[12]Laboratory of Navigational Redox Lipidomics, IM Sechenov Moscow Medical State University, Russian Federation

[13]Children's Neuroscience Institute, Children's Hospital of Pittsburgh, PA

3.2.1 Acknowledgements

This work was supported by grants from the NIH (U19 AI068021, R01 NS061817, R01 NS076511, F30 HL142130).

The authors would like to thank Mark Ross and Morgan Jessup for their microscopy technical assistance, Renee Fisher for technical assistance in irradiation experiments, Karolina Mikulska-Ruminska for simulation modelling assistance, and Valentyna Kapralova for her technical assistance in the tissue total lipid extraction, and Siddharth Balachandran (Fox Chase Cancer Center, Philadelphia, PA) for the kind gift of *Mlkl*$^{-/-}$ mice.

3.2.2 Copyright

3.2.3 Note

Correspondence: Hülya Bayır, M.D., bayihx@ccm.upmc.edu
Valerian Kagan, PhD, DSc, kagan@pitt.edu
Michael J. Whalen, M.D., pwipf@pitt.edu

Author Contributions: AML, HB, and VEK designed/planned the study and wrote the paper; AML, ZH, GW, HD, GS, and QY performed experiments with different cell types and enteroids,

analyzed data; MWE, LW, JSG, and MJW performed whole body irradiation experiments and AML analyzed data; TSA, AML, AAA, and ZEH performed MS measurements and analyzed data; AML, CSC and SW performed imaging analysis; AML, ZH, JCR, AAK, HLM, QY, GVS, and APV performed in vitro biochemical experiments; HS performed computational modeling; IB supervised computational studies and participated in paper writing; KPM, MJW, PJG and JB participated in the discussion of experiments and paper writing.

3.2.4 Summary

Necroptosis and ferroptosis are two regulated cell death pathways that contribute to several major cardiovascular and neurological pathologies. Necroptosis program relies on the activation of RIP1, RIP3 kinases and MLKL. Ferroptotic death is triggered by 15-Lipoxygenase (15LOX) catalyzed oxidation of arachidonoyl- (AA) or adrenoyl- (AdA) phosphatidylethanolamines (PE). 15LOX-mediated PE oxidation is regulated by phosphatidylethanolamine-binding protein 1 (PEBP1), which also displays promiscuity towards multiple protein partners, including RAF kinase. Given the structural homology between RAF kinase and RIP3 kinase, we hypothesized that PEBP1 acts as a necroptosis-to-ferroptosis switch via interacting with either RIP3 or 15LOX. Here we employed genetic, biochemical, redox lipidomics and computational approaches and uncovered that binding of PEBP1 with either RIP3 or 15LOX acts as a necroptosis-ferroptosis rheostat. We show that PEBP1 liberated from RAF kinase binds and inhibits RIP3, thus turning-off necroptosis. Elevated expression and higher affinity enable 15LOX to pilfer PEBP1 from RIP3, thereby promoting ferroptosis via PE oxidation. This novel PEBP1 mechanism can serve multiple and diverse cell death regulatory functions across various human disease states.

Keywords: Regulated necrosis; Ferroptosis; Necroptosis; PEBP1; RIP3; 15LOX; Total body irradiation

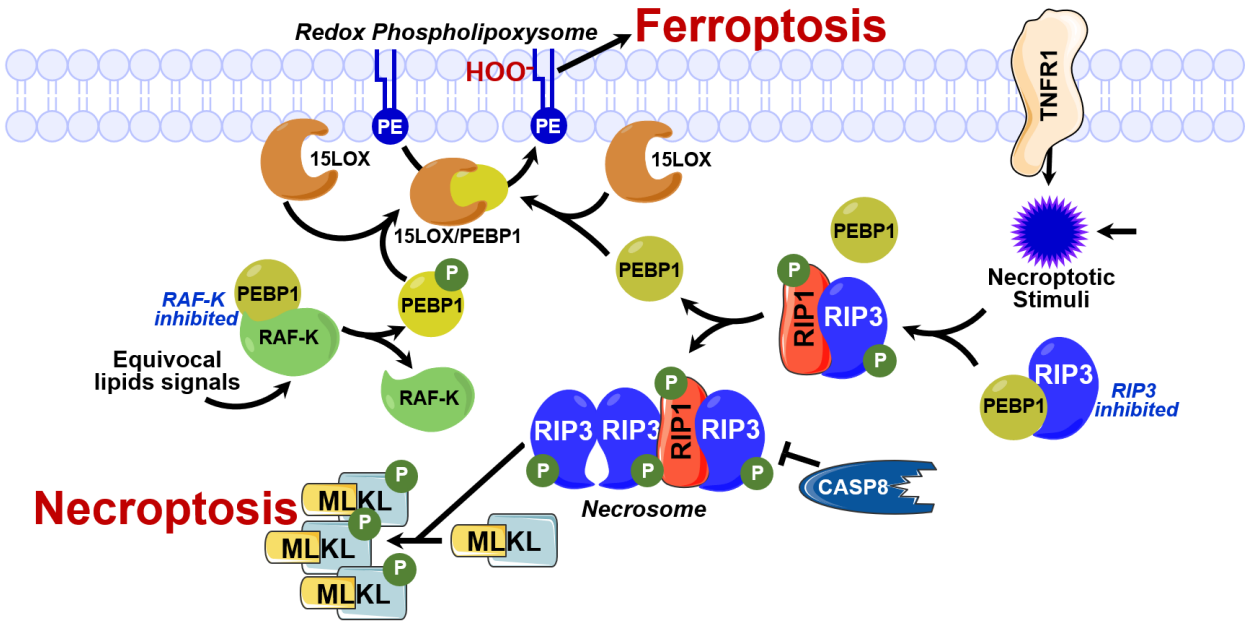

Figure 16. Graphical Abstract. Divergent role of PEBP1 in Necroptosis and Ferroptosis.

3.2.5 Introduction

Irreparably damaged cells are destined to die via one of several genetically pre-determined and evolutionarily conserved programs (Conrad, Angeli, Vandenabeele, & Stockwell, 2016). Failure of one of these processes to execute inevitably triggers another death pathway to fulfill the task, altering the spread of perilous materials from damaged cells to their local communities. This can be beneficial in facilitating functional restoration or detrimentally disseminate pro-death signals (Martinez, 2017). Key switching mechanisms between regulated cell death pathways are themselves genetically predetermined (Berghe, Linkermann, Jouan-Lanhouet, Walczak, & Vandenabeele, 2014). One important programs of cell demise is ferroptosis (Scott J. Dixon et al., 2012). We previously identified several enzymatic players essential for ferroptosis, but its overall regulatory schema and interactions with other cell death programs are only beginning to emerge.

Ferroptosis is inexorably linked to functional deficiency of the selenoprotein, glutathione peroxidase 4 (GPX4) – the only one out of eight GPX isoforms capable of reducing phospholipid hydroperoxides (PL-OOH) (Angeli et al., 2014). Equally irrefutable is the requirement for Acyl-Coenzyme A (CoA) Synthetase Long Chain 4 (ACSL4) that yields arachidonoyl(C20:4, AA)- or adrenoyl(C22:4, AdA)-CoA substrates necessary for AA-phosphatidylethanolamine (PE; AA-PE) and AdA-PE synthesis. Under pro-ferroptotic conditions, AA- and AdA-PE are peroxidized and serve as ferroptotic signaling effectors, HOO-AA-PE (e.g., hydroperoxyeicosatetraenoyl-PE, HpETE-PE) and HOO-AdA-PE (S. Doll et al., 2017). The enzymatic oxidation of PE is carried out by 15-lipoxygenase (15LOX), complexed with a scaffolding protein, phosphatidylethanolamine-binding protein 1 (PEBP1) (V. E. Kagan et al., 2017; Wenzel et al., 2017). The catalytic mechanisms governing ferroptotic PE oxidation (PEox) process are well defined, but the fate of PEox in executing death are still debated.

Ferroptosis is implicated in several common and severe disease states (e.g., traumatic brain injury, ischemia-reperfusion, asthma, acute kidney injury) (Wenzel et al., 2017). Necroptosis is similarly well represented in acute and chronic pathologies (W. Zhou & Yuan, 2014) and often found commingling with other cell death pathways. Mechanistically divergent from ferroptosis, necroptosis relies upon the ubiquitination and (auto)phosphorylation-driven assembly of Receptor Interacting Kinase 1 (RIP1) and RIP3 complexes, which culminates in (*1*) Mixed Lineage Kinase domain-like protein (MLKL) phosphorylation, (*2*) rapid membrane permeabilization, and (*3*) release of nuclear factor kappa-light chain enhancer of activated B cells (NF-κB)-associated cytokines and pro-inflammatory damage-associated molecular patterns (DAMPs) (Grootjans, Vanden Berghe, & Vandenabeele, 2017; Pasparakis & Vandenabeele, 2015).

PEBP1, also known as RAF kinase inhibitory protein, is an endogenous serine-/threonine-kinase inhibitor and displays “regulatory promiscuity” towards multiple protein partners (Corbit et al., 2003; Deiss, Kisker, Lohse, & Lorenz, 2012; K. C. Yeung et al., 2001). When complexed with 15LOX, PEBP1 enables 15LOX to switch from its preferred substrate (polyunsaturated free fatty acids, PUFA) to AA-PE and AdA-PE, whose subsequent oxidation and accumulation commits cells to ferroptosis. Given a distinct structural homology between RAF kinase and RIP3 kinase, we hypothesized that PEBP1 may act as a switch in a ferroptosis-necroptosis connection. Using computational, genetic, biochemical, and redox lipidomics approaches, here we show that PEBP1 can alternatively bind and (*1*) inhibit RIP3 activity thus turning-off necroptosis and/or (*2*) activate 15LOX-mediated AA-PE/AdA-PE oxidation and ferroptosis.

3.2.6 Methods

3.2.6.1 Cell Cultures

All cell lines used in this study were cultured in an atmosphere of 37°C, 5% CO2, 95% humidity. The cell lines used are outlined within individual legends and the STAR methods table (where information regarding the sex of cells is also found, if relevant). All cell lines were authenticated by Short Tandem Repeat (STR) profiling and confirmed negative for mycoplasma prior to experiments commencing. HT22 cells were a generous gift from Dr. David Schubert (The Salk Institute, La Jolla, CA). HT22, L929 (NTCT clone 929, ATCC, Manassas, VA), IEC18 (CRL-1589, ATCC), and HEK 293T (CRL-3216, ATCC) cells were maintained in Dulbecco’s modified Eagle’s medium (DMEM, ATCC 30-2002) supplemented with 10% fetal calf serum (A3160401, US Origin, ThermoFisher, Waltham, MA) and 1× penicillin/streptomycin (15140122, ThermoFisher). Cells were passaged using 0.25% Trypsin-EDTA (25200056, ThermoFisher) at

80-90% confluence every 2-4 days. The methods for culturing and maintenance of primary long-term bone marrow (BM) cells and enteroid monolayers are described in further detail below.

3.2.6.2 Animal Studies

All procedures were performed according to the protocols established by the Institutional Animal Care and Use Committee of the University of Pittsburgh. The *Rip3*$^{K51A/K51A}$ knock-in strategy was designed and performed by genOway as described previously (Mandal et al., 2014). Briefly, the RIP3 gene-targeting vector was constructed from the C57BL/6 mouse genome. The K51A point mutation was inserted into RIP3 exon 2, while a neomycin resistance gene cassette was inserted in intron 3, flanked by FRT sites for further Flp-mediated excision. Exon 2 including the K51A point mutation was flanked by loxP sites enabling access to constitutive or conditional deletion using Cre-mediated recombination. Similarly, *Rip1*$^{K45A/K45A}$ mice were created by using a RIP1 gene-targeting vector constructed from the C57BL/6 mouse genome. The K45A point mutation was inserted into RIP1 exon 3. A neomycin cassette was placed in intron 3 and flanked by FRT sites for FLP excision. LoxP sites were placed flanking exon 3 to allow for Cre mediated deletion.

Liproxstatin-1 (Lip-1, 50 mg/kg), Ferrostatin16-86 (Fer16-86, SRS16-86, 15 mg/kg), z-VAD-fmk (2 mg/kg), or vehicle (1:3, [50:50 Cremophor:Ethanol] to normal saline) was administered intraperitoneally (i.p.) at 24 h before and after whole-body irradiation (IR). Eight to twelve week old wild-type C57BL/6J, *Rip1*$^{K45A/K45A}$, and *Rip3*$^{K51A/K51A}$ mice were irradiated to 9.25 Gy using a Shepherd Mark 1 Model 68 cesium irradiator at a dose rate of 310 cGy/minute, as described (Huang et al., 2016). Alternatively, *Mlkl*$^{-/-}$ mice (J. M. Murphy et al., 2013) were irradiated using a RS2000 Model X-Ray irradiator at a dose rate of 100 cGy/minute to 9.25 Gy. Mice were monitored for the development of severe hematopoietic or gastrointestinal syndrome

and were sacrificed after losing >20% original body weight for >24 hours *or* >15% weight loss while demonstrating signs of a moribund state. At the time of sacrifice, animals were transcardially perfused with 5 ml calcium-/magnesium-free (CCF) phosphate buffered saline (PBS) and ileum was snap frozen. Tissue was mechanically homogenized in cold 1x PBS buffer containing 1x Protease & Phosphatase Inhibitor cocktail (ThermoFisher). Proteolyic enzyme activity (i.e., caspase-3/7) was measured in homogenate prepared without protease/phosphatase inhibitor. For histological analysis, mice were perfused with heparinized saline followed with 2% paraformaldehyde. Ileum was excised and immersion-fixed for 2 hours, and cryoprotected in 30% sucrose, then frozen in dry ice-cooled methalbutane. Transverse ileum sections were cut on a freezing sliding microtome with a thickness of 5 µm.

3.2.6.3 Total Lipid Extraction & Liquid Chromatography Mass Spectrometry Lipidomics

Lipids were extracted from using the Folch method (Folch, Lees, & Sloane Stanley, 1957). Total phospholipid content was quantified using the micro method for phosphorus measurement (Böttcher, Van gent, & Pries, 1961). Tissue CL and PE content was quantified as described previously (Wenzel et al., 2017). For CL analysis, lipid extract (equivalent to 90 µl of plasma) and internal standard (15 pmol of tetramyristoyl cardiolipin) were dried and re-suspended in 15 µl of n- hexane:2-propanol:water, 43:56:1 (v/v/v) (solvent A). For phospholipid analysis, lipid extract (equivalent to 30 µl of plasma) and internal standards (7.5 pmol of each) were dried and re-suspended in 15 µl of solvent A. In duplicate, 5 µl of each sample was injected into the liquid chromatography tandem-mass spectrometry (LC-MS/MS) system for lipid identification and quantification. LC-MS/MS analysis was performed using a Dionex Ultimate 3000 RSLCnano System coupled online to a Q-Exactive hybrid Quadrupole-Orbitrap and Orbitrap Fusion Lumos Tribrid mass spectrometers (ThermoFisher Scientific, San Jose, CA). Extracted lipids were

injected into a normal phase column (Silica Luna 3 µm, 100 Å, 150x2 mm, Phenomenex, Torrance CA), and chromatography was performed using a gradient system of solvent A and solvent B (n-hexane:2-propanol:water, 43:57:8 [v/v/v]) with 10 mM ammonium acetate at the following intervals: 0-15 min, linear gradient of 10% to 37% B at 200 µl/min flow rate; 15-23 min, linear gradient of 65% B at 200 µl/min; 23-25 min, linear gradient of 100% B at 225 µl/min; 25-47 min, isocratic flow of 100% B at 225 µl/min; 47-57 min, linear gradient of 10% B at 200 µl/min; 57-70 min, re-equilibration of 10% B at 200 µl/min. The eluent from the LC system was sprayed into the mass spectrometer via Heated Electron Spray Ionization (HESI) source with 3.2 kV spray voltage, 320°C capillary temperature, 8 units sheath gas flow rate, and 65 Rf level at the S-Lens. For CL analysis, the spectra were recorded in negative ion mode with the scan range of 1220 to 1600 m/z, whereas the range for other phospholipid analysis (PE) was set as 300 to 1300 m/z. The resolution for the full spectrum was set at 140,000 full width at half maximum (FWHM) at 200 m/z. Fragmentation was triggered in a data-independent mode. The top-5 intensity ions from the inclusion list were isolated and fragmented by high collision dissociation (HCD) with a normalized collision energy (NCE) of 24.

3.2.6.4 Identification and Quantification of Lipid Species

Identification and quantitation of the lipid species were performed with an optimized workflow developed for lipid analysis using SIEVETM v2.2 software (ThermoFisher Scientific, San Jose, CA). In brief, the targeted *m/z* list was generated for all possible acyl chain combinations of phospholipids. The retention time (RT) for CL class was fixed as ≤10 min from the RT of the internal standard [CL internal standard: CL(14:0-14:0-14:0-14:0)]. The peaks of the lipids based on the m/z and the RT were then identified from data files that were initially aligned for the RT. The peaks with signal-to-noise ratio (S/N) greater than 3 and sample-to-blank intensity ratio

greater than 1.5 were included. The integrated intensity values obtained from the software were normalized to the intensity of the internal standard, and absolute quantity was calculated using the calibration curve generated from the reference standards.

3.2.6.5 Western Blotting and Far-western Blotting

For standard protein-expression western blot, sample proteins were separated by SDS-PAGE on Novex 8~16% Tris-Glycine Mini Gels (ThermoFisher) and electrically transferred onto a PVDF membrane. Bands were probed with primary antibodies against GPX4, ACSL4, 15LOX, PEBP1, RIPK3 (RIP3) or actin (loading control) followed by horseradish peroxidase-coupled detection of species-specific secondary antibody using SuperSignal West Pico Substrate (ThermoFisher Scientific).

The interaction between PEBP1 and RIPK3 in vitro was examined by far-western blotting. Recombinant human RIPK3 (Abcam, Cat. Ab125566) and bovine serum albumin (Sigma, Cat. A2153) were separated on 8~16% Tris-Glycine SDS-PAGE and electrically transferred to a nitrocellulose membrane. Proteins were renatured by incubation of the membrane in denaturing and renaturing buffer (100 mM NaCl, 20 mM Tris (pH 7.6), 0.5 mM EDTA, 10% glycerol, 0.1% Tween-20, 2% skim milk powder and 1 mM DTT) containing decreasing concentration of guanidine HCl (6 M, 3 M, 1 M, 0.1 M, 0 M) and the membrane was blocked with 5% skim milk. Then the membrane was incubated in 0.5 mL of protein-binding buffer (100 mM NaCl, 20 mM Tris (pH 7.6), 0.5 mM EDTA, 10% glycerol, 0.1% Tween-20, 2% skim milk powder and 1 mM DTT) containing 1 μg/mL of recombinant PEBP1 (see supplemental methods PEBP1 expression/purification) at 4 ˚C overnight. Excess PEBP1 was washed away and bound PEBP1 was immunodetected with PEBP1-specific antibodies (Santa Cruz, #SC-28837, Rabbit, 1:1000)

after 1.5 hr incubation at room temperature. HRP-conjugated goat anti-rabbit/mouse IgG H&L (Sigma, #A0545, 1:1000) was applied as the secondary antibody.

3.2.6.6 Coimmunoprecipitation

Adherent cells were collected with trypsin-EDTA, collected (200 xg, 5 min.), and washed with PBS. Cells were then snap-frozen. Thawed pellet was resuspended in IP lysis buffer containing 150 mM NaCl, 50 mM Tris pH 7.4, 0.1% NP40, 0.5 mM EDTA along with protease and phosphatase inhibitor cocktail (ThermFisher, 78440) and PMSF (1 mM) on ice for 30 min. The cell lysate was centrifuged at 14000 rpm, 4°C for 12 min and the supernatant was collected and used for IP (0.5-1 mg per sample, kept constant for a given experiment) after estimation of protein concentration by BCA protein determination kit. Cell lysate was incubated with no antibody, control (IgG), PEBP1, or RIP3 antibody (4 ug/IP) overnight at 4°C. Alternatively, antibody was first crosslinked to magnetic beads (ThermoFisher, 88805) according to manufactures direction (7 µg antibody/reaction), and then incubated overnight with cell lysate. Beads (ThermoFisher, 88802) were washed with 1% BSA in IP lysis buffer for an additional 4 hours, followed by several quick washes (4x, 1 min). Immunocomplexes were dissociated into 2X protein loading buffer or using a low pH elution approach (followed by neutralization and addition of 4X loading buffer). All samples were heated to 95°C for 10 min before loading on tris-glycine SDS-Page gel.

3.2.6.7 Cell Culture γ-irradiation

Mouse intestinal enteroid monolayers and bone marrow cells were prepared in fresh medium with Liproxstatin-1 (effective concentration: 1-10 µM), Ferrostatin-1 (0.5-10 µM), Sanglifehrin A (100 nM), Nec-1s (20-40 µM), or z-VAD-fmk (10-25 µM) for 30-60 min. before

irradiation. Samples were γ-irradiated with a Shepherd model 143-45A irradiator (J.L. Shepherd & Associates, CA) at the indicated dose (5, 10, 20 Gy). Irradiated cells were returned to 37°C in 5% CO_2 incubator (*timepoint*: 0 hours post-IR) for the indicated duration.

3.2.6.8 Cell Death Assays

Cell death was assessed either by LDH release using CytoTox-ONE kit (Promega) according to manufacturer's instructions or by flow cytometry-based Annexin V-FITC + PI (BioVision, Milpitas, CA) labeling. For LDH assay, the activity of enzyme present in culture medium was used as an index of cell death. To determine the upper limit of LDH activity, adherent cells were lysed in 0.9% Triton X-100 (100% death index). Cell death was calculated as the ratio between treatment-induced LDH release and the range between Triton X-100 and untreated culture medium-associated LDH signal. For flow cytometric cell death determination, harvested cells were washed in cold PBS and were stained with Annexin V-fluorescein isothiocyanate (FITC) and PI for 15 min in the dark before counting. Dead and dying cells stained for either/both AnnexinV or PI. Cell debris, represented by low forward and side scatter, were gated out of analysis. A minimum of ten thousand events were collected for each analyzed group using a FACScan Flow Cytometer (BD Biosciences, Rutherford, NJ) and associated CellQuest software.

3.2.6.9 Isolation of Crypts and Small Intestinal Culture

Small intestinal organoids were established following the Stem Cell Technologies protocol. In brief, small intestinal organoids were established by isolating 10 cm of the most proximal portion of the small bowel from an adult C57BL/6 (n=3) or *Rip3*$^{K51A/K51A}$ (n=3) animals and placing it in a petri dish containing 10 mL of ice-cold DPBS. The small intestine was flushed three times with 1 mL DPBS to removal luminal contents before opening the tissue longitudinally

and cutting into 2 mm^2 sized pieces. The intestinal pieces were washed 15 times with ice-cold DPBS or until the supernatant was clear. Tissue fragments were transferred to a new tube containing 25mL of Gentle Dissociation Buffer and placed on a rotating plating platform (20rpm) for 15 minutes. Tissues were resuspended in 10ml of DPBS supplemented with 0.1% BSA and pipetted vigorously to dislodge intact crypts before filtering through 70-um strainer to remove tissue debris. Isolated crypts were centrifuged at 290g for 5 minutes and resuspended in 10mL ice-cold DMEM/Advanced F12 supplemented with 2mM Glutmax, 10mM HEPES, and 1x Pen/Strep (Mouse Wash Media). Crypts were resuspended in growth factor reduced matrigel at a density of 5-10 crypts/µL and 45ul droplets were plated on a pre-warmed 24-well plate. Once the matrigel solidifed, small intestinal organoid growth media (Mouse Wash Media supplemented with 1x R-spondin conditioned media, 1mM N-acetyl cysteine, 50ng/mL EGF, 100ng/mL Noggin, 1x N2 supplement, 1x B27 supplement, and 10uM Y27632 was added to each well and changed every other day after. Small intestinal organoids were passaged twice before using in any downstream experimentation.

3.2.6.10 2-D Monolayers from Established Small Intestinal Organoids

Culturing of 2-D monolayers from murine small intestinal tissue has been previously described in a detailed protocol established by Kozuka et al. Briefly, intestinal organoids were extracted from the Matrigel by placing 1mL of Gentle Disassociation Buffer in each well for 1 minute before gently pipetting 20 times and transferring suspension into a 15mL conical tube. Each well was washed with an additional 1mL of Gentle Disassociation buffer, which was added to the previous 15mL conical tube. The organoid suspension was placed on a rotating platform (20rpm) for 10 minutes prior to centrifugation at 290g for 5 minutes, 4C. The supernatant was decanted and the organoids were resuspended in 10mL ice-cold Mouse Wash Buffer before

centrifugation at 200g for 5 minutes, 4C. The intact crypts were resuspended in small intestinal monolayer growth media (Mouse Wash Media supplemented with 1x R-spondin conditioned media, 50ng/mL EGF, 100ng/mL Noggin, 1x N2 supplement, 1x B27 supplement, 10uM Y27632, 2mM Valproic Acid, and 2.5uM CHIR99021) at 1 crypt unit/ul concentration and 150ul was placed on the apical side of a 24-well transwell (0.4um transparent PET membrane) coated with a 1:30 dilution of matrigel in Mouse Wash Media. 500ul of monolayer growth media was added to the basal side of the transwell. Media was changed 18-24 hours later and 150ul(apical) and 500ul(basal) of Differentiation Media (Mouse Wash Media supplemented 50ng/mL EGF, 300ng/mL BMP-4, 1x N2 supplement, 1x B27 supplement, and 10uM Y27632) was placed in each well. Monolayers were cultured an additional 48 hours before using in downstream assays.

3.2.6.11 RNA Isolation and cDNA Synthesis

Total RNA was isolated from murine small intestinal monolayers using the RNeasy kit (Qiagen, Valencia, CA, USA) according to the manufacturer's instructions. The concentration and purity of each RNA sample were measured via spectrophotometry (ND-2000 spectrophotometer; NanoDrop Technologies, Inc., Wilmington, DE, USA). First-strand cDNA (0.5 µg of RNA) was prepared by using QuantiTect reverse transcription kit (Qiagen) according to the manufacturer's instructions. cDNA was diluted to 0.5 ng/µl and stored at -20°C until further use.

3.2.6.12 Quantitative Real-time PCR (qPCR) and Analysis

Gene expression was measured relative to the housekeeping gene 50s ribosomal subunit protein L15 (RPLO) as previously described (Cunningham et al., 2019; Kozuka et al., 2017). In brief, cDNA was amplified using a Applied Biosystems (ABI) QuantStudio 3 real-time PCR detection system (ABI, Model # A28131), with a final reaction volume of 10 µl containing 2.5 ng

of cDNA, primers (500 nM final concentration), and 1x PowerUp SYBR Mastermix, ROX (ABI, Cat # A25741). The amplification conditions for the qPCR reactions were as follows: 1 cycle of initial denaturation at 95°C for 4 minutes followed by 40 cycles of denaturation at 95°C for 15 seconds, annealing at 56°C for 30 seconds, and elongation at 72°C for 30 seconds. All reactions were carried out in triplicate. Primer efficiencies were validated to be similar, which allowed the qPCR data to be analyzed using the comparative Ct method ($2^{-\Delta\Delta Ct}$ method).

Table 1. Oligonucleotides for qPCR Analysis of Differentiated Enteroid Monolayer Culture

REAGENT or RESOURCE	SOURCE	IDENTIFIER
Oligonucleotides		
CCTACTCGAAGACTTACCCAGT	Integrated DNA Technologies (IDT)	Mouse LGR5 - 1F
GCATTGGGGTGAATGATAGCA	Integrated DNA Technologies (IDT)	Mouse LGR5 - 1R
AAGCTGGCTGACTGGGTGTGTTTA	Integrated DNA Technologies (IDT)	mouse Lysozyme - 1F
CACTGCAATTGATCCCACAGGCAT	Integrated DNA Technologies (IDT)	mouse Lysozyme - 1R
TAGTGGAGATTGTGCCGCTGAAGT	Integrated DNA Technologies (IDT)	mouse MUC2 - 1F
AGAGCCCATCGAAGGTGACAAAGT	Integrated DNA Technologies (IDT)	mouse MUC2 - 1R
GGCGACCTGGAAGTCCAACT	Integrated DNA Technologies (IDT)	RPL0 – F
CCATCAGCACCACAGCCTTC	Integrated DNA Technologies (IDT)	RPL0 – R

3.2.6.13 Primary IL-3 Dependent Long-Term Bone Marrow (BM) Culture

Non-adherent IL-3 dependent cells were segregated from the mixed population long-term culture of bone marrow cells derived from wild type (*Rip3*$^{+/+}$) and *Rip3*$^{K51A/K51A}$ mice. These were cultured in six-well tissue culture plates with 4.0 mL of Iscoves modified Eagles medium supplemented with 20% fetal calf serum (US Origin, ThermoFisher), 1× penicillin/streptomycin, and 1.0 ng/mL of recombinant murine IL-3 (Peprotech, Rocky Hill, NJ, USA). The cells were

passaged at high density weekly for 10 weeks by cytocentrifugation at 300 xg and replenished with 4.0 mL medium. At week 10, the culture was split in two and frozen at -80°C for one week. Cells were then thawed, cultured, and passaged in the same medium as described above. BM were passaged every 3 - 4 days and maintained at high density. For RSL3 experiments, cells were plated in 35mm dishes containing RSL3 (0-500 nM), Fer-1 (500-1000 nM) and/or other compounds in normal growth media for 18-24 h before cell death assay. For irradiation experiments, $8 \cdot 10^4$ cells in 3 - 4 mL media were plated in 60mm dishes with 1 - 5% FBS for 48 h, followed by media change into normal 20% FBS media prior to IR. Drug dose ranges are listed with γ-irradiation exposure methods.

3.2.6.14 PEBP1 Knockdown and Necroptosis Induction

PEBP1 knockdown in L929 cells was accomplished by transfected using RNAiMax (Invitrogen) according to manufacturer's instruction 48 hours before secondary treatment. Necroptosis was induced in PEBP1 siRNA-treated cells via combination of z-VAD-fmk (10 μM), SM164 (100 nM), and TNFα (1, 5, 10 ng/mL) in the presence or absence of Nec-1s (20-40 μM). CRISPR-mediated PEBP1 knockdown was performed using a CRISPR double nickase (sc-42393-NIC, SCBT) or non-targeted control (sc-418922, SCBT) system according to the manufacturer's protocols. Two clones were created and screened using puromycin. Necroptosis induction in CRISPR clones was accomplished by combination of z-VAD-fmk (10 μM), SM164 (100 nM), and TNFα (1ng/mL) ± Nec-1s. LDH cytotoxicity was measured at 18-24 h following necroptosis induction.

Table 2. PEBP1 knockdown and knockout constructs

REAGENT or RESOURCE	SOURCE	IDENTIFIER
Oligonucleotides		
rUrCrArUrUrCrUrGrUrUrGrUrUrGrArUrArUrArArArArAAA	Integrated DNA Technologies (IDT)	mm.Ri.pebp1.13.1
rUrUrUrUrUrUrArUrArUrCrArArCrArArCrArGrArArUrGrArCrU	Integrated DNA Technologies (IDT)	mm.Ri.pebp1.13.1
rArGrUrCrArUrUrCrUrGrUrUrGrUrUrGrArUrArUrArArArAAA	Integrated DNA Technologies (IDT)	mm.Ri.pebp1.13.2
rUrUrUrUrUrArUrArUrCrArArCrArArCrArGrArArUrGrArCrUrCrC	Integrated DNA Technologies (IDT)	mm.Ri.pebp1.13.2
Recombinant DNA		
Non-targeted Control CRISPR	Santa Cruz Biotechnology	Cat#sc-418922
PEBP1 cDNA	OriGene	Cat#RC206355
RKIP Double Nickase Plasmid (m)	Santa Cruz Biotechnology	Cat#sc-423929-NIC

3.2.6.15 Ferroptosis Synergy in HT22, IEC18, and Enteroid Monolayers

For GSK'872 ferroptosis experiments, HT22 or IEC18 cells were plated in 24-well plates (~$2 \cdot 10^4$ cells/well). After 18h, cells were treated with RSL3 (50 - 75 nM) ± GSK'872 (25 - 50 μM) ± Lip-1 or Fer-1 (1 or 10 μM). For enteroid monolayers, 50 enteroids were seeded in 24-well transwells and treated on day 3 post-differentiation, using the above drug dose ranges and those specific in legends. For RAF inhibitor-related ferroptosis experiments, HT22 cells were plated in 24-well plate ($1.7 – 2 \cdot 10^4$ cells/well). After 8-12 h incubation, cells were treated with RSL3 (75 nM) for 18-20h ± Raf-1 inhibitors (5 μM: Sorafenib, PLX4720, or SB590885) ± Fer-1 (400 nM). Collectively, cell death was determined by measuring released lactate dehydrogenase (LDH) activity at 18-24h post-exposure.

3.2.6.16 PEBP1 Expression and Purification

Full-length human PEBP1 and related mutants were cloned into a pET21-derived (EMD Millipore, Billerica, MA) bacterial expression plasmid modified to express PEBP1 with N-terminal His_{10}- and mRuby2 tags as described previously (Wenzel et al., 2017). All PEBP1 constructs were cloned into the modified pET21-mRuby2 vector by Gibson Assembly (New England Biolabs, Billerica, MA) using primers with homology at the upstream (sense) NdeI site (5′-GGTCTGAGGGGATACACTCATATG-3′) and downstream (antisense) EcoRI site (5′-GCTTGTCGACGGAGCTCGAATTC-3′) of the vector. All primers were ordered from Life Technologies (Carlsbad, CA). Clones were evaluated by diagnostic restriction digest and sequencing (Genewiz, South Plainfield, NJ). Protein expression was performed in the *Escherichia coli* strain BL21 (DE3) Codon+ (Agilent, Santa Clara, CA). Following initial growth to OD_{600} of 0.6, cells were induced using 0.2 mM isopropylthio-beta-galactosidase (IPTG) and cultured overnight at room temperature. Cells were harvested by centrifugation and lysed in buffer containing 20 mM Tris (pH 8.0), 500 mM NaCl, 5 % glycerol, 5 mM imidazole, 1 mM β-mercaptoethanol, and protease inhibitors. Lysates were cleared by centrifugation at 29,000 *xg*. Protein was initially purified by nickel affinity chromatography (Qiagen, Hilden, Germany), followed by overnight digestion with TEV protease to remove the N-terminal His_{10}-mRuby2 tag. After digestion, PEBP1 was isolated via a second round of nickel affinity chromatography. The protein was then dialyzed overnight at 4 °C into a buffer containing 20mM sodium acetate (pH 5.5) before cation exchange chromatography was performed in sodium acetate (pH 5.5) using a HiTrap SP column (GE Healthcare, Little Chalfont, UK). The resulting fractions were further refined by size exclusion chromatography in 20 mM HEPES (pH 8.0), 500 mM NaCl buffer using

a Sephacryl S-200 column (GE Healthcare). Before performing experiments, PEBP1 was desalted into 5 mM Bis-Tris (pH 6.5), 25 mM NaCl as described previously (Wenzel et al., 2017).

3.2.6.17 Kinase Activity Assay

Full-length human RIP3 (Abcam, Cambridge, UK) activity, alone (200-400 ng/reaction) or preequilibrated (30 min, RT) in the presence of equimolar concentrations of recombinant PEBP1 or a specific RIP3 inhibitor, GSK'872 (100 nM), was determined using the Promega Kinase Glo-Max assay (Promega, Madison, WI) per manufacturer's instructions. Activity of recombinant human RIP1 (SignalChem, R07-10G-10) and MAPK14 (ThermoFisher, PV3304) in the presence or absence of PEBP1 was also assessed. Reactions containing a final concentration of 200 μg/mL myelin basic protein (Abcam) and 12.5 μM ATP as the kinase substrates proceeded for 1 hour at room temperature in an opaque white 96-well plate. Relative inhibition is presented as percent loss of maximum observed kinase ATP consumption in the presence of equimolar PEBP1 or GSK'872.

3.2.6.18 Immunostaining and Confocal Microscopy

Cells were fixed in 2 % paraformaldehyde at 4 °C for 15 min and then permeabilized with 0.1 % Triton X-100 in PBS+ 0.5 % BSA (PBB) for 15 min. Tissue sections and cells were blocked with 5 % donkey serum for 45 min and incubated for 2 h at room temperature with the primary antibodies:15-LO2 (Santa Cruz sc67143), PEBP1 (Abcam ab196832), RIP3 (ProSci 2283). Alexa 488, cy3 and cy5 conjugated secondary antibodies were from Thermo-Fisher Scientific and Jackson Immuno. Cells were counterstained with Hoescht (Sigma B2883) 1mg/100ml dH_20 and mounted using Gelvatol. Terminal deoxynucleotidyl transferase (TdT)-mediated dUTP nick end labelling (TUNEL) was accomplished using the TMR Red kit (Cat. 12156792910) according to

the manufacturer's instructions (Roche, Basel, Switzerland). Images were collected in 200 nm z-steps using a Nikon A1R equipped with GAsP detectors and a 60X (1.4NA) objective.

3.2.6.19 Object-based Co-localization Analyses

Object-based methods take into account the spatial and intensity distribution of the fluorescent signal and is superior to pixel (intensity) based approaches at colocalization – such as Pearson's correlations (Dunn, Kamocka, & McDonald, 2011). 3D confocal (Nikon A1, 60X, 1.4NA) stacks (200 nm optical sections) were processed using blind deconvolution (10 iterations, NIS Elements, Nikon Inc., Melville NY) in order to maximize the information in each image and improve the accuracy of the subsequent object-based analysis (Biggs, 2010). Puncta (objects) were then segmented based on size and intensity using the 3D spot detection tool in NIS Elements General Analysis 3 (GA3), which generated a binary layer containing the spatial positioning of each object in the x-, y- and z- axis for each individual protein label (i.e., 15LOX, PEBP1 and RIP3). Co-localization was tested using a Boolean "having" operation. This logical argument tests the intersection of selected binary layers and will identify objects that have both protein A "and" protein B (e.g., 15LOX/PEBP1 or RIP3/PEBP1).

3.2.6.20 Fluorescence Resonance Energy Transfer

FRET based analyses can resolve the proximity of interacting proteins within 1–10 nm. The FRET phenomenon is the non-radiative (dipole-dipole) energy transfer from a fluorescent donor to an acceptor fluorophore. Because the efficiency of FRET decreases as the sixth power of the distance between the donor and acceptor, when the proteins are separated by >10 nm, no FRET occurs. PEBP1 and RIP3 were labelled with cy3 (donor) and cy5 (acceptor) and imaged at 10X zoom using a Leica SP8 spectral confocal microscope equipped with a 60X (1.4NA) optic. FRET

was confirmed by acceptor (cy5) photo-bleaching. With this method, if true FRET is present, the donor will show an increased intensity in the bleached region.

3.2.6.21 Isolation and Multicolored Cell Cycle Flow Analysis of Mouse Ileum Epithelial Cells

Isolation of epithelial cells from mouse small intestine (ileum) for multicolored flow analysis was performed as described previously (Gracz, Puthoff, & Magness, 2012; Vignon et al., 2013). Briefly, ileum was removed and washed with CMF-PBS (CMF: Ca^{2+}, Mg^{2+} free), opened longitudinally, and cut into 1.5 cm pieces. Tissue was dissociated in a 50 mL tube containing 30 mL of pre-warmed CMF-HBSS/FBS and 2 mM EDTA, then placed on a linear shaker (20 min, 250 rpm, 37 °C). Dissociated cells were separated from remaining tissue fragments using a cell strainer (40 µm pores). Cells were counted centrifuged and diluted to $1.67 \cdot 10^6$ cell/mL and fixed in CMF-PBS containing ethanol (66% v/v, overnight, 4 °C). Intestinal cells were then stained with PI (Propidium Iodide Flow Cytometry Kit, ab139418, Abcam), anti-γH2Ax antibody (PerCP/Cy5.5 anti-H2A.X-Phosphorylated (Ser139) antibody, 613414, Biolegend) and anti-CD326 antibody (CD326 (EpCAM)-APC, 130-102-234, Miltenyi Biotec). Labelled cells were analyzed using FACS Canto II (BD Bioscience) flow cytometer and FlowJo X Software (Becton, Dickinson & Company).

3.2.6.22 Molecular Docking Simulations

Protein-protein docking of RIP3, PEBP1, and RAF1. Simulations of RIP3/PEBP1 complex predictions have been performed using the CLUSPRO (Kozakov et al., 2017) respectively with PDB structures: RIP3(4M66) (T. Xie, Peng, Yan, et al., 2013), PEBP1(1BEH) (Banfield, Barker, Perry, & Brady, 1998), RAF1(3Q4C) (P. Xie et al., 2009). Molecular docking has been performed

with the SMINA package, which is a fork of AutoDock Vina (Trott & Olson, 2010); customized to better support scoring function development and high-performance energy minimization. For each structure, 10 independent runs were performed.

All-atom Molecular Dynamics Simulations. All-atom MD simulations were performed for human PEBP1 (1BEH) in complex with RIP3 (4M66), RIP3-K51A, or RIP1 (4ITJ) (T. Xie, Peng, Liu, et al., 2013) using the GROMACS MD simulation software (Hess, Kutzner, van der Spoel, & Lindahl, 2008) with CHARMM27 force fields (Mayaan, Moser, MacKerell, & York, 2007). The PEBP1 to RIP3/RIP3^{K51A}/RIP1 protein interaction has been identified using the molecular docking approach described above. In preparatory simulations with explicit water models (TIP3P), we adopted the following protocol: 0.2 ns of water equilibration, 10,000 steps of minimization, 0.35 ns of heating from 0 to 300 K, and 0.15 ns equilibration of the whole system before initiating production MD run. Three independent MD trajectories were generated, each 200 ns duration with 2 fs time step. A cutoff of 12 Å for non-bonded interactions was applied. Langevin dynamics and the Langevin piston algorithm were used to maintain the temperature at 300 K and the pressure at 1 atm. PYMOL were used for visualization.

Coarse-Grained Molecular Dynamics Simulations. The MARTINI force field version 2.2 (Marrink, Risselada, Yefimov, Tieleman, & de Vries, 2007) was used to simulate protein-protein interactions at the Coarse-grained level. Here, atoms are grouped together to form a single group, reducing the size of the system to be simulated, and reducing computational time The crystal structures of 15LOX (4NRE) (Kobe, Neau, Mitchell, Bartlett, & Newcomer, 2014), RIP3 (4M66) and PEBP1 (1BEH) were used to build the coarse-grained models. Three simulation systems were set up: All the three systems included 15LOX and PEBP1, system 1 had an additional one RIP3 molecule, system 2 had two RIP3 molecules and system 3 had three RIP3 molecules. The purpose

being to observe if the PEBP1's preferred binding partners. For each system, three different orientations of the proteins was created, to generate three trajectories (MD1, MD2, MD3).

The CHARMM-GUI interface (Jo, Kim, Iyer, & Im, 2008) was used to set up the simulation models. GROMACS version 5.1.4 was used to perform the molecular dynamics simulations with the standard parameter settings for the MARTINI force field. The system was simulated using the isothermal-isobaric (NPT) ensemble Prior to the production run of 150 ns, the simulation system was energy minimized and a series of equilibration simulations were performed to relax the protein and the solvent system. During the equilibration phase the force-constant of 4000 kJ mol^{-1} nm^{-2} is used and a standard value of 0.9 nm is the cut-off. The simulation temperature was 303.15 K. The v-rescale thermostat was used to control the temperature with a coupling constant τ_p = 1.0 ps. The pressure was isotropically coupled to an external bath of τ_p = 5.0 ps and compressibility of 4.5 x 10^{-5} bar^{-1} using the Berendsen barostat. The electrostatic interactions were calculated using a shifted potential with a cut-off of 1.2 nm, while for the van der Waals interactions, a shifted potential was used with a cutoff of 1.2 nm and switch at 0.9 nm. The interaction between the proteins is calculated as a minimum distance between any atom pair on the respective proteins.

3.2.6.23 Statistical Analysis

Data are expressed as Mean ± SEM or Mean ± S.D. as indicated in figure legends. Differences between treatment groups were analyzed by Student's t-test (two groups) and ANOVA (more than two groups, corrected for multiple comparisons) – or their non-parametric counterparts for non-normally distributed data. Differences were considered significant at $p<0.05$. The log-rank test (Mantel-Cox) was used for analysis of overall animal survival that is defined as the time from the date of radiation to the 30 days post-radiation between drug vs. vehicle-treated groups.

3.2.7 Results

3.2.7.1 Increased Ferroptotic Burden in Necroptosis-deficient *Rip3$^{K51A/K51A}$* Mice Following Irradiation

To investigate the interplay between necroptosis and ferroptosis, we utilized an animal model of whole-body γ-irradiation (IR) that induces a time-dependent mix of regulated cell death. Apoptosis begins within hours, regulated necrosis over the following days (Tyurina, Tyurin, Epperly, Greenberger, & Kagan, 2008). Our previous work showed that necrostatin-1 (Nec-1) improved survival after IR (Huang et al., 2016). We reasoned that total necroptosis blockade through genetic inactivation/knockout of (***i***) RIP1 *(Rip1$^{K45A/K45A}$*), (***ii***) RIP3 (*Rip3$^{-/-}$*, *Rip3$^{K51A/K51A}$*) or (***iii***) MLKL (*Mlkl$^{-/-}$*) would similarly reduce mortality. Neither *Rip1$^{K45A/K45A}$* (**Figure 17A**) nor *Rip3$^{-/-}$* animals (Castle et al., 2018) showed any IR survival advantage vs. wild type. Unexpectedly, IR elicited significantly greater mortality in both *Rip3$^{K51A/K51A}$* kinase-inactive knock-in (**Figure 18A**) and *Mlkl$^{-/-}$* knockout mice (**Figure 17B**) compared to wild type. RIP3 is the master regulator of necroptosis, and its kinase activity is indispensable for subsequent MLKL phosphorylation and necroptosis execution. Therefore, we explored the mechanisms and alternative death pathways responsible for *Rip3$^{K51A/K51A}$*-mediated IR mortality. The fast dividing epithelial cells of the small intestinal mucosa are particularly sensitive to IR (Somosy, Horvath, Telbisz, Rez, & Palfia, 2002). Corroborating this, *Rip3$^{K51A/K51A}$* ileal villi had greater nuclear terminal deoxynucleotidyl transferase dUTP nick end labeling (TUNEL) staining (**Figure 18B**) vs. wild type at a time point (day 3) when caspase 3/7 activity was not different between wild type vs. *Rip3$^{K51A/K51A}$* ileum after IR. Since increases in TUNEL staining can be observed in non-apoptotic death (Andreas Linkermann et al., 2014), we postulated that alternative regulated death pathways were likely upregulated in necroptosis deficient RIP3^{K51A} mice.

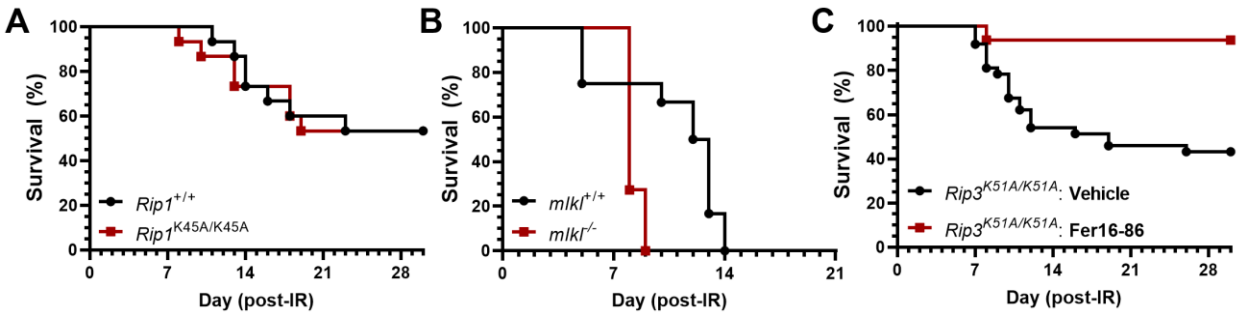

Figure 17. RIP1 kinase inhibition does not affect IR survival but MLKL deficiency enhances mortality

(A) Genetic inhibition of necroptosis via *Rip1*$^{K45A/K45A}$ kinase inactivation does not affect survival following total body irradiation (9.25 Gy) vs. wild type (*Rip1*$^{+/+}$) mice [Log-rank Mantel-Cox test, p = 0.934, n = 10-12 animals/group]

(B) Mixed linage kinase-like (MLKL) knockout (*Mlkl*$^{-/-}$, *red line*) mice exhibit greater mortality following whole-body IR vs. *Mlkl*$^{+/+}$ animals *(black line*) [Log-rank Mantel-Cox test, p < 0.05, n =11-12 animals/group]

(C) Ferrostatin16-86 (Fer16-86, SRS16-86) protected *Rip3*$^{K51A/K51A}$ mice compared to vehicle treatment [Log-rank [Mantel-Cox] test, p < 0.05, n = 10-16 animals/group, 2-3 independent experiments]

Data generated in collaboration with Michael W. Epperly and Michael J. Whalen.

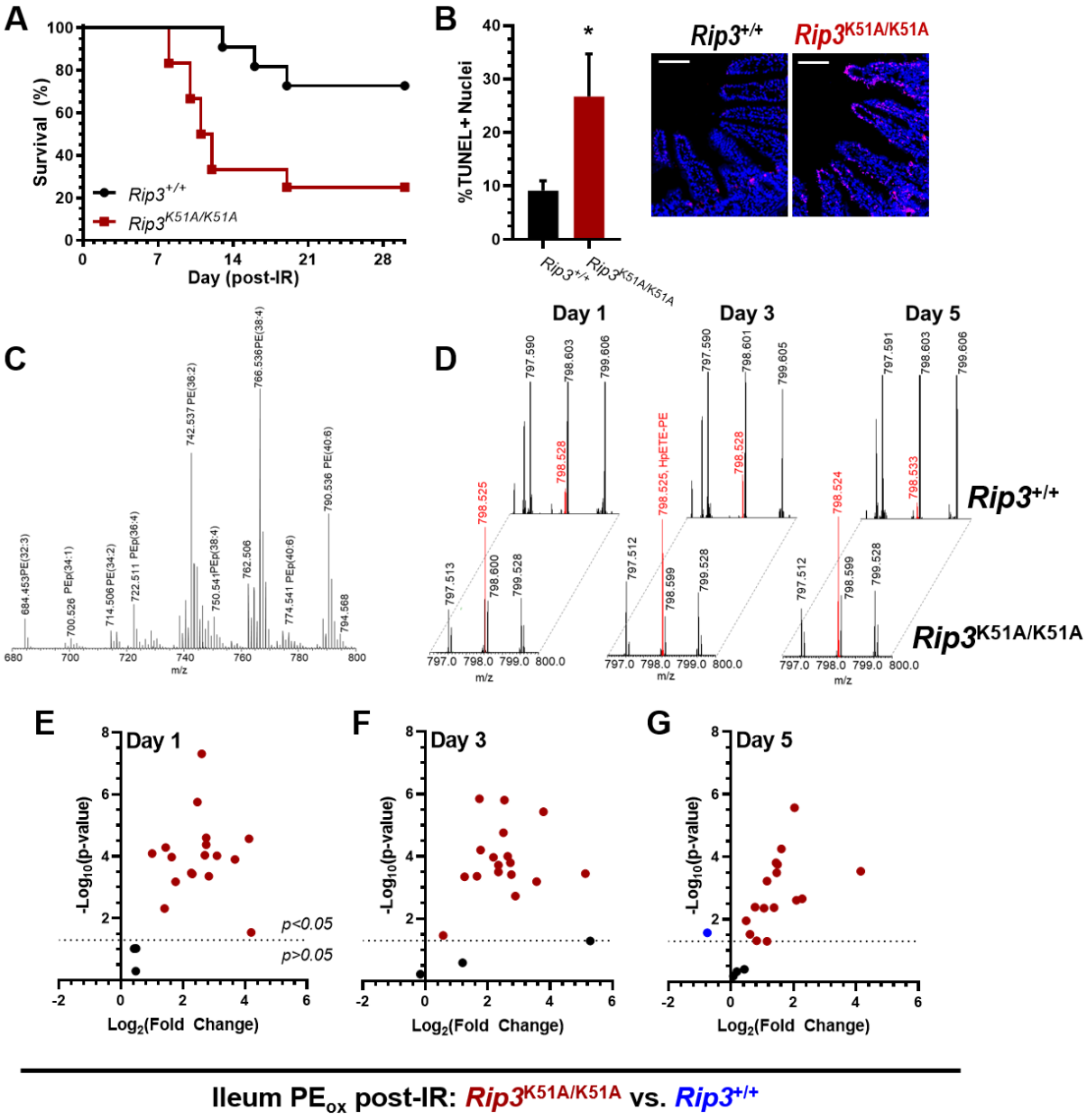

Figure 18. *Rip3*$^{K51A/K51A}$ mice experience greater total body irradiation-induced mortality vs. wild-type

(A) Mice expressing the kinase inactive RIP3^{K51A} died at a significantly higher rate compared to wild type control following total body irradiation (IR) [Log-rank (Mantel-Cox) test, $p < 0.05$, n =11-12 animals/group]

(B) Ileal mucosal injury was greater in *Rip3*$^{K51A/K51A}$ vs. *Rip3*$^{+/+}$ on post-IR (day 3), demonstrated by an increased proportion of TUNEL^{+} nuclei [Mean ± SEM, *p<0.05, n=6-7 mice/per group, *scale*: 100 μm].

(C) Representative mass spectrum demonstrating the relative ion identities and abundances of phosphatidylethanolamine (PE) and plasmalogen-PE (PEp) species found in naïve *Rip3*$^{K51A/K51A}$ ileum. Peaks are labeled as PE(X:Y) and PEp(X:Y) where "X" indicates the number of acyl carbons (Sn1 & Sn2 positions), and "Y" represents the total number of unsaturated acyl chain bonds.

(D) Representative mass spectrum showing higher abundance of pro-ferroptotic hydroperoxyeicosatetraenoicacid-PE (15-HpETE-PE, m/z 798.528) in *Rip3*$^{K51A/K51A}$ (lower panel) vs. wild type (upper panel) ileum at various times post-IR.

(E-F) PEox expression in *Rip3*$^{K51A/K51A}$ vs. *Rip3*$^{+/+}$ ileum on **(E)** day 1, **(F)** day 3, and **(G)** day 5 after IR. Proferroptotic PEox was increased in *Rip3*$^{K51A/K51A}$ ileum compared to *Rip3*$^{+/+}$ [volcano plots: $\log_2$(fold-change: *Rip3*$^{K51A/K51A}$ versus *Rip3*$^{+/+}$) vs. -$\log_{10}$(statistical *p*-value); *red* = increased levels & *blue* = decreased levels] Data gathered in collaboration with Michael W. Epperly and Claudette M. St Croix.

To identify the cell death mechanisms differentially engaged in RIP3^{K51A} animals, we used *Rip3*$^{K51A/K51A}$ vs. *Rip3*$^{+/+}$ primary (*1*) ileum-derived differentiated enteroid monolayer culture (**Figure 19A**) and (*2*) IL-3 dependent long-term bone marrow (BM) systems. Like animals, *Rip3*$^{K51A/K51A}$ enteroid monolayers (**Figure 19B**) and BM (**Figure 19C**) displayed greater IR-induced death vs. wild type. We used these systems to test the radioprotective efficacy of several small molecule death inhibitors and test which, if any, alternative cell death mechanism(s) had been upregulated by RIP3 kinase inactivation. As expected, necrostatin-1s (Nec-1s), a specific RIP1 inhibitor, protected *Rip3*$^{+/+}$ wild type but not mutant necroptosis-deficient *Rip3*$^{K51A/K51A}$ BM cells. The pan-caspase inhibitor, z-VAD-fmk, benefited both wild type and RIP3^{K51A} BM significantly. In contrast, sanglifehrin, a cyclophilin D (CyD) inhibitor, was ineffective in both BM groups. Notably, execution of ferroptosis was different between *Rip3*$^{+/+}$ and *Rip3*$^{K51A/K51A}$ cells. Anti-ferroptotic ferrostatin-1 (Fer-1) and liproxstatin-1 (Lip-1) provided robust radioprotection in *Rip3*$^{K51A/K51A}$ enteroids (**Figure 19B**) and BM (**Figure 19C**) but afforded no benefit to *Rip3*$^{+/+}$ cells. This prompted us to explore the differential role of ferroptosis in *Rip3*$^{K51A/K51A}$ vs. *Rip3*$^{+/+}$ *in vivo*.

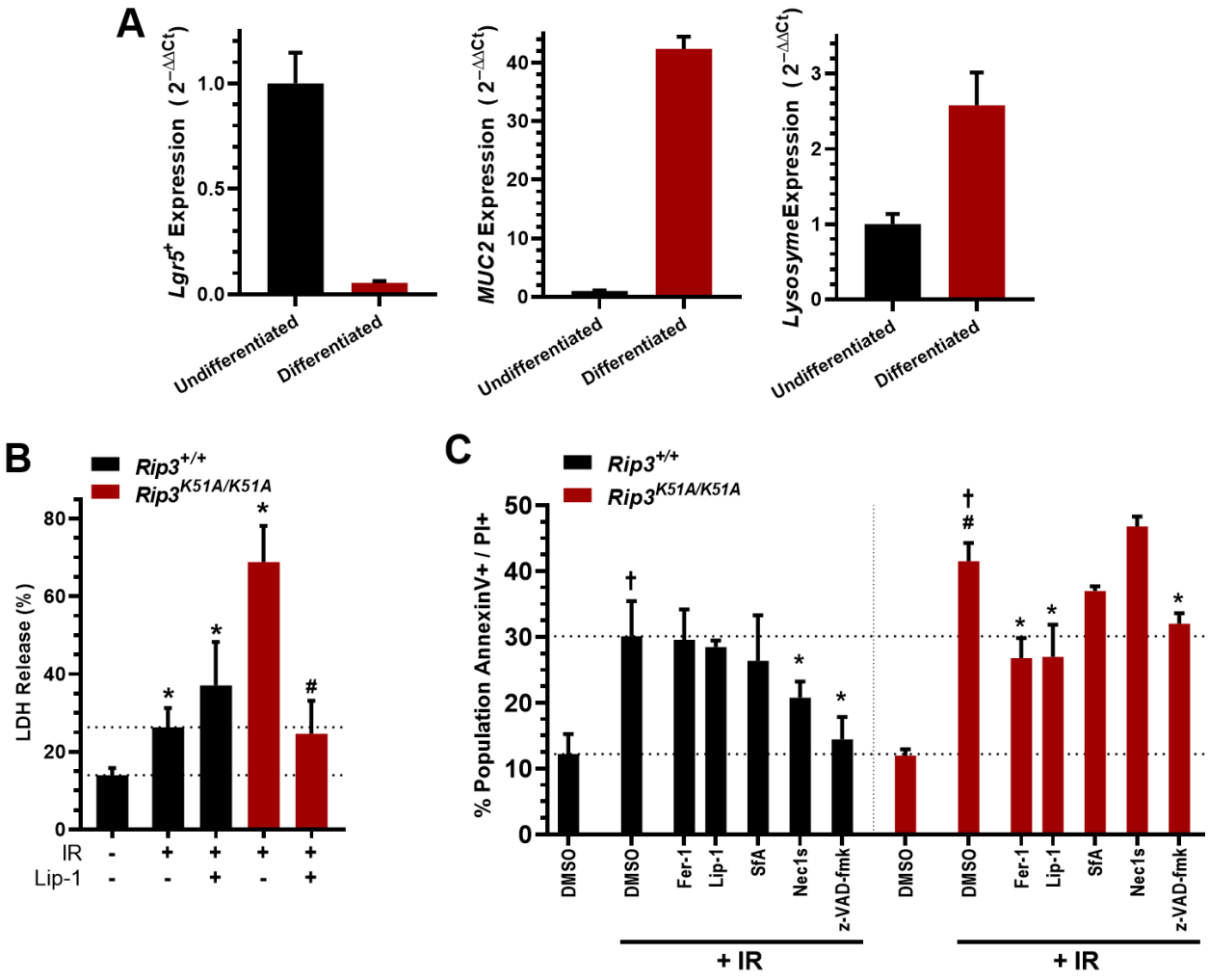

Figure 19. Primary *Rip3*$^{K51A/K51A}$ bone marrow cells and enteroids are more sensitive to ferroptotic death

(A) Real-time PCR mRNA characterization of undifferentiated vs. differentiated mouse primary ileum monolayer organoids. Treatment with differentiation medium (3 day) results in reduced expression of the stem cell marker, *Lgr5*$^{+}$. Concurrently, expression of Goblet cell (*Muc2)* and Paneth cell (*lysozyme)* markers was upregulated [$2^{-\Delta\Delta Ct}$ Mean ± SD, *p< 0.05, n = 3/group, representative of 3 independent experiments]

(B) Primary differentiated enteroid monolayers derived from *Rip3*$^{K51A/K51A}$ mice are significantly more sensitive to irradiation-induced death compared to wild type cells. *Rip3*$^{K51A/K51A}$ enteroid mortality was reduced with anti-ferroptotic Lip-1. Cell death measured by LDH release at 22-24 h, Mean ± SEM, *p< 0.05 vs. 0 Gy group, #p< 0.05 vs. matched IR + vehicle group, n = 3-6 transwells/group.

(C) *Rip3*$^{K51A/K51A}$ primary mouse BM cells are more sensitive to IR (20 Gy) injury compared to *Rip3*$^{+/+}$ wild type cells. Only *Rip3*$^{K51A/K51A}$ BM cells benefited from anti-ferroptotic agents, Fer-1 or Lip-1. Neither group benefited significantly from the cyclophilin-D and mPTP inhibitor, sanglifehrin-A. Anti-apoptotic z-VAD-fmk was protective in both groups. Nec-1s was only protective in wild type cells but not *Rip3*$^{K51A/K51A}$, confirming the functional necroptosis knockout. Cell death measured by Annexin V-FITC + Propidium iodide (PI) flow cytometry, Mean ± SD,

*p< 0.05 vs. same genotype IR+DMSO group, †p<0.05 vs. respective DMSO-only (no IR), #p< 0.05 vs. wild-type IR+DMSO group, n = 4-6 dishes.

Data gathered in collaboration with Heather L. Mentrup.

Ferroptosis susceptibility and execution of the death pathway have been linked to the expression of four proteins – ACSL4, GPX4, 15LOX, and PEBP1. Thus, we examined the expression of these components in radiosensitive ileal tissue of both *Rip3*$^{K51A/K51A}$ and wild type mice using immunoblot (**Figure 20A**). IR markedly upregulated ACSL4 expression – priming cells for ferroptosis – in ileum of both *Rip3*$^{K51A/K51A}$ and wild type mice. Pre-injury levels of ACSL4-synthesized AA- and AdA-PE were not different (**Figure 20B**), implying the differences in basal ACSL4 activity did not drive ferroptosis sensitization. Expression of the PEox generators – 15LOX and PEBP1 – increased in *Rip3*$^{K51A/K51A}$ vs. wild type, consistent with a greater ferroptotic burden. We next quantified doubly-/triply-oxidized AA-PE and AdA-PE (PEox) – the most sensitive and specific markers of ongoing ferroptosis – using high resolution liquid chromatography tandem mass spectrometry (LC-MS/MS)-based redox lipidomics (**Figure 18C,D; Figure 20C**). Pro-ferroptotic PEox expression was indeed greater in *Rip3*$^{K51A/K51A}$ ileum at day 1, 3, and 5 post-IR compared to wild type (**Fig. 18E-G; Fig. 20D**).

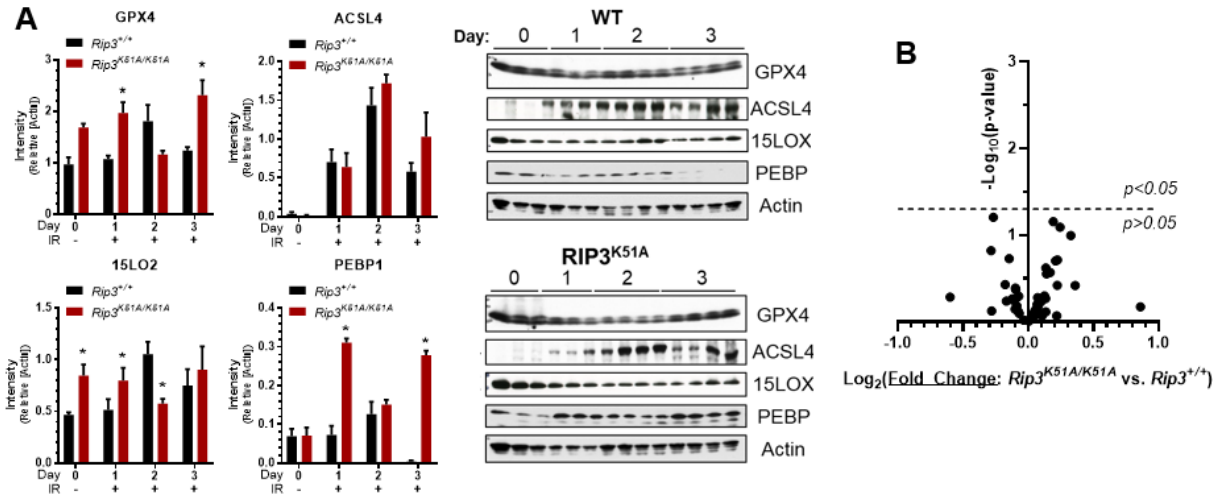

C

***Rip3*$^{K51A/K51A}$ Ileum: Oxidized Phosphatidylethanolamine (PEox) post-irradiation**
(Significantly Changed)

Day 1 vs. Day 0			Day 3 vs. Day 0			Day 5 vs. Day 0		
Decreased	Increased		Decreased	Increased		Decreased	Increased	
PE(34:3)+2O	PE(36:2)+2O	PE(42:7)+4O	PE(34:3)+2O	PE(36:2)+2O	PE(42:7)+2O	(n/a)	PE(36:2)+2O	PE(42:5)+3O
	PE(38:5)+2O	PE(42:8)+2O	PE(42:4)+2O	PE(38:5)+2O	PE(42:7)+3O		PE(38:4)+2O	PE(42:6)+3O
	PE(38:5)+3O	PE(42:8)+4O	PE(44:6)+2O	PE(38:5)+3O	PE(42:7)+4O		PE(38:5)+3O	PE(42:8)+3O
	PE(40:4)+2O	PE(42:9)+4O	PE(46:6)+3O	PE(38:6)+3O	PE(42:8)+3O		PE(40:4)+2O	PE(44:10)+3O
	PE(40:5)+2O	PE(44:10)+2O		PE(40:4)+2O	PE(42:8)+4O		PE(40:4)+3O	PE(44:4)+2O
	PE(40:5)+3O	PE(44:10)+3O		PE(40:5)+2O	PE(42:9)+4O		PE(40:5)+2O	PE(44:5)+2O
	PE(40:6)+3O	PE(44:12)+3O		PE(40:5)+3O	PE(44:10)+3O		PE(40:5)+3O	PE(44:5)+3O
	PE(40:7)+2O	PE(44:5)+2O		PE(40:6)+2O	PE(44:5)+2O		PE(40:6)+2O	PE(44:6)+3O
	PE(40:7)+3O	PE(44:5)+3O		PE(40:6)+3O	PE(44:5)+3O		PE(40:6)+3O	PE(44:6)+4O
	PE(42:3)+4O	PE(44:6)+3O		PE(40:7)+3O	PE(44:7)+2O		PE(40:7)+2O	PE(44:7)+2O
	PE(42:4)+4O	PE(44:7)+2O		PE(42:5)+3O	PE(44:7)+3O		PE(40:7)+3O	PE(44:7)+3O
	PE(42:5)+2O	PE(44:7)+3O		PE(42:6)+2O	PE(44:7)+4O		PE(42:5)+2O	PE(44:7)+4O

D

***Rip3*$^{K51A/K51A}$ *vs. Rip3*$^{+/+}$ Ileum: Oxidized Phosphatidylethanolamine (PEox) post-irradiation**
(Significantly Changed)

Day 1			Day 3			Day 5		
Decreased	Increased		Decreased	Increased		Decreased	Increased	
(none)	PE(38:4)+2O	PE(40:7)+2O	(none)	PE(36:4)+2O	PE(40:6)+2O	PE(38:6)+2O	PE(38:4)+2O	PE(40:7)+3O
	PE(38:5)+2O	PE(40:7)+3O		PE(38:4)+2O	PE(40:6)+3O		PE(38:5)+3O	PE(40:7)+4O
	PE(38:5)+3O	PE(40:7)+4O		PE(38:5)+2O	PE(40:7)+2O		PE(38:6)+3O	PE(40:8)+2O
	PE(38:6)+3O	PE(40:8)+2O		PE(38:5)+3O	PE(40:7)+3O		PE(40:4)+2O	PE(40:8)+3O
	PE(40:4)+2O	PE(40:8)+3O		PE(38:6)+3O	PE(40:7)+4O		PE(40:4)+3O	PE(42:10)+3O
	PE(40:4)+3O	PE(42:10)+3O		PE(40:4)+2O	PE(40:8)+2O		PE(40:5)+3O	PE(42:4)+2O
	PE(40:5)+3O	PE(42:4)+2O		PE(40:4)+3O	PE(40:8)+3O		PE(40:6)+2O	PE(42:5)+2O
	PE(40:6)+2O	PE(42:5)+2O		PE(40:5)+3O	PE(42:4)+2O		PE(40:6)+3O	
	PE(40:6)+3O			PE(42:5)+2O				

E

***Rip3*$^{K51A/K51A}$ Ileum: Oxidized Phosphatidylethanolamine (PEox) post-irradiation ± Liproxstatin-1**
(Significantly Changed)

Day 1: Lip-1 vs. Vehicle		Day 3: Lip-1 vs. Vehicle		Day 5: Lip-1 vs. Vehicle		
Decreased	Increased	Decreased	Increased	Decreased	Increased	
PE(38:3)+2O	PE(42:10)+2O	PE(42:10)+2O	PE(38:6)+3O	PE(38:4)+2O	PE(40:7)+2O	PE(44:10)+2O
PE(40:6)+4O	PE(38:5)+3O	PE(42:6)+2O		PE(38:5)+3O	PE(42:6)+3O	PE(44:10)+3O
PE(42:4)+4O	PE(38:6)+3O	PE(42:9)+2O			PE(42:7)+2O	PE(44:6)+4O
PE(44:6)+3O	PE(40:4)+3O	PE(44:7)+4O			PE(42:7)+3O	PE(44:7)+2O
PE(44:7)+3O	PE(40:7)+3O				PE(42:7)+4O	PE(44:7)+4O
PE(46:6)+3O	PE(42:9)+3O				PE(42:8)+3O	PE(46:7)+2O
						PE(46:7)+3O

Figure 20. Expression profile of ferroptotic proteins in RIP3^{K51A} vs wild type ileum before and after IR

(A) Immunoblots of ferroptotic regulatory proteins demonstrating increased 15LOX & PEBP1 expression, supportive of a greater ferroptotic burden in *Rip3*$^{K51A/K51A}$ ileum compared to wild type. Mean ± SEM, intensity normalized to actin, *p< 0.05, n = 4-5 animals/group.

(B) Abundance of ACSL4 synthesized AA- and AdA-containing PE species, important for ferroptotic signaling, are not different between *Rip3*$^{+/+}$ and *Rip3*$^{K51A/K51A}$ animals at baseline (0 Gy). Volcano plot: $\log_2$(fold-change: *Rip3*$^{K51A/K51A}$ versus *Rip3*$^{+/+}$) vs. $\log_{10}$(statistical *p*-value); *species above horizontal dash line are significantly changed*

(C-E) Liquid chromatography mass spectrometry (LC-MS) redox lipidomics results showing significantly increasing (*red*) or decreasing (*blue*) PEox species on the indicated day post-irradiation in *Rip3*$^{K51A/K51A}$ ileum compared to **(C)** 0 Gy [vehicle only, *Rip3*$^{K51A/K51A}$], **(D)** Wild-type (*Rip3*$^{+/+}$) ileum, **(E)** Lip-1 treatment [Lip-1 vs. vehicle, time matched] Data gathered in collaboration with Michael W. Epperly, Tamil S. Anthonymuthu, Zachary E. Hier, and Andrew A. Amoscato.

To further test the contribution of ferroptotic death to IR-induced intestinal injury in wild type and *Rip3*$^{K51A/K51A}$ mice, we utilized anti-ferroptotic compound Lip-1 and a novel pharmacokinetically advanced homolog of Fer-1, Ferrostatin16-86 (Fer16-86) *in vivo*. Both Lip-1 and Fer16-86 protected *Rip3*$^{K51A/K51A}$ mice against lethal IR (**Fig. 21A, 17C**) but were ineffective in *Rip3*$^{+/+}$ animals. Immunocytochemistry and object-based co-localization analysis showed the formation of the ferroptotic redox phospholipoxysome (PEBP1 and 15LOX complex) in *Rip3*$^{K51A/K51A}$ ileum after IR (**Fig. 21B**). Pro-ferroptotic PEox generated by PEBP1_15LOX complex in *Rip3*$^{K51A/K51A}$ tissue (**Fig. 21C**) was significantly reduced by Lip-1. Using tandem LC-MS/MS analysis, we verified the identity of specific 15LOX-synthesized PE[38:4]+2O (HpETE-PE) and other ferroptotic PEox species (**Fig. 20E**). Lip-1-induced downregulation of doubly-/triply-oxidized PE coincided with increased detection of chemically reduced, ferroptotically-inactive singly-oxygenated hydroxy-PE counterparts (**Fig. 21D**). Collectively, these data indicate that (*1*) RIP3^{K51A} expression enhances IR mortality and (2) increased PEBP1_15LOX mediated PEox synthesis, mitigatable by Lip-1, drove this effect.

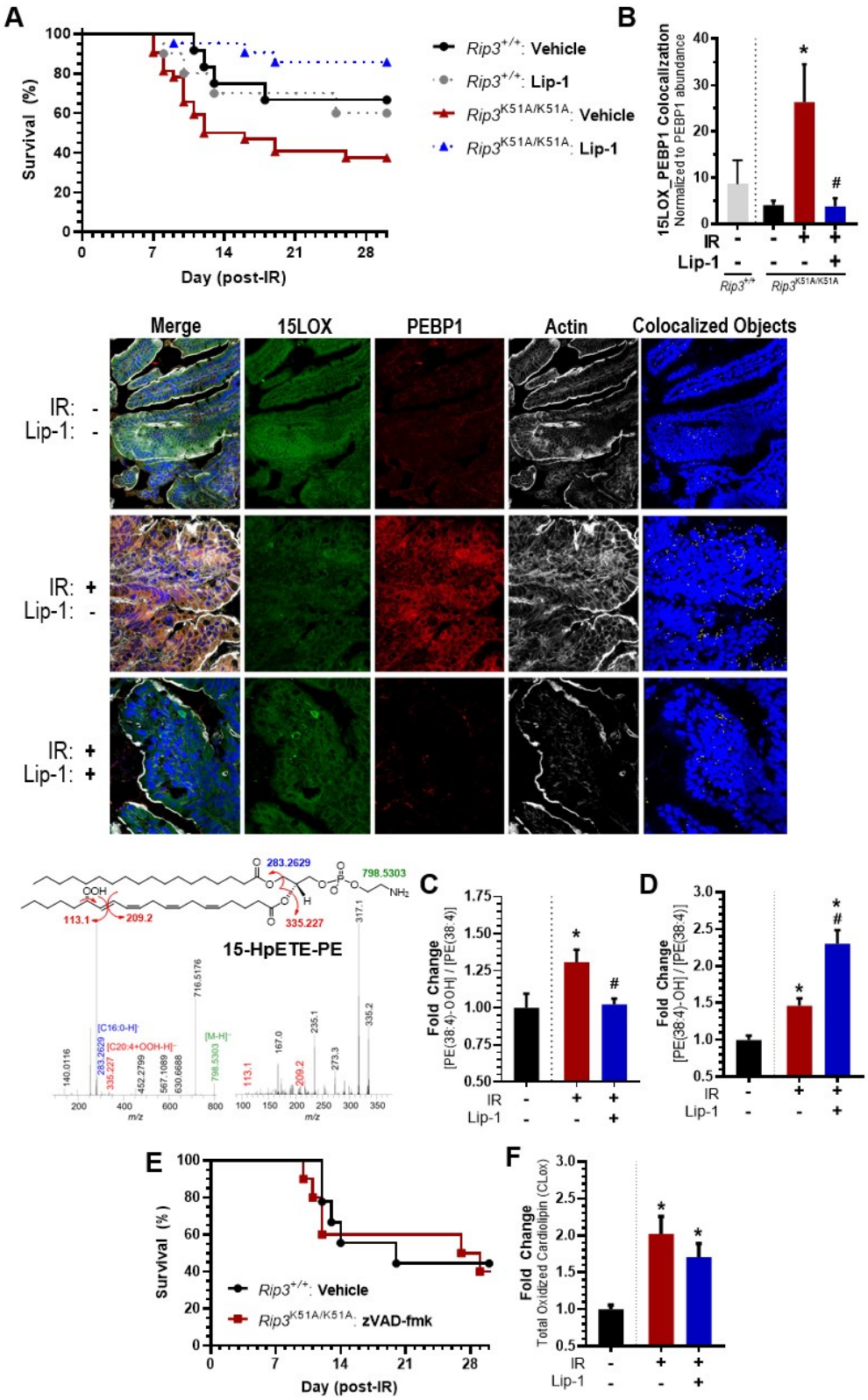

Figure 21. Liproxstatin-1 rescues Rip3$^{K51A/K51A}$ mice from IR and attenuates ferroptotic PEBP1_15LOX activity

(A) Liproxstatin-1 (Lip-1) was radioprotective and reduced IR mortality of *Rip3*$^{K51A/K51A}$ but not *Rip3*$^{+/+}$ mice [Log-rank (Mantel-Cox) test, $p < 0.05$, n = 10-12 animals/group, data shown from 2-3 independent experiments/group]

(B) IR promotes the colocalization and formation of ferroptoticPEBP1_15LOX2 complexes (day 3) in *Rip3*$^{K51A/K51A}$ ileum villi. Lip-1 treatment reduces PEBP1_15LOX2 colocalization [*Left,* Bar graph of PEBP1_15LOX colocalization normalized to PEBP1 abundance, Mean ± SEM, *p< 0.05 vs. non-irradiated, #p<0.05 vs. IR + vehicle; *Right,* Representative micrographs: "Merge" (*upper panels*): PEBP1 (*red*), 15LOX2 (*green*), nuclei (*blue*), and actin (*white*). "Colocalized objects" (*lower panels*): PEBP1_15LOX colocalized objects (*yellow*), n = 3 animals/group, scale: 50 μm]

(C) IR leads to accumulation of pro-ferroptotic PE(38:4)-OOH (15-HpETE-PE) levels increased in ileum post-IR (day 5). (*Left*) Lip-1 reduced PEox to pre-injury levels. (*Right*) MS2/3 fragmentation mass spectra confirming identity of 15LOX-synthesized pro-ferroptotic 15-HpETE-PE [fold change PE(38:4)+2O concentration, normalized to parent ion [PE(38:4)] abundance, n=5/group, Mean ± SEM, *p< 0.05 vs. 0 Gy, #p< 0.05 versus IR + vehicle]

(D) Lip-1 treatment increased levels of PE(38:4)-OH (15-HETE-PE), the chemically reduced and ferroptotically inert metabolite of 15-HpETE-PE [fold change PE(38:4)+OH concentration, normalized to parent ion ([PE(38:4)] abundance, n=5/group, Mean ± SEM, *p< 0.05 vs. 0 Gy, #p< 0.05 versus IR + vehicle].

(E) The anti-apoptotic, pan-caspase inhibitor, z-VAD-fmk (*red line*), did not improve post-IR survival outcomes in *Rip3*$^{K51A/K51A}$ animals compared to vehicle treatment (*black line*) [Log-rank Mantel-Cox test, p = 0.180, n=11-12 animals/group].

(F) Liproxstatin-1 does not alter irradiation-induced pro-apoptotic oxidized CL (CLox) accumulation. CLox levels were increased in *Rip3*$^{K51A/K51A}$ whole ileum on day 3 following whole-body irradiation. Lip-1 did not reduce ileal CLox levels [Mean ± SEM, *p< 0.05 vs. 0 Gy control, n = 5 animals/group].

Data gathered in collaboration with Michael W. Epperly, Claudette M. St Croix, and Tamil S. Anthonymuthu, Zachary E. Hier, and Andrew A. Amoscato.

3.2.7.2 Contribution of Alternate Cell Death Pathways to *Rip3*$^{K51A/K51A}$ IR Mortality

Cell death programs are triggered when the relevant components are in place and activated. Beyond these regulated pathways, IR-induced genomic injury can prompt death by mitotic catastrophe (MC) (Castedo et al., 2004). MC-associated death proceeds in the absence of a clear suicide signal (Fragkos & Beard, 2011), but it prompts classical regulated death pathways, like intrinsic apoptosis. Irrespective of the exact execution mechanism, two common denominators are found in all cases of MC. First, MC follows DNA damage and/or perturbation of the mitotic apparatus. Second, MC is accompanied by mitotic arrest (G2/M arrest), cell death, senescence,

and/or aneuploidy. We quantified IR's effects on the extent of DNA damage and cell cycle arrest between wild type (*Rip3*$^{+/+}$) and *Rip3*$^{K51A/K51A}$ animals *in vivo*. Phosphorylation of H2AX at Ser139 (γH2AX) is a highly sensitive marker indicating the extent and persistence of DNA lesions (Sharma, Singh, & Almasan, 2012). We found γH2AX was upregulated globally throughout the ileum at 24 and 72h post-IR (**Fig. 22A**) and specifically within CD326+ intestinal epithelial cells (**Fig. 22B**). However, no differences were observed between *Rip3*$^{+/+}$ and *Rip3*$^{K51A/K51A}$ animals. We next assessed IR's effect on CD326+ cell G2/M phase arrest. While IR-induced mitotic delay at a rate of 1h per Gy has been reported (Hua et al., 2017), we did not observe an accumulation of G2/M cells by 12h following 9.25 Gy exposure in both groups. Increased G2/M arrest was detected by day 3 post-IR, but the injury effect was independent of animal genotype (**Fig. 22C,D**).

Further, based on our *in vitro* BM results and previously published work on alternate RIP3 kinase inactivated mutants, we considered that differences in apoptosis execution might contribute to *Rip3*$^{K51A/K51A}$ IR susceptibility. While no differences were noted on day 3 after IR, increased caspase-3/7 activity was observed in *Rip3*$^{K51A/K51A}$ whole ileum both prior to (day 0) and on day 1 following IR (**Fig. 22E**). Similarly, ileum levels of oxidized cardiolipin (CLox) – a sensitive and early apoptotic signal (Valerian E Kagan et al., 2005) – increased with IR (**Fig. 21F**). Levels of non-oxidized reduced CL were reciprocally reduced (**Fig. 22G**). z-VAD-fmk administration, however, did not rescue *Rip3*$^{K51A/K51A}$ mice from IR-induced lethality suggesting caspase-dependent apoptosis does not contribute to overall mortality (**Fig. 21E**). Finally, to verify that Lip-1 radioprotection observed only in *Rip3*$^{K51A/K51A}$ animals was not partially due to an unrecognized anti-apoptotic effect, we measured ileal CLox in Lip-1 treated animals. There were no changes in post-IR CLox levels (**Fig. 21F**) or caspase-3/7 activity (**Fig. 22F**) between Lip-1 and vehicle groups, indicating Lip-1 radioprotection was specifically realized by ferroptosis inhibition.

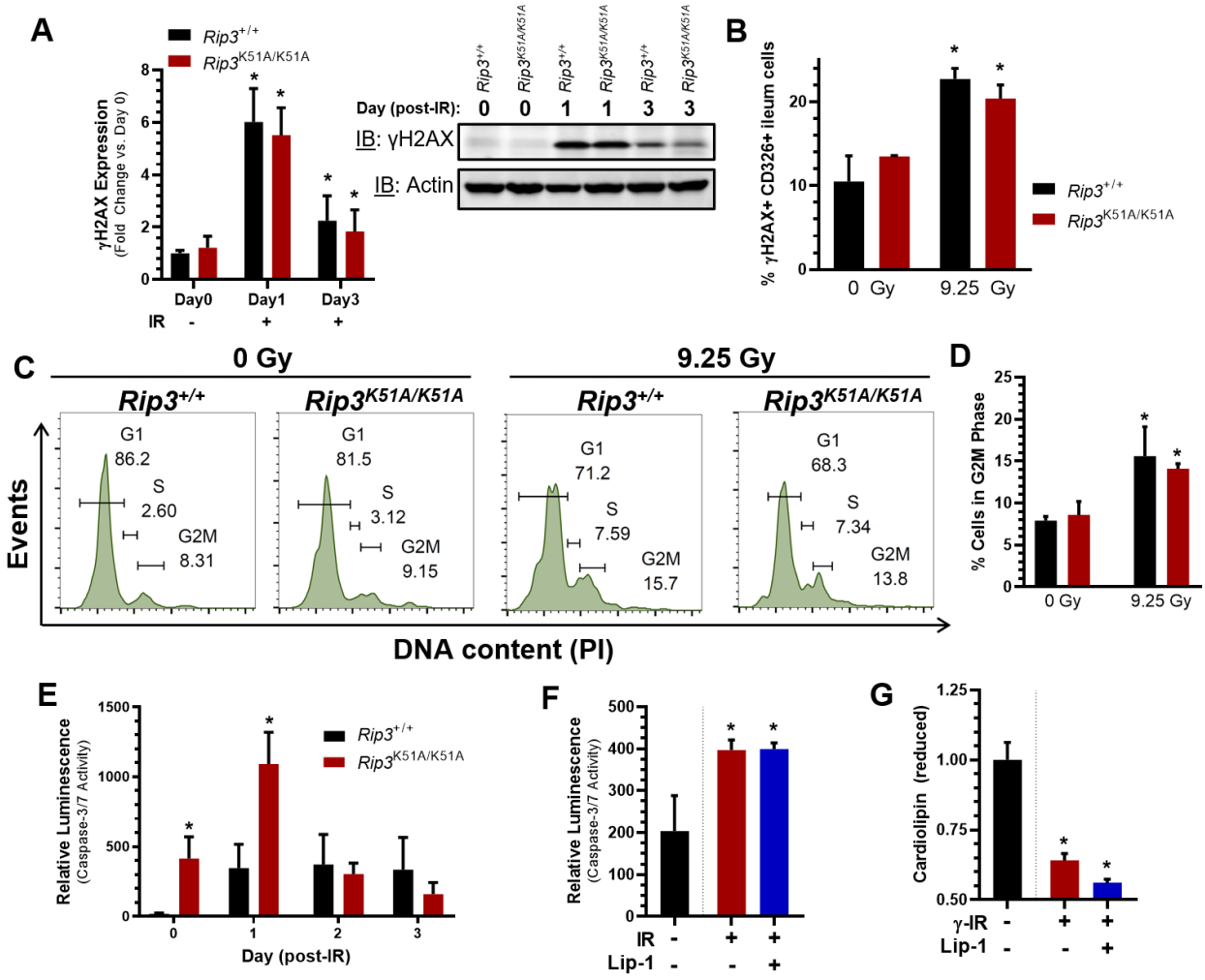

Figure 22. Irradiation-induced DNA damage, cell cycle arrest, and apoptosis execution were similar between Rip3$^{K51A/K51A}$ and Rip3$^{+/+}$ animals.

(A) γH2AX is a marker of DNA damage, including IR-induced double stranded breaks. γH2AX expression in ileum is increased following IR (day 1, 3), quantified using immunoblot densitometry. IR-induced γH2AX upregulation was equivalent between *Rip3$^{K51A/K51A}$* and *Rip3$^{+/+}$* animals. Actin normalized γH2AX signal intensity, Mean ± SD, n = 5 animals/group, *p<0.05 vs. respective 0 Gy group.

(B) IR (9.25 Gy) enhanced proportions of CD326^{+} & γH2AX^{+} double positive intestinal epithelial cells (day 3) isolated from *Rip3$^{K51A/K51A}$* and *Rip3$^{+/+}$* mice, but this effect was independent of animal genotype. Mean ± SD, n = 3 animals/group, *p<0.05 vs. respective 0 Gy group.

(C-D) Representative histograms showing cell cycle analysis of CD326+ ileum epithelial cells by assessment of DNA content using flow cytometry from *Rip3$^{K51A/K51A}$* or *Rip3$^{+/+}$* animals pre- (0 Gy) and post-IR (9.25 Gy). Increased proportion of cells in G2/M phase (IR, day 3) independent of animal genotype was observed. No IR effect was observed at earlier timepoints (day 1 post-IR, *data not shown*). *Histograms*: CD326^{+} epithelial cells (events) vs. PI fluorescent intensity (DNA content), Mean ± SD, n = 3 animals/group, *p<0.05 vs. respective 0 Gy group.

(E) Caspase-3/7 activity in *Rip3*$^{K51A/K51A}$ ileum vs. *Rip3*$^{+/+}$ prior to and on day 1, 2 and 3 post-IR. Caspase-3/7 activity was higher at baseline and day 1 after IR. Arbitrary units (AU), normalized to total protein concentration, Mean ± SEM, *p< 0.05 vs. time matched wild type, n = 5/group.

(F) Lip-1 did not alter IR-induced caspase-3/7 activation and enzyme activity in *Rip3*$^{K51A/K51A}$ mouse ileum (day 1) [arbitrary units (AU), normalized to total protein concentration, Mean ± SD, *p< 0.05 vs. IR+vehicle, n = 5 animals/group]

(G) Loss of non-oxidized, tetraacylated cardiolipin (CL) following IR is a sensitive but non-specific sign of mitochondrial injury. Lip-1 did not alter *Rip3*$^{K51A/K51A}$ mouse ileum CL content by day 3 following IR vs. vehicle [Mean ± SEM, *p< 0.05 vs. 0 Gy control, n = 5 animals/group]

Data gathered in collaboration with Qin Yang, Aleksandr A. Kapralov, Galina Shruin, and Tamil S. Anthonymuthu.

3.2.7.3 PEBP1 forms complexes with RIP3

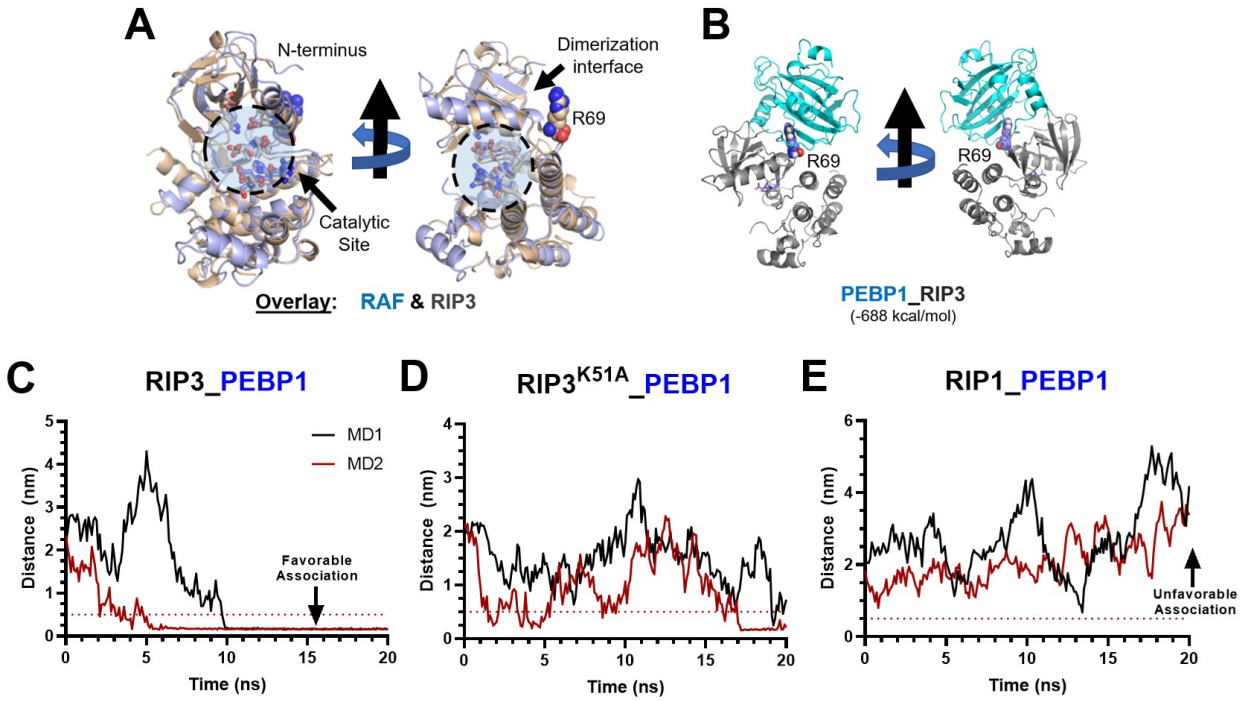

Figure 23. RIP3_PEBP1 Interaction

(A) The structures of RAF and RIP3 are highly similar, as shown by superimposition of the two x-ray structures of RAF1 (pdbid: 3c4c) and RIP3 (pdbid: 4m66). The catalytic site region (enclosed in dashed circle) are highly conserved both sequentially and structurally between the two kinases.

(B) Lowest energy binding pose of PEBP1 on RIP3 from docking simulations. RIP3 kinase is shown in grey and PEBP1 in cyan, where the arginine (R69) at RIP3's dimerization interface is highlighted (spacefilling model) and the conserved DGF motif is indicated (stick model).

(C) Specific and close interaction of PEBP1 with RIP3 is also observed in Full Atomistic Molecular Dynamics (FAMD) Simulations. The plot shows minimum distance between any atom on PEBP1 and wild type RIP3 ($RIP3^{WT}$) (*left*), PEBP1_$RIP3^{K51A}$ mutant (*middle*) and PEBP1_RIP1 (*right*) as a function of time. The red dotted line indicates minimum distance required for interaction (≤0.5 nm). PEBP1 does not interact with either RIP1 or $RIP3^{K51A}$ mutant but does interact with $RIP3^{WT}$.
Data gathered in collaboration with Indira Shrivastava.

As we established that *Rip3*$^{K51A/K51A}$ mutant cells and animals had higher sensitivity to radiation via ferroptotic death, we next examined the mechanism of enhanced ferroptosis and the role of K51A mutation in this. Given that PEBP1 levels were increased in *Rip3*$^{K51A/K51A}$ vs. wild type mice post-IR (**Fig. 20A**), we asked whether this could be the switching mechanism to ferroptosis. PEBP1 displays regulatory promiscuity towards multiple protein partners, including

its canonical partner RAF1 kinase. By assessing the structural conservancy between RIP kinase family members and RAF1 kinase, we found that RIP3 was the most similar (**Fig. 23A**). While RAF1 and RIP3 have expectedly similar Ser/Thr kinase domains, we noted their similarities also included a conserved (*1*) ASP_GLY_PHE (DGF, Mg^{2+} binding site) motif, (*2*) HIS_ARG_ASP_LEU motif (HRDL, ATP binding site) (**Fig. 23A**), and (*3*) an arginine at their respective dimerization interfaces (**Fig. 24A-C**) (Lavoie & Therrien, 2015). Molecular docking simulations showed that the interaction of PEBP1 with RIP3 was energetically favorable (**Fig. 23B**). The top 10 lowest energy binding poses all oriented such that (*1*) PEBP1 was proximal to RIP3's catalytic site and necroptosis-obligate homodimerization interface (Raju et al., 2018) and (*2*) PEBP1 bound RIP3 via its heterodimerization loop region that includes residues 127-150 (Banfield et al., 1998). Enhancing the validity of this modeled interaction, we found the experimentally-verified PEBP1→RAF1 dimer binding orientation matched that of our computed PEBP1→RIP3 interaction (Deiss et al., 2012; Wenzel et al., 2017). Full atomistic molecular dynamics (FAMD) simulations showed the formation of PEBP1–RIP3 complexes (**Fig. 23C, left**) within tens of nanoseconds (ns) with wild type RIP3 (**Fig. 23C**) – but not with $RIP3^{K51A}$ mutant (**Fig. 23E**) or RIP1 (**Fig. 23D**). The specific RIP3 kinase-inactivating K51A mutation disrupts salt-bridges between E61 on αHC helix and D161 on the conserved DFG motif (**Fig. 24D**) at the catalytic site. This lack of complex formation in FAMD between PEBP1 and $RIP3^{K51A}$ suggests these salt-bridges underlie the RIP3→PEBP1 interaction interface. Notably, a specific RIP3 inhibitor, GSK'872, had a similar salt-bridge disrupting effect (**Fig. 24E**).

A

Sequence Identity			
Protein	cRAF	RIP1	RIP3
bRAF	76.07	25.37	27.92
cRAF		25.18	27.24
RIP1			32.14
RIP3			

B

Structural Homology			
Motif	cRAF	RIP1	RIP3
DFG	486-488	--------	161-163
HRDL	466-M469	136-K137_139	141-144
P-Loop	468	F28	F33
Dimerization	R401	R71	R69
N-term. Phosp-Sites	Y340_ Y341		
Salt-Bridge1	K375-E393	K45-E63	K51-E61
Salt-Bridge2	K375-D486	K45-D149	K51-D161

C

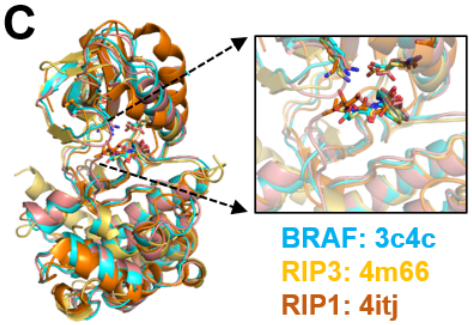

Protein Pair	Root-mean-square Deviation (RMSD, Å)
bRAF_RIP3	1.36
bRAF_RIP1	1.32
bRAF_cRAF	0.9

Although sequence similarity is low, the structural similarity is significant (i.e., low RMSD with bRAF, cRAF).

The catalytic site is highly conserved structurally (inset)

D

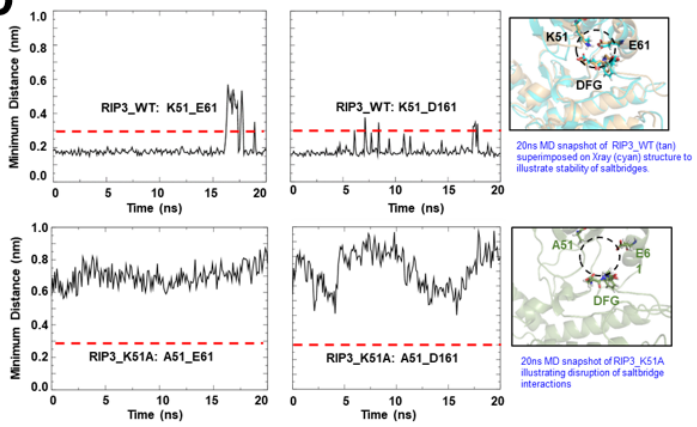

E

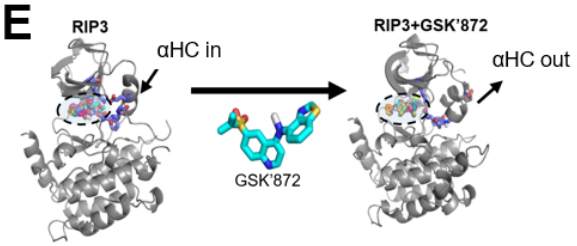

F

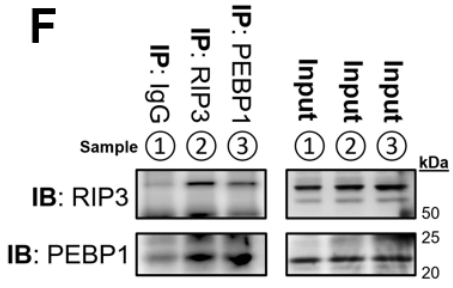

G

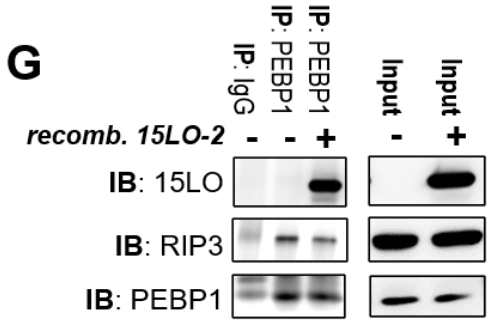

Figure 24. RIP3 is structurally homologous to RAF1 and able to complex with PEBP1

(A) Primary protein sequence identity analysis between bRAF, cRAF kinase, RIP1 and RIP3 displaying percent similarity.

(B) List of common conserved structural domains between cRAF kinase and RIP1 or RIP3

(C) Structural overlay of bRAF, cRAF, RIP1, and RIP3. Inset highlights some key structural domains proximal to the serine/threonine kinase active site including the conserved DFG motif and the Lys and Glu residues which form salt bridges with K51 in wild type, but not in the $RIP3^{K51A}$ mutant.

(D) Full atomistic molecular dynamic analysis demonstrating catalysis critical salt bridges (K51_E61, K51_D161) form in wild type (*upper panels*) but not $RIP3^{K51A}$ (*lower panels*)

(E) Ligand docking of GSK872 onto RIP3 structure in which αhelix-C (αHC) is out (right) (pdb: 4m69). The docking site of the GSK872 molecule suggests it disrupts the K51_D161 salt bridge (shown in left figure, pdb: 4m66)

(F) Reciprocal coimmunoprecipitation of RIP3 and PEBP1 in naïve human embryonic kidney (HEK) 293T cells [representative of 3 independent experiments]

(G) RIP3 is coimmunoprecipitated with PEBP1 in L929 cells. Addition of recombinant 15LOX2 (an alternate and pro-ferroptotic PEBP1 binding partner) to the system resulted in reduced RIP3 pulldown but increased PEBP1 pulldown of 15LOX2 [representative of 3 independent experiments]

Data gathered in collaboration with Haider Dar and Indira Shrivastava.

To test these computational predictions, we used four biochemical and cell-based methods to evince PEBP1's direct interaction with RIP3: (*1*) object-based colocalization, (*2*) fluorescent resonance energy transfer (FRET), (*3*) far western blotting, and (*4*) coimmunoprecipitation (coIP). We began with a 3D (voxel) object based colocalization method, which preserves Z-plane spatial and fluorescent intensity information, unlike traditional 2-dimentional Pearson correlation strategies (Wenzel et al., 2017). We found that RIP3 and PEBP1 colocalize within wild type ($Rip3^{+/+}$) primary BM cells (**Fig. 25A**), but $RIP3^{K51A}$_PEBP1 colocalization in $Rip3^{K51A/K51A}$ cells was significantly reduced vs. wild type. RIP3 inhibitor and salt-bridge disruptor, GSK'872, similarly reduced RIP3-PEBP1 association in cells (**Fig. 28C**). Next, we applied FRET techniques to assess whether RIP3_PEBP1 colocalization signified *close* proximity. Because the efficiency of FRET decreases as the sixth power of the distance between the donor and acceptor fluorophores, labeled proteins separated by >10 nm will not produce a FRET response. We detected a FRET reaction between RIP3 and PEBP1 (**Fig. 25B**), corroborating our colocalization finding. While FRET can define an upper distance limit (10 nm), we wished to determine whether PEBP1 and RIP3 physically interact. To address this, we used a far western blotting method – in which an

antibody-detectable “bait” protein (PEBP1) is used to detect the membrane-immobilized target “prey” protein (RIP3). We noted that PEBP1 was bound to and detected with RIP3 (**Fig. 25C**) but not non-specifically with GST or BSA. Finally, we performed several coimmunoprecipitation (coIP) experiments where we independently and reciprocally pulled down RIP3 and PEBP1. Endogenous PEBP1 reciprocally coimmunoprecipitated with RIP3 (**Fig. 25D**) in primary BM cells. Further substantiating our colocalization findings, the reciprocal coIP between $RIP3^{K51A}$ and PEBP1 was reduced compared to that seen with wild type RIP3. Similarly, we observed that endogenous RIP3 and PEBP1 coimmunoprecipitated in murine L929 and HT22 cells, as well as human embryonic kidney (HEK) 293T cells (**Fig. 24F**).

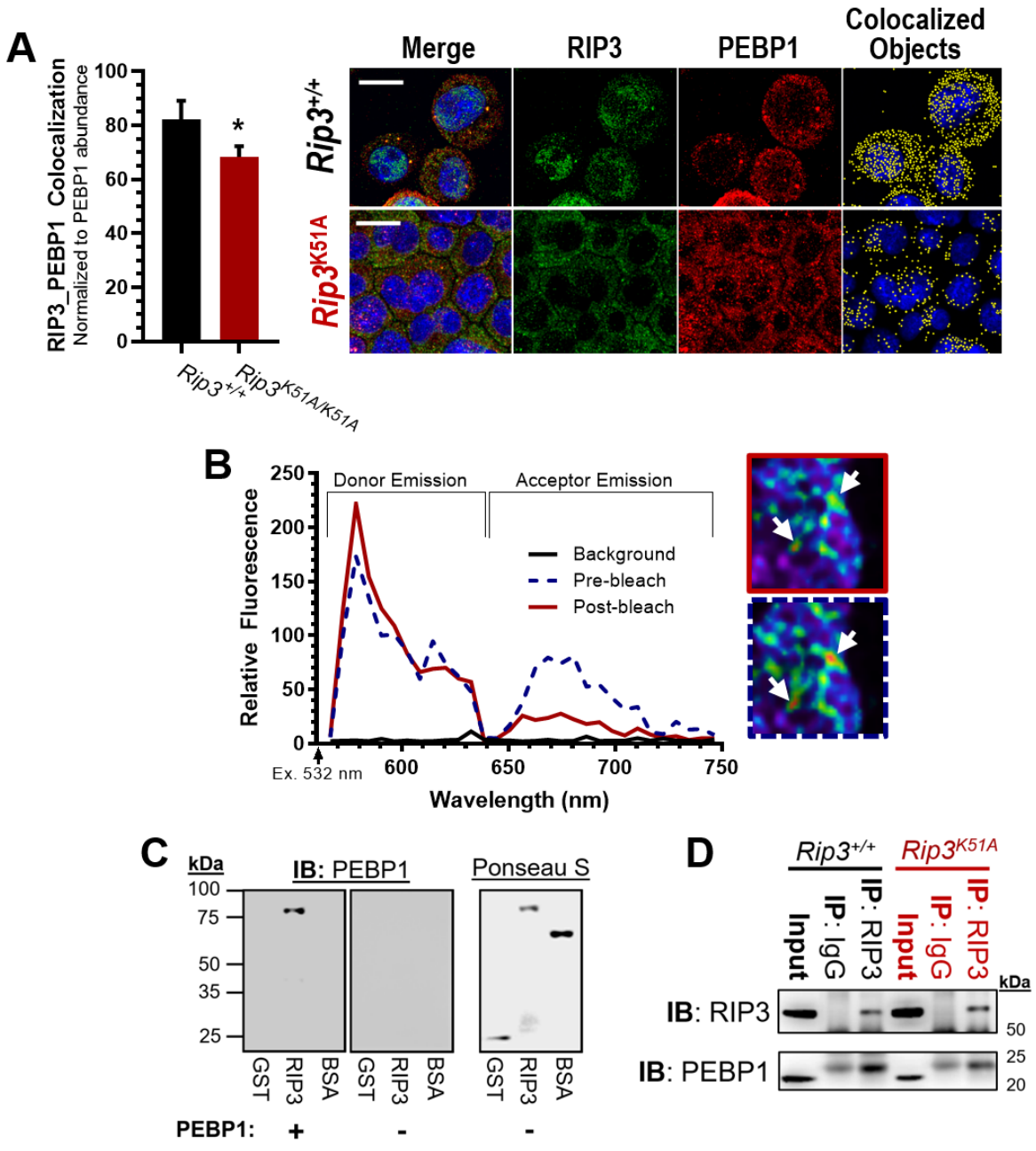

Figure 25. PEBP1 associates with RIP3 within cells

(A) Colocalization between RIP3 and PEBP1 is reduced in *Rip3*$^{K51A/K51A}$ vs. *Rip3*$^{+/+}$ primary bone marrow (BM) cells. (*i*) Representative micrographs showing "Merge" (*left panels*): PEBP1 (*red*), RIP3 (*green*), and nuclei (*blue*). "Colocalized objects" (*right panels*): PEBP1_RIP3 colocalized objects (*yellow*). (*ii*) Bar graph of PEBP1_RIP3 colocalization normalized to PEBP1 abundance, Mean ± SD, n = 3/group, *p< 0.05, scale: 20 μm.

(B) Fluorescence resonance energy transfer (FRET) analysis showing the close physical proximity (≤10 nm) of RIP3 with PEBP1 in naive HT22 cells. (*i*) The FRET effect was confirmed through acceptor (cy5) photobleaching (*dashed box*) where photobleaching abolished the FRET emission while reciprocally increasing donor (cy3) emission intensity (donor unquenching) within the regions indicated (*white arrows*). Line graph (*left*) Representative relative fluorescent

intensity (RFU) vs. single excitation (Ex) wavelength; Cy3 vs. Cy5 emission (Em) wavelengths are indicated. Micrograph (*right*): FRET ratio (donor/acceptor RFU) has been pseudo-colored (range 0-10, violet-red)

(C) Far Western blotting demonstrating specific interaction of recombinant human PEBP1 with RIP3. Representative PEBP1 non-denaturing immunoblots showing PEBP1 binds to membrane-immobilized RIP3 (*left*) but not GST or BSA control proteins. No PEBP1 signal is detected if the blot is not incubated with recombinant PEBP1 (*middle*). Ponceau S staining prior to immunoblotting verifying protein loading (*right*).

(D) Coimmunoprecipitation (coIP) of RIP3 and PEBP1 in $Rip3^{K51A/K51A}$ vs. $Rip3^{+/+}$ naïve primary BM cells. Reduced PEBP1 pulldown is observed in $RIP3^{K51A}$ mutant expressing cells compared to wild type RIP3 (representative of 3 independent experiments).

Data gathered in collaboration with Zhentai Huang and Claudette M. St Croix.

3.2.7.4 PEBP1 Negatively Regulates Necroptotic RIP3 Activity

To define the functional role of the PEBP1-RIP3 interaction, we modulated PEBP1 content and measured resultant RIP3 activity. An equimolar amount of PEBP1 substantially reduced RIP3's kinase activity but not RIP1 or MAPK14 (p38α) (**Fig. 5A**). Compared to non-targeted (NT) siRNA-treated control L929 cells, PEBP1 knockdown ($PEPB1^{KD}$) by siRNA enhanced [TNFα + z-VAD-fmk + SM164]-induced activation and phosphorylation of RIP3 (pRIP3, murine S231/232) and MLKL (pMLKL, murine S345) by a factor of 1.8 ± 0.7 and 1.5 ± 0.3-fold, respectively (**Fig. 27A**). Levels of pRIP1 were unchanged by PEBP1 siRNA. Matching this, necroptotic execution and cell death was enhanced in $PEBP1^{KD}$ cells, prepared by either siRNA (**Fig. 26B**) or CRISPR methods (**Fig. 26C, Fig. 27B**). We further tested PEBP1's necroptotic role in TNFα gradient experiments. Increasing TNFα dose produced marginally greater death in control NT siRNA L929 cells. In contrast, cell death in $PEPB1^{KD}$ was notably increased with increasing TNFα concentrations. In both cases, Nec-1s was completely protective. Collectively, these results support the causal relationship between necroptosis susceptibility and PEBP1 expression.

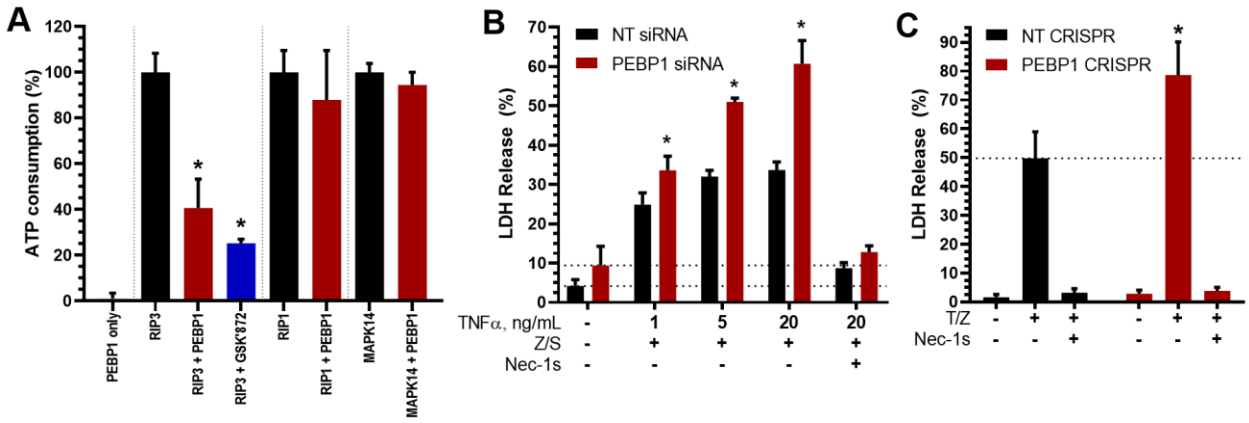

Figure 26. PEBP1 negatively regulates necroptotic death.

(A) Human recombinant RIP3 kinase activity is specifically and potently inhibited by equimolar PEBP1 or the small molecule inhibitor, GSK'872. Human recombinant RIP1 kinase and another canonical serine/threonine kinase, MAPK14 (p38α), are not inhibited by equimolar PEBP1. PEBP1 alone has no effect on ATP concentration. [Mean ± SD, n=3, *p< 0.05 vs. uninhibited enzyme]

(B) PEBP1 siRNA knockdown L929 cells experienced a greater increase in necroptosis at higher TNFα (5, 20 ng/mL) doses compared to NT siRNA cells. Cell death was specifically rescued by Nec-1s. [Z/S: z-VAD-fmk + SM164; cell death measured by LDH release at 18-20h, Mean ± SD, *p< 0.05 vs. non-targeted (NT) siRNA, n = 3/group]

(C) PEBP1 knockdown CRISPR sensitizes L929 cells to necroptotic death [T/Z: TNFα (10 ng/mL) + z-VAD-fmk; cell death measured by LDH release, Mean ± SD, *p< 0.05 vs. non-targeted (NT) CRISPR, n = 3/group]

Data gathered in collaboration with Zhentai Huang and Aleksandr A. Kapralov.

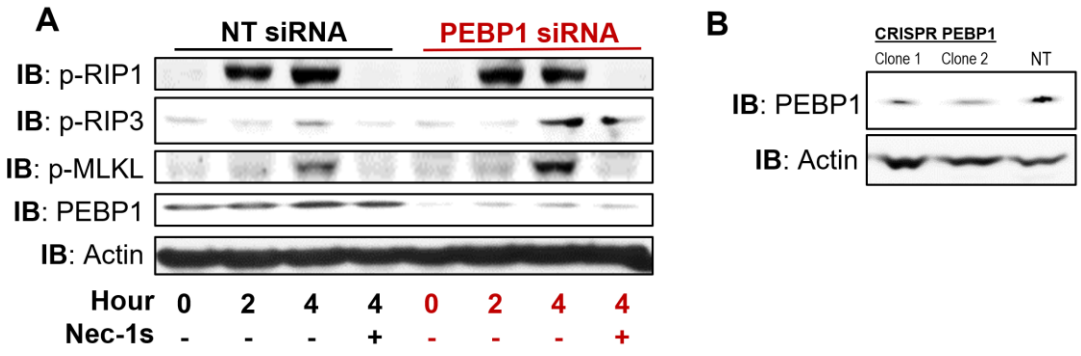

Figure 27. Necroptosis sensitization by PEBP1^{KD} corresponds to increased MLKL phosphorylation.

(A) Representative immunoblots showing reduced PEBP1 expression is associated with greater p-RIP3 and p-MLKL levels following necroptosis induction. Immunoblot of lysates from L929 cells transfected with PEBP1 or non-targeted (NT) siRNA for 48 h prior to TNFα, z-VAD-fmk, and SM-164 (T/Z/S)-induced necroptosis, either in the presence or absence of Nec-1s. RIP1 activation was unaffected by PEBP1 expression.

(B) Immunoblot of lysates from L929 with PEBP1 knockdown by CRISPR Cas9 system.

Data gathered in collaboration with Zhentai Huang.

3.2.7.5 Increased PEBP1 Availability Sensitizes to Ferroptosis whereas Formation of PEBP1-RIP3 Kinase Complex Suppresses Necroptosis

Given the established duality of PEBP1 interactions with RIP3 and 15LOX, we studied the role of PEBP1 in necroptosis-ferroptosis crosstalk. We assumed that conditions influencing PEBP1 to bind/inhibit RIP3 or alternatively bind/activate 15LOX may serve as a rheostat between necroptosis and ferroptosis, respectively. Weakening of PEBP1's interaction with alternative partners and increased expression of 15LOX would enhance the 15LOX's capacity to bind PEBP1 resulting in pro-ferroptotic response. Modeling and experimental data indicated PEBP1 does not associate with K51A mutant RIP3 to the same extent as with wild type. BM expressing the weak PEBP1 partner, $RIP3^{K51A}$ mutant, were sensitive to GPX4 inhibition-induced death by RSL3 while wild type BM were resistant (**Fig. 28A**). Increased PEBP1_15LOX co-localization preceded death (**Fig. 28B**). This cell death was rescued by Fer-1, whereas other programmed death inhibitors – z-VAD-fmk, Nec-1s, or Bafilomycin-A1 (BafA1, anti-autophagic death) – did not reverse *Rip3*$^{K51A/K51A}$-associated RSL3-induced death (**Fig. 29A**).

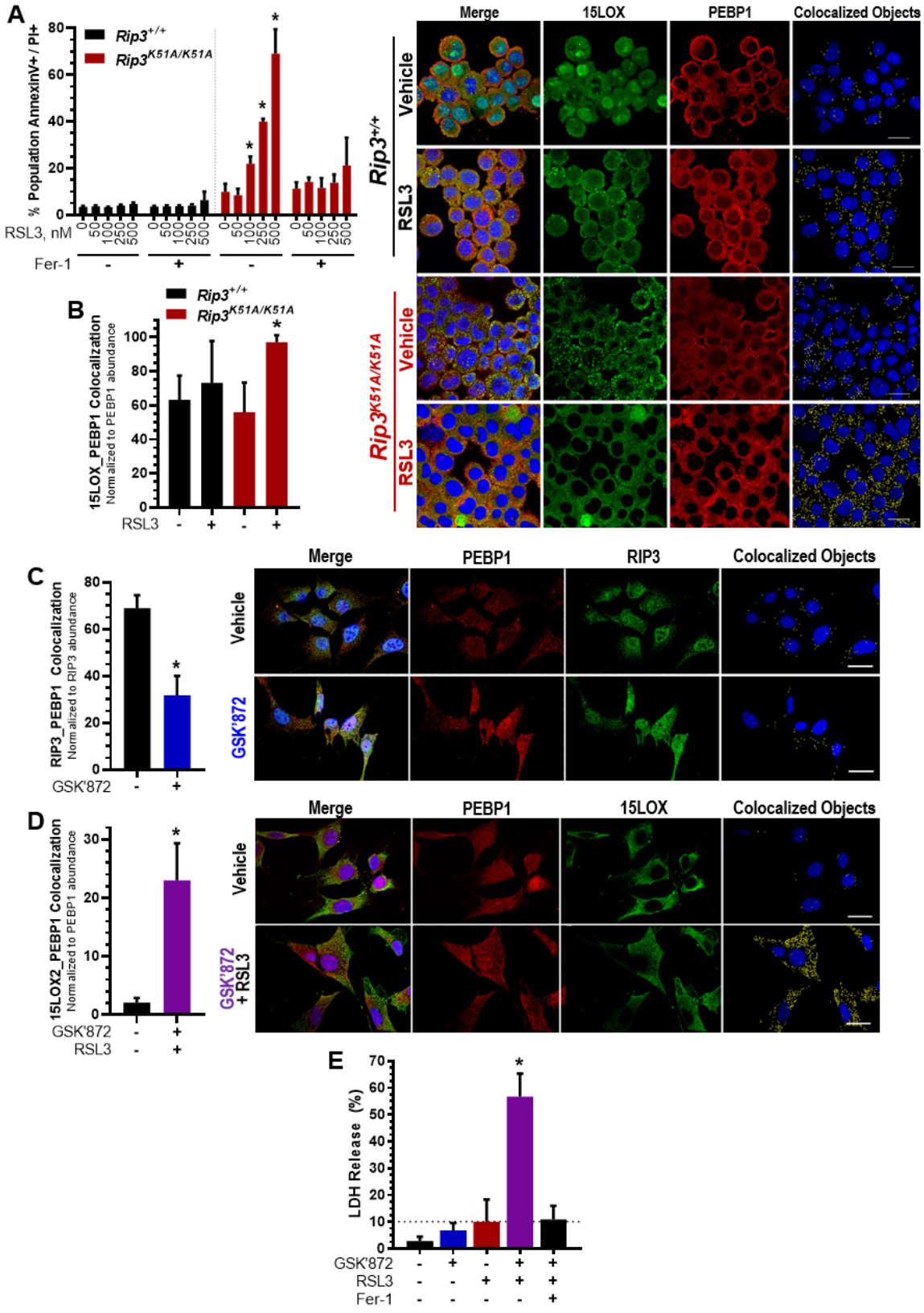

Figure 28. Genetic or pharmacological disruption of PEBP1_RIP3 interaction enhances ferroptosis.

(A) *Rip3*$^{K51A/K51A}$ (red bars) primary BM cells were dose-dependently sensitive to the GPX4 inhibitor and ferroptosis-inducer, RSL3 (*dose range*: 0 - 500 nM). Ferrostatin-1 (Fer-1, 1 μM), but not z-VAD-fmk, Nec-1s, or BafA1, rescued RSL3 cell death (see Fig. S7A). *Rip3*$^{+/+}$ cells (black bars) were comparably resistant to RSL3. Cell death measured by AnnexinV-FITC & PI flow cytometry, Mean ± SD, n = 6-9 dishes/group, *p< 0.05 vs. genotype-specific DMSO vehicle group

(B) Formation of the redox phospholipoxysome (PEBP1_15LOX2 complex) increased in *Rip3*$^{K51A/K51A}$ but not *Rip3*$^{+/+}$ wild type primary BM cells following RSL3 treatment. Representative micrographs showing "Merge" (*left panels*): PEBP1 (*red*), 15LOX2 (*green*), and nuclei (*blue*) and "Colocalized objects" (*right panels*): PEBP1_15LOX2 colocalized puncta (*yellow*). Bar graph of PEBP1_15LOX2 colocalization normalized to PEBP1 abundance, Mean ± SD, n = 3/group, representative of 3 independent experiments, *p< 0.05 vs. respective DMSO vehicle group, scale: 20 μm.

(C) GSK'872 reduces RIP3_PEBP1 object-based colocalization in HT22 cells. Representative micrographs show "Merge" (*left panels*): PEBP1 (*red*), RIP3 (*green*), and nuclei (*blue*) and "Colocalized objects" (*right panels*): RIP3_PEBP1 colocalized puncta (*yellow*). RIP3_PEBP1 colocalization normalized to RIP3 abundance, Mean ± SD, n = 3/group, *p< 0.05 vs. DMSO vehicle group, scale: 20 μm.

(D) GSK'872 and RLS3 cotreatment enhances 15LOX2_PEBP1 colocalization in HT22 cells. Representative micrographs show "Merge" (*left panels*): PEBP1 (*red*), 15LOX2 (*green*), and nuclei (*blue*) and "colocalized objects" (*right panels*): 15LOX2_PEBP1 colocalized puncta (*yellow*). 15LOX2_PEBP1 colocalization normalized to PEBP1 abundance, Mean ± SD, n = 3/group, *p< 0.05 vs. DMSO vehicle group, scale: 20 μm.

(E) GSK'872 synergistically enhances RSL3-induced ferroptosis in HT22 cells. Toxicity was only observed with the GSK'872 + RSL3 cotreatment, not individually. Synergistic injury was rescued completely by Fer-1. Cytotoxicity measured by LDH release, Mean ± SD, *p< 0.05 versus vehicle, n = 3/group.

Data gathered in collaboration with Claudette M. St Croix and Zhentai Huang.

To verify that ferroptosis sensitivity is modulated by 15LOX's access to PEBP1, we used pharmacologic means to liberate PEBP1 from RIP3 or RAF. We hypothesized that, similar to *Rip3*$^{K51A/K51A}$ mutant cells, increased PEBP1 availability for 15LOX binding would prime cells for ferroptotic signaling. Previous modeling work indicated that GSK'872 disrupts RIP3's catalysis-critical salt bridges, giving rise to its inhibitory activity. However, docking of GSK'872 causes an out-rotation of wild type RIP3's R69-proximate αHelix-C (αHC) (**Fig. 24E**), which is also seen with the RIP3^{K51A} mutant. Indeed, non-toxic GSK'872 concentrations rapidly reduced RIP3-PEBP1 colocalization (**Fig. 28C**). This effect, combined with RSL3 cotreatment, lead to increased

15LOX_PEBP1 complex formation (**Fig. 28D**) and a synergistic increase in ferroptosis (**Fig. 28E**). GSK'872 ferroptosis-sensitizing effect was observed in several models, including wild type primary enteroid monolayer cells (**Fig. 29B**) and rat small IEC18 intestinal epithelial cells (**Fig. 29C**).

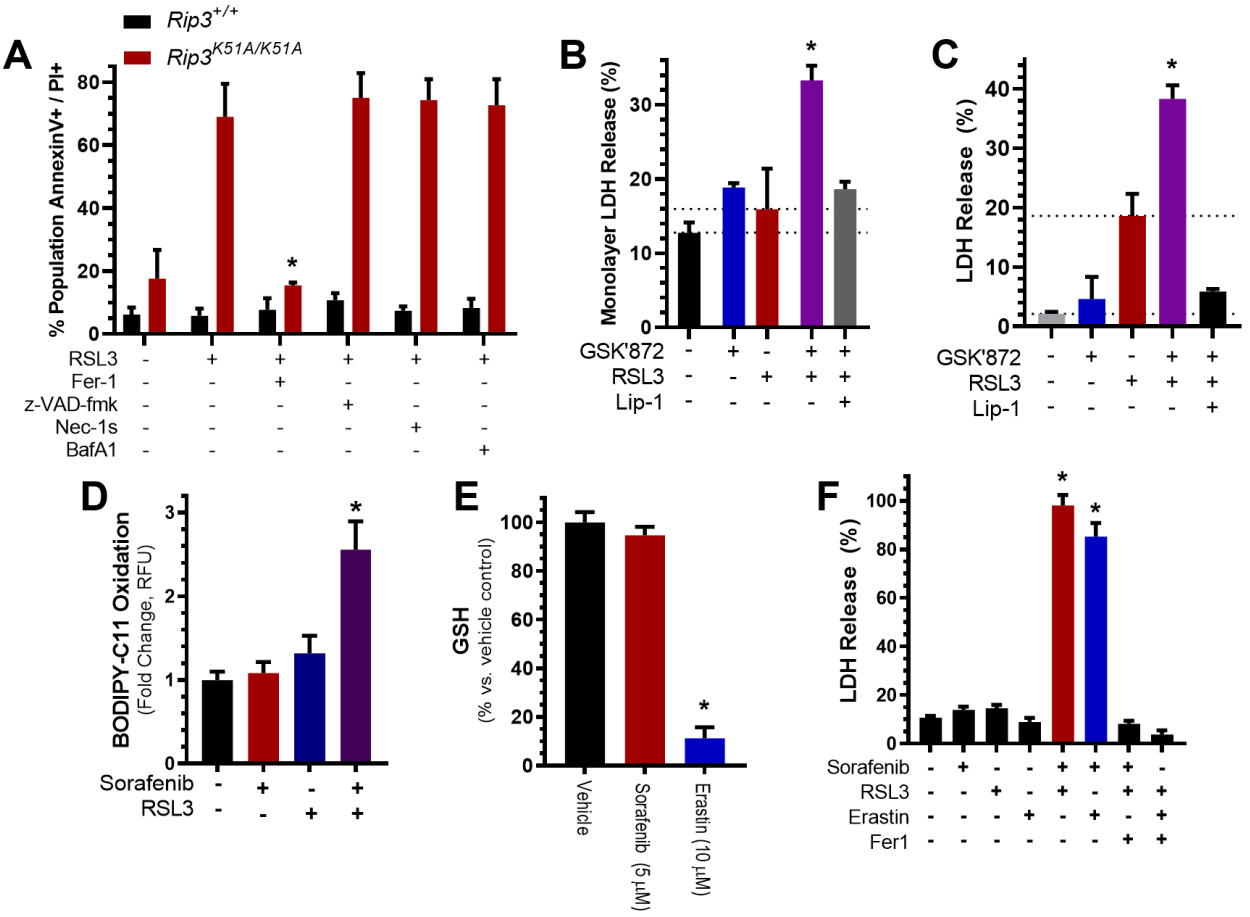

Figure 29. PEBP1 availability for 15LOX2 association drives ferroptosis sensitivity.

(A) Cell death induced by RSL3 (500 nM) in primary bone marrow (BM) cell obtained from *Rip3*$^{K51A/K51A}$ mice can be reversed by anti-ferroptotic Fer-1 but not z-VAD-fmk (caspase-dependent apoptosis), Nec-1s (necroptosis), or Baf1A (autophagic death). Cell death measured by Annexin V-FITC + Propidium iodide (PI) flow cytometry, Mean ± SD, *p< 0.05 versus RSL3 only, n = 6-9/group.

(B) RIP3 inhibitor, GSK'872, synergistically enhances RSL3-induced ferroptotic cell death in wild type primary mouse small intestinal enteroid monolayers. Compared to RSL3 or GSK'872 monotreatment, cotreatment significantly increased enteroid death. The synergistic injury was rescued by anti-ferroptotic Lip-1. Cell death measured by LDH release at 22-24 h, Mean ± SEM, *p< 0.05 vs. RSL3 only group, n = 3 transwells/group.

(C) Similarly, GSK'872 sensitized immortalized wild type rat intestinal epithelial cells (IEC18) to ferroptosis. Lip-1 reversed the GSK'872 + RSL3 cotreatment effect. Cell death measured by LDH release at 18-20 h, Mean ± SD, *p< 0.05 vs. RSL3 only group, n = 3/group.

(D) Individually, sorafenib or low dose RSL3 had no effect on the redox state of the reporter lipid (BODIPY-C11). Cotreatment of RSL3 and sorafenib increased lipid peroxidation in HK2 cells. Mean ± SD, *p< 0.05, n = 3/group.

(E) Sorafenib did not inhibit system Xc^- (SLC7A11) mediated GSH synthesis at the dose used to sensitize cells to ferroptosis. Monotreatment with erastin (10 μM), a specific system Xc^- inhibitor, reduced GSH levels in A549 cells (% GSH per mg protein, relative to vehicle control group). Mean ± SD, *p< 0.05, n = 3/group.

(F) Sorafenib (5 μM) enhanced ferroptosis induced by both GPX4 inhibition (RSL3) and system Xc^- inhibition (erastin) in A549 cells. Mean ± SD, *p< 0.05, n = 3/group.

Data gathered in collaboration with Qin Yang, Heather L. Mentrup, and Gaowei Mao.

Alternatively, we used FAMD simulations to model the effects of several RAF inhibitors on the PEBP1_RAF interaction. Sorafenib and, to a lesser extent, PLX4720 disrupted the RAF_PEBP1 interaction in our MD simulations (**Fig. 30A**). The dissociating effects of sorafenib were experimentally supported by reduced PEBP1_RAF association (**Fig. 30B**). Cotreatment of sorafenib with an *individually* non-toxic concentration of RSL3 prompted increased PEBP1_15LOX colocalization (**Fig. 30C**), lipid peroxidation (BODIPY-C11, **Fig. 29D**), and ultimately death (**Fig. 30D**). Sorafenib concentrations used were carefully titrated such that they did not independently inhibit GSH synthesis via system Xc^- inhibition (**Fig. 29E**) (Dixon et al., 2014). PLX4720 also synergistically enhanced RSL3 death, but to a lesser degree, fitting our FAMD predictions. Importantly, the computationally predicted ineffectiveness of another RAF inhibitor, SB590885, as a disruptor of the RAF1_PEBP1 interaction was experimentally confirmed by its inability to enhance ferroptosis (**Fig. 30D**).

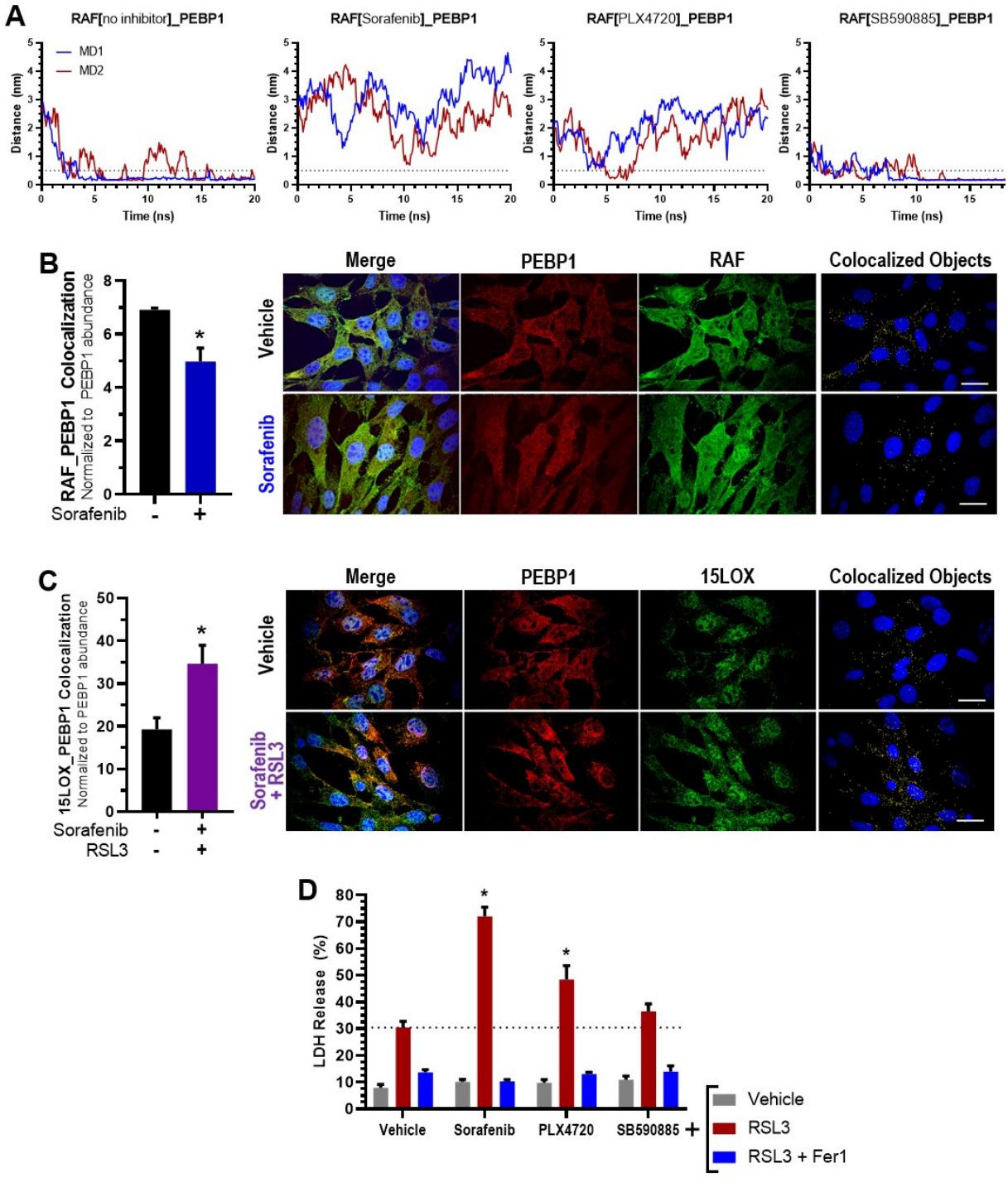

Figure 30. Disruption of the PEBP1_RAF interaction enhances ferroptosis.

(A) Full Atomistic Molecular Dynamics (MD) Simulations (n=2) between PEPB1 and RAF or [*inhibitor*]-bound RAF. The plots show minimum distance between any atom on PEBP1 and RAF, and *red dotted line* indicates the threshold maximum distance for positive protein-protein interaction (≤0.5 nm). In the presence of RAF inhibitors (sorafenib and

to a lesser extent PLX4720), PEBP1 does not associate with RAF. This frees PEBP1 for alternative interactions (e.g., 15LOX). With SB590885, PEBP1 remains bound with RAF, suggesting the inhibitor does not dissociate PEBP1.

(B) Sorafenib (sora) reduces RAF_PEBP1 colocalization in HT22 cells. Representative micrographs show "Merge" (*left panels*): PEBP1 (*red*), RAF1 (*green*), and nuclei (*blue*) and "colocalized objects" (*right panels*): RAF_PEBP1 colocalized puncta (*yellow*). RAF1_PEBP1 colocalization normalized to PEBP1 abundance, Mean ± SD, n = 3/group, *p< 0.05 vs. DMSO vehicle group, scale: 20 μm.

(C) Sorafenib and RSL3 cotreatment enhances 15LOX2_PEBP1 colocalization in HT22 cells. Representative micrographs demonstrate "Merge" (*left panels*): PEBP1 (*red*), 15LOX2 (*green*), and nuclei (*blue*) and "Colocalized objects" (*right panels*): 15LOX_PEBP1 colocalized puncta (*yellow*). 15LOX2_PEBP1 colocalization normalized to PEBP1 abundance, Mean ± SD, n = 3/group, *p< 0.05 vs. DMSO vehicle group, scale: 20 μm

(D) Sorafenib and, to a lesser extent, PLX4720 synergistically enhance RSL3-induced ferroptotic cell death in HT22 cells. Sorafenib's effects were independent of system Xc^- inhibition (see Fig. S7E). Synergistic death was rescued completely by Fer-1. Cytotoxicity measured by LDH release, Mean ± SD, *p< 0.05 vs. vehicle, n = 3/group.

Data gathered in collaboration with Indira Shrivastava, Claudette M. St Croix, Gaowei Mao, and Margarita A. Artyukova.

3.2.8 Discussion

Damaged, dysfunctional cells complete their lives by one of several tightly controlled pathways. The mechanisms of programmed cell death touch closely on one-another; up- or downregulation of one death pathway affects the execution of others. We demonstrated that RIP3 kinase can interact with the promiscuous endogenous serine-/threonine-kinase inhibitor, PEBP1. The nature of the PEBP1_RIP3 interaction is likely analogous to that of PEBP1_RAF. PEBP1 binding inhibits RIP3 essential kinase function, thus regulating the necroptotic program. Our previous work established that 15LOX is yet another partner of PEBP1 (Anthonymuthu et al., 2018; Wenzel et al., 2017). Binding of PEBP1 with 15LOX alters the dioxygenase catalytic selectivity, leading to the generation of pro-ferroptotic 15-HpETE-PE signals (V. E. Kagan et al., 2017). Computational assessment of the relative affinities of PEBP1 for RIP3 versus 15LOX (**Figure 31**), indicated that 15LOX is the preferred PEBP1 partner. A 3:1 ratio of RIP3:15LOX

was required for RIP3's to outcompete 15LOX for PEBP1 in our simulations. This suggests the PEBP1_RIP3 interaction may be transient and subordinate to the formation of the ferroptotic 15LOX_PEBP1 complex. Easing 15LOX's access to PEBP1 by genetically or pharmacologically disrupting alternative interactions of PEBP1 (i.e., with RAF, RIP3) enhances this pro-ferroptotic effect.

A

	Receptor§	Ligand	ZDOCK	CLUSPRO	CGMD
1	15LOX1_RIP3	PEBP1	90% (15LOX1)	100% (15LOX1)	66% (15LOX1)
2	15LOX1_PEBP1	RIP3	90% (15LOX1)	100% (15LOX1)	
3	15LOX1_PEBP1	PEBP1	100% (15LOX1)	100% (15LOX1)	
4	$RIP3^{WT}$_$RIP3^{K51A}$	PEBP1	60% ($RIP3^{WT}$)	60% ($RIP3^{WT}$)	
5	15LOX1_RIP3	RIP3	80% (15LOX1)	80% (15LOX1)	

§ "Receptors" complex was pre-equilibrated in lowest energy (most favorable) binding pose prior to addition of the competitive ligand

B

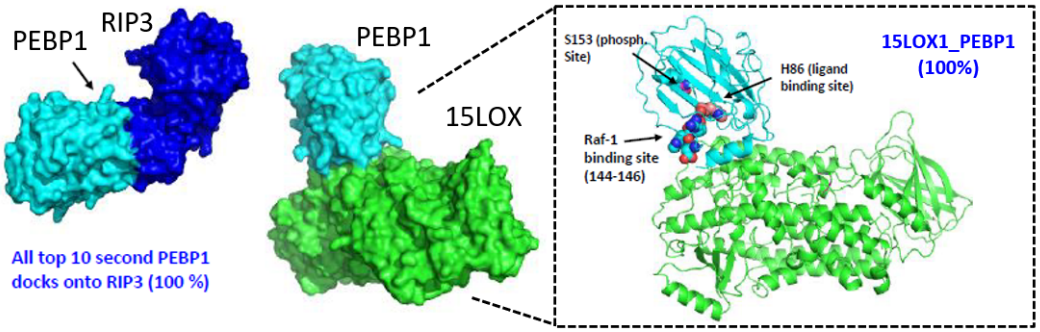

C

MD Input: 15LOX1 + PEBP1	MD1	MD2	Conclusion
+ RIP3 (1 molecule)	15LOX1_PEBP1 (**37 ns**†)	15LO_PEBP1 (**39 ns**)	15LOX1_PEBP1 Complex Favored
+ RIP3 (2 molecules)	15LOX1_PEBP1 (**63 ns**)	*No complex formed*	15LOX1_PEBP1 Complex Favored
+ RIP3 (3 molecules)	*No complex formed*	RIP3_PEBP1 (**62 ns**)	RIP3_PEBP1 Complex Favored

† time to formation of specified complex with PEBP1 after initial simulation pre-equilibration

Figure 31. Computational assessment of relative affinities of PEBP1 for RIP3 and 15LOX.

(A) Multi-Protein docking systems. Here, "Receptor" represents the protein complex which are 'rigid'; "Ligand" represents the protein which is 'free' to move in the docking simulations. ZDOCK, CLUSPRO are two docking softwares used for rigid-docking. Coarse-grained Molecular Dynamics (CGMD) simulations allowed both Receptor and Ligand to move freely in solvent environment. Based on five independent simulations, the values indicated represent the probability at which the 'Ligand' interacted with the specified 'Receptor' protein. The Receptor complex binding pose was selected based on the lowest binding energy complex of the respective proteins, e.g. 15LOX_RIP3 receptor was the top (lowest binding energy conformation) obtained from docking of 15LOX and RIP3 only. To this pre-formed complex, the Ligand was then docked. The pdb ids for the respective proteins are (15LOX: 1LOX, PEBP1:1BEH, RIP3:4M66). RIP3 prefers to bind the larger 15LOX

(B) When the first PEBP1 (*cyan*) is docked in the presence of two proteins, 15LOX (*green*) and RIP3 (*blue*), it is seen to dock on 15LOX at the same position in all top 10 (100%) of the lowest energy binding poses (inset), indicating 15LOX is the preferred PEBP1 binding partner. However, when a second PEBP1 molecule was added to the 15LOX_PEBP1 + RIP3 system, the second PEBP1 preferred docking with RIP3 (dark blue). The weakened interaction of PEBP1 with 15LOX in the presence of RIP3 molecules was confirmed in CGMD simulations.

(C) CGMD simulation containing PEBP1, 15LOX, and either 1, 2, or 3 (indicated in parenthesis in first column) RIP3 molecules were run in presence of water molecules. Two MD simulations of 100 nanoseconds each (MD1 and MD2) for each system was run. The table shows the formation of complex between the proteins at the time indicated in parenthesis, which remained a complex for the rest of the simulation period. "NONE" indicates no complex was formed with either 15LOX or RIP3. The data suggests that PEBP1's preference for 15LOX was reduced at higher RIP3-to-15LOX ratios (≥2:1 RIP3-to-15LOX). It may be that low pre-injury expression of 15LOX that is observed in many tissues indirectly favor RIP3 inhibition, whereas post-injury induction of 15LOX favors both ferroptosis and necroptosis. The proteins were at a distance of at least 50 Å or more from each other at the start of the simulations.

Data gathered in collaboration with Indira Shrivastava.

Cells closely regulate the initiation and propagation of cell death programs. Our work shows the binding of PEBP1 with RIP3 results in kinase inhibition and may represent yet another high-fidelity regulatory mechanism to prevent unintentional necroptosis execution (Kearney, Cullen, Clancy, & Martin, 2014). However, under disease conditions leading to GPX4/GSH deficiency, irreparably damaged cells destined to die can activate ferroptosis by complex formation between PEBP1 and 15LOX that results in the formation of PEox. The switch to ferroptosis does not come without cost. Ferroptotic signaling results in a paracrine-like spreading death effect (Kim et al., 2016; A. Linkermann et al., 2014) and necroinflammation. These effects offer an explanation of why the switch to ferroptosis results in *more* cellular injury and IR mortality. Necroptosis and ferroptosis act in parallel under several common and complex disease pathologies, for example in various forms of acute kidney injury (AKI). Folic acid (FA)-induced AKI is notably pro-ferroptotic (Müller et al., 2017). Similar to our observation of worsened outcome of $Rip^{K51A/K51A}$ and $Mlkl^{-/-}$ mice upon IR, knockout of MLKL also exacerbates FA-AKI. Complimentary to any undefined

protective role of MLKL, we suggest that activation and homodimerization of RIP3 disrupts its interaction with PEBP1. In the absence of the MLKL executioner, progressive RIP3 activation furthers PEBP1 liberation, enhancing PEBP1_15LOX association and driving ferroptotic tissue injury. Likewise, the weakened interaction between $RIP3^{K51A}$ and PEBP1 is permissive to PEBP1_15LOX complex formation. We observed that pharmacologically disrupting the RIP3_PEBP1 or RAF1_PEBP1 interaction with GSK'872 or sorafenib/PLX4720, respectively, sensitized cells to secondary RSL3-induced ferroptosis. Finally, it was previously shown that high millimolar concentrations of GSK'872 induces caspase-dependent apoptosis reliant on RIP3's RIP homotypic interaction motif (RHIM) domain – but not its kinase activity (Mandal et al., 2014). Our results suggest that the cytotoxic effects of GSK'872 on RIP3 activity are dependent on both the dose and the costimulatory factors, able to either inhibit necroptosis or enhance apoptosis and ferroptosis.

The newly described connection between ferroptosis and necroptosis mediated by PEBP1's preferential interaction with 15LOX or RIP3 raises questions on how these two intact death pathways interact bidirectionally. If wild type RIP1/RIP3-mediated phosphorylation and necrosome assembly prompts PEBP1_RIP3 dissociation, then cells with activated necroptotic machinery might be increasingly sensitive to ferroptosis under pro-oxidative conditions. Alternatively, unchallenged cells with high basal expression of necroptotic machinery (i.e., high RIP3 levels) or RAF1 may be resistant to ferroptosis. Crosstalk in the opposite direction, ferroptosis-to-necroptosis, may be reflected in when injury-induced upregulation of ferroptotic 15LOX leads to pilfering of PEBP1 from RIP3 and increased necroptosis susceptibility. In addition, alternative ferroptosis-necroptosis connections outside the direct PEBP1_RIP3 mechanism may be operational. A number of proteins have been shown to associate with the

activated RIP3-immunocomplex, including the glutamine transporter, SLC1A5 (Fettweis et al., 2017). Activation of SLC1A5 and glutamine (Gln) transporters promotes ferroptosis by upregulation of glutaminolysis (Minghui Gao et al., 2015). Altering RIP3's interaction with these Gln transporters by pharmacologic or genetic means may similarly affect ferroptosis. Overall, simultaneous inhibition of both necroptosis and ferroptosis may be necessary to maximize protection and likelihood of clinical benefit in disease states where *either* programmed necrotic pathway are suspected to operate.

In summary, we demonstrated that PEBP1 serves as a regulator of cell death by sterically inhibiting pro-necroptotic RIP3 activity while activating 15LOX to generate pro-ferroptotic peroxy-AA/AdA-PE signals. Using computational, genetic, biochemical, and redox lipidomics approaches, we demonstrated that PEBP1 can alternatively bind and (*1*) inhibit necroptotic RIP3 activity and/or (*2*) activate 15LOX-mediated ferroptosis. These newly established regulatory functions of PEBP1 may serve multiple and diverse roles across various human disease states.

4.0 General Conclusion and Future Directions

4.1 Mitochondrial PARP1: Future Directions

In the first part of this dissertation, we developed a novel mitochondria-targeted PARP1 inhibitor, XJB-veliparib. Injury-induced genotoxic stress hyperactivates PARP1, causing **1**) NAD^+ depletion and bioenergetic catastrophe; **2**) mitochondrial depolarization (↓$\Delta\psi m$), ETC inhibition, decreased mtDNA integrity, and MOMP opening; and **3**) mitochondria-to-nuclear translocation of AIF triggering MIF-mediated large-scale DNA fragmentation and parthanotic death (Y. Wang et al., 2016; Yu et al., 2002). Inhibiting PARP1 throughout all cellular compartments prevents parthanatos and associated mitochondrial pathology. However, this approach renders cells increasingly vulnerable to senescence, apoptosis, and autophagic death (Alotaibi et al., 2016; Filipovic et al., 1999). PARP1 is vital for most nDNA repair mechanisms, including BER, NER, SSBR, and a-NHEJ. Therefore, efficient nuclear PARP1 activity is required to preserve DNA integrity following acute oxidizing injury. Nuclear PARP1 activity is particularly important in post-mitotic cells since they often lack effective PARP1-independent nDNA repair pathways, such as HR. Mitochondrial PARP1 (mt-PARP1) mediates mitochondrial pathology in parthanatos independent of nuclear PARP1 by promoting AIF release, inhibiting ETC oxygen consumption, and hindering mtDNA repair (Brunyanszki et al., 2016a). A clinically effective anti-parthanotic treatment must balance between compartment-specific – nuclear vs. mitochondria – adaptive and maladaptive PARP1 activity, respectively.

The XJB moiety has successfully delivered diverse payloads to mitochondria, including nitroxides (Wipf et al., 2005); a nitric oxide synthase (NOS) antagonist (AMT) (Kanai et al., 2007);

and a pleiotropic antineoplastic compound, β-lapachone (J. Ma et al., 2015). XJB-veliparib localizes to mitochondria, particularly IMM and matrix, where it mediates its protective effects without impeding beneficial nDNA repair. Mitochondria-targeted PARP inhibitors could have clinical efficacy in diseases where the pathophysiology includes mitochondrial dysfunction, but efficient nuclear DNA repair is desired – such as ischemia-reperfusion injury, ionizing irradiation injury, excitotoxic injury, and others pro-oxidative injury states. Our work warrants further evaluation and development of this class of mt-PARP inhibitors.

Questions remain concerning the pathogenic mechanism of mitochondrial PARP1: **1**) how is mt-PARP1 activated after injury, and **2**) what are the specific pathologic effects for mt-PARP1?

First, do mtDNA lesions activate mt-PARP1? Understanding this question has important implications in the design of specific mt-PARP1 inhibitors. For example, inhibitors with high PARP trapping activity should be avoided as PARP trapping lesions may be more common in mtDNA vs. nDNA (Wanrooij & Chabes, 2019; Zimmermann et al., 2018). Current evidence indicates mt-PARP1 activity is enhanced by activation of β-adrenergic receptor/cAMP/PKA axis and phosphorylation at Ser465 (automodification domain) and Ser782/785 (catalytic domain) (A. Brunyanszki et al., 2014). JNK1, RIP1, and TRAF2 are also associated with parthanotic mitochondrial dysfunction, but their relation to mt-PARP1 is unknown (Xu et al., 2006). Mt-PARP1 is hypothesized to activate via ligand-dependent dimerization upon detecting mtDNA oxidized, SSB, and DSB lesions, similar to nuclear PARP1. Live- and fixed-cell microscopy provides means to measure the kinetics of mt-PARP1 vs. nuclear PARP1 response following targeted mtDNA or nDNA SSB lesioning, respectively. If mt-PARP1 binds mtDNA SSBs, then targeted mtDNA damage will incite the rapid formation of mt-PARP1 fluorescent foci (C-terminal-tagged enhanced green fluorescent protein [EGFP]-fusion PARP1 or EGPF-fusion

truncated PARP1 DNA binding domains [PARP1-DBD]) colocalized with SYBR Green I- or EdU-labeled mitochondrial nucleoids (Sasaki, Sato, Higashiyama, & Sasaki, 2017). Disruption of mt-PARP1 foci in cells expressing PARP1 DNA binding incompetent mutants (ZnF1 (R34E) or ZnF2 (R138E)) would confirm the specificity of mt-PARP1's interaction with damaged mtDNA (Ali et al., 2012). Proximity ligation assay (PLA) or FRET interaction between PARP1 ZnF1 and ZnF2 domains following confirmed mtDNA injury would specifically support the ligand-dependent dimerization activation mechanism. However, this approach requires careful construct design or antibody selection to avoid interdomain PLA/FRET response in the absence of true PARP1 dimerization.

If mtDNA lesion-activated mt-PARP1 is responsible for mitochondrial PARylation events, then mt-PARP1 foci formation should precede mitochondrial PAR accumulation, and AIF release will occur independently from nDNA damage. Two techniques to induce targeted mtDNA damage for live cell imaging are *in situ* microbeam irradiation or mitochondrial-targeted oxidizing/alkylating agents (Walsh et al., 2017; Wisnovsky, Jean, & Kelley, 2016). First, microbeam irradiation uses a beamspot (<1 μm) to deposit particle (carbon, proton) or electromagnetic (UV, gamma) energy on a chosen mitochondrion (Walsh et al., 2017). This live cell approach provides high spatial specificity, minimizes off-target DNA damage, and, if paired with a photoactivated mitochondrial label, enables tracking of the damaged mitochondrion as it is trafficked through the network. Second, chemical agents – including mt-Ox, mt-DSB, and mt-NS – induce specific types of mtDNA lesions and may be particularly useful for fixed cell imaging and biochemical assays (Wisnovsky et al., 2016). Additionally, chromatin immunoprecipitation (ChIP) and surface plasmon resonance (SPR) can be used to determine whether mt-PARP1 displays preference for a given type of DNA lesion (e.g., SSB, AP sites, oxidized/alkylated bases).

If mt-PARP1 is primarily activated by mtDNA lesions, and its inhibitory effect on mtDNA repair is the dominant pathogenic mechanism, then matrix-targeted TPP-veliparib may be more efficacious compared to IMS/IMM-localized XJB-veliparib at preventing mt-PARP1 foci formation and PAR accumulation (**Figure 6**).

Second, how does mt-PARP1 contribute to parthanotic mitochondrial pathology? Current reports suggest nuclear-synthesized PAR translocates to mitochondria and induces AIF release (Yingfei Wang et al., 2011). However, these studies overlook mt-PARP1. The kinetics of EGFP-fusion AIF nuclear translocation can be measured using *in situ* whole cells vs. nuclear vs. mitochondria-targeted microbeam irradiation in wild-type vs. *Parp1*$^{-/-}$, untargeted veliparib-treated, and XJB-veliparib treated cells. Modulating mt-PARP1 and nuclear PARP1 localization via by mitofilin knockdown or removal of PARP1's nuclear localization sequence, respectively, can verify the relation between specific mt-PARP1 activity and mt-veliparib efficacy while ruling out off-target effects. Superoxide levels, mitochondrial calcium ion flux, and $\Delta\psi m$ can be measured in this model using mitoSOX, rhod-2, and tetramethylrhodamine ethyl ester (TMRE) (Davidson & Duchen, 2012). Imaging results and other proposed mt-PARP1 pathologic mechanisms should also be explored using XJB-veliparib and TPP-veliparib (**Table 1**). As the mechanisms of mt-PARP1 pathology are validated, computational lead optimization and *in vivo* pharmacokinetic/pharmacodynamic studies will be necessary to generate a clinically effective mt-PARP1 inhibitor.

Table 3. Proposed mt-PARP1 targets, consequences of PARylation, mechanism of injury, and assay to quantify these effects.

mt-PARP1 Target	PARylation Consequence	Hypothesized Mechanism	Assay
Exo/Endonuclease G Polymerase-γ	Reduced mtDNA integrity	Negatively charged, bulky PAR inhibits catalytic activity and/or delay assembly of repair complex	• Co-immunoprecipitation (IP: PolG/ExoG/Polθ, WB: PAR) • qPCR analysis of mtDNA and nDNA damage (lesions/10kb, amplification efficiency)
Electron Transport Chain Complex 1, 2, 4	Reduced O_2 consumption, reduced ATP production	Reduced ETC flux, increased reverse e^- flow	• Co-immunoprecipitation (IP: ETC complex 1, WB: PAR) • JC-1 (Δψm), MitoSOX (mito. $O_2^{\cdot-}$) flow cytometry • Respirometry (Clark Electrode/Seahorse)
Apoptosis-Inducing Factor (AIF)	MIF activation, Parthanatos execution	Intramitochondrial PAR binding to AIF prompting nuclear translocation	• Fractionation and semi-quantitative analysis (western blot) of mitochondrial vs. extramitochondrial/nuclear [AIF] • Co-immunoprecipitation (IP: AIF, WB: PAR)
Mitochondrial NAD^+	Depletion of mitochondrial NAD^+ pool	Use of NAD^+ as a substrate	• Total mitochondrial PARylation state (western blot) • Immunoprecip. of mt-PARP1 (WB: phosphoserine, PAR) • Fractionation, MS assay of mito. vs. extramito. [NAD+]

[X]=concentration X, WB=western blot

4.2 Ferroptosis-Necroptosis Crosstalk: Future Directions

In the second part of this dissertation, we demonstrate through computational, genetic, biochemical, and redox lipidomics approaches that PEBP1 coregulates the ferroptosis and necroptosis death programs. Each RCD mode is initiated and propagated by distinct molecular mechanisms but, to varying degrees, are all interconnected. We present the first mechanistic explanation for the ferroptosis-necroptosis connection (Angeli et al., 2014; Martin-Sanchez et al., 2017; Moerke, Bleibaum, Kunzendorf, & Krautwald, 2019). PEBP1 allosterically regulates RIP3 kinase activity to inhibit necroptosis. Genetic or pharmacologic conditions that dissociate PEBP1 from RIP3 and alternate binding partners (e.g., RAF, RIP3) promotes ferroptosis. Interaction of PEBP1 with 15LOX generates ferroptosis death signals by changing the LOX substrate selectivity (arachidonic acid [AA] esterified to phosphatidylethanolamine [PE] instead of free AA) and product specificity (15-hydroperoxy-AA-containing PE instead of oxygenated forms of AA)

(Anthonymuthu et al., 2018; V. E. Kagan et al., 2017; Wenzel et al., 2017). Our work indicates that anti-RND therapies must simultaneously target the ferroptosis and necroptosis pathways to maximize clinical benefit.

Future efforts should focus on verifying and defining the structure-function relationship of the novel PEBP1-RIP3 interaction. PEBP1 structural analyses show the presence of a highly malleable pocket that adopts multiple confirmations along a microsecond-millisecond time scale (Granovsky et al., 2009). This highly plastic characteristic offers the structural reasoning for PEBP1's diverse ligand interactions – from lipids to polypeptides (Banfield et al., 1998; K. Yeung et al., 1999). However, there is often a tradeoff between interaction energetics and multispecificity (Fromer & Shifman, 2009). The kinetics and stoichiometry of the RIP3-PEBP1 interaction should be determined by PLA, isothermal titration calorimetry (ITC), or similar technique. If the RIP3-PEBP1 interaction is strong (low K_d), the role of PEBP1 as a physiologically important mediator of RIP3 activation and necroptosis would be validated. If the interaction is weak, then the fraction of PEBP1 bound-to-free RIP3 may be low and highly dependent on PEBP1 expression/availability. A weak PEBP1-RIP3 interaction may indicate that direct RIP3-PEBP1 interaction is not the dominant mechanism mediating PEBP1's anti-necroptotic effect. However, even in this case, RIP3 can still serve as an important PEBP1 buffering system, such as for ferroptosis (**Figure 31**). Alternate mechanisms of PEBP1 necroptosis modulation should also be interrogated, specifically focusing on PEBP1's role in RAF/MEK/ERK signaling, IKKα/β (NF-κB pathway), the PI3K/AKT/mTOR pathway, or LC3-II autophagy (Frank, Vaux, Murphy, Vince, & Lindqvist, 2019; Q. Liu et al., 2014; Royce, Brown-Borg, & Deepa, 2019; Y. Xie et al., 2020).

We demonstrate that PEBP1 and RIP3 directly interact, but the mechanism of PEBP1-mediated necroptosis inhibition is unclear. PEBP1 inhibits RAF activation by two complementary

mechanisms. **1**) PEBP1 sterically blocks p21-activated kinase (PAK) and Src family kinases' access to c-RAF phosphorylation sites (S338 and Y341) (Granovsky et al., 2009). Docking studies indicate PEBP1 does not shield the necroptosis critical RIP3 T231/S232 (human: S227) sites (**Figure 23, Figure 32**) (Cho et al., 2009). However, we demonstrate that PEBP1 inhibits *in vitro* RIP3 kinase activity and prevents TNFα/zVAD-fmk induced T231/S232 phosphorylation (**Figure 26, Figure 27**). Therefore, while PEBP1 may not sterically block access to T231/S232, it does inhibit their *cis*-autophosphorylation. **2**) PEBP1 competitively inhibits RAF homodimerization. Dimerization is critical for both RAF and RIP3 activation (Wu et al., 2014; T. Xie, Peng, Yan, et al., 2013). RIP3 homodimers adopt a side-by-side "handshake pose" like that formed by b-RAF or c-RAF. RIP3's R69 residue in the αC-β4 loop interfaces with R69 on its partner RIP3, and this interaction is reinforced by R96 and H156 of the first RIP3 with E71 and E154 on the opposing protomer (Raju et al., 2018). PEBP1 docks with RIP3 proximal to R69 and likely prohibits dimerization necessary for necroptosis (**Figure 32**). We propose that PEBP1 inhibits necroptosis by blocking both intrinsic RIP3 kinase activity and dimerization. The relative importance of these complementary mechanisms is yet to be resolved *in vivo*.

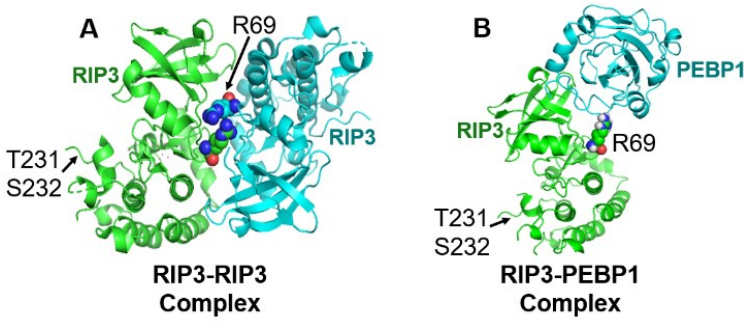

Figure 32. Proposed mechanism of PEBP1-dependent necroptosis inhibition

RIP3 homodimerization (**A**) and S227 phosphorylation is required for RIP3 kinase activation. RIP3 dimerization is mediated by the R69 residue. $RIP3^{R69H}$ mutant cannot dimerize, and cells expressing this variant are resistant to necroptosis. PEBP1 binds to RIP3 (**B**) proximal to RIP3 R69 and may preclude dimerization analogous to the R69H mutation.

The PEBP1-RIP3 complex must dissociate for necroptosis to proceed. Canonical PEPB1 interactions, such as with RAF or microtubule-associated proteins 1A/1B light chain 3 (LC3), are regulated by protein kinase C (PKC) mediated phosphorylation of S153 (Corbit et al., 2003; Noh et al., 2016). A similar mechanism may govern PEBP1-RIP3 dissociation. Overexpression of PEBP1 or expression of a RIP3-PEBP1 fusion protein (*Rip3*$^{-/-}$ background) is predicted to confer necroptosis resistance by increasing the likelihood of RIP3-PEBP1 interaction. In contrast, if PEBP1 S153 phosphorylation mediates dissociation from RIP3, expression of the PEBP1^{P74L} PKC activator, phosphomimic PEBP1^{S153E}, or RIP3-PEBP1^{S153E} fusion will sensitize cells to necroptosis compared to wild-type (Granovsky et al., 2009). It is conceivable that PEBP1 pS153 strengthens the RIP3-PEBP1 interaction, compared to compared to unmodified PEBP1, as it does with 15LOX (Wenzel et al., 2017). Therefore, RIP3 post-translational modification (RIP1-mediated phosphorylation or PELI1-dependent ubiquitination) or protein-protein interaction may drive PEBP1 affinity (Huibing Wang et al., 2017). This mechanism has PEBP1 serve as a passive check against spontaneous RIP3 activation. Similar mechanisms have been described. Inactive RIP1 directly suppresses spontaneous RIP3 autophosphorylation and necroptosis (Kaiser et al., 2014). PEBP1 may simply be displaced upon RIP3's RHIM-dependent high-affinity interaction with phospho-RIP1. By understanding the precise nature of the RIP3-PEBP1 interaction via nuclear magnetic resonance (NMR) or x-ray crystallography studies, the residue important for interaction can be determined and probable mechanisms of regulation predicted.

4.3 Concluding Remarks

This dissertation, and my work as a graduate student, has focused on the uncovering the core mechanisms and coregulatory schema of RND pathways – ferroptosis, necroptosis, and parthanatos – with the goal of using this knowledge in rational drug design and application. In the first part of this work, we interrogate the role of mtPARP1 in parthanotic mitochondrial dysfunction and cell death. We developed a novel neuroprotective mitochondria targeted PARP inhibitor, XJB-veliparib, which mitigates mitochondrial pathology while preserving genomic DNA repair capacity. XJB-veliparib provides opportunity to integrate mtPARP1 pathology and enables development of clinically effective anti-parthanotic therapies. In the second part of this work, we provide the first mechanistic evidence for interaction between ferroptosis and necroptosis. We demonstrate through computational, genetic, biochemical, and redox lipidomics approaches that PEBP1 coregulates the ferroptosis and necroptosis death programs *in vitro* and *in vivo*. Our work indicates that anti-RND therapies must simultaneously target the ferroptosis and necroptosis pathways to maximize clinical benefit.

RND pathways are core feature of acute injury. Due to environmental heterogeneity and mechanistic interconnection, RND pathways rarely operate independent of one another. Further, RND mechanisms are both temporally delayed and intrinsically tided to inflammation – necroinflammation. These features make RND a prime target for therapeutic intervention. Effective anti-RND therapies must recognize the overlapping nature of RND by devising strategies that jointly targets all major RND mechanisms.

Thank you for reading.

Bibliography

Adam-Vizi, V., & Tretter, L. (2013). The role of mitochondrial dehydrogenases in the generation of oxidative stress. *Neurochem Int, 62*(5), 757-763. doi:10.1016/j.neuint.2013.01.012

Ali, A. A. E., Timinszky, G., Arribas-Bosacoma, R., Kozlowski, M., Hassa, P. O., Hassler, M., . . . Oliver, A. W. (2012). The zinc-finger domains of PARP1 cooperate to recognize DNA strand breaks. *Nature Structural & Molecular Biology, 19*(7), 685-692. doi:10.1038/nsmb.2335

Alotaibi, M., Sharma, K., Saleh, T., Povirk, L. F., Hendrickson, E. A., & Gewirtz, D. A. (2016). Radiosensitization by PARP Inhibition in DNA Repair Proficient and Deficient Tumor Cells: Proliferative Recovery in Senescent Cells. *Radiat Res, 185*(3), 229-245. doi:10.1667/RR14202.1

Amaral, E. P., Conceição, E. L., Costa, D. L., Rocha, M. S., Marinho, J. M., Cordeiro-Santos, M., . . . Andrade, B. B. (2016). N-acetyl-cysteine exhibits potent anti-mycobacterial activity in addition to its known anti-oxidative functions. *BMC microbiology, 16*(1), 251-251. doi:10.1186/s12866-016-0872-7

Andrabi, S. A., Kang, H. C., Haince, J. F., Lee, Y. I., Zhang, J., Chi, Z., . . . Dawson, V. L. (2011). Iduna protects the brain from glutamate excitotoxicity and stroke by interfering with poly(ADP-ribose) polymer-induced cell death. *Nat Med, 17*(6), 692-699. doi:10.1038/nm.2387

Angeli, J. P. F., Schneider, M., Proneth, B., Tyurina, Y. Y., Tyurin, V. A., Hammond, V. J., . . . Conrad, M. (2014). Inactivation of the ferroptosis regulator Gpx4 triggers acute renal failure in mice. *Nat Cell Biol, 16*(12), 1180-1191. doi:10.1038/ncb3064

Anthonymuthu, T. S., Kenny, E. M., Shrivastava, I., Tyurina, Y. Y., Hier, Z. E., Ting, H. C., . . . Bayir, H. (2018). Empowerment of 15-Lipoxygenase Catalytic Competence in Selective Oxidation of Membrane ETE-PE to Ferroptotic Death Signals, HpETE-PE. *J Am Chem Soc, 140*(51), 17835-17839. doi:10.1021/jacs.8b09913

Audebert, M., Salles, B., & Calsou, P. (2004). Involvement of poly(ADP-ribose) polymerase-1 and XRCC1/DNA ligase III in an alternative route for DNA double-strand breaks rejoining. *J Biol Chem, 279*(53), 55117-55126. doi:10.1074/jbc.M404524200

Ayala, A., Muñoz, M. F., & Argüelles, S. (2014). Lipid Peroxidation: Production, Metabolism, and Signaling Mechanisms of Malondialdehyde and 4-Hydroxy-2-Nonenal. *Oxidative Medicine and Cellular Longevity, 2014*, 360438. doi:10.1155/2014/360438

Bachhawat, A. K., Thakur, A., Kaur, J., & Zulkifli, M. (2013). Glutathione transporters. *Biochimica et Biophysica Acta (BBA)-General Subjects, 1830*(5), 3154-3164.

Bai, P. (2015). Biology of Poly(ADP-Ribose) Polymerases: The Factotums of Cell Maintenance. *Molecular cell, 58*(6), 947-958. doi:10.1016/j.molcel.2015.01.034

Bai, P., Canto, C., Oudart, H., Brunyanszki, A., Cen, Y., Thomas, C., . . . Auwerx, J. (2011). PARP-1 inhibition increases mitochondrial metabolism through SIRT1 activation. *Cell metabolism, 13*(4), 461-468. doi:10.1016/j.cmet.2011.03.004

Banfield, M. J., Barker, J. J., Perry, A. C., & Brady, R. L. (1998). Function from structure? The crystal structure of human phosphatidylethanolamine-binding protein suggests a role in membrane signal transduction. *Structure, 6*(10), 1245-1254.

Berger, N. A., Besson, V. C., Boulares, A. H., Burkle, A., Chiarugi, A., Clark, R. S., . . . Szabo, C. (2017). Opportunities for the repurposing of PARP inhibitors for the therapy of non-oncological diseases. *Br J Pharmacol*. doi:10.1111/bph.13748

Berghe, T. V., Linkermann, A., Jouan-Lanhouet, S., Walczak, H., & Vandenabeele, P. (2014). Regulated necrosis: the expanding network of non-apoptotic cell death pathways. *Nature reviews Molecular cell biology, 15*, 135. doi:10.1038/nrm3737

Berhane, H., Epperly, M. W., Goff, J., Kalash, R., Cao, S., Franicola, D., . . . Greenberger, J. S. (2014). Radiologic differences between bone marrow stromal and hematopoietic progenitor cell lines from Fanconi Anemia (Fancd2(-/-)) mice. *Radiat Res, 181*(1), 76-89. doi:10.1667/RR13405.1

Biggs, D. S. (2010). 3D deconvolution microscopy. *Curr Protoc Cytom, Chapter 12*, Unit 12.19.11-20. doi:10.1002/0471142956.cy1219s52

Borchert, A., Kalms, J., Roth, S. R., Rademacher, M., Schmidt, A., Holzhutter, H.-G., . . . Scheerer, P. (2018). Crystal structure and functional characterization of selenocysteine-containing glutathione peroxidase 4 suggests an alternative mechanism of peroxide reduction. *Biochimica et Biophysica Acta (BBA) - Molecular and Cell Biology of Lipids, 1863*(9), 1095-1107. doi:https://doi.org/10.1016/j.bbalip.2018.06.006

Böttcher, C. J. F., Van gent, C. M., & Pries, C. (1961). A rapid and sensitive sub-micro phosphorus determination. *Analytica Chimica Acta, 24*, 203-204. doi:http://dx.doi.org/10.1016/0003-2670(61)80041-X

Boyington, J. C., Gaffney, B. J., & Amzel, L. M. (1993). The three-dimensional structure of an arachidonic acid 15-lipoxygenase. *Science, 260*(5113), 1482-1486.

Brigelius-Flohé, R., & Maiorino, M. (2013). Glutathione peroxidases. *Biochimica et Biophysica Acta (BBA) - General Subjects, 1830*(5), 3289-3303. doi:https://doi.org/10.1016/j.bbagen.2012.11.020

Brown, J. S., Kaye, S. B., & Yap, T. A. (2016). PARP inhibitors: the race is on. *British Journal of Cancer, 114*(7), 713-715. doi:10.1038/bjc.2016.67

Brunyanszki, A., Olah, G., Coletta, C., Szczesny, B., & Szabo, C. (2014). Regulation of mitochondrial poly(ADP-Ribose) polymerase activation by the beta-adrenoceptor/cAMP/protein kinase A axis during oxidative stress. *Mol Pharmacol, 86*(4), 450-462. doi:10.1124/mol.114.094318

Brunyanszki, A., Olah, G., Coletta, C., Szczesny, B., & Szabo, C. (2014). Regulation of Mitochondrial Poly(ADP-Ribose) Polymerase Activation by the β-Adrenoceptor/cAMP/Protein Kinase A Axis during Oxidative Stress. *Mol Pharmacol, 86*(4), 450-462. doi:10.1124/mol.114.094318

Brunyanszki, A., Szczesny, B., Virag, L., & Szabo, C. (2016a). Mitochondrial poly(ADP-ribose) polymerase: The Wizard of Oz at work. *Free Radic Biol Med, 100*, 257-270. doi:10.1016/j.freeradbiomed.2016.02.024

Brunyanszki, A., Szczesny, B., Virag, L., & Szabo, C. (2016b). Mitochondrial poly(ADP-ribose) polymerase: The Wizard of Oz at work. *Free Radic Biol Med*. doi:10.1016/j.freeradbiomed.2016.02.024

Bryant, H. E., Petermann, E., Schultz, N., Jemth, A. S., Loseva, O., Issaeva, N., . . . Helleday, T. (2009). PARP is activated at stalled forks to mediate Mre11-dependent replication restart and recombination. *Embo j, 28*(17), 2601-2615.

Burzio, L. O., Saez, L., & Cornejo, R. (1981). Poly (ADP-ribose) synthetase activity in rat testis mitochondria. *Biochem Biophys Res Commun, 103*(1), 369-375. Retrieved from https://www.ncbi.nlm.nih.gov/pubmed/6274347

Castedo, M., Perfettini, J.-L., Roumier, T., Andreau, K., Medema, R., & Kroemer, G. (2004). Cell death by mitotic catastrophe: a molecular definition. *Oncogene, 23*(16), 2825-2837. doi:10.1038/sj.onc.1207528

Castle, K. D., Daniel, A. R., Moding, E. J., Luo, L., Lee, C. L., & Kirsch, D. G. (2018). Mice Lacking RIP3 Kinase are not Protected from Acute Radiation Syndrome. *Radiat Res, 189*(6), 627-633. doi:10.1667/rr15001.1

Chakrabarti, M., Cockrell, A. L., Park, J., McCormick, S. P., Lindahl, L. S., & Lindahl, P. A. (2015). Speciation of iron in mouse liver during development, iron deficiency, IRP2 deletion and inflammatory hepatitis. *Metallomics, 7*(1), 93-101. doi:10.1039/c4mt00215f

Chan, F. K.-M. (2007). Three is better than one: Pre-ligand receptor assembly in the regulation of TNF receptor signaling. *Cytokine, 37*(2), 101-107. doi:https://doi.org/10.1016/j.cyto.2007.03.005

Cheng, Q., Barboule, N., Frit, P., Gomez, D., Bombarde, O., Couderc, B., . . . Calsou, P. (2011). Ku counteracts mobilization of PARP1 and MRN in chromatin damaged with DNA double-strand breaks. *Nucleic Acids Research, 39*(22), 9605-9619. doi:10.1093/nar/gkr656

Chiarugi, A., Meli, E., Calvani, M., Picca, R., Baronti, R., Camaioni, E., . . . Moroni, F. (2003). Novel isoquinolinone-derived inhibitors of poly(ADP-ribose) polymerase-1: pharmacological characterization and neuroprotective effects in an in vitro model of cerebral ischemia. *J Pharmacol Exp Ther, 305*(3), 943-949. doi:10.1124/jpet.103.048934

Cho, Y. S., Challa, S., Moquin, D., Genga, R., Ray, T. D., Guildford, M., & Chan, F. K. (2009). Phosphorylation-driven assembly of the RIP1-RIP3 complex regulates programmed necrosis and virus-induced inflammation. *Cell, 137*(6), 1112-1123. doi:10.1016/j.cell.2009.05.037

Choi, J., Liu, R.-M., Kundu, R. K., Sangiorgi, F., Wu, W., Maxson, R., & Forman, H. J. (2000). Molecular Mechanism of Decreased Glutathione Content in Human Immunodeficiency Virus Type 1 Tat-transgenic Mice. *Journal of Biological Chemistry, 275*(5), 3693-3698. doi:10.1074/jbc.275.5.3693

Clinical Trials Using Veliparib. (2020). Retrieved from https://www.cancer.gov/about-cancer/treatment/clinical-trials/intervention/veliparib

Combs, J. A., & DeNicola, G. M. (2019). The Non-Essential Amino Acid Cysteine Becomes Essential for Tumor Proliferation and Survival. *Cancers, 11*(5), 678. Retrieved from https://www.mdpi.com/2072-6694/11/5/678

Conrad, M., Angeli, J. P. F., Vandenabeele, P., & Stockwell, B. R. (2016). Regulated necrosis: disease relevance and therapeutic opportunities. *Nature Reviews Drug Discovery, 15*, 348. doi:10.1038/nrd.2015.6

Corbit, K. C., Trakul, N., Eves, E. M., Diaz, B., Marshall, M., & Rosner, M. R. (2003). Activation of Raf-1 signaling by protein kinase C through a mechanism involving Raf kinase inhibitory protein. *J Biol Chem, 278*(15), 13061-13068. doi:10.1074/jbc.M210015200

Corcoran, N. M., Clarkson, M. J., Stuchbery, R., & Hovens, C. M. (2016). Molecular Pathways: Targeting DNA Repair Pathway Defects Enriched in Metastasis. *Clinical Cancer Research, 22*(13), 3132-3137. doi:10.1158/1078-0432.Ccr-15-1050

Cozza, G., Rossetto, M., Bosello-Travain, V., Maiorino, M., Roveri, A., Toppo, S., . . . Ursini, F. (2017). Glutathione peroxidase 4-catalyzed reduction of lipid hydroperoxides in membranes: The polar head of membrane phospholipids binds the enzyme and addresses the fatty acid hydroperoxide group toward the redox center. *Free Radical Biology and Medicine, 112*, 1-11. doi:https://doi.org/10.1016/j.freeradbiomed.2017.07.010

Cozzi, A., Orellana, D. I., Santambrogio, P., Rubio, A., Cancellieri, C., Giannelli, S., . . . Rovida, E. (2019). Stem Cell Modeling of Neuroferritinopathy Reveals Iron as a Determinant of Senescence and Ferroptosis during Neuronal Aging. *Stem cell reports, 13*(5), 832-846.

Csomos, R. A., Brady, G. F., & Duckett, C. S. (2009). Enhanced cytoprotective effects of the inhibitor of apoptosis protein cellular IAP1 through stabilization with TRAF2. *J Biol Chem, 284*(31), 20531-20539. doi:10.1074/jbc.M109.029983

Cunningham, K. E., Novak, E. A., Vincent, G., Siow, V. S., Griffith, B. D., Ranganathan, S., . . . Mollen, K. P. (2019). Calcium/calmodulin-dependent protein kinase IV (CaMKIV) activation contributes to the pathogenesis of experimental colitis via inhibition of intestinal epithelial cell proliferation. *Faseb j, 33*(1), 1330-1346. doi:10.1096/fj.201800535R

Curtin, N. J., & Szabo, C. (2013). Therapeutic applications of PARP inhibitors: anticancer therapy and beyond. *Mol Aspects Med, 34*(6), 1217-1256. doi:10.1016/j.mam.2013.01.006

Dalle-Donne, I., Rossi, R., Colombo, G., Giustarini, D., & Milzani, A. (2009). Protein S-glutathionylation: a regulatory device from bacteria to humans. *Trends in biochemical sciences, 34*(2), 85-96.

Dantzer, F., Ame, J. C., Schreiber, V., Nakamura, J., Menissier-de Murcia, J., & de Murcia, G. (2006). Poly(ADP-ribose) polymerase-1 activation during DNA damage and repair. *Methods Enzymol, 409*, 493-510. doi:10.1016/s0076-6879(05)09029-4

Davidson, S. M., & Duchen, M. R. (2012). Imaging mitochondrial calcium signalling with fluorescent probes and single or two photon confocal microscopy. *Methods Mol Biol, 810*, 219-234. doi:10.1007/978-1-61779-382-0_14

Davila, A., Liu, L., Chellappa, K., Redpath, P., Nakamaru-Ogiso, E., Paolella, L. M., . . . Baur, J. A. (2018). Nicotinamide adenine dinucleotide is transported into mammalian mitochondria. *eLife, 7*, e33246. doi:10.7554/eLife.33246

de Almagro, M. C., Goncharov, T., Izrael-Tomasevic, A., Duttler, S., Kist, M., Varfolomeev, E., . . . Vucic, D. (2017). Coordinated ubiquitination and phosphorylation of RIP1 regulates necroptotic cell death. *Cell Death & Differentiation, 24*(1), 26-37. doi:10.1038/cdd.2016.78

de Murcia, J. M., Niedergang, C., Trucco, C., Ricoul, M., Dutrillaux, B., Mark, M., . . . de Murcia, G. (1997). Requirement of poly(ADP-ribose) polymerase in recovery from DNA damage in mice and in cells. *Proceedings of the National Academy of Sciences of the United States of America, 94*(14), 7303-7307. Retrieved from http://www.ncbi.nlm.nih.gov/pubmed/9207086

Deiss, K., Kisker, C., Lohse, M. J., & Lorenz, K. (2012). Raf Kinase Inhibitor Protein (RKIP) Dimer Formation Controls Its Target Switch from Raf1 to G Protein-coupled Receptor Kinase (GRK) 2. *J Biol Chem, 287*(28), 23407-23417. doi:10.1074/jbc.M112.363812

Dempsey, P. W., Doyle, S. E., He, J. Q., & Cheng, G. (2003). The signaling adaptors and pathways activated by TNF superfamily. *Cytokine & Growth Factor Reviews, 14*(3), 193-209. doi:https://doi.org/10.1016/S1359-6101(03)00021-2

Dixon, S. J. (2017). Ferroptosis: bug or feature? *Immunol Rev, 277*(1), 150-157. doi:10.1111/imr.12533

Dixon, S. J., Lemberg, K. M., Lamprecht, M. R., Skouta, R., Zaitsev, E. M., Gleason, C. E., . . . Stockwell, B. R. (2012). Ferroptosis: an iron-dependent form of nonapoptotic cell death. *Cell, 149*(5), 1060-1072. doi:10.1016/j.cell.2012.03.042

Dixon, S. J., Lemberg, K. M., Lamprecht, M. R., Skouta, R., Zaitsev, E. M., Gleason, C. E., . . . Stockwell, B. R. (2012). Ferroptosis: An Iron-Dependent Form of Non-Apoptotic Cell Death. *Cell, 149*(5), 1060-1072. doi:10.1016/j.cell.2012.03.042

Dixon, S. J., Patel, D. N., Welsch, M., Skouta, R., Lee, E. D., Hayano, M., . . . Stockwell, B. R. (2014). Pharmacological inhibition of cystine–glutamate exchange induces endoplasmic reticulum stress and ferroptosis. *eLife, 3*, e02523. doi:10.7554/eLife.02523

Doll, S., Freitas, F. P., Shah, R., Aldrovandi, M., da Silva, M. C., Ingold, I., . . . Conrad, M. (2019). FSP1 is a glutathione-independent ferroptosis suppressor. *Nature, 575*(7784), 693-698. doi:10.1038/s41586-019-1707-0

Doll, S., Proneth, B., Tyurina, Y. Y., Panzilius, E., Kobayashi, S., Ingold, I., . . . Conrad, M. (2017). ACSL4 dictates ferroptosis sensitivity by shaping cellular lipid composition. *Nat Chem Biol, 13*(1), 91-98. doi:10.1038/nchembio.2239

Donawho, C. K., Luo, Y., Luo, Y., Penning, T. D., Bauch, J. L., Bouska, J. J., . . . Frost, D. J. (2007). ABT-888, an Orally Active Poly(ADP-Ribose) Polymerase Inhibitor that Potentiates DNA-Damaging Agents in Preclinical Tumor Models. *Clinical Cancer Research, 13*(9), 2728-2737. doi:10.1158/1078-0432.CCR-06-3039

Donawho, C. K., Luo, Y., Luo, Y., Penning, T. D., Bauch, J. L., Bouska, J. J., . . . Frost, D. J. (2007). ABT-888, an orally active poly(ADP-ribose) polymerase inhibitor that potentiates DNA-damaging agents in preclinical tumor models. *Clinical Cancer Research, 13*(9), 2728-2737. doi:10.1158/1078-0432.Ccr-06-3039

Dondelinger, Y., Declercq, W., Montessuit, S., Roelandt, R., Goncalves, A., Bruggeman, I., . . . Vandenabeele, P. (2014). MLKL compromises plasma membrane integrity by binding to phosphatidylinositol phosphates. *Cell Rep, 7*(4), 971-981. doi:10.1016/j.celrep.2014.04.026

Dondelinger, Y., Jouan-Lanhouet, S., Divert, T., Theatre, E., Bertin, J., Gough, P. J., . . . Bertrand, M. J. (2015). NF-κB-Independent Role of IKKα/IKKβ in Preventing RIPK1 Kinase-Dependent Apoptotic and Necroptotic Cell Death during TNF Signaling. *Molecular cell, 60*(1), 63-76. doi:10.1016/j.molcel.2015.07.032

Dringen, R. (2000). Metabolism and functions of glutathione in brain. *Prog Neurobiol, 62*(6), 649-671. doi:https://doi.org/10.1016/S0301-0082(99)00060-X

Du, L., Zhang, X., Han, Y. Y., Burke, N. A., Kochanek, P. M., Watkins, S. C., . . . Clark, R. S. B. (2003). Intra-mitochondrial poly-ADP-ribosylation contributes to NAD+ depletion and cell death induced by oxidative stress. *J Biol Chem, 278*, 18426-18433. Retrieved from http://www.ncbi.nlm.nih.gov/entrez/query.fcgi?cmd=Retrieve&db=PubMed&dopt=Citation&list_uids=12626504

Dunn, K. W., Kamocka, M. M., & McDonald, J. H. (2011). A practical guide to evaluating colocalization in biological microscopy. *Am J Physiol Cell Physiol, 300*(4), C723-742. doi:10.1152/ajpcell.00462.2010

Ea, C.-K., Deng, L., Xia, Z.-P., Pineda, G., & Chen, Z. J. (2006). Activation of IKK by TNFα Requires Site-Specific Ubiquitination of RIP1 and Polyubiquitin Binding by NEMO. *Molecular cell, 22*(2), 245-257. doi:https://doi.org/10.1016/j.molcel.2006.03.026

Elguindy, M. M., & Nakamaru-Ogiso, E. (2015). Apoptosis-inducing factor (AIF) and its family member protein, AMID, are rotenone-sensitive NADH: ubiquinone oxidoreductases (NDH-2). *Journal of Biological Chemistry, 290*(34), 20815-20826.

Eliasson, M. J., Sampei, K., Mandir, A. S., Hurn, P. D., Traystman, R. J., Bao, J., . . . Dawson, V. L. (1997). Poly(ADP-ribose) polymerase gene disruption renders mice resistant to cerebral ischemia. *Nat Med, 3*(10), 1089-1095. Retrieved from https://www.ncbi.nlm.nih.gov/pubmed/9334719

Escobales, N., Nunez, R. E., Jang, S., Parodi-Rullan, R., Ayala-Pena, S., Sacher, J. R., . . . Javadov, S. (2014). Mitochondria-targeted ROS scavenger improves post-ischemic recovery of cardiac function and attenuates mitochondrial abnormalities in aged rats. *J Mol Cell Cardiol, 77*, 136-146. doi:10.1016/j.yjmcc.2014.10.009

Fan, J., Dawson, T. M., & Dawson, V. L. (2017). Cell Death Mechanisms of Neurodegeneration. *Adv Neurobiol, 15*, 403-425. doi:10.1007/978-3-319-57193-5_16

Fatokun, A. A., Dawson, V. L., & Dawson, T. M. (2014). Parthanatos: mitochondrial-linked mechanisms and therapeutic opportunities. *Br J Pharmacol, 171*(8), 2000-2016. doi:10.1111/bph.12416

Feoktistova, M., Geserick, P., Kellert, B., Dimitrova, D. P., Langlais, C., Hupe, M., . . . Leverkus, M. (2011). cIAPs block Ripoptosome formation, a RIP1/caspase-8 containing intracellular cell death complex differentially regulated by cFLIP isoforms. *Molecular cell, 43*(3), 449-463. doi:10.1016/j.molcel.2011.06.011

Fettweis, G., Di Valentin, E., L'Homme, L., Lassence, C., Dequiedt, F., Fillet, M., . . . Piette, J. (2017). RIP3 antagonizes a TSC2-mediated pro-survival pathway in glioblastoma cell death. *Biochimica et Biophysica Acta (BBA) - Molecular Cell Research, 1864*(1), 113-124. doi:https://doi.org/10.1016/j.bbamcr.2016.10.014

Filipovic, D. M., Meng, X., & Reeves, W. B. (1999). Inhibition of PARP prevents oxidant-induced necrosis but not apoptosis in LLC-PK1 cells. *Am J Physiol, 277*(3), F428-436. doi:10.1152/ajprenal.1999.277.3.F428

Fisher, A. E., Hochegger, H., Takeda, S., & Caldecott, K. W. (2007). Poly(ADP-ribose) polymerase 1 accelerates single-strand break repair in concert with poly(ADP-ribose) glycohydrolase. *Mol Cell Biol, 27*(15), 5597-5605. doi:10.1128/mcb.02248-06

Flora, P. K., & Gregory, C. D. (1994). Recognition of apoptotic cells by human macrophages: inhibition by a monocyte/macrophage-specific monoclonal antibody. *European journal of immunology, 24*(11), 2625-2632.

Folch, J., Lees, M., & Sloane Stanley, G. (1957). A simple method for the isolation and purification of total lipids from animal tissues. *J Biol Chem, 226*(1), 497-509.

Fragkos, M., & Beard, P. (2011). Mitotic catastrophe occurs in the absence of apoptosis in p53-null cells with a defective G1 checkpoint. *PLoS One, 6*(8), e22946-e22946. doi:10.1371/journal.pone.0022946

Frank, D., Vaux, D. L., Murphy, J. M., Vince, J. E., & Lindqvist, L. M. (2019). Activated MLKL attenuates autophagy following its translocation to intracellular membranes. *Journal of Cell Science, 132*(5), jcs220996. doi:10.1242/jcs.220996

Frantz, M. C., & Wipf, P. (2010). Mitochondria as a target in treatment. *Environ Mol Mutagen, 51*(5), 462-475. doi:10.1002/em.20554

Frei, B., Kim, M. C., & Ames, B. N. (1990). Ubiquinol-10 is an effective lipid-soluble antioxidant at physiological concentrations. *Proceedings of the National Academy of Sciences, 87*(12), 4879-4883.

Frey, A. G., Nandal, A., Park, J. H., Smith, P. M., Yabe, T., Ryu, M.-S., . . . Philpott, C. C. (2014). Iron chaperones PCBP1 and PCBP2 mediate the metallation of the dinuclear iron enzyme deoxyhypusine hydroxylase. *Proceedings of the National Academy of Sciences, 111*(22), 8031. doi:10.1073/pnas.1402732111

Friedman, J. I., & Stivers, J. T. (2010). Detection of damaged DNA bases by DNA glycosylase enzymes. *Biochemistry, 49*(24), 4957-4967. doi:10.1021/bi100593a

Fromer, M., & Shifman, J. M. (2009). Tradeoff Between Stability and Multispecificity in the Design of Promiscuous Proteins. *PLOS Computational Biology, 5*(12), e1000627. doi:10.1371/journal.pcbi.1000627

Furukawa, T., Meydani, S., & Blumberg, J. (1987). Reversal of age-associated decline in immune responsiveness by dietary glutathione supplementation in mice. *Mechanisms of ageing and development, 38*(2), 107-117.

Gagné, J.-P., Isabelle, M., Lo, K. S., Bourassa, S., Hendzel, M. J., Dawson, V. L., . . . Poirier, G. G. (2008). Proteome-wide identification of poly(ADP-ribose) binding proteins and

poly(ADP-ribose)-associated protein complexes. *Nucleic Acids Research, 36*(22), 6959-6976. doi:10.1093/nar/gkn771

Gagné, J.-P., Pic, E., Isabelle, M., Krietsch, J., Ethier, C., Paquet, E., . . . Poirier, G. G. (2012). Quantitative proteomics profiling of the poly(ADP-ribose)-related response to genotoxic stress. *Nucleic Acids Research, 40*(16), 7788-7805. doi:10.1093/nar/gks486

Galluzzi, L., Vitale, I., Aaronson, S. A., Abrams, J. M., Adam, D., Agostinis, P., . . . Kroemer, G. (2018). Molecular mechanisms of cell death: recommendations of the Nomenclature Committee on Cell Death 2018. *Cell Death & Differentiation, 25*(3), 486-541. doi:10.1038/s41418-017-0012-4

Gao, M., Monian, P., Pan, Q., Zhang, W., Xiang, J., & Jiang, X. (2016). Ferroptosis is an autophagic cell death process. *Cell Res, 26*(9), 1021-1032. doi:10.1038/cr.2016.95

Gao, M., Monian, P., Quadri, N., Ramasamy, R., & Jiang, X. (2015). Glutaminolysis and Transferrin Regulate Ferroptosis. *Molecular cell, 59*(2), 298-308. doi:https://doi.org/10.1016/j.molcel.2015.06.011

Gao, M., Yi, J., Zhu, J., Minikes, A. M., Monian, P., Thompson, C. B., & Jiang, X. (2019). Role of Mitochondria in Ferroptosis. *Molecular cell, 73*(2), 354-363.e353. doi:https://doi.org/10.1016/j.molcel.2018.10.042

Geng, J., Ito, Y., Shi, L., Amin, P., Chu, J., Ouchida, A. T., . . . Yuan, J. (2017). Regulation of RIPK1 activation by TAK1-mediated phosphorylation dictates apoptosis and necroptosis. *Nat Commun, 8*(1), 359. doi:10.1038/s41467-017-00406-w

Gracz, A. D., Puthoff, B. J., & Magness, S. T. (2012). Identification, isolation, and culture of intestinal epithelial stem cells from murine intestine. *Methods Mol Biol, 879*, 89-107. doi:10.1007/978-1-61779-815-3_6

Granovsky, A. E., Clark, M. C., McElheny, D., Heil, G., Hong, J., Liu, X., . . . Rosner, M. R. (2009). Raf Kinase Inhibitory Protein Function Is Regulated via a Flexible Pocket and Novel Phosphorylation-Dependent Mechanism. *Mol Cell Biol, 29*(5), 1306-1320. doi:10.1128/MCB.01271-08

Griffith, O. W., & Meister, A. (1985). Origin and turnover of mitochondrial glutathione. *Proceedings of the National Academy of Sciences, 82*(14), 4668. doi:10.1073/pnas.82.14.4668

Grootjans, S., Vanden Berghe, T., & Vandenabeele, P. (2017). Initiation and execution mechanisms of necroptosis: an overview. *Cell Death Differ, 24*(7), 1184-1195. doi:10.1038/cdd.2017.65

Guarente, L. (2014). Linking DNA damage, NAD(+)/SIRT1, and aging. *Cell metabolism, 20*(5), 706-707. doi:10.1016/j.cmet.2014.10.015

Guo, X., Yin, H., Chen, Y., Li, L., Li, J., & Liu, Q. (2016). TAK1 regulates caspase 8 activation and necroptotic signaling via multiple cell death checkpoints. *Cell Death & Disease, 7*(9), e2381-e2381. doi:10.1038/cddis.2016.294

Haince, J.-F., Kozlov, S., Dawson, V. L., Dawson, T. M., Hendzel, M. J., Lavin, M. F., & Poirier, G. G. (2007). Ataxia telangiectasia mutated (ATM) signaling network is modulated by a

novel poly (ADP-ribose)-dependent pathway in the early response to DNA-damaging agents. *Journal of Biological Chemistry, 282*(22), 16441-16453.

Haince, J.-F., McDonald, D., Rodrigue, A., Déry, U., Masson, J.-Y., Hendzel, M. J., & Poirier, G. G. (2008). PARP1-dependent kinetics of recruitment of MRE11 and NBS1 proteins to multiple DNA damage sites. *Journal of Biological Chemistry, 283*(2), 1197-1208.

Hanzlikova, H., Gittens, W., Krejcikova, K., Zeng, Z., & Caldecott, K. W. (2017). Overlapping roles for PARP1 and PARP2 in the recruitment of endogenous XRCC1 and PNKP into oxidized chromatin. *Nucleic Acids Res, 45*(5), 2546-2557. doi:10.1093/nar/gkw1246

Hassa, P. O., & Hottiger, M. O. (2008). The diverse biological roles of mammalian PARPS, a small but powerful family of poly-ADP-ribose polymerases. *Front Biosci, 13*(13), 3046-3082.

He, S., Wang, L., Miao, L., Wang, T., Du, F., Zhao, L., & Wang, X. (2009). Receptor interacting protein kinase-3 determines cellular necrotic response to TNF-alpha. *Cell, 137*(6), 1100-1111. doi:10.1016/j.cell.2009.05.021

Hess, B., Kutzner, C., van der Spoel, D., & Lindahl, E. (2008). GROMACS 4: Algorithms for Highly Efficient, Load-Balanced, and Scalable Molecular Simulation. *J Chem Theory Comput, 4*(3), 435-447. doi:10.1021/ct700301q

Hider, R. C., & Kong, X. (2013). Iron speciation in the cytosol: an overview. *Dalton Transactions, 42*(9), 3220-3229.

Hoch, N. C., Hanzlikova, H., Rulten, S. L., Tétreault, M., Komulainen, E., Ju, L., . . . Caldecott, K. W. (2017). XRCC1 mutation is associated with PARP1 hyperactivation and cerebellar ataxia. *Nature, 541*(7635), 87-91. doi:10.1038/nature20790

Holler, N., Zaru, R., Micheau, O., Thome, M., Attinger, A., Valitutti, S., . . . Tschopp, J. (2000). Fas triggers an alternative, caspase-8–independent cell death pathway using the kinase RIP as effector molecule. *Nature Immunology, 1*, 489. doi:10.1038/82732

Hong, S. J., Dawson, T. M., & Dawson, V. L. (2004). Nuclear and mitochondrial conversations in cell death: PARP-1 and AIF signaling. *Trends Pharmacol Sci, 25*(5), 259-264. doi:10.1016/j.tips.2004.03.005

Horton, T. M., Jenkins, G., Pati, D., Zhang, L., Dolan, M. E., Ribes-Zamora, A., . . . Berg, S. L. (2009). Poly(ADP-ribose) polymerase inhibitor ABT-888 potentiates the cytotoxic activity of temozolomide in leukemia cells: influence of mismatch repair status and O6-methylguanine-DNA methyltransferase activity. *Molecular cancer therapeutics, 8*(8), 2232-2242. doi:10.1158/1535-7163.MCT-09-0142

Hoye, A. T., Davoren, J. E., Wipf, P., Fink, M. P., & Kagan, V. E. (2008). Targeting mitochondria. *Acc Chem Res, 41*(1), 87-97. doi:10.1021/ar700135m

Hu, J., Ahuja, L. G., Meharena, H. S., Kannan, N., Kornev, A. P., Taylor, S. S., & Shaw, A. S. (2015). Kinase regulation by hydrophobic spine assembly in cancer. *Mol Cell Biol, 35*(1), 264-276. doi:10.1128/mcb.00943-14

Hua, G., Wang, C., Pan, Y., Zeng, Z., Lee, S. G., Martin, M. L., . . . Kolesnick, R. (2017). Distinct Levels of Radioresistance in Lgr5(+) Colonic Epithelial Stem Cells versus Lgr5(+) Small

Intestinal Stem Cells. *Cancer Research, 77*(8), 2124-2133. doi:10.1158/0008-5472.CAN-15-2870

Huang, Z., Epperly, M., Watkins, S. C., Greenberger, J. S., Kagan, V. E., & Bayır, H. (2016). Necrostatin-1 rescues mice from lethal irradiation. *Biochim Biophys Acta, 1862*(4), 850-856. doi:10.1016/j.bbadis.2016.01.014

Imai, H., Hirao, F., Sakamoto, T., Sekine, K., Mizukura, Y., Saito, M., . . . Nakagawa, Y. (2003). Early embryonic lethality caused by targeted disruption of the mouse PHGPx gene. *Biochem Biophys Res Commun, 305*(2), 278-286. doi:10.1016/s0006-291x(03)00734-4

Ito, S., Murphy, C. G., Doubrovina, E., Jasin, M., & Moynahan, M. E. (2016). PARP Inhibitors in Clinical Use Induce Genomic Instability in Normal Human Cells. *PLoS One, 11*(7), e0159341. doi:10.1371/journal.pone.0159341

Jastroch, M., Divakaruni, A. S., Mookerjee, S., Treberg, J. R., & Brand, M. D. (2010). Mitochondrial proton and electron leaks. *Essays In Biochemistry, 47*, 53-67. doi:10.1042/bse0470053

Ji, J., Baart, S., Vikulina, A. S., Clark, R. S., Anthonymuthu, T. S., Tyurin, V. A., . . . Bayir, H. (2015). Deciphering of mitochondrial cardiolipin oxidative signaling in cerebral ischemia-reperfusion. *J Cereb Blood Flow Metab, 35*(2), 319-328. doi:10.1038/jcbfm.2014.204

Ji, J., Kline, A. E., Amoscato, A., Samhan-Arias, A. K., Sparvero, L. J., Tyurin, V. A., . . . Bayir, H. (2012). Lipidomics identifies cardiolipin oxidation as a mitochondrial target for redox therapy of brain injury. *Nat Neurosci, 15*(10), 1407-1413. doi:10.1038/nn.3195

Jiang, J., Kurnikov, I., Belikova, N. A., Xiao, J., Zhao, Q., Amoscato, A. A., . . . Kagan, V. E. (2007). Structural Requirements for Optimized Delivery, Inhibition of Oxidative Stress, and Antiapoptotic Activity of Targeted Nitroxides. *Journal of Pharmacology and Experimental Therapeutics, 320*(3), 1050-1060. doi:10.1124/jpet.106.114769

Jiang, L., Kon, N., Li, T., Wang, S.-J., Su, T., Hibshoosh, H., . . . Gu, W. (2015). Ferroptosis as a p53-mediated activity during tumour suppression. *Nature, 520*(7545), 57-62. doi:10.1038/nature14344

Jo, S., Kim, T., Iyer, V. G., & Im, W. (2008). CHARMM-GUI: a web-based graphical user interface for CHARMM. *J Comput Chem, 29*(11), 1859-1865. doi:10.1002/jcc.20945

Jozefczak, M., Remans, T., Vangronsveld, J., & Cuypers, A. (2012). Glutathione is a key player in metal-induced oxidative stress defenses. *International journal of molecular sciences, 13*(3), 3145-3175. doi:10.3390/ijms13033145

Jubin, T., Kadam, A., Jariwala, M., Bhatt, S., Sutariya, S., Gani, A. R., . . . Begum, R. (2016). The PARP family: insights into functional aspects of poly (ADP-ribose) polymerase-1 in cell growth and survival. *Cell Prolif, 49*(4), 421-437. doi:10.1111/cpr.12268

Kagan, V. E., Bayır, H. A., Belikova, N. A., Kapralov, O., Tyurina, Y. Y., Tyurin, V. A., . . . Kochanek, P. M. (2009). Cytochrome c/cardiolipin relations in mitochondria: a kiss of death. *Free Radical Biology and Medicine, 46*(11), 1439-1453.

Kagan, V. E., Bayir, H. A., Belikova, N. A., Kapralov, O., Tyurina, Y. Y., Tyurin, V. A., . . . Borisenko, G. (2009). Cytochrome c/cardiolipin relations in mitochondria: a kiss of death. *Free Radic Biol Med, 46*(11), 1439-1453. doi:10.1016/j.freeradbiomed.2009.03.004

Kagan, V. E., Mao, G., Qu, F., Angeli, J. P., Doll, S., Croix, C. S., . . . Bayir, H. (2017). Oxidized arachidonic and adrenic PEs navigate cells to ferroptosis. *Nat Chem Biol, 13*(1), 81-90. doi:10.1038/nchembio.2238

Kagan, V. E., Tyurin, V. A., Jiang, J., Tyurina, Y. Y., Ritov, V. B., Amoscato, A. A., . . . Kini, V. (2005). Cytochrome c acts as a cardiolipin oxygenase required for release of proapoptotic factors. *Nat Chem Biol, 1*(4), 223.

Kaiser, W. J., Daley-Bauer, L. P., Thapa, R. J., Mandal, P., Berger, S. B., Huang, C., . . . Mocarski, E. S. (2014). RIP1 suppresses innate immune necrotic as well as apoptotic cell death during mammalian parturition. *Proceedings of the National Academy of Sciences of the United States of America, 111*(21), 7753-7758. doi:10.1073/pnas.1401857111

Kaiser, W. J., Sridharan, H., Huang, C., Mandal, P., Upton, J. W., Gough, P. J., . . . Mocarski, E. S. (2013). Toll-like Receptor 3-mediated Necrosis via TRIF, RIP3, and MLKL. *J Biol Chem, 288*(43), 31268-31279. doi:10.1074/jbc.M113.462341

Kameshita, I., Matsuda, Z., Taniguchi, T., & Shizuta, Y. (1984). Poly (ADP-Ribose) synthetase. Separation and identification of three proteolytic fragments as the substrate-binding domain, the DNA-binding domain, and the automodification domain. *J Biol Chem, 259*(8), 4770-4776.

Kanai, A., Zabbarova, I., Amoscato, A., Epperly, M., Xiao, J., & Wipf, P. (2007). Mitochondrial targeting of radioprotectants using peptidyl conjugates. *Org Biomol Chem, 5*(2), 307-309. doi:10.1039/b613334g

Kanner, J., German, J. B., & Kinsella, J. E. (1987). Initiation of lipid peroxidation in biological systems. *Crit Rev Food Sci Nutr, 25*(4), 317-364. doi:10.1080/10408398709527457

Kapralov, A. A., Yang, Q., Dar, H. H., Tyurina, Y. Y., Anthonymuthu, T. S., Kim, R., . . . Kagan, V. E. (2020). Redox lipid reprogramming commands susceptibility of macrophages and microglia to ferroptotic death. *Nat Chem Biol, 16*(3), 278-290. doi:10.1038/s41589-019-0462-8

Karch, J., Kanisicak, O., Brody, M. J., Sargent, M. A., Michael, D. M., & Molkentin, J. D. (2015). Necroptosis Interfaces with MOMP and the MPTP in Mediating Cell Death. *PLoS One, 10*(6), e0130520. doi:10.1371/journal.pone.0130520

Karlberg, T., Hammarstrom, M., Schutz, P., Svensson, L., & Schuler, H. (2010). Crystal structure of the catalytic domain of human PARP2 in complex with PARP inhibitor ABT-888. *Biochemistry, 49*(6), 1056-1058. doi:10.1021/bi902079y

Kearney, C. J., Cullen, S. P., Clancy, D., & Martin, S. J. (2014). RIPK1 can function as an inhibitor rather than an initiator of RIPK3-dependent necroptosis. *Febs j, 281*(21), 4921-4934. doi:10.1111/febs.13034

Kenny, E. M., Fidan, E., Yang, Q., Anthonymuthu, T. S., New, L. A., Meyer, E. A., . . . Bayir, H. (2019). Ferroptosis Contributes to Neuronal Death and Functional Outcome After Traumatic Brain Injury. *Crit Care Med, 47*(3), 410-418. doi:10.1097/ccm.0000000000003555

Kerr, J. (1971). Shrinkage necrosis: a distinct mode of cellular death. *The Journal of pathology, 105*(1), 13-20.

Kerr, J. F., Wyllie, A. H., & Currie, A. R. (1972). Apoptosis: a basic biological phenomenon with wide-ranging implications in tissue kinetics. *British Journal of Cancer, 26*(4), 239-257. doi:10.1038/bjc.1972.33

Kim, S. E., Zhang, L., Ma, K., Riegman, M., Chen, F., Ingold, I., . . . Overholtzer, M. (2016). Ultrasmall nanoparticles induce ferroptosis in nutrient-deprived cancer cells and suppress tumour growth. *Nature nanotechnology, 11*(11), 977-985. doi:10.1038/nnano.2016.164

King, B. S., Cooper, K. L., Liu, K. J., & Hudson, L. G. (2012). Poly (ADP-ribose) contributes to an association between poly (ADP-ribose) polymerase-1 and xeroderma pigmentosum complementation group A in nucleotide excision repair. *Journal of Biological Chemistry, 287*(47), 39824-39833.

Kobe, M. J., Neau, D. B., Mitchell, C. E., Bartlett, S. G., & Newcomer, M. E. (2014). The structure of human 15-lipoxygenase-2 with a substrate mimic. *J Biol Chem, 289*(12), 8562-8569. doi:10.1074/jbc.M113.543777

Kouyama, K., Mayanagi, K., Nakae, S., Nishi, Y., Miwa, M., & Shirai, T. (2019). Single-particle analysis of full-length human poly(ADP-ribose) polymerase 1. *Biophysics and physicobiology, 16*, 59-67. doi:10.2142/biophysico.16.0_59

Kozakov, D., Hall, D. R., Xia, B., Porter, K. A., Padhorny, D., Yueh, C., . . . Vajda, S. (2017). The ClusPro web server for protein-protein docking. *Nature Protocols, 12*(2), 255-278. doi:10.1038/nprot.2016.169

Kozuka, K., He, Y., Koo-McCoy, S., Kumaraswamy, P., Nie, B., Shaw, K., . . . Siegel, M. (2017). Development and Characterization of a Human and Mouse Intestinal Epithelial Cell Monolayer Platform. *Stem Cell Reports, 9*(6), 1976-1990. doi:10.1016/j.stemcr.2017.10.013

Krietsch, J., Rouleau, M., Pic, É., Ethier, C., Dawson, T. M., Dawson, V. L., . . . Gagné, J.-P. (2013). Reprogramming cellular events by poly (ADP-ribose)-binding proteins. *Molecular Aspects of Medicine, 34*(6), 1066-1087.

Kroemer, G., El-Deiry, W., Golstein, P., Peter, M., Vaux, D., Vandenabeele, P., . . . Knight, R. (2005). Classification of cell death: recommendations of the Nomenclature Committee on Cell Death. *Cell Death Differ, 12*(12), 1463-1467.

Küch, E. M., Vellaramkalayil, R., Zhang, I., Lehnen, D., Brügger, B., Sreemmel, W., . . . Füllekrug, J. (2014). Differentially localized acyl-CoA synthetase 4 isoenzymes mediate the metabolic channeling of fatty acids towards phosphatidylinositol. *Biochim Biophys Acta, 1841*(2), 227-239. doi:10.1016/j.bbalip.2013.10.018

Kun, E., Zimber, P. H., Chang, A. C., Puschendorf, B., & Grunicke, H. (1975). Macromolecular enzymatic product of NAD+ in liver mitochondria. *Proc Natl Acad Sci U S A, 72*(4), 1436-1440. Retrieved from https://www.ncbi.nlm.nih.gov/pubmed/165508

Lai, Y., Chen, Y., Watkins, S. C., Nathaniel, P. D., Guo, F., Kochanek, P. M., . . . Clark, R. S. (2008). Identification of poly-ADP-ribosylated mitochondrial proteins after traumatic brain injury. *J Neurochem, 104*(6), 1700-1711. doi:10.1111/j.1471-4159.2007.05114.x

Lamade, A. M., Kenny, E. M., Anthonymuthu, T. S., Soysal, E., Clark, R. S. B., Kagan, V. E., & Bayir, H. (2019). Aiming for the target: Mitochondrial drug delivery in traumatic brain injury. *Neuropharmacology, 145*(Pt B), 209-219. doi:10.1016/j.neuropharm.2018.07.014

Langelier, M.-F., Planck, J. L., Roy, S., & Pascal, J. M. (2011). Crystal structures of poly (ADP-ribose) polymerase-1 (PARP-1) zinc fingers bound to DNA structural and functional insights into DNA-dependent PARP-1 activity. *Journal of Biological Chemistry, 286*(12), 10690-10701.

Langelier, M. F., Planck, J. L., Roy, S., & Pascal, J. M. (2011). Crystal structures of poly(ADP-ribose) polymerase-1 (PARP-1) zinc fingers bound to DNA: structural and functional insights into DNA-dependent PARP-1 activity. *J Biol Chem, 286*(12), 10690-10701. doi:10.1074/jbc.M110.202507

Lash, L. H. (2006). Mitochondrial glutathione transport: physiological, pathological and toxicological implications. *Chemico-biological interactions, 163*(1-2), 54-67.

Laster, S. M., Wood, J., & Gooding, L. (1988). Tumor necrosis factor can induce both apoptic and necrotic forms of cell lysis. *The Journal of Immunology, 141*(8), 2629-2634.

Lavoie, H., & Therrien, M. (2015). Regulation of RAF protein kinases in ERK signalling. *Nature reviews Molecular cell biology, 16*, 281. doi:10.1038/nrm3979

https://www.nature.com/articles/nrm3979#supplementary-information

Lee, J. M., Lee, H., Kang, S., & Park, W. J. (2016). Fatty acid desaturases, polyunsaturated fatty acid regulation, and biotechnological advances. *Nutrients, 8*(1), 23.

Leidgens, S., Bullough, K. Z., Shi, H., Li, F., Shakoury-Elizeh, M., Yabe, T., . . . Philpott, C. C. (2013). Each member of the poly-r(C)-binding protein 1 (PCBP) family exhibits iron chaperone activity toward ferritin. *J Biol Chem, 288*(24), 17791-17802. doi:10.1074/jbc.M113.460253

Li, H., Kobayashi, M., Blonska, M., You, Y., & Lin, X. (2006). Ubiquitination of RIP is required for tumor necrosis factor alpha-induced NF-kappaB activation. *J Biol Chem, 281*(19), 13636-13643. doi:10.1074/jbc.M600620200

Li, J., McQuade, T., Siemer, A. B., Napetschnig, J., Moriwaki, K., Hsiao, Y.-S., . . . McDermott, A. (2012). The RIP1/RIP3 necrosome forms a functional amyloid signaling complex required for programmed necrosis. *Cell, 150*(2), 339-350.

Li, M., & Yu, X. (2013). Function of BRCA1 in the DNA damage response is mediated by ADP-ribosylation. *Cancer cell, 23*(5), 693-704.

Li, X., Delzer, J., Voorman, R., de Morais, S. M., & Lao, Y. (2011). Disposition and drug-drug interaction potential of veliparib (ABT-888), a novel and potent inhibitor of poly(ADP-ribose) polymerase. *Drug Metabolism and Disposition: The Biological Fate of Chemicals, 39*(7), 1161-1169. doi:10.1124/dmd.110.037820

Lin, J., Kumari, S., Kim, C., Van, T. M., Wachsmuth, L., Polykratis, A., & Pasparakis, M. (2016). RIPK1 counteracts ZBP1-mediated necroptosis to inhibit inflammation. *Nature, 540*(7631), 124-128. doi:10.1038/nature20558

Linkermann, A., Chen, G., Dong, G., Kunzendorf, U., Krautwald, S., & Dong, Z. (2014). Regulated Cell Death in AKI. *Journal of the American Society of Nephrology, 25*(12), 2689-2701. doi:10.1681/asn.2014030262

Linkermann, A., Skouta, R., Himmerkus, N., Mulay, S. R., Dewitz, C., De Zen, F., . . . Krautwald, S. (2014). Synchronized renal tubular cell death involves ferroptosis. *Proc Natl Acad Sci U S A, 111*(47), 16836-16841. doi:10.1073/pnas.1415518111

Liu, L., Kong, M., Gassman, N. R., Freudenthal, B. D., Prasad, R., Zhen, S., . . . Van Houten, B. (2017). PARP1 changes from three-dimensional DNA damage searching to one-dimensional diffusion after auto-PARylation or in the presence of APE1. *Nucleic Acids Res, 45*(22), 12834-12847. doi:10.1093/nar/gkx1047

Liu, Q., Qiu, J., Liang, M., Golinski, J., van Leyen, K., Jung, J. E., . . . Whalen, M. J. (2014). Akt and mTOR mediate programmed necrosis in neurons. *Cell death & disease, 5*(2), e1084-e1084. doi:10.1038/cddis.2014.69

Liu, S., Liu, H., Johnston, A., Hanna-Addams, S., Reynoso, E., Xiang, Y., & Wang, Z. (2017). MLKL forms disulfide bond-dependent amyloid-like polymers to induce necroptosis. *Proceedings of the National Academy of Sciences, 114*(36), E7450-E7459. doi:10.1073/pnas.1707531114

Liu, Y., Wang, W., Li, Y., Xiao, Y., Cheng, J., & Jia, J. (2015). The 5-Lipoxygenase Inhibitor Zileuton Confers Neuroprotection against Glutamate Oxidative Damage by Inhibiting Ferroptosis. *Biol Pharm Bull, 38*(8), 1234-1239. doi:10.1248/bpb.b15-00048

Lockshin, R. A., & Williams, C. M. (1964). Programmed cell death—II. Endocrine potentiation of the breakdown of the intersegmental muscles of silkmoths. *Journal of Insect Physiology, 10*(4), 643-649. doi:https://doi.org/10.1016/0022-1910(64)90034-4

Locksley, R. M., Killeen, N., & Lenardo, M. J. (2001). The TNF and TNF Receptor Superfamilies: Integrating Mammalian Biology. *Cell, 104*(4), 487-501. doi:https://doi.org/10.1016/S0092-8674(01)00237-9

Lonskaya, I., Potaman, V. N., Shlyakhtenko, L. S., Oussatcheva, E. A., Lyubchenko, Y. L., & Soldatenkov, V. A. (2005). Regulation of poly (ADP-ribose) polymerase-1 by DNA structure-specific binding. *Journal of Biological Chemistry, 280*(17), 17076-17083.

Loschen, G., Azzi, A., Richter, C., & Flohé, L. (1974). Superoxide radicals as precursors of mitochondrial hydrogen peroxide. *FEBS Lett, 42*(1), 68-72.

Lu, S. C. (2009). Regulation of glutathione synthesis. *Molecular Aspects of Medicine, 30*(1), 42-59. doi:https://doi.org/10.1016/j.mam.2008.05.005

Luijsterburg, M. S., de Krijger, I., Wiegant, W. W., Shah, R. G., Smeenk, G., de Groot, A. J. L., . . . van Attikum, H. (2016). PARP1 Links CHD2-Mediated Chromatin Expansion and H3.3 Deposition to DNA Repair by Non-homologous End-Joining. *Molecular cell, 61*(4), 547-562. doi:10.1016/j.molcel.2016.01.019

Luo, M., Wu, L., Zhang, K., Wang, H., Zhang, T., Gutierrez, L., . . . Yang, Y. (2018). miR-137 regulates ferroptosis by targeting glutamine transporter SLC1A5 in melanoma. *Cell Death & Differentiation, 25*(8), 1457-1472. doi:10.1038/s41418-017-0053-8

Ma, J., Lim, C., Sacher, J. R., Van Houten, B., Qian, W., & Wipf, P. (2015). Mitochondrial targeted beta-lapachone induces mitochondrial dysfunction and catastrophic vacuolization in cancer cells. *Bioorg Med Chem Lett, 25*(21), 4828-4833. doi:10.1016/j.bmcl.2015.06.073

Ma, Y., de Groot, H., Liu, Z., Hider, R. C., & Petrat, F. (2006). Chelation and determination of labile iron in primary hepatocytes by pyridinone fluorescent probes. *Biochemical Journal, 395*(1), 49-55.

Macias, C. A., Chiao, J. W., Xiao, J., Arora, D. S., Tyurina, Y. Y., Delude, R. L., . . . Fink, M. P. (2007). Treatment with a novel hemigramicidin-TEMPO conjugate prolongs survival in a rat model of lethal hemorrhagic shock. *Ann Surg, 245*(2), 305-314. doi:10.1097/01.sla.0000236626.57752.8e

00000658-200702000-00021 [pii]

Mailloux, R. J., Young, A., O'Brien, M., & Gill, R. M. (2018). Simultaneous Measurement of Superoxide/Hydrogen Peroxide and NADH Production by Flavin-containing Mitochondrial Dehydrogenases. *Journal of Visualized Experiments : JoVE*(132). doi:10.3791/56975

Maltseva, E. A., Rechkunova, N. I., Sukhanova, M. V., & Lavrik, O. I. (2015). Poly(ADP-ribose) Polymerase 1 Modulates Interaction of the Nucleotide Excision Repair Factor XPC-RAD23B with DNA via Poly(ADP-ribosyl)ation. *J Biol Chem, 290*(36), 21811-21820. doi:10.1074/jbc.M115.646638

Mandal, P., Berger, S. B., Pillay, S., Moriwaki, K., Huang, C., Guo, H., . . . Kaiser, W. J. (2014). RIP3 induces apoptosis independent of pronecrotic kinase activity. *Molecular cell, 56*(4), 481-495. doi:10.1016/j.molcel.2014.10.021

Mandir, A. S., Poitras, M. F., Berliner, A. R., Herring, W. J., Guastella, D. B., Feldman, A., . . . Dawson, V. L. (2000). NMDA but not non-NMDA excitotoxicity is mediated by Poly(ADP-ribose) polymerase. *J Neurosci, 20*(21), 8005-8011. Retrieved from https://www.ncbi.nlm.nih.gov/pubmed/11050121

Marrink, S. J., Risselada, H. J., Yefimov, S., Tieleman, D. P., & de Vries, A. H. (2007). The MARTINI force field: coarse grained model for biomolecular simulations. *J Phys Chem B, 111*(27), 7812-7824. doi:10.1021/jp071097f

Martin-Sanchez, D., Ruiz-Andres, O., Poveda, J., Carrasco, S., Cannata-Ortiz, P., Sanchez-Niño, M. D., . . . Sanz, A. B. (2017). Ferroptosis, but Not Necroptosis, Is Important in Nephrotoxic Folic Acid–Induced AKI. *Journal of the American Society of Nephrology, 28*(1), 218-229. doi:10.1681/asn.2015121376

Martinez, J. (2017). Prix Fixe: Efferocytosis as a Four-Course Meal. *Current topics in microbiology and immunology, 403*, 1-36. doi:10.1007/82_2015_467

Martire, S., Mosca, L., & d'Erme, M. (2015). PARP-1 involvement in neurodegeneration: A focus on Alzheimer's and Parkinson's diseases. *Mech Ageing Dev, 146-148*, 53-64. doi:10.1016/j.mad.2015.04.001

Masmoudi, A., Islam, F., & Mandel, P. (1988a). ADP-ribosylation of highly purified rat brain mitochondria. *J Neurochem, 51*(1), 188-193. Retrieved from https://www.ncbi.nlm.nih.gov/pubmed/2837535

Masmoudi, A., Islam, F., & Mandel, P. (1988b). ADP-Ribosylation of Highly Purified Rat Brain Mitochondria. *J Neurochem, 51*(1), 188-193. doi:10.1111/j.1471-4159.1988.tb04854.x

Masmoudi, A., & Mandel, P. (1987). ADP-ribosyl transferase and NAD glycohydrolase activities in rat liver mitochondria. *Biochemistry, 26*(7), 1965-1969. doi:10.1021/bi00381a027

Mayaan, E., Moser, A., MacKerell, A. D., Jr., & York, D. M. (2007). CHARMM force field parameters for simulation of reactive intermediates in native and thio-substituted ribozymes. *J Comput Chem, 28*(2), 495-507. doi:10.1002/jcc.20474

Mehta, A., & Haber, J. E. (2014). Sources of DNA double-strand breaks and models of recombinational DNA repair. *Cold Spring Harb Perspect Biol, 6*(9), a016428-a016428. doi:10.1101/cshperspect.a016428

Meijer, A., Brouwer, A., Reijngoud, D., Hoek, J., & Tager, J. (1972). Transport of glutamate in rat-liver mitochondria. *Biochimica et Biophysica Acta (BBA)-Bioenergetics, 283*(3), 421-429.

Meister, A. (1988). Glutathione metabolism and its selective modification. *Journal of Biological Chemistry, 263*(33), 17205-17208.

Meister, A., & Anderson, M. E. (1983). Glutathione. *Annu Rev Biochem, 52*, 711-760. doi:10.1146/annurev.bi.52.070183.003431

Meng, H., Liu, Z., Li, X., Wang, H., Jin, T., Wu, G., . . . Yuan, J. (2018). Death-domain dimerization-mediated activation of RIPK1 controls necroptosis and RIPK1-dependent apoptosis. *Proceedings of the National Academy of Sciences of the United States of America, 115*(9), E2001-E2009. doi:10.1073/pnas.1722013115

Merkofer, M., Kissner, R., Hider, R. C., Brunk, U. T., & Koppenol, W. H. (2006). Fenton chemistry and iron chelation under physiologically relevant conditions: electrochemistry and kinetics. *Chem Res Toxicol, 19*(10), 1263-1269.

Meyer-Ficca, M. L., Meyer, R. G., Coyle, D. L., Jacobson, E. L., & Jacobson, M. K. (2004). Human poly(ADP-ribose) glycohydrolase is expressed in alternative splice variants yielding isoforms that localize to different cell compartments. *Exp Cell Res, 297*(2), 521-532. doi:10.1016/j.yexcr.2004.03.050

Meyer, R. G., Meyer-Ficca, M. L., Whatcott, C. J., Jacobson, E. L., & Jacobson, M. K. (2007). Two small enzyme isoforms mediate mammalian mitochondrial poly(ADP-ribose) glycohydrolase (PARG) activity. *Exp Cell Res, 313*(13), 2920-2936. doi:10.1016/j.yexcr.2007.03.043

Micheau, O., & Tschopp, J. (2003). Induction of TNF receptor I-mediated apoptosis via two sequential signaling complexes. *Cell, 114*(2), 181-190.

Moerke, C., Bleibaum, F., Kunzendorf, U., & Krautwald, S. (2019). Combined Knockout of RIPK3 and MLKL Reveals Unexpected Outcome in Tissue Injury and Inflammation. *Frontiers in Cell and Developmental Biology, 7*(19). doi:10.3389/fcell.2019.00019

Moroni, F., Meli, E., Peruginelli, F., Chiarugi, A., Cozzi, A., Picca, R., . . . Pellegrini-Giampietro, D. E. (2001). Poly(ADP-ribose) polymerase inhibitors attenuate necrotic but not apoptotic neuronal death in experimental models of cerebral ischemia. *Cell Death Differ, 8*(9), 921-932. doi:10.1038/sj.cdd.4400884

Mosgoeller, W., Steiner, M., Hozák, P., Penner, E., & Wesierska-Gadek, J. (1996). Nuclear architecture and ultrastructural distribution of poly(ADP-ribosyl)transferase, a multifunctional enzyme. *J Cell Sci, 109 (Pt 2)*, 409-418.

Müller, T., Dewitz, C., Schmitz, J., Schröder, A. S., Bräsen, J. H., Stockwell, B. R., . . . Krautwald, S. (2017). Necroptosis and ferroptosis are alternative cell death pathways that operate in acute kidney failure. *Cellular and Molecular Life Sciences, 74*(19), 3631-3645. doi:10.1007/s00018-017-2547-4

Murai, J., Huang, S. Y., Das, B. B., Renaud, A., Zhang, Y., Doroshow, J. H., . . . Pommier, Y. (2012). Trapping of PARP1 and PARP2 by Clinical PARP Inhibitors. *Cancer Res, 72*(21), 5588-5599. doi:10.1158/0008-5472.CAN-12-2753

Murphy, J. M., Czabotar, P. E., Hildebrand, J. M., Lucet, I. S., Zhang, J. G., Alvarez-Diaz, S., . . . Alexander, W. S. (2013). The pseudokinase MLKL mediates necroptosis via a molecular switch mechanism. *Immunity, 39*(3), 443-453. doi:10.1016/j.immuni.2013.06.018

Murphy, M. P. (2008). Targeting lipophilic cations to mitochondria. *Biochim Biophys Acta, 1777*(7-8), 1028-1031. doi:10.1016/j.bbabio.2008.03.029

Nailwal, H., & Chan, F. K.-M. (2019). Necroptosis in anti-viral inflammation. *Cell Death & Differentiation, 26*(1), 4-13. doi:10.1038/s41418-018-0172-x

Narne, P., Pandey, V., Simhadri, P. K., & Phanithi, P. B. (2017). Poly(ADP-ribose)polymerase-1 hyperactivation in neurodegenerative diseases: The death knell tolls for neurons. *Semin Cell Dev Biol, 63*, 154-166. doi:10.1016/j.semcdb.2016.11.007

Nogueira, V., & Hay, N. (2013). Molecular pathways: reactive oxygen species homeostasis in cancer cells and implications for cancer therapy. *Clinical cancer research : an official journal of the American Association for Cancer Research, 19*(16), 4309-4314. doi:10.1158/1078-0432.CCR-12-1424

Noh, H. S., Hah, Y.-S., Zada, S., Ha, J. H., Sim, G., Hwang, J. S., . . . Kim, D. R. (2016). PEBP1, a RAF kinase inhibitory protein, negatively regulates starvation-induced autophagy by direct interaction with LC3. *Autophagy, 12*(11), 2183-2196. doi:10.1080/15548627.2016.1219013

Nowsheen, S., & Yang, E. S. (2012). THE INTERSECTION BETWEEN DNA DAMAGE RESPONSE AND CELL DEATH PATHWAYS. *Experimental oncology, 34*(3), 243-254. Retrieved from http://www.ncbi.nlm.nih.gov/pmc/articles/PMC3754840/

O'Brien, M., Chalker, J., Slade, L., Gardiner, D., & Mailloux, R. J. (2017). Protein S-glutathionylation alters superoxide/hydrogen peroxide emission from pyruvate dehydrogenase complex. *Free Radic Biol Med, 106*, 302-314. doi:10.1016/j.freeradbiomed.2017.02.046

Oikawa, A., Tohda, H., Kanai, M., Miwa, M., & Sugimura, T. (1980). Inhibitors of poly (adenosine diphosphate ribose) polymerase induce sister chromatid exchanges. *Biochem Biophys Res Commun, 97*(4), 1311-1316.

Oliver, F. J., Ménissier-de Murcia, J., Nacci, C., Decker, P., Andriantsitohaina, R., Muller, S., . . . de Murcia, G. (1999). Resistance to endotoxic shock as a consequence of defective NF-

kappaB activation in poly (ADP-ribose) polymerase-1 deficient mice. *Embo j, 18*(16), 4446-4454. doi:10.1093/emboj/18.16.4446

Pachkowski, B. F., Tano, K., Afonin, V., Elder, R. H., Takeda, S., Watanabe, M., . . . Nakamura, J. (2009). Cells deficient in PARP-1 show an accelerated accumulation of DNA single strand breaks, but not AP sites, over the PARP-1-proficient cells exposed to MMS. *Mutation Research/Fundamental and Molecular Mechanisms of Mutagenesis, 671*(1-2), 93-99.

Pasparakis, M., & Vandenabeele, P. (2015). Necroptosis and its role in inflammation. *Nature, 517*(7534), 311-320. doi:10.1038/nature14191

Patel, S. J., Frey, A. G., Palenchar, D. J., Achar, S., Bullough, K. Z., Vashisht, A., . . . Philpott, C. C. (2019). A PCBP1–BolA2 chaperone complex delivers iron for cytosolic [2Fe–2S] cluster assembly. *Nat Chem Biol, 15*(9), 872-881.

Penning, T. D., Zhu, G. D., Gandhi, V. B., Gong, J., Liu, X., Shi, Y., . . . Giranda, V. L. (2009). Discovery of the Poly(ADP-ribose) polymerase (PARP) inhibitor 2-[(R)-2-methylpyrrolidin-2-yl]-1H-benzimidazole-4-carboxamide (ABT-888) for the treatment of cancer. *J Med Chem, 52*(2), 514-523. doi:10.1021/jm801171j

Petrat, F., de Groot, H., Sustmann, R., & Rauen, U. (2002). The chelatable iron pool in living cells: a methodically defined quantity. *Biological chemistry, 383*(3-4), 489-502.

Philpott, C. C., & Jadhav, S. (2019). The ins and outs of iron: Escorting iron through the mammalian cytosol. *Free Radical Biology and Medicine, 133*, 112-117.

Pines, A., Vrouwe, M. G., Marteijn, J. A., Typas, D., Luijsterburg, M. S., Cansoy, M., . . . Matsumoto, S. (2012). PARP1 promotes nucleotide excision repair through DDB2 stabilization and recruitment of ALC1. *Journal of Cell Biology, 199*(2), 235-249.

Pion, E., Ullmann, G. M., Amé, J.-C., Gérard, D., de Murcia, G., & Bombarda, E. (2005). DNA-induced dimerization of poly (ADP-ribose) polymerase-1 triggers its activation. *Biochemistry, 44*(44), 14670-14681.

Polykratis, A., Hermance, N., Zelic, M., Roderick, J., Kim, C., Van, T.-M., . . . Kelliher, M. A. (2014). Cutting edge: RIPK1 Kinase inactive mice are viable and protected from TNF-induced necroptosis in vivo. *J Immunol, 193*(4), 1539-1543. doi:10.4049/jimmunol.1400590

Polyzos, A., Holt, A., Brown, C., Cosme, C., Wipf, P., Gomez-Marin, A., . . . McMurray, C. T. (2016). Mitochondrial targeting of XJB-5-131 attenuates or improves pathophysiology in HdhQ150 animals with well-developed disease phenotypes. *Hum Mol Genet, 25*(9), 1792-1802. doi:10.1093/hmg/ddw051

Polyzos, A. A., Wood, N. I., Williams, P., Wipf, P., Morton, A. J., & McMurray, C. T. (2018). XJB-5-131-mediated improvement in physiology and behaviour of the R6/2 mouse model of Huntington's disease is age- and sex- dependent. *PLoS One, 13*(4), e0194580. doi:10.1371/journal.pone.0194580

Pommier, Y., O'Connor, M. J., & de Bono, J. (2016). Laying a trap to kill cancer cells: PARP inhibitors and their mechanisms of action. *Sci Transl Med, 8*(362), 362ps317. doi:10.1126/scitranslmed.aaf9246

R, T. B., Jeffrey, A., Siahaan, T. J., Gangwar, S., & Pauletti, G. M. (1997). Improvement of oral peptide bioavailability: Peptidomimetics and prodrug strategies. *Adv Drug Deliv Rev, 27*(2-3), 235-256. Retrieved from http://www.ncbi.nlm.nih.gov/pubmed/10837560

Raju, S., Whalen, D. M., Mengistu, M., Swanson, C., Quinn, J. G., Taylor, S. S., . . . Shaw, A. S. (2018). Kinase domain dimerization drives RIPK3-dependent necroptosis. *Sci Signal, 11*(544), eaar2188. doi:10.1126/scisignal.aar2188

Ray Chaudhuri, A., & Nussenzweig, A. (2017). The multifaceted roles of PARP1 in DNA repair and chromatin remodelling. *Nature reviews Molecular cell biology, 18*(10), 610-621. doi:10.1038/nrm.2017.53

Reimann, I., Huth, A., Thiele, H., & Thiele, B. J. (2002). Suppression of 15-lipoxygenase synthesis by hnRNP E1 is dependent on repetitive nature of LOX mRNA 3'-UTR control element DICE. *J Mol Biol, 315*(5), 965-974. doi:10.1006/jmbi.2001.5315

Reshi, M. L., Su, Y.-C., & Hong, J.-R. (2014). RNA Viruses: ROS-Mediated Cell Death. *International Journal of Cell Biology, 2014*, 467452. doi:10.1155/2014/467452

Reynolds, P., Cooper, S., Lomax, M., & O'Neill, P. (2015). Disruption of PARP1 function inhibits base excision repair of a sub-set of DNA lesions. *Nucleic Acids Res, 43*(8), 4028-4038. doi:10.1093/nar/gkv250

Richter, C., Winterhalter, K. H., Baumhuter, S., Lotscher, H. R., & Moser, B. (1983). ADP-ribosylation in inner membrane of rat liver mitochondria. *Proc Natl Acad Sci U S A, 80*(11), 3188-3192. Retrieved from https://www.ncbi.nlm.nih.gov/pubmed/6574480

Rodriguez, D. A., Weinlich, R., Brown, S., Guy, C., Fitzgerald, P., Dillon, C. P., . . . Green, D. R. (2016). Characterization of RIPK3-mediated phosphorylation of the activation loop of MLKL during necroptosis. *Cell Death Differ, 23*(1), 76-88. doi:10.1038/cdd.2015.70

Rossi, M. N., Carbone, M., Mostocotto, C., Mancone, C., Tripodi, M., Maione, R., & Amati, P. (2009). Mitochondrial Localization of PARP-1 Requires Interaction with Mitofilin and Is Involved in the Maintenance of Mitochondrial DNA Integrity. *Journal of Biological Chemistry, 284*(46), 31616-31624. doi:10.1074/jbc.M109.025882

Royce, G. H., Brown-Borg, H. M., & Deepa, S. S. (2019). The potential role of necroptosis in inflammaging and aging. *GeroScience, 41*(6), 795-811. doi:10.1007/s11357-019-00131-w

Ruscetti, T., Lehnert, B. E., Halbrook, J., Le Trong, H., Hoekstra, M. F., Chen, D. J., & Peterson, S. R. (1998). Stimulation of the DNA-dependent protein kinase by poly(ADP-ribose) polymerase. *J Biol Chem, 273*(23), 14461-14467. doi:10.1074/jbc.273.23.14461

Sagristá, M. L., GarcÍa, A. F., De Madariaga, M. A., & Mora, M. (2002). Antioxidant and pro-oxidant effect of the thiolic compounds N-acetyl-L-cysteine and glutathione against free radical-induced lipid peroxidation. *Free Radic Res, 36*(3), 329-340.

Sarhan, M., Land, W. G., Tonnus, W., Hugo, C. P., & Linkermann, A. (2018). Origin and Consequences of Necroinflammation. *Physiol Rev, 98*(2), 727-780. doi:10.1152/physrev.00041.2016

Sasaki, T., Sato, Y., Higashiyama, T., & Sasaki, N. (2017). Live imaging reveals the dynamics and regulation of mitochondrial nucleoids during the cell cycle in Fucci2-HeLa cells. *Scientific Reports, 7*(1), 11257. doi:10.1038/s41598-017-10843-8

Satchell, M. A., Zhang, X., Kochanek, P. M., Dixon, C. E., Jenkins, L. W., Melick, J., . . . Clark, R. S. (2003). A dual role for poly-ADP-ribosylation in spatial memory acquisition after traumatic brain injury in mice involving NAD+ depletion and ribosylation of 14-3-3gamma. *J Neurochem, 85*(3), 697-708.

Schopfer, F. J., Cipollina, C., & Freeman, B. A. (2011). Formation and signaling actions of electrophilic lipids. *Chemical reviews, 111*(10), 5997-6021. doi:10.1021/cr200131e

Schultz, N., Lopez, E., Saleh-Gohari, N., & Helleday, T. (2003). Poly(ADP-ribose) polymerase (PARP-1) has a controlling role in homologous recombination. *Nucleic Acids Research, 31*(17), 4959-4964. doi:10.1093/nar/gkg703

Schweichel, J. U., & Merker, H. J. (1973). The morphology of various types of cell death in prenatal tissues. *Teratology, 7*(3), 253-266.

Seiler, A., Schneider, M., Forster, H., Roth, S., Wirth, E. K., Culmsee, C., . . . Conrad, M. (2008). Glutathione peroxidase 4 senses and translates oxidative stress into 12/15-lipoxygenase dependent- and AIF-mediated cell death. *Cell metabolism, 8*(3), 237-248. doi:10.1016/j.cmet.2008.07.005

Seo, J., Lee, E. W., Sung, H., Seong, D., Dondelinger, Y., Shin, J., . . . Song, J. (2016). CHIP controls necroptosis through ubiquitylation- and lysosome-dependent degradation of RIPK3. *Nat Cell Biol, 18*(3), 291-302. doi:10.1038/ncb3314

Shah, R., Shchepinov, M. S., & Pratt, D. A. (2018). Resolving the Role of Lipoxygenases in the Initiation and Execution of Ferroptosis. *ACS Central Science, 4*(3), 387-396. doi:10.1021/acscentsci.7b00589

Sharma, A., Singh, K., & Almasan, A. (2012). Histone H2AX phosphorylation: a marker for DNA damage. *Methods Mol Biol, 920*, 613-626. doi:10.1007/978-1-61779-998-3_40

Shen, Y., Aoyagi-Scharber, M., & Wang, B. (2015). Trapping Poly(ADP-Ribose) Polymerase. *J Pharmacol Exp Ther, 353*(3), 446-457. doi:10.1124/jpet.114.222448

Simbulan-Rosenthal, C. M., Haddad, B. R., Rosenthal, D. S., Weaver, Z., Coleman, A., Luo, R., . . . Smulson, M. E. (1999). Chromosomal aberrations in PARP(-/-) mice: genome stabilization in immortalized cells by reintroduction of poly(ADP-ribose) polymerase cDNA. *Proceedings of the National Academy of Sciences of the United States of America, 96*(23), 13191-13196. Retrieved from http://www.ncbi.nlm.nih.gov/pubmed/10557296

Sisay, M., & Edessa, D. (2017). PARP inhibitors as potential therapeutic agents for various cancers: focus on niraparib and its first global approval for maintenance therapy of gynecologic cancers. *Gynecol Oncol Res Pract, 4*, 18. doi:10.1186/s40661-017-0055-8

Skoda, E. M., Davis, G. C., & Wipf, P. (2012). Allylic Amines as Key Building Blocks in the Synthesis of (E)-Alkene Peptide Isosteres. *Org Process Res Dev, 16*(1), 26-34. doi:10.1021/op2002613

Somosy, Z., Horvath, G., Telbisz, A., Rez, G., & Palfia, Z. (2002). Morphological aspects of ionizing radiation response of small intestine. *Micron, 33*(2), 167-178.

Spickett, C. M. (2013). The lipid peroxidation product 4-hydroxy-2-nonenal: advances in chemistry and analysis. *Redox Biology, 1*(1), 145-152.

Stein, L. R., & Imai, S. (2012). The dynamic regulation of NAD metabolism in mitochondria. *Trends Endocrinol Metab, 23*(9), 420-428. doi:10.1016/j.tem.2012.06.005

Stoyanovsky, D. A., Tyurina, Y. Y., Shrivastava, I., Bahar, I., Tyurin, V. A., Protchenko, O., . . . Kagan, V. E. (2019). Iron catalysis of lipid peroxidation in ferroptosis: Regulated enzymatic or random free radical reaction? *Free Radic Biol Med, 133*, 153-161. doi:10.1016/j.freeradbiomed.2018.09.008

Sturgeon, B. E., Sipe, H. J., Barr, D. P., Corbett, J. T., Martinez, J. G., & Mason, R. P. (1998). The fate of the oxidizing tyrosyl radical in the presence of glutathione and ascorbate implications for the radical sink hypothesis. *Journal of Biological Chemistry, 273*(46), 30116-30121.

Sun, X., Ou, Z., Xie, M., Kang, R., Fan, Y., Niu, X., . . . Tang, D. (2015). HSPB1 as a novel regulator of ferroptotic cancer cell death. *Oncogene, 34*(45), 5617-5625. doi:10.1038/onc.2015.32

Sun, X., Shih, A. Y., Johannssen, H. C., Erb, H., Li, P., & Murphy, T. H. (2006). Two-photon imaging of glutathione levels in intact brain indicates enhanced redox buffering in developing neurons and cells at the cerebrospinal fluid and blood-brain interface. *Journal of Biological Chemistry, 281*(25), 17420-17431.

Suthanthiran, M., Anderson, M. E., Sharma, V. K., & Meister, A. (1990). Glutathione regulates activation-dependent DNA synthesis in highly purified normal human T lymphocytes stimulated via the CD2 and CD3 antigens. *Proceedings of the National Academy of Sciences, 87*(9), 3343-3347.

Szczesny, B., Brunyanszki, A., Olah, G., Mitra, S., & Szabo, C. (2014). Opposing roles of mitochondrial and nuclear PARP1 in the regulation of mitochondrial and nuclear DNA integrity: implications for the regulation of mitochondrial function. *Nucleic Acids Res, 42*(21), 13161-13173. doi:10.1093/nar/gku1089

Szczesny, B., Brunyanszki, A., Olah, G., Mitra, S., & Szabo, C. (2014). Opposing roles of mitochondrial and nuclear PARP1 in the regulation of mitochondrial and nuclear DNA integrity: implications for the regulation of mitochondrial function. *Nucleic Acids Research, 42*(21), 13161-13173. doi:10.1093/nar/gku1089

Teloni, F., & Altmeyer, M. (2016). Readers of poly(ADP-ribose): designed to be fit for purpose. *Nucleic Acids Res, 44*(3), 993-1006. doi:10.1093/nar/gkv1383

Thevakumaran, N., Lavoie, H., Critton, D. A., Tebben, A., Marinier, A., Sicheri, F., & Therrien, M. (2015). Crystal structure of a BRAF kinase domain monomer explains basis for allosteric regulation. *Nat Struct Mol Biol, 22*(1), 37-43. doi:10.1038/nsmb.2924

Thompson, C. B. (1995). Apoptosis in the pathogenesis and treatment of disease. *Science, 267*(5203), 1456-1462.

Tonnus, W., Meyer, C., Paliege, A., Belavgeni, A., von Mässenhausen, A., Bornstein, S. R., . . . Linkermann, A. (2019). The pathological features of regulated necrosis. *The Journal of pathology, 247*(5), 697-707. doi:10.1002/path.5248

Trachootham, D., Alexandre, J., & Huang, P. (2009). Targeting cancer cells by ROS-mediated mechanisms: a radical therapeutic approach? *Nat Rev Drug Discov, 8*(7), 579-591. doi:10.1038/nrd2803

Trott, O., & Olson, A. J. (2010). AutoDock Vina: improving the speed and accuracy of docking with a new scoring function, efficient optimization, and multithreading. *Journal of computational chemistry, 31*(2), 455-461. doi:10.1002/jcc.21334

Tyurina, Y. Y., Tyurin, V. A., Epperly, M. W., Greenberger, J. S., & Kagan, V. E. (2008). Oxidative lipidomics of gamma-irradiation-induced intestinal injury. *Free Radic Biol Med, 44*(3), 299-314. doi:10.1016/j.freeradbiomed.2007.08.021

Ursini, F., & Bindoli, A. (1987). The role of selenium peroxidases in the protection against oxidative damage of membranes. *Chem Phys Lipids, 44*(2-4), 255-276. doi:10.1016/0009-3084(87)90053-3

Van Houten, B., Hunter, S. E., & Meyer, J. N. (2016). Mitochondrial DNA damage induced autophagy, cell death, and disease. *Frontiers in bioscience (Landmark edition), 21*, 42-54. Retrieved from http://www.ncbi.nlm.nih.gov/pmc/articles/PMC4750375/

Vanden Berghe, T., Kaiser, W. J., Bertrand, M. J. M., & Vandenabeele, P. (2015). Molecular crosstalk between apoptosis, necroptosis, and survival signaling. *Molecular & Cellular Oncology, 2*(4), e975093. doi:10.4161/23723556.2014.975093

Veliparib (ABT-888), an Oral PARP Inhibitor, and VX-970, an ATR Inhibitor, in Combination With Cisplatin in People With Refractory Solid Tumors. (2020). *NCT02723864.* Retrieved from https://clinicaltrials.gov/ct2/show/NCT02723864

Vignon, C., Debeissat, C., Georget, M. T., Bouscary, D., Gyan, E., Rosset, P., & Herault, O. (2013). Flow cytometric quantification of all phases of the cell cycle and apoptosis in a two-color fluorescence plot. *PLoS One, 8*(7), e68425. doi:10.1371/journal.pone.0068425

Virág, L., & Szabó, C. (2002). The therapeutic potential of poly(ADP-ribose) polymerase inhibitors. *Pharmacol Rev, 54*(3), 375-429. doi:10.1124/pr.54.3.375

Vodenicharov, M. D., Ghodgaonkar, M. M., Halappanavar, S. S., Shah, R. G., & Shah, G. M. (2005). Mechanism of early biphasic activation of poly(ADP-ribose) polymerase-1 in response to ultraviolet B radiation. *J Cell Sci, 118*(Pt 3), 589-599. doi:10.1242/jcs.01636

Vogt, K. C. (1842). *Untersuchungen über die Entwicklungsgeschichte der Geburtshelferkröte (Alytes obstetricans)*: Jent & Gassmann.

Vyas, S., Chesarone-Cataldo, M., Todorova, T., Huang, Y.-H., & Chang, P. (2013). A systematic analysis of the PARP protein family identifies new functions critical for cell physiology. *Nature communications, 4*(1), 2240. doi:10.1038/ncomms3240

Wagner, L. M. (2015). Profile of veliparib and its potential in the treatment of solid tumors. *Onco Targets Ther, 8*, 1931-1939. doi:10.2147/OTT.S69935

Wajant, H., & Scheurich, P. (2011). TNFR1-induced activation of the classical NF-κB pathway. *Febs j, 278*(6), 862-876. doi:10.1111/j.1742-4658.2011.08015.x

Walsh, D. W. M., Siebenwirth, C., Greubel, C., Ilicic, K., Reindl, J., Girst, S., . . . Dollinger, G. (2017). Live cell imaging of mitochondria following targeted irradiation in situ reveals

rapid and highly localized loss of membrane potential. *Scientific Reports, 7*, 46684-46684. doi:10.1038/srep46684

Wang, H., Meng, H., Li, X., Zhu, K., Dong, K., Mookhtiar, A. K., . . . Yuan, J. (2017). PELI1 functions as a dual modulator of necroptosis and apoptosis by regulating ubiquitination of RIPK1 and mRNA levels of c-FLIP. *Proceedings of the National Academy of Sciences, 114*(45), 11944-11949. doi:10.1073/pnas.1715742114

Wang, H., Sun, L., Su, L., Rizo, J., Liu, L., Wang, L. F., . . . Wang, X. (2014). Mixed lineage kinase domain-like protein MLKL causes necrotic membrane disruption upon phosphorylation by RIP3. *Molecular cell, 54*(1), 133-146. doi:10.1016/j.molcel.2014.03.003

Wang, L., Chang, X., Feng, J., Yu, J., & Chen, G. (2020). TRADD Mediates RIPK1-Independent Necroptosis Induced by Tumor Necrosis Factor. *Frontiers in cell and developmental biology, 7*, 393-393. doi:10.3389/fcell.2019.00393

Wang, M., Wu, W., Wu, W., Rosidi, B., Zhang, L., Wang, H., & Iliakis, G. (2006). PARP-1 and Ku compete for repair of DNA double strand breaks by distinct NHEJ pathways. *Nucleic Acids Res, 34*(21), 6170-6182. doi:10.1093/nar/gkl840

Wang, Y., An, R., Umanah, G. K., Park, H., Nambiar, K., Eacker, S. M., . . . Dawson, T. M. (2016). A nuclease that mediates cell death induced by DNA damage and poly(ADP-ribose) polymerase-1. *Science, 354*(6308), aad6872. doi:10.1126/science.aad6872

Wang, Y., Kim, N. S., Haince, J.-F., Kang, H., David, K. K., Andrabi, S. A., . . . Dawson, T. M. (2011). Poly (ADP-ribose) (PAR) Binding to Apoptosis-Inducing Factor Is Critical For PAR Polymerase-1-Dependent Cell Death (Parthanatos). *Sci Signal, 4*(167), ra20. doi:10.1126/scisignal.2000902

Wang, Y., Kim, N. S., Haince, J. F., Kang, H. C., David, K. K., Andrabi, S. A., . . . Dawson, T. M. (2011). Poly(ADP-ribose) (PAR) binding to apoptosis-inducing factor is critical for PAR polymerase-1-dependent cell death (parthanatos). *Sci Signal, 4*(167), ra20. doi:10.1126/scisignal.2000902

Wang, Y. Q., Wang, P. Y., Wang, Y. T., Yang, G. F., Zhang, A., & Miao, Z. H. (2016). An Update on Poly(ADP-ribose)polymerase-1 (PARP-1) Inhibitors: Opportunities and Challenges in Cancer Therapy. *J Med Chem*. doi:10.1021/acs.jmedchem.6b00055

Wanrooij, P. H., & Chabes, A. (2019). Ribonucleotides in mitochondrial DNA. *FEBS Lett, 593*(13), 1554-1565. doi:10.1002/1873-3468.13440

Watford, M. (2000). Glutamine and Glutamate Metabolism across the Liver Sinusoid. *The Journal of Nutrition, 130*(4), 983S-987S. doi:10.1093/jn/130.4.983S

Welty, S., Teng, Y., Liang, Z., Zhao, W., Sanders, L. H., Greenamyre, J. T., . . . Lan, L. (2018). RAD52 is required for RNA-templated recombination repair in post-mitotic neurons. *J Biol Chem, 293*(4), 1353-1362. doi:10.1074/jbc.M117.808402

Wen, J. J., Yin, Y. W., & Garg, N. J. (2018). PARP1 depletion improves mitochondrial and heart function in Chagas disease: Effects on POLG dependent mtDNA maintenance. *PLoS pathogens, 14*(5), e1007065-e1007065. doi:10.1371/journal.ppat.1007065

Wenzel, S. E., Tyurina, Y. Y., Zhao, J., St Croix, C. M., Dar, H. H., Mao, G., . . . Kagan, V. E. (2017). PEBP1 Wardens Ferroptosis by Enabling Lipoxygenase Generation of Lipid Death Signals. *Cell, 171*(3), 628-641.e626. doi:10.1016/j.cell.2017.09.044

Whalen, M. J., Clark, R. S., Dixon, C. E., Robichaud, P., Marion, D. W., Vagni, V., . . . Kochanek, P. M. (1999). Reduction of cognitive and motor deficits after traumatic brain injury in mice deficient in poly(ADP-ribose) polymerase. *Journal of Cerebral Blood Flow and Metabolism: Official Journal of the International Society of Cerebral Blood Flow and Metabolism, 19*(8), 835-842. doi:10.1097/00004647-199908000-00002

Williams, R. J. P. (1982). Free manganese(II) and iron(II) cations can act as intracellular cell controls. *FEBS Lett, 140*(1), 3-10. doi:10.1016/0014-5793(82)80508-5

Wipf, P., Xiao, J., Jiang, J., Belikova, N. A., Tyurin, V. A., Fink, M. P., & Kagan, V. E. (2005). Mitochondrial targeting of selective electron scavengers: synthesis and biological analysis of hemigramicidin-TEMPO conjugates. *J Am Chem Soc, 127*(36), 12460-12461. doi:10.1021/ja053679l

Wipf, P., Xiao, J., & Stephenson, C. R. (2009). Peptide-Like Molecules (PLMs): A Journey from Peptide Bond Isosteres to Gramicidin S Mimetics and Mitochondrial Targeting Agents. *Chimia (Aarau), 63*(11), 764-775. doi:10.2533/chimia.2009.764

Wisnovsky, S., Jean, S. R., & Kelley, S. O. (2016). Mitochondrial DNA repair and replication proteins revealed by targeted chemical probes. *Nat Chem Biol, 12*(7), 567-573. doi:10.1038/nchembio.2102

Wisnovsky, S., Sack, T., Pagliarini, D. J., Laposa, R. R., & Kelley, S. O. (2018). DNA Polymerase θ Increases Mutational Rates in Mitochondrial DNA. *ACS Chem Biol, 13*(4), 900-908. doi:10.1021/acschembio.8b00072

Witt, A., & Vucic, D. (2017). Diverse ubiquitin linkages regulate RIP kinases-mediated inflammatory and cell death signaling. *Cell Death Differ, 24*(7), 1160-1171. doi:10.1038/cdd.2017.33

Wu, X. N., Yang, Z. H., Wang, X. K., Zhang, Y., Wan, H., Song, Y., . . . Han, J. (2014). Distinct roles of RIP1-RIP3 hetero- and RIP3-RIP3 homo-interaction in mediating necroptosis. *Cell Death Differ, 21*(11), 1709-1720. doi:10.1038/cdd.2014.77

Xiao, J., Weisblum, B., & Wipf, P. (2005). Electrostatic versus steric effects in peptidomimicry: synthesis and secondary structure analysis of gramicidin S analogues with (E)-alkene peptide isosteres. *J Am Chem Soc, 127*(16), 5742-5743. doi:10.1021/ja051002s

Xiao, J., Weisblum, B., & Wipf, P. (2006). Trisubstituted (E)-alkene dipeptide isosteres as beta-turn promoters in the gramicidin S cyclodecapeptide scaffold. *Org Lett, 8*(21), 4731-4734. doi:10.1021/ol0617704

Xie, J., Marusich, M. F., Souda, P., Whitelegge, J., & Capaldi, R. A. (2007). The mitochondrial inner membrane protein Mitofilin exists as a complex with SAM50, metaxins 1 and 2, coiled-coil-helix coiled-coil-helix domain-containing protein 3 and 6 and DnaJC11. *FEBS Lett, 581*(18), 3545-3549. doi:10.1016/j.febslet.2007.06.052

Xie, P., Streu, C., Qin, J., Bregman, H., Pagano, N., Meggers, E., & Marmorstein, R. (2009). The crystal structure of BRAF in complex with an organoruthenium inhibitor reveals a

mechanism for inhibition of an active form of BRAF kinase. *Biochemistry, 48*(23), 5187-5198. doi:10.1021/bi802067u

Xie, T., Peng, W., Liu, Y., Yan, C., Maki, J., Degterev, A., . . . Shi, Y. (2013). Structural basis of RIP1 inhibition by necrostatins. *Structure, 21*(3), 493-499. doi:10.1016/j.str.2013.01.016

Xie, T., Peng, W., Yan, C., Wu, J., Gong, X., & Shi, Y. (2013). Structural insights into RIP3-mediated necroptotic signaling. *Cell Rep, 5*(1), 70-78. doi:10.1016/j.celrep.2013.08.044

Xie, Y., Song, X., Sun, X., Huang, J., Zhong, M., Lotze, M. T., . . . Tang, D. (2016). Identification of baicalein as a ferroptosis inhibitor by natural product library screening. *Biochem Biophys Res Commun, 473*(4), 775-780. doi:10.1016/j.bbrc.2016.03.052

Xie, Y., Zhao, Y., Shi, L., Li, W., Chen, K., Li, M., . . . Xiao, H. (2020). Gut epithelial TSC1/mTOR controls RIPK3-dependent necroptosis in intestinal inflammation and cancer. *J Clin Invest, 130*(4), 2111-2128. doi:10.1172/jci133264

Xu, Y., Huang, S., Liu, Z.-G., & Han, J. (2006). Poly(ADP-ribose) polymerase-1 signaling to mitochondria in necrotic cell death requires RIP1/TRAF2-mediated JNK1 activation. *J Biol Chem, 281*(13), 8788-8795. doi:10.1074/jbc.M508135200

Xun, Z., Rivera-Sanchez, S., Ayala-Pena, S., Lim, J., Budworth, H., Skoda, E. M., . . . McMurray, C. T. (2012). Targeting of XJB-5-131 to mitochondria suppresses oxidative DNA damage and motor decline in a mouse model of Huntington's disease. *Cell Rep, 2*(5), 1137-1142. doi:10.1016/j.celrep.2012.10.001

Yamada, Y., & Harashima, H. (2008). Mitochondrial drug delivery systems for macromolecule and their therapeutic application to mitochondrial diseases. *Adv Drug Deliv Rev, 60*(13-14), 1439-1462. doi:10.1016/j.addr.2008.04.016

Yamamoto, N., Koga, N., & Nagaoka, M. (2012). Ferryl–Oxo species produced from Fenton's Reagent via a two-step pathway: minimum free-energy path analysis. *The Journal of Physical Chemistry B, 116*(48), 14178-14182.

Yanatori, I., Richardson, D. R., Imada, K., & Kishi, F. (2016). Iron export through the transporter ferroportin 1 is modulated by the iron chaperone PCBP2. *Journal of Biological Chemistry, 291*(33), 17303-17318.

Yanatori, I., Richardson, D. R., Toyokuni, S., & Kishi, F. (2017). The iron chaperone poly (rC)-binding protein 2 forms a metabolon with the heme oxygenase 1/cytochrome P450 reductase complex for heme catabolism and iron transfer. *Journal of Biological Chemistry, 292*(32), 13205-13229.

Yang, J. L., Sykora, P., Wilson, D. M., 3rd, Mattson, M. P., & Bohr, V. A. (2011). The excitatory neurotransmitter glutamate stimulates DNA repair to increase neuronal resiliency. *Mech Ageing Dev, 132*(8-9), 405-411. doi:10.1016/j.mad.2011.06.005

Yang, W. S., Kim, K. J., Gaschler, M. M., Patel, M., Shchepinov, M. S., & Stockwell, B. R. (2016). Peroxidation of polyunsaturated fatty acids by lipoxygenases drives ferroptosis. *Proceedings of the National Academy of Sciences, 113*(34), E4966. Retrieved from http://www.pnas.org/content/113/34/E4966.abstract

Yang, W. S., SriRamaratnam, R., Welsch, M. E., Shimada, K., Skouta, R., Viswanathan, V. S., . . . Stockwell, B. R. (2014). Regulation of Ferroptotic Cancer Cell Death by GPX4. *Cell, 156*(0), 317-331. doi:10.1016/j.cell.2013.12.010

Yang, W. S., & Stockwell, B. R. (2008). Synthetic lethal screening identifies compounds activating iron-dependent, nonapoptotic cell death in oncogenic-RAS-harboring cancer cells. *Chem Biol, 15*(3), 234-245. doi:10.1016/j.chembiol.2008.02.010

Yant, L. J., Ran, Q., Rao, L., Van Remmen, H., Shibatani, T., Belter, J. G., . . . Prolla, T. A. (2003). The selenoprotein GPX4 is essential for mouse development and protects from radiation and oxidative damage insults. *Free Radic Biol Med, 34*(4), 496-502. doi:10.1016/s0891-5849(02)01360-6

Yao, X., Zhang, Y., Hao, J., Duan, H.-Q., Zhao, C.-X., Sun, C., . . . Li, W.-X. (2019). Deferoxamine promotes recovery of traumatic spinal cord injury by inhibiting ferroptosis. *Neural Regeneration Research, 14*(3), 532.

Yeung, K., Seitz, T., Li, S., Janosch, P., McFerran, B., Kaiser, C., . . . Kolch, W. (1999). Suppression of Raf-1 kinase activity and MAP kinase signalling by RKIP. *Nature, 401*, 173. doi:10.1038/43686

Yeung, K. C., Rose, D. W., Dhillon, A. S., Yaros, D., Gustafsson, M., Chatterjee, D., . . . Sedivy, J. M. (2001). Raf kinase inhibitor protein interacts with NF-kappaB-inducing kinase and TAK1 and inhibits NF-kappaB activation. *Mol Cell Biol, 21*(21), 7207-7217. doi:10.1128/mcb.21.21.7207-7217.2001

Ying, W., Alano, C. C., Garnier, P., & Swanson, R. A. (2005). NAD+ as a metabolic link between DNA damage and cell death. *J Neurosci Res, 79*(1-2), 216-223. doi:10.1002/jnr.20289

Yoo, S.-E., Chen, L., Na, R., Liu, Y., Rios, C., Van Remmen, H., . . . Ran, Q. (2012). Gpx4 ablation in adult mice results in a lethal phenotype accompanied by neuronal loss in brain. *Free Radic Biol Med, 52*(9), 1820-1827. doi:10.1016/j.freeradbiomed.2012.02.043

Yu, S. W., Wang, H., Poitras, M. F., Coombs, C., Bowers, W. J., Federoff, H. J., . . . Dawson, V. L. (2002). Mediation of poly(ADP-ribose) polymerase-1-dependent cell death by apoptosis-inducing factor. *Science, 297*(5579), 259-263. doi:10.1126/science.1072221

Yuan, J., Ng, W. H., Lam, P. Y. P., Wang, Y., Xia, H., Yap, J., . . . Hu, J. (2018). The dimer-dependent catalytic activity of RAF family kinases is revealed through characterizing their oncogenic mutants. *Oncogene, 37*(43), 5719-5734. doi:10.1038/s41388-018-0365-2

Zhang, J., Dawson, V. L., Dawson, T. M., & Snyder, S. H. (1994). Nitric oxide activation of poly(ADP-ribose) synthetase in neurotoxicity. *Science, 263*(5147), 687-689.

Zhang, X., Chen, J., Graham, S. H., Du, L., Kochanek, P. M., Draviam, R., . . . Clark, R. S. (2002). Intranuclear localization of apoptosis-inducing factor (AIF) and large scale DNA fragmentation after traumatic brain injury in rats and in neuronal cultures exposed to peroxynitrite. *J Neurochem, 82*(1), 181-191. Retrieved from https://www.ncbi.nlm.nih.gov/pubmed/12091479

Zhang, Y., Su, S. S., Zhao, S., Yang, Z., Zhong, C.-Q., Chen, X., . . . Han, J. (2017). RIP1 autophosphorylation is promoted by mitochondrial ROS and is essential for RIP3

recruitment into necrosome. *Nature communications, 8*(1), 14329. doi:10.1038/ncomms14329

Zheng, L., Bidere, N., Staudt, D., Cubre, A., Orenstein, J., Chan, F. K., & Lenardo, M. (2006). Competitive control of independent programs of tumor necrosis factor receptor-induced cell death by TRADD and RIP1. *Mol Cell Biol, 26*(9), 3505-3513.

Zhou, H. Z., Swanson, R. A., Simonis, U., Ma, X., Cecchini, G., & Gray, M. O. (2006). Poly(ADP-ribose) polymerase-1 hyperactivation and impairment of mitochondrial respiratory chain complex I function in reperfused mouse hearts. *Am J Physiol Heart Circ Physiol, 291*(2), H714-723. doi:10.1152/ajpheart.00823.2005

Zhou, W., & Yuan, J. (2014). Necroptosis in health and diseases. *Seminars in Cell & Developmental Biology, 35*, 14-23. doi:https://doi.org/10.1016/j.semcdb.2014.07.013

Zilka, O., Shah, R., Li, B., Friedmann Angeli, J. P., Griesser, M., Conrad, M., & Pratt, D. A. (2017). On the Mechanism of Cytoprotection by Ferrostatin-1 and Liproxstatin-1 and the Role of Lipid Peroxidation in Ferroptotic Cell Death. *ACS Central Science, 3*(3), 232-243. doi:10.1021/acscentsci.7b00028

Zimmermann, M., Murina, O., Reijns, M. A. M., Agathanggelou, A., Challis, R., Tarnauskaitė, Ž., . . . Durocher, D. (2018). CRISPR screens identify genomic ribonucleotides as a source of PARP-trapping lesions. *Nature, 559*(7713), 285-289. doi:10.1038/s41586-018-0291-z